SEISMIC INVESTIGATION OF DEEP 2D, 3D AND 4D STRUCTURES USING BODY WAVE INTERFEROMETRY, COMPUTER SIMULATIONS AND SEMI-CONVENTIONAL PROCESSING

A Dissertation

Presented to the Faculty of the Graduate School

of Cornell University

in Partial Fulfillment of the Requirements for the Degree of

Doctor of Philosophy

by

Anastasija Cabolova

February 2016

SEISMIC INVESTIGATION OF DEEP 2D, 3D AND 4D STRUCTURES USING BODY WAVE INTERFEROMETRY, COMPUTER SIMULATIONS AND SEMI-CONVENTIONAL PROCESSING

Anastasija Cabolova, Ph.D.

Cornell University 2016

The main focus of this dissertation is retrieval and imaging with virtual body wave reflections extracted from ambient noise record. The advantage of these virtual reflections over surface waves, which require inversion, is the direct relationship between the recorded arrival times and the depth of the imaged interface. However, the virtual reflection retrieval from a seismic noise record can be problematic due to limited amount of body wave sources in the ground. Furthermore, body wave interferometry is sensitive to the 3D distribution of these sources as oppose to effectively 2D distribution of surface wave sources.

The work presented here is focused on the effect of source distribution on the virtual body wave arrivals. We generate models and synthetic seismograms for various source distributions and apply interferometric technique (i.e. cross- and auto-correlation) to retrieve the synthetic virtual direct, reflected and refracted arrivals. We then analyze source distributions that lead to the distortion of these arrivals and rise of spurious arrivals that do not directly correspond to the modeled subsurface structure. Finally, we are able to use the conclusions of this analysis for interpretation of the real data to differentiate between the arrivals directly related to the subsurface and artifacts.

In addition to the main focus of the dissertation, we are presenting work on seismic basement reflections in South-East New Mexico. We have applied ex-

tended correlation technique to extend the vibroseis 3D recording to image deep structures (potentially to crust-mantle discontinuity). We are able to recover a 3D structure associated with the Precambrian basement using conventional processing applied to the extended recording and propose a collaboration between the industry and academia to enable the latter to systematically probe for the deep structures using oil and gas provided datasets. This collaboration will expand the existing database of deep reflections and in some cases can provide a high resolution depth maps of these structures.

The last chapter of this presentation is part of a summer internship project in Shell Oil Company (Houston, TX). This project involved seismic 4D simulations of subsurface response in an enhanced oil recovery (EOR) field. We have established that frequent 4D seismic repeats are necessary in order to confidently interpret dynamic changes in the subsurface properties (e.g. pressure, fluid saturation, temperature) beneath oil production fields that undergo steam injections

.

BIOGRAPHICAL SKETCH

Anastasija was born in Riga, Latvia on September 16th, 1985. She graduated high-school in 2003 Riga and obtained Bachelor Degree in Physics in 2007 from University of Latvia. Anastasija then moved to Boca Raton, Florida with a plan of obtaining a PhD Degree in Physics from Florida Atlantic University (FAU), majoring in Astrophysics. After passing all the qualifying exams Anastasija has decided to graduate FAU with Master's Degree in 2010 and switch the her major to Geophysics. She has entered a PhD program in Geophysics at Cornell University and joined Earth and Atmospheric Sciences Department in CU the same year.

Anastasija moved to Ithaca in summer of 2010. She met her future husband while in grad-school, who at the time was also graduate student in the same department. They got married on September 11th, 2014 in Ithaca, NY.

Anastasija has interned with Shell Oil Company in 2012, 2013 and 2014, and received a full-time job offer at the end of her last internship. She is to begin her new position as Geophysicist after graduating Cornell.

This dissertation is dedicated to all the people I have ever known because interactions with all of them have brought me here. Special thanks to my parents, Viktorija Cabolova and Vladimir Ivanov, whom I love so much and my husband, Andrew K. Melkonian, for his never ending moral support. I also thank my aunt for inviting me to US for the first time when I was 13 and who helped me acclimate to the new life in US once I moved to Florida in 2007. Finally, I would also like to thank my new in-law family, as they have quickly become very close to me, especially Susan Riha, Jeffrey Melkonian, Margaret Riha and Carlo Mandrone.

ACKNOWLEDGEMENTS

I would like to thank TM Schlumberger (Gedco) for providing Vista Seismic processing software and the technical support. Vista seismic processing software was extensively used throughout the duration of my graduate program.

Also, thanks to Robert Herrmann for his software and guidance in surface wave modeling, which is a included in 4th chapter of this dissertation.

I would like to acknowledge the generosity of Fairfield Nodal for providing the New-Mexico seismic data and guidance on the details of the survey, with special thanks to Rob Windels and Joe Dryer.

I thank Lee Bell, Christof Stork and Dace Yacco from Geokinetics for graciously providing Bradford, PE survey recording for our ambient noise interferometry study.

Finally, I would like to thank many colleagues at Shell for their input and guidance: Marcus Patterson, Hossein (Ali) Dortaj, Rob Bialas, Kurang Mehta, Gunnar Holmes, Izu Ariwodo, Barbara Cox, Bob Whale, Barbara Wingate. Also I thank Shell Company for permission to publish the last chapter of this dissertation.

TABLE OF CONTENTS

LIST OF TABLES

LIST OF FIGURES

CHAPTER 1

INTRODUCTION

Seismic interferometry has become a widespread technique to extract subsurface response function from generally discarded portion of seismic recording (i.e. ambient noise). This response function is then transformed into an image of the subsurface by means of inversion or conventional reflection processing. The interest in the buried structures ranges from purely scientific to more practical (e.g. hydro-carbon exploration, well drilling, etc.). Often scientific interest focuses on deeper structures well below sedimentary cover. These structures can be difficult to image using conventional seismic techniques due to limitation of seismic wave penetration depth. On the other hand, unconventional imaging (e.g. seismic interferometry) often lacks resolution of conventional studies.

Some of the sources of the ambient noise used in interferometry are earthquakes, oceanic wave action, ground vibrations produced by human activities etc. These sources produce predominantly surface waves (e.g. Shapiro et al., 2005). Therefore interferometry has been more successful in retrieval of virtual surface wave energy (e.g. Shapiro et al., 2005; Bensen et al., 2007; Yao et al., 2006; Lin et al., 2008).

Body waves can be more problematic to recover using interferometry for reasons discussed in more details in various chapters of this dissertation: proximity of sources and receivers to the surface, sensitivity to 3D source distribution etc. There have been some recent advances made with the body wave interferometry from seismic noise (e.g. Gerstoft et al., 2008; Draganov et al., 2007, 2009; Ruigrok et al., 2011; Poli et al., 2012a; Lin et al., 2013a). Virtual body wave reflection can provide a direct way of imaging subsurface in higher resolution

than imaging with surface waves or teleseismic body waves.

This dissertation's main focus is on imaging of the subsurface using the virtual body wave energy. We analyze distortion in arrival times of these waves and methods of identification of spurious or artificial arrivals (i.e. arrivals that do not correspond to conventional seismic phases) that arise for different distributions of seismic sources. In addition to the work with seismic interferometry, this dissertation includes a demonstration of how modern oil exploration surveys can be analyzed to look deeper into the crust, and a study of 4D monitoring of temporal changes in an oil reservoir. This dissertation is divided into five main chapters.

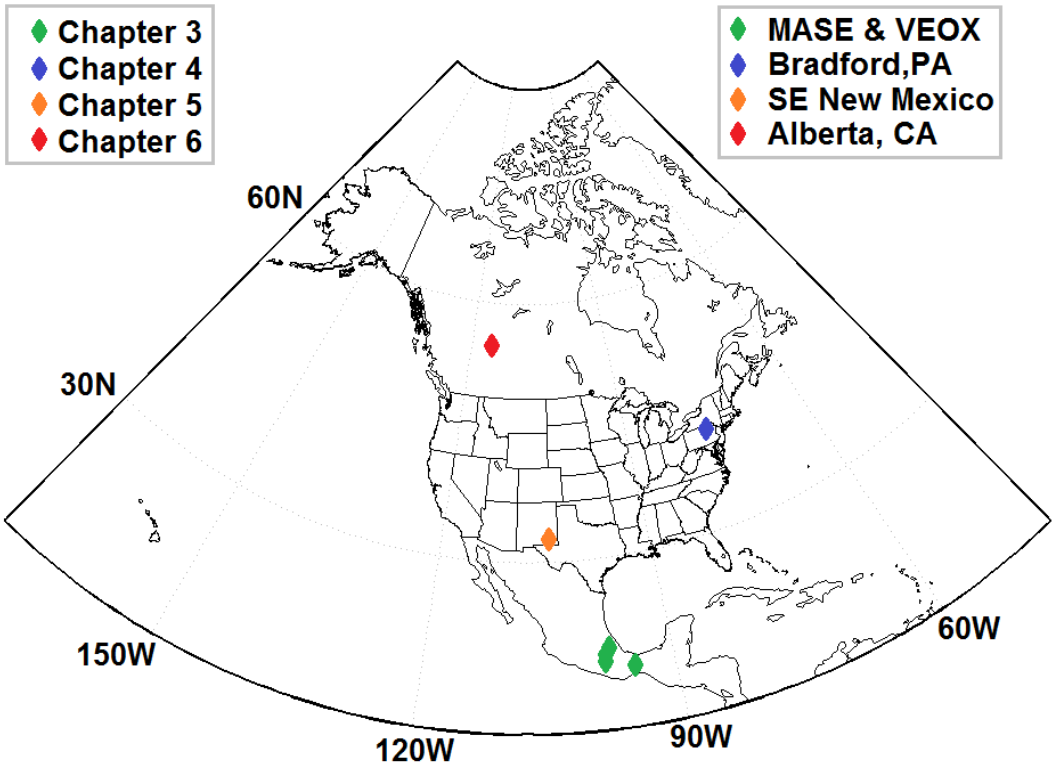

Figure 1.1: Seismic survey locations

The second chapter focuses on results from our synthetic seismic models.

Here, we model virtual source gather and zero-offset reflection profiles produced by body wave interferometry of various 2D P-wave source distributions. Even though a number of models exists that investigate virtual arrivals produced by interferometry (e.g Draganov et al., 2006; Halliday and Curtis, 2008; Mikesell et al., 2009; Snieder and Wapenaar, 2010, etc.), they are often focused on surface waves only (Halliday and Curtis, 2008; Snieder and Wapenaar, 2010) or do not examine the spurious virtual arrivals in significant detail. Therefore, here we focus on body wave interferometry of biased (i.e. asymmetrical relative to the location of a station array) P-wave source distributions to identify and interpret coherent seismic arrivals that do not correspond to conventional seismic phases and are thus often labeled as artifacts. These arrivals often exhibit unrealistic apparent velocities (e.g. too fast for physical waves) and non-causal arrival times. We discuss the appearance of these artifacts in both synthetic reflection profiles produced by auto-correlation as well as shot gathers generated using cross-correlations of seismograms from sources with various depth distributions. We show that relatively deep sources produce stronger and more coherent reflections, especially at small offsets, while shallow sources are more effective in retrieving direct and refracted arrivals. We also show how energy associated with critically refracted energy can be shifted during cross-correlation (Mikesell et al., 2009) with corresponding loss of information about the depth of velocity gradient causing the refraction.

In the third chapter (Chapter 3, Figure 1.1) we focus on a particular geologic setting: the subduction zone. The reasons for our interest in this setting are: (1) in spite of a very great scientific interest, there are still very few high resolution images (by oil industry conventional imaging standards) of the subducting slab, (2) subduction zone setting represents a fertile environment for the application

of seismic interferometry for body wave imaging due to generally high seismic activity, which generates a lot of body wave energy, and (3) they are the setting for major earthquakes and volcanic eruptions that represent major threats to society. Thus, this study investigates 2D reflectivity profiles generated from cross-correlation of local earthquakes in a subduction setting. In this chapter, we compute synthetic seismograms for various quasi-random distributions of subsurface sources (earthquakes) and generate virtual reflection profiles using conventionally processed virtual source gathers. The goal is to identify acquisition strategies that favor the effective extraction of virtual P-wave reflection for a robust common reflection point (CRP) imaging of subducting slabs. Our synthetics shows that this imaging is insensitive to origin time errors. However having an adequate lateral distribution (aperture) of sources is critical. We thus suggest that relatively robust imaging is achievable with modern dense array technologies and levels of seismicity that is characteristic of active subduction zones. We then apply these imaging techniques (both zero-offset and CRP) to earthquakes recorded by MASE and VEOX seismic lines in Mexico (MASE, 2007; VEOX, 2010)

The fourth chapter (Chapter 4, Figure 1.1) describes a passive 3D seismic survey near Bradford, Pennsylvania. The survey was carried out by Geokinetics and consists of approximately 400 vertical component geophones in a sparse areal array (880 ft or 268m) and dense areal array (220 ft or 67m). Here, we evaluate existing methods of extracting unconventional body and surface wave information by applying interferometry. Following tests of various preprocessing sequences, we successfully recovered virtual surface waves from 6.5 days of continuous seismic recording. However, our analysis of these surface waves shows that they appear to be generated by two distinct sources. We

found only hints of direct body (P waves) arrivals at the higher frequencies and some indications of critically refracted arrivals in the virtual records. The lack of body waves in the virtual records may be due to the lack of ambient source and relatively short observation period of the array. Given the limited azimuthal distribution of the surface wave energy, velocity estimation based on dispersion of the surface waves was also problematic. However the results we obtained are consistent with the geology of the area and nearby seismic observations with artificial sources.

The fifth chapter (Chapter 5, Figure 1.1) is focused on imaging deep seismic structures using an oil exploration dataset in South-East New Mexico to examine basement structure at depth. The dataset consists of a 21 second long uncorrelated recording of vibroseis sources with a 16 second long up-sweep (increasing frequency with time). Deconvolution of the sweep from the raw record conventionally produces a 5 second seismic record. We were able to produce a full 21-second seismic record using the extended correlation technique (Okaya, 1986). Although signal penetration in this particular area is limited by an extremely thick ($> 20,000$ ft) overlying sedimentary cover, the exercise demonstrates the tremendous potential of systematically mining the rapidly expanding database of continuously recorded oil exploration data, and the clear need to preserve rather than discard the unconventional portions of those records. We argue, that in locations with shallower basement, where energy is less attenuated by sediments, even 3D Moho reflections can potentially be obtained.

The final chapter (Chapter 6, Figure 1.1) is work done with Shell Oil during a 2013 Internship. The publication focuses on synthetic seismic modeling using a history matched dynamic reservoir model. The model represents a heavy oil

reservoir in Alberta, Canada, where various approaches of steam injections (e.g. Cyclic Steam Stimulation, Steam Drive, etc.) were applied to stimulate oil production. Here, we investigate the 4D seismic effects from these steam injections and oil production. We show, that frequent seismic repeats are necessary in order to confidently interpret 4D changes in reservoir, especially during the steam injection phase of operation. In addition, we argue that seismic modeling of the reservoir is also necessary in order to disentangle the effects of simultaneously changing variables like pressure, fluid saturations and temperatures.

CHAPTER 2

INTERPRETING ARTIFACTS OF BODY WAVE INTERFEROMETRY

2.1 Abstract

Modeling of virtual source gathers (VSG) and reflection profiles produced by body wave interferometry of biased source distributions is used here to identify and interpret coherent seismic arrivals that do not correspond to conventional seismic phases. These seismic arrivals are often labeled as "artifacts" (or "spurious arrivals") due to their unrealistic apparent velocities (e.g. too fast for physical waves) and non-causal arrival times. We discuss their appearance on both reflection profiles produced by auto-correlation as well shot gathers generated using cross-correlation of seismograms from sources with various depth distributions. We show that relatively deep sources (below the imaged interface) produce stronger and more coherent reflections especially at small offsets, while shallow sources are more effective in retrieving direct and refracted arrivals. We also show how energy associated with critically refracted energy can be shifted during cross-correlation with corresponding loss of information about the depth of velocity gradient causing the refraction. Furthermore, we describe how the contribution of such artifacts can be minimized by proper design of recording arrays, and how useful information can be extracted from the artifacts themselves by modeling.

Part of this paper published in Cabolova, A., and L. D. Brown. "Ultra-Deep Seismic Reflection Profiles of the Western US from Autocorrelation of USArray Recordings." AGU Fall Meeting Abstracts. Vol. 1. 2012.

2.2 Introduction

Seismic interferometry has its roots in the recognition that the reflection response of a layered medium can be synthesized from a transmission response by application of cross-correlation. Claerbout (1964,1968), Aki (1967) and more recently Weaver and Lobkis (2001) are among the first to propose cross-correlation as a technique for generation of the reflection response (Green's) function from an ambient noise field.

Extraction and inversion of surface waves from ambient noise sources has become a well-established technique for estimation of subsurface velocity variations (e.g. Shapiro et al., 2005; Bensen et al., 2007; Yao et al., 2006). It is generally assumed that given enough time the ambient noise field can be considered azimuthally homogeneous. This homogeneity is a requirement for successful response function retrieval, and no explicit knowledge of the locations of the noise sources is needed (Lin et al., 2008). However, it is recognized that azimuthal homogeneity of sources is not always the case (e.g Toksöz and Lacoss, 1968; Horike, 1985; Satoh et al., 2001; Pedersen and Krüger, 2007).

Body wave interferometry has not been as widely successful as surface wave interferometry, perhaps in part because ambient sources do not generate as much body wave energy (Shapiro et al., 2005). However, there have been several cases where body waves have been recovered from cross-correlation of ambient noise (e.g. Roux et al., 2005; Draganov et al., 2007, 2009; Brown et al., 2009; Zhan et al., 2010; Ryberg, 2011; Poli et al., 2012a,b; Lin et al., 2013a). A special case of cross-correlation is auto-correlation, which was argued by Ito and Shiomi (2012) and Ruigrok and Wapenaar (2012) to produce zero-offset reflectivity profiles be-

neath the stations analyzed. An advantage of auto-correlation is even a single station's recording can be used retrieve zero-offset response as a borehole measurement of the subsurface .

There are several possible reasons for the greater difficulty of successful body wave interferometry. One is that surface wave energy is much more abundant (perhaps even overwhelmingly so) (Shapiro et al., 2005) and uniform in most environments. Another is that body wave interferometry is sensitive to the 3D distribution rather than 2D distribution of sources. An inherent complication in the application of seismic interferometry is the generation of coherent energy, which does not correspond to conventional seismic arrivals. Here we investigate this energy (labeled as "spurious arrivals" or "artifacts") with the help of synthetic seismograms generated for various distributions of seismic sources. We also discuss the appearance of these artifacts in virtual source gathers (VSG) and zero-offset profiles (ZOP) generated by interferometry of sources with these distribution. This analysis is intended to help guide interpretation of interferometric results from real seismic recordings.

2.3 Seismic interferometry in 1D

Figure 2.1 illustrates Claerbout's (1964) concept for retrieval of a zero-offset reflection response by means of auto-correlations. Here, a 1D P-wave impedance model with 3 layers (Figure 2.1a) is used to compute a surface recording that would be expected from a subsurface source. First, a single receiver is placed on the surface of the model and a source is placed directly below within the lowermost layer. Then the resulting seismic trace, which includes both direct and

multiply reflected (i.e. reflection and its multiples) energy is computed (Figure 2.1b). For illustration purposes the computed trace here is replicated 10 times to mimic the seismic profile that would be obtained by moving the source and receiver laterally. The source function was assumed to be a minimum phase wavelet (15-40Hz). Since this model is 1D the incidence angle of all arrivals is 0 and therefore the time difference between all of the arrivals depends only on the thickness and the velocity of the layers. Once this "real" record of the source is generated, it is cross-correlated with itself to produce a virtual record (Figure 2.1c). For comparison, the expected reflection response for 1D model was also computed for a source on the surface and zero-phase wavelet of the same frequency (Figure 2.1d).

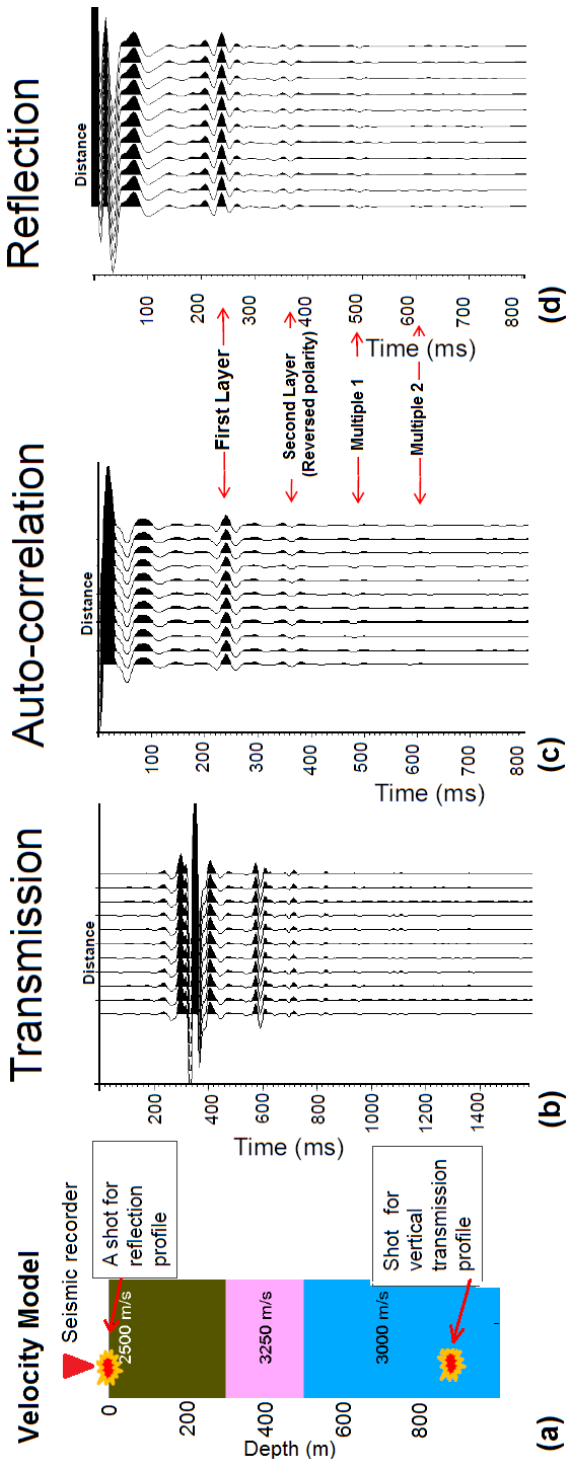

Figure 2.1: From transmission response to reflection response for simple 3 layer geometry (a). (b) Transmission response generated for a zero-offset station (the recording is copied 10 times), (c) zero-offset reflection response computed from transmission by means of auto-correlation and (d) zero-offset reflection trace for a surface source

The auto-correlation replicates the reflection response in terms of the predicted travel times of reflections from both layers. Note that the second layer (pink in Figure 2.1a) is higher velocity than the layers above and below it, which would result in a positive polarity for the first reflection and negative, or reversed, polarity for the second reflection. These polarity reversals are apparent in both surface source reflection and the auto-correlation profiles. Multiples of the reflections from both layers are also present in both profiles. Note, however, the reflection resulting from auto-correlation is the zero-phase, amplitude spectral equivalent of the original minimum-phase wavelet used for the source. It is also important to note that within a scaling factor, this result would be the same for a source at any depth (Figure 2.2).

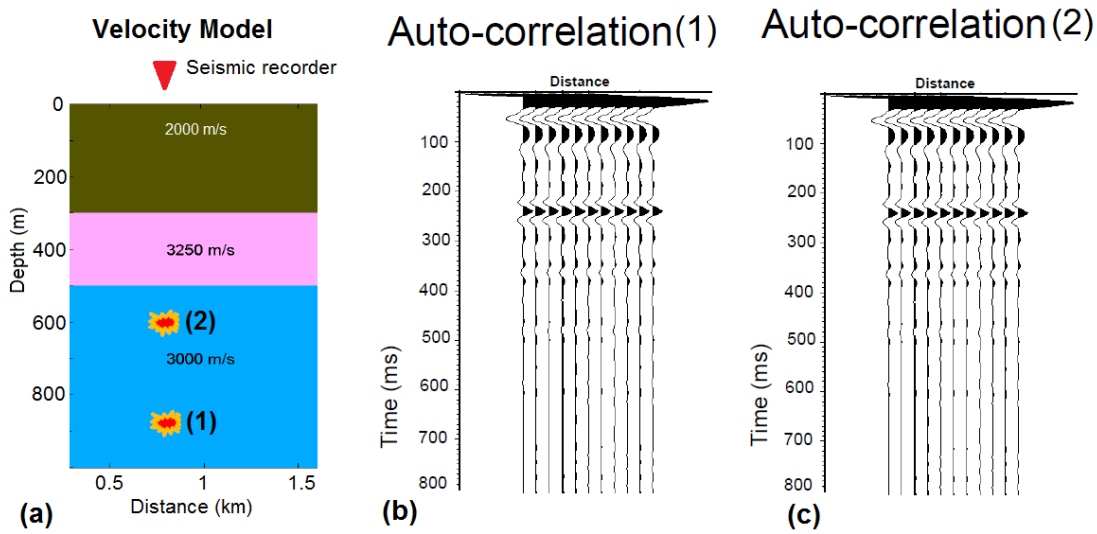

Figure 2.2: (a) Velocity model from the Figure 2.1 with sources at different depth, (b) auto-correlation profile from source 1, and (c) auto-correlation profile from source 2

2.4 Synthetic seismic interferometry in 2D

Surface wave extraction from ambient noise is an excellent example of seismic interferometry in 2D since surface waves propagate parallel to the earth's surface (e.g. Shapiro et al., 2005; Bensen et al., 2007; Yao et al., 2006; Lin et al., 2008, etc.). The conditions that lead to an effective virtual source for surface waves are illustrated in Figure 2.3 modified from Snieder and Wapenaar (2010). In this figure the blue and red dots are locations of the sources, which are randomly scattered about a disk surrounding the two receivers A and B (purple circles). The differences in arrival times of the surface wave for each source between station A and B are represented by a sinusoidal curve in Figure 2.3(b), which is defined by the individual cross-correlations of the seismograms for the two stations for each source. It is important to note that the azimuth ϕ is computed for each source separately, which results in smooth variation of the arrival times with ϕ despite the randomness of the source radii (distances to the stations). For a source perpendicular to the array (azimuth 90^o and -90^o), the energy comes at the same time to both stations and therefore the time difference is zero. For sources in-line with the two stations, the travel time difference is equal to the distance between two receivers divided by the surface wave velocity. This time is constant for all the sources located along the axis passing through the two stations (gray dotted line). Thus when all the cross-correlations are summed over all sources in Figure 2.3(a), only the energy traveling along the axis between stations A and B is aligned, which results in the occurrence of the constructive interference (Figure 2.3c). For all other azimuths, the randomization of the arrivals time differences results in a sum that goes to zero as the number of sources grows very large. As a result we get two wavelets (Figure 2.3c) at times that cor-

responds to the signal traveling from station A to B (negative correlation lag, A is virtual source) and from B to A (positive correlation lag, B is a virtual source). The maximum and minimum in the differential travel time sinusoid are often referred to as stationary phases: i.e. the phase lags where the rate of change in differential travel time with azimuth goes to zero. For a perfectly impulsive source function, constructive interference would occur only for a source located at the axis connecting both recording stations. Energy from all the other directions would interfere destructively. However, due to finite bandwidth of the real signal, even sources slightly off-line from the axis will contribute to constructive interference (e.g. sources marked blue in Figure 2.3(a), which are said to be stationary points or stationary sources for stations A and B (Snieder et al., 2006; Wapenaar and Fokkema, 2006; Halliday and Curtis, 2008; Forghani and Snieder, 2010; Poletto and Farina, 2010)). The travel path from such source to the receivers is referred to as a stationary path.

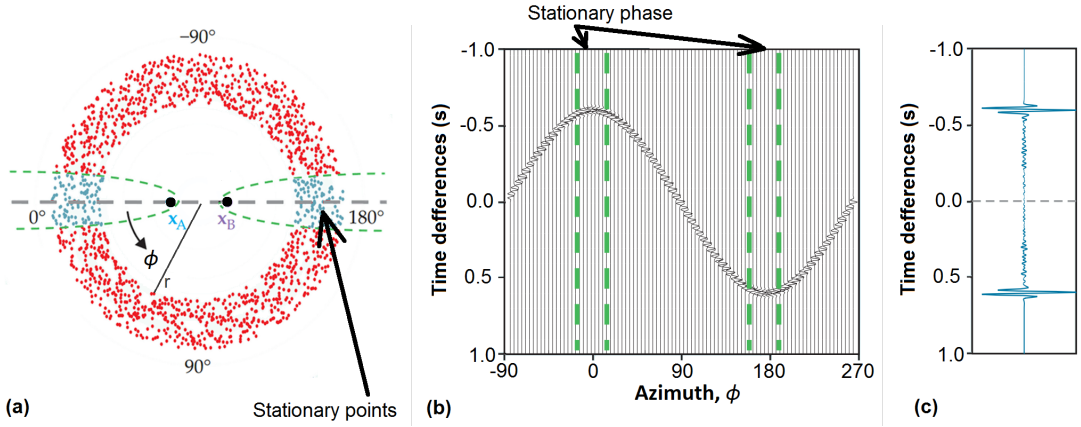

Figure 2.3: Surface wave interferometry in 2D: (a) source distribution relative to the 2 receivers, (b) Time-difference between all sources (equivalent to cross-correlation of receiver A with receiver B for each source) vs. azimuth angle, and (c) sum of all traces from (b), modified from (Snieder and Wapenaar, 2010)

The distribution of ambient sources is very important for constructive interference of seismic energy. If only a portion of the annulus in Figure 2.3 is populated by sources, energy from azimuths that do not correspond to the stationary phase will remain in the summed cross-correlations to appear as artifacts (e.g Halliday and Curtis, 2008; Harmon et al., 2010). This situation is even more complex for body waves, since (1) the source distribution is in 3D, and (2) body waves of included ray paths (e.g. direct and reflected) would correspond to different stationary geometries (Figure 2.4). In fact, any source along a green dotted line is a stationary point for receivers A and B for the reflection phase, and all the others are non-stationary sources (like in Figure 2.4b). Changing the geometry of the stations results in a change of the stationary paths and therefore different locations of stationary sources.

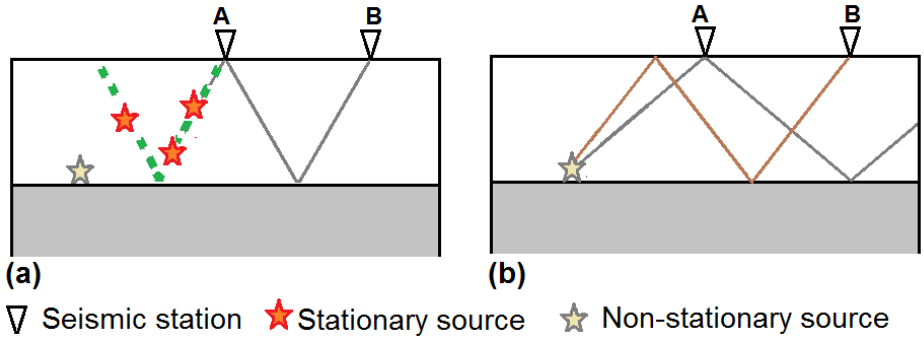

Figure 2.4: Source-receiver position for (a) stations sharing a stationary point, and (b) stations not in stationary phase for the source displayed. Seismic energy traveling from the source obeys Snell's law (incident angle equals to reflection angle).

Figure 2.3 suggests that body wave interferometry would work best for two stations located within spherical distributions of randomly but uniformly distributed sources. However, since the Earth's surface acts as a near-ideal reflector, this condition can be relaxed to consist of a uniform, random distribution of

sources in subsurface hemispheres (any enclosing surface geometry) surrounding the stations.

The actual distribution is dependent upon the nature of the source. For surface waves, the primary sources of the energy are believed to be microseisms associated with wave action on coast lines (e.g Friedrich et al., 1998; Tanimoto, 1999; Rhie and Romanowicz, 2004). Wave action may also be a source for body waves (Landès et al., 2010). Recently scattered earthquake energy has been identified as useful source of body wave energy for interferometric analysis (e.g Lin et al., 2013a). Anthropogenic noise may also prove to be useful in body wave interferometry (Nakata et al., 2011; Quiros et al., 2014). Whatever the source, we often assume that once we sum over all these sources, the arrivals which do not share stationary paths are canceling each other and the only seismic arrivals that contribute to the resulting seismogram are those that lie along a useful stationary path (Wapenaar et al., 2010). However, it is also possible, if not likely, that sources of body wave energy are neither as common nor as directionally diverse as surface wave energy. As a result artifacts may prove to be a more serious concern for body wave versus surface wave interferometry, as demonstrated in Figure 2.5, where an acausal arrival that does not originate from the virtual shot location (offset 0) is highlighted in blue.

Here we investigate the nature of such potential artifacts in body wave interferometry using synthetic seismograms. We have investigated these artifacts with two approaches: (a) estimating zero-offset reflectivity from autocorrelations and (2) estimating finite-offset reflectivity from cross-correlations.

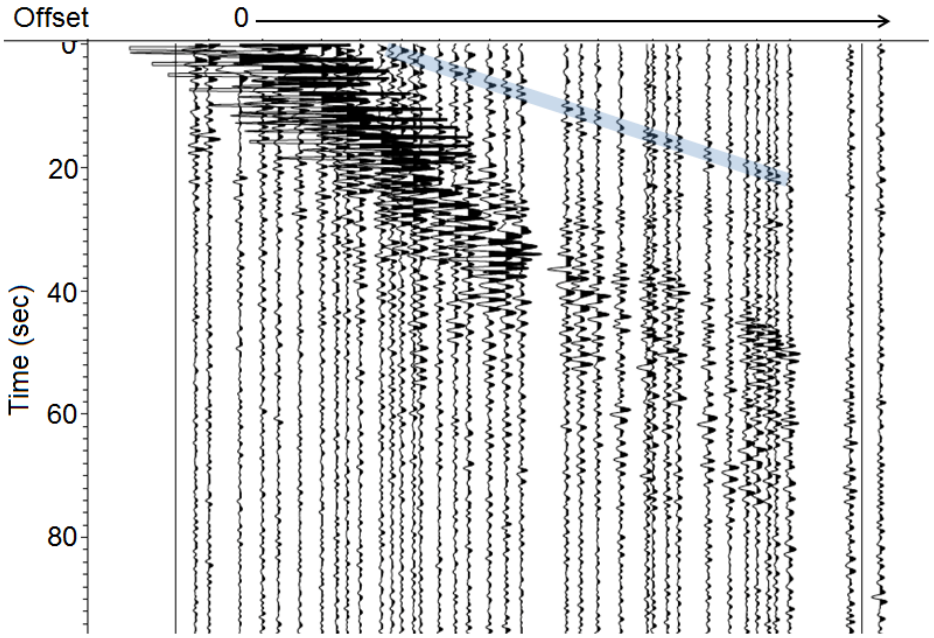

Figure 2.5: Virtual source seismograms sorted by offset. Arrival marked by blue has a body wave velocity but does not originate from the virtual source location at zero offset (computed from recordings of the MASE array in southeastern Mexico (MASE, 2007))

We show results for different source distributions for zero and finite source-receiver offset recording geometries. All of the synthetic seismograms are computed for a surface receiver array and sources which are distributed randomly within various depth and offset ranges. We have focused our attention solely on P waves because S waves involve an additional layer of cross-correlation complexity. We use 50 sources for each model in order to keep the processing time within reasonable limits (e.g. days versus weeks). The basic geologic models used here are: (1) a two layer media with the sources within the deepest layer (referred to as deep sources); (2) a two layer media with the sources within a few wavelength of the surface (referred to as shallow sources); (3) a two layer medium with the sources distributed asymmetrically relative to the receivers;

(4) and a two layer medium with dipping interface.

2.5 Synthetic seismic generation

All models presented here were generated using the CREWES Matlab toolbox (Margrave, 2003). After a 2D velocity model is defined, the toolbox generates a rectangular grid, which depends on the distance between receivers. The sampling is chosen to accurately propagate the acoustic wave with specified wavelet (in our case zero-phase with frequencies of 15-40Hz) from the source to the receivers using second-order finite differences technique.

For each model one of the 50 sources was placed within a range of depth and offsets, and the synthetic seismogram generated for each of 1000 receivers on the "surface". Thus, 50 separate source gathers were created for each source location. The position of each source was computed using a pseudo-random number generator (randi, Matlab) for a specified range of depths and offsets.

One of the issues associated with finite difference synthetics are the boundary reflections from the sides and the bottom of the model. In order to eliminate interference of these unwanted reflections, the size of the model was increased and traces recorded by the receivers close to the boundaries were not used. As a result, the horizontal extent of the model is 10 km, but the sources were placed between 4 and 6 km distances from the model origin.

Because the stationary path depends not only on the geometry of the stations relative to the seismic source locations but also on the virtual phase (direct, reflected, refracted), we will examine two types of source distribution separately:

(1) relatively deep sources below the imaged interface and (2) relatively shallow sources above the interface of interest.

2.6 Zero-offset reflectivity from auto-correlations

Auto-correlation is cross-correlation of a signal with itself. It corresponds to a seismic station serving as both the source and the receiver for a virtual seismogram. Theoretically, every seismic recorder on Earth can be used to generate a zero-offset reflectivity measurement beneath the station. However, it can be especially difficult to recognize spurious arrivals when only one station is used. Here, we compute profiles of zero-offset seismograms for entire 2D array of 1000 stations spanning each subsurface course distribution.

2.6.1 Deep sources of seismic energy

Figure 2.6(a) is a velocity model with an interface at 0.4 km and 50 sources distributed between 1.5 and 2 km depth. Figure 2.6(b) is an example of the seismic record for just one of these sources (source gathers). The direct arrival is marked by red, the first reflection from the horizontal boundary between layers is marked in green. Subsequent reflections of subsurface multiples are marked in blue. The ray paths corresponding to these arrivals are shown in Figure 2.7. The side reflections from the model boundary are marked in purple. However, we are restricting our analysis to the central portion of the model where these side arrivals arrive too late to be relevant.

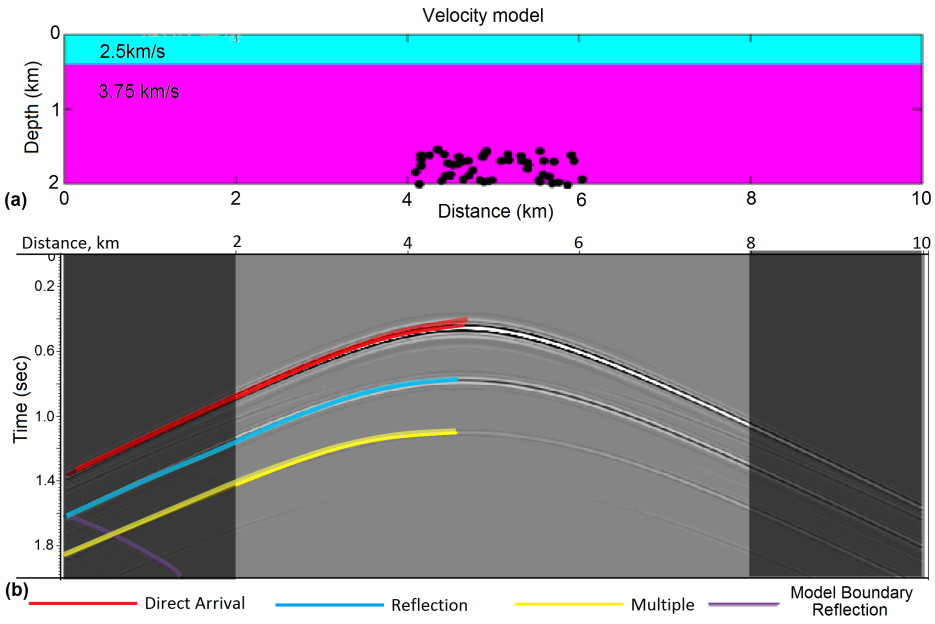

Figure 2.6: (a) Input velocity model for Crewes modeling software (Margrave, 2003). Black dots are locations of seismic sources(total of 50 shots); (b) Sample shot record for corresponding velocity model.

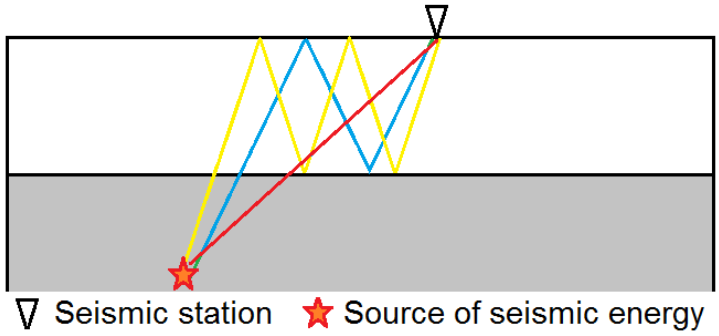

Figure 2.7: Rays from a source at depth corresponding to the model in Figure 2.6(a) (red is a direct arrival, green is the first reflection and blue is the first multiple)

After all 50 source gathers are generated (Figure 2.6), each trace in each record is auto-correlated (Figure 2.8b). Then the auto-correlations for each station are summed over all sources, constituting a common-receiver stack (Fig-

ure 2.8c). Again note that the model boundary reflections occur at times much greater than those of interest for the distance range of 4-6 km. For these distances the boundary reflections are not present within the window of auto-correlation and, therefore, are not contributing to the virtual profile.

Figure 2.8(b) shows the auto-correlations of all the stations for a single source (yellow circle in the model). The very first arrival (1) is a characteristic of auto-correlation and yields the maximum correlation coefficient at zero lag. The second arrival corresponds to the reflector in our model. Note that the maximum arrival time of this event is recorded by the station directly above the source and corresponds to the two-way travel time from the surface to the reflector in our model. Also note that the time of this arrival decreases as the stations move away from the source, but that this time shift is small relative to the period of the wavelet for a number of stations directly to the left and to the right of the overlying the yellow dot receiver. In other words, the stationary path is vertical for auto-correlation over flat layers. Arrival (2) emerges from correlating the first arrival (red) with the second arrival (green) in Figure 2.6(b). Note that as the reflection time of the auto-correlation decreases with offset from the source, it converges to a constant 0.22 seconds (in this example at approximately 3km from the source epicenter). Arrival (3) has a similar shape to the reflector with maximum arrival time twice that of the reflection and corresponds to the first surface multiple of the reflector. Figure 2.8(c) is a summation of auto-correlations over all sources for each receiver (common-receiver stack).

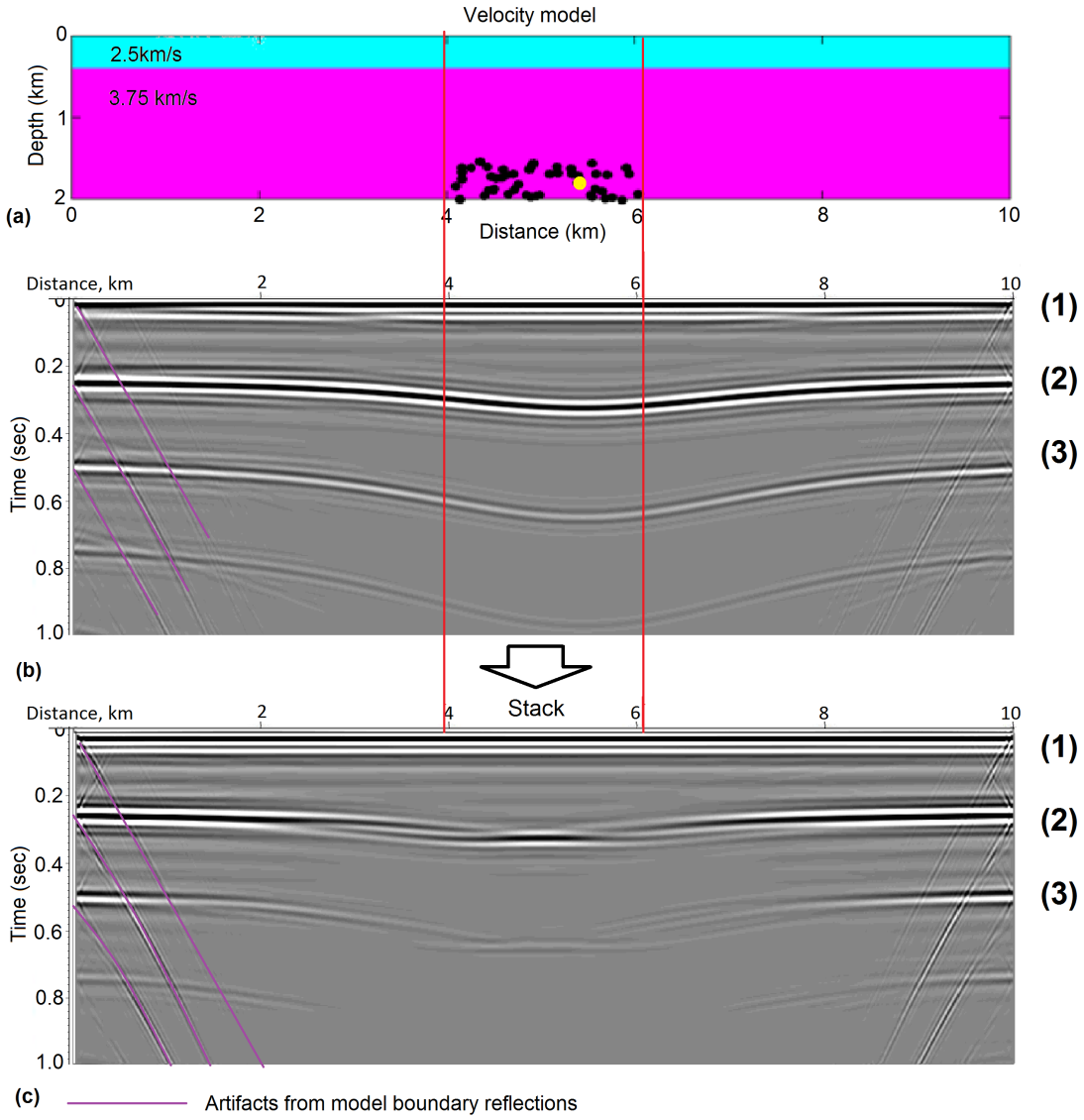

Figure 2.8: (a) Velocity model and source (black dots) distribution within the model, (b) Autocorrelation of a single shot at depth (arrivals marked by purple lines are due to the side reflection from the boundaries of the model), (c) Receiver-stack of autocorrelations over all sources

In Figure 2.9 we use only the portion of the zero-reflectivity profile that corresponds to stations directly above the group of physical sources. Figure 2.9 is a common-receiver stack for stations between 4 and 6km distances. The reflector

arrival time of 0.32 seconds in Figure 2.9 corresponds to the two way zero-offset travel time from the surface to the layer in model 2.8 and is effectively the same for all the stations. Figure 2.10(b) compares the single zero-offset trace generated from the stacked auto-correlation profile (at x=5km, in the middle of the model) with the to zero-offset trace from a surface source record (2.10a), generated for the same velocity model using zero-phase wavelet (Figure 2.10b and c). Both clearly show the reflection at 0.32 seconds and a much lower amplitude multiple of this reflection at 0.64 seconds, which is more distinct in Figure 2.9 than 2.8.

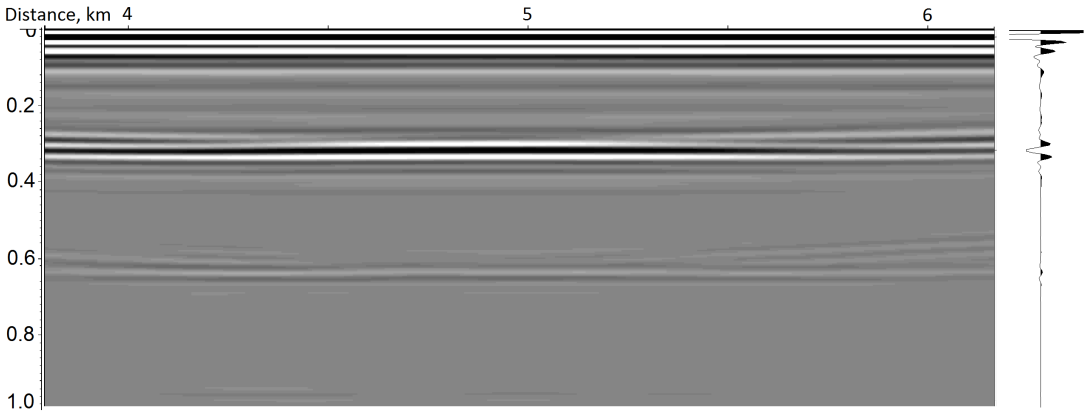

Figure 2.9: Receiver-stack of auto-correlations over all shots zoomed on stations between 4 and 6km

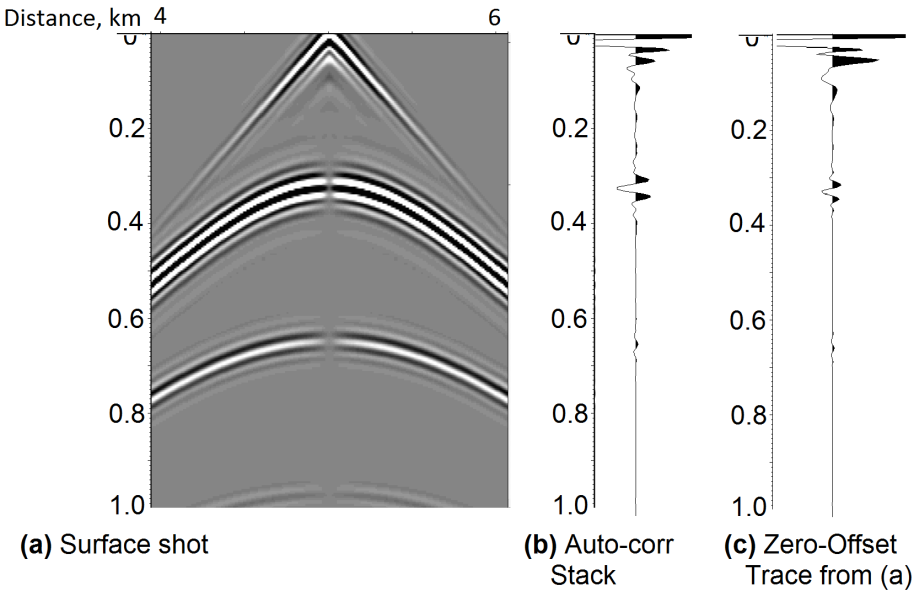

Figure 2.10: (a) Surface shot for the same velocity model, middle offset, (b) virtual reflection trace at 5km, (c) zero-offset trace from (a)

Thus the image of the reflection from the layer boundary (and its multiples) is accurately recovered from the stacked auto-correlation profile but only for those stations near the center of the source distribution. Figure 2.11 illustrates how the reflector emerges after stacking auto-correlations for all the sources. Figure 2.11(a) is the detail of the signal corresponding to the reflected phase in a single autocorrelation from the synthetic, with different colors representing three different source gathers. The maximum arrival time recorded by the stations directly above the source corresponds to the vertical reflection travel time. The curvature of this arrival depends on the offset of the station, the depth of the source and the velocity of the medium. Therefore, for all the sources, the signal arriving at maximum time will tend to interfere constructively among nearby stations (black arrow (2) in Figure b) but interferes destructively at all other apparent arrival times (gray arrow (1)).

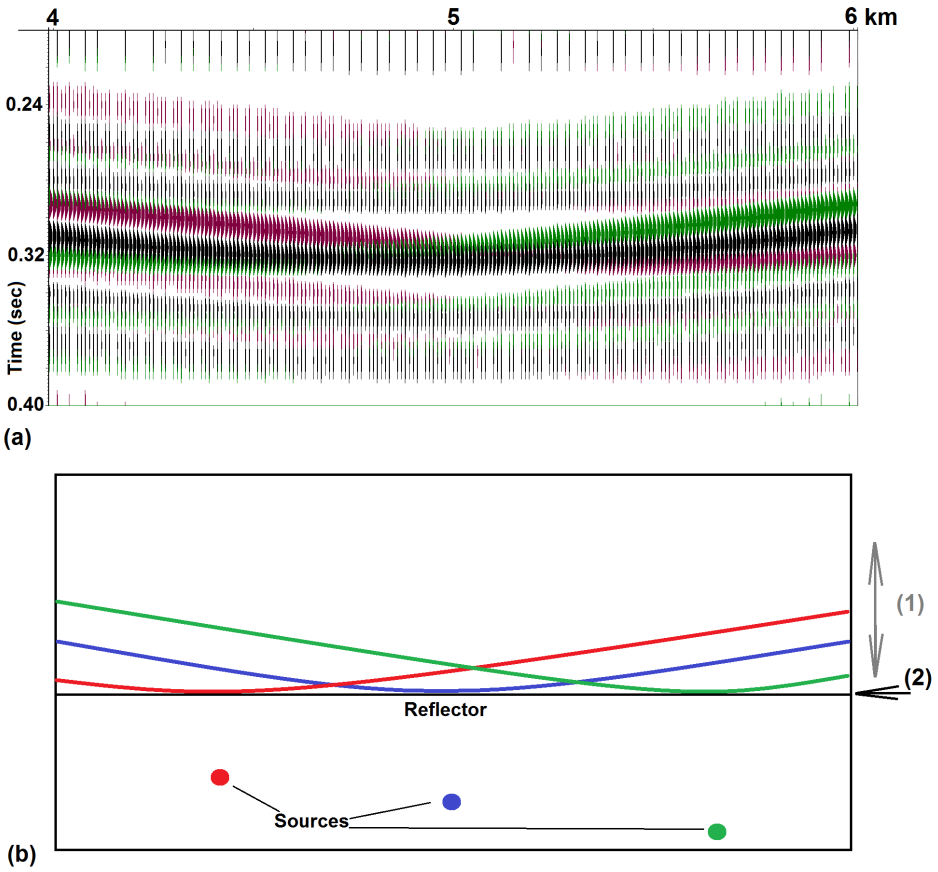

Figure 2.11: Constructive interference (a) synthetic data, (b) representation of the arrivals

In summary, auto-correlation of the signal from sources at depths that are greater than an interface of interest results in an image of the reflection from that interface when the sources are distributed symmetrically beneath the recording array. This image is equivalent to a zero-offset surface reflection profile. Next, we examine the effect of asymmetric (i.e. biased relative to the recording array) source distributions.

2.6.2 Asymmetric deep source distribution

We define an asymmetric distribution to be one in which not all of the sources are positioned directly below the recording station array. In Figure 2.12 we use the same model as previously (Figure 2.6) but include only data from the receivers that are offset from the center of the source distribution (Figure 2.12a). The velocity model, the source distribution and the processing are exactly the same as in Figures 2.8 and 2.9, but we only sum the recordings by the stations positioned at 5-7km, instead of 4-6km.

Figure 2.12(b) shows that for the stations with sources directly below (5-6km), the auto-correlation is able to recover true zero-offset travel time for the reflection. However, for receivers offset from the sources (6-7km), the apparent travel time to the reflector decreases asymptotically as we move away from the sources. If the actual source distribution is unknown, these sections could be easily misinterpreted as a change in layer depth.

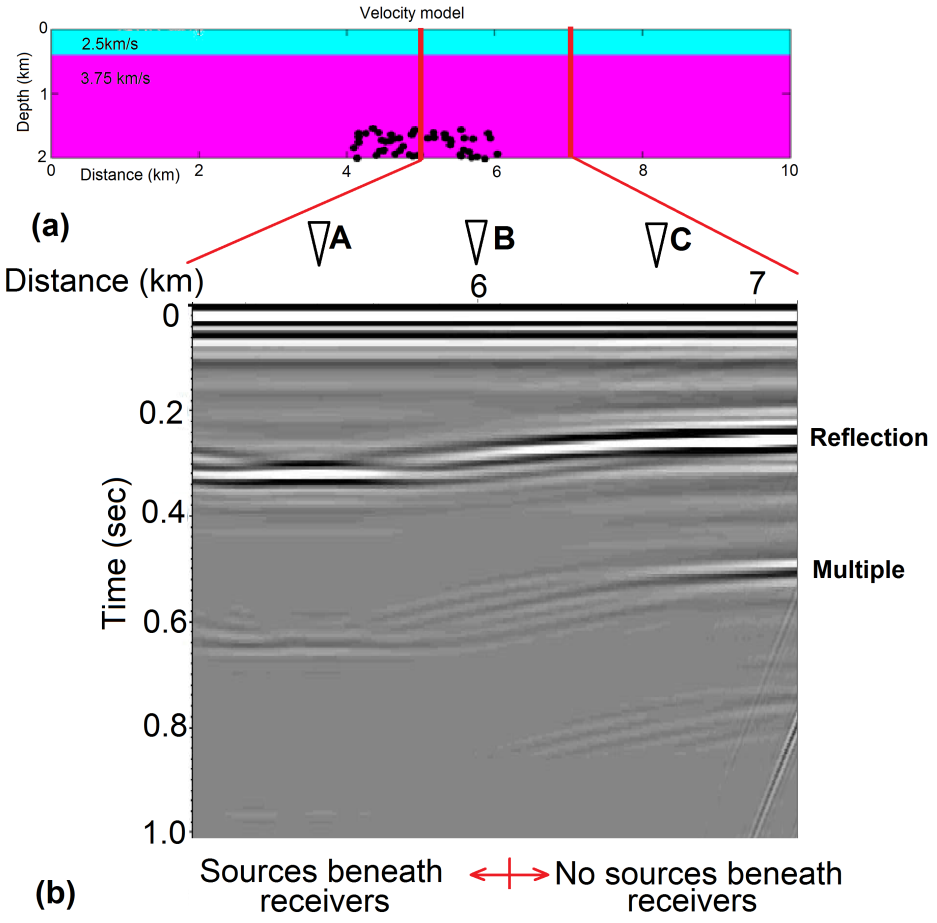

Figure 2.12: (a) Velocity model, and (b) Stack of auto-correlations for stations directly above and at an offset from the shots.

We now examine more closely the auto-correlation for receivers A, B and C (Figure 2.12) in order to examine the apparent shift in the reflection times. Just as in the case of a symmetrical source distribution, the reflection is the result of correlation of the direct arrival (red) with the second arrival (green) in Figure 2.6. Station A is positioned within the region of well-distributed sources (meaning there are sources directly below receiver A), station C is in the portion of the array that does not have sources directly beneath it, and station B is on the edge between the two regions.

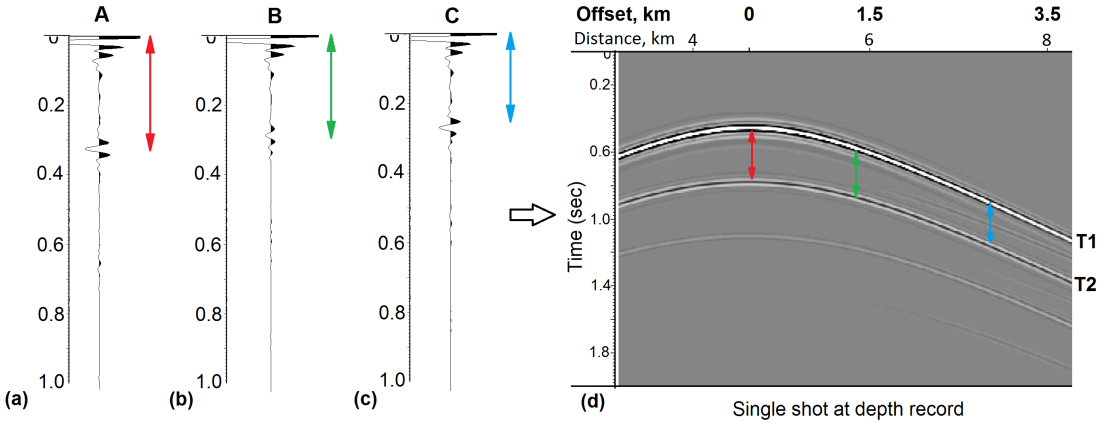

Figure 2.13: Recording from station (a) **A**, (b) **B**, and (c) **C** from Figure 2.12 and (d) A shot at depth record with corresponding arrival correlations shown with colored arrows

Figure 2.13(d) is a single source recording for a stations at 3-8km and a source epicenter at 4.5km, where T1 is the direct arrival and T2 is the second arrival. Figures 2.13(a-c) are traces extracted from auto-correlation stack at positions 5.5 km (**A**), 6km (**B**) and 6.5km (**C**) from the profile in Figure 2.12(b). The apparent arrival times of the recovered reflection in each case are simply the difference in the T1 and T2 arrival times at each position contributing from all sources after the stack. As we cannot present the analysis of all 50 source gathers at once, we examine only a single source gather (Figure 2.13d). Station A records the sources directly beneath it, and therefore is compared to the zero-offset trace in the single source recording. Trace B is positioned at the edge of the source distribution, and although it may have a small number of sources directly below the station, most of the sources contribution to the stack is in mid range offset. Finally, station C is not positioned above the sources, and therefore the apparent virtual reflection is recovered only from the arrivals coming at large offsets.

The maximum time separation between these two arrivals (T1 and T2) in the

shot record corresponds to the zero-offset between the source at depth and a receiver (red arrow, trace A). Therefore, for a receiver directly above the sources the true reflection time is recovered. As the offset between the source location and a station increases, the time separation between T1 and T2 decreases (trace **B**, green, mid range). This phenomenon results in a shorter recovered reflection time. Also note that the difference in arrival times T1 and T2 changes relatively rapidly with offset at mid range. This gradient results in a smaller amplitude for the apparent virtual reflection for trace **B**, also observed in Figure 2.12(b). However, at offsets higher than approximately 2km for our model (position 7km for this shot), the time separation between T1 and T2 becomes approximately constant. This results in a very coherent arrival with high amplitude but an apparent travel time much smaller than zero-offset travel time of the virtual reflection. Note, that the changes in the amplitudes of the reflection with position in the virtual zero-offset reflection profile are not due to the scaling or spherical divergence but rather due to interference as a function of offset.

Thus, biased source distribution results in erroneous (shorter) recovered reflection times and distorted amplitudes within the reflection.

2.6.3 Shallow sources

Previously, we had only considered sources positioned exclusively below the reflecting layer in the bottom quarter of the model. Here we analyze zero-offset reflectivity for shallow sources located in the top quarter of the model, almost all within the layer whose base we image .

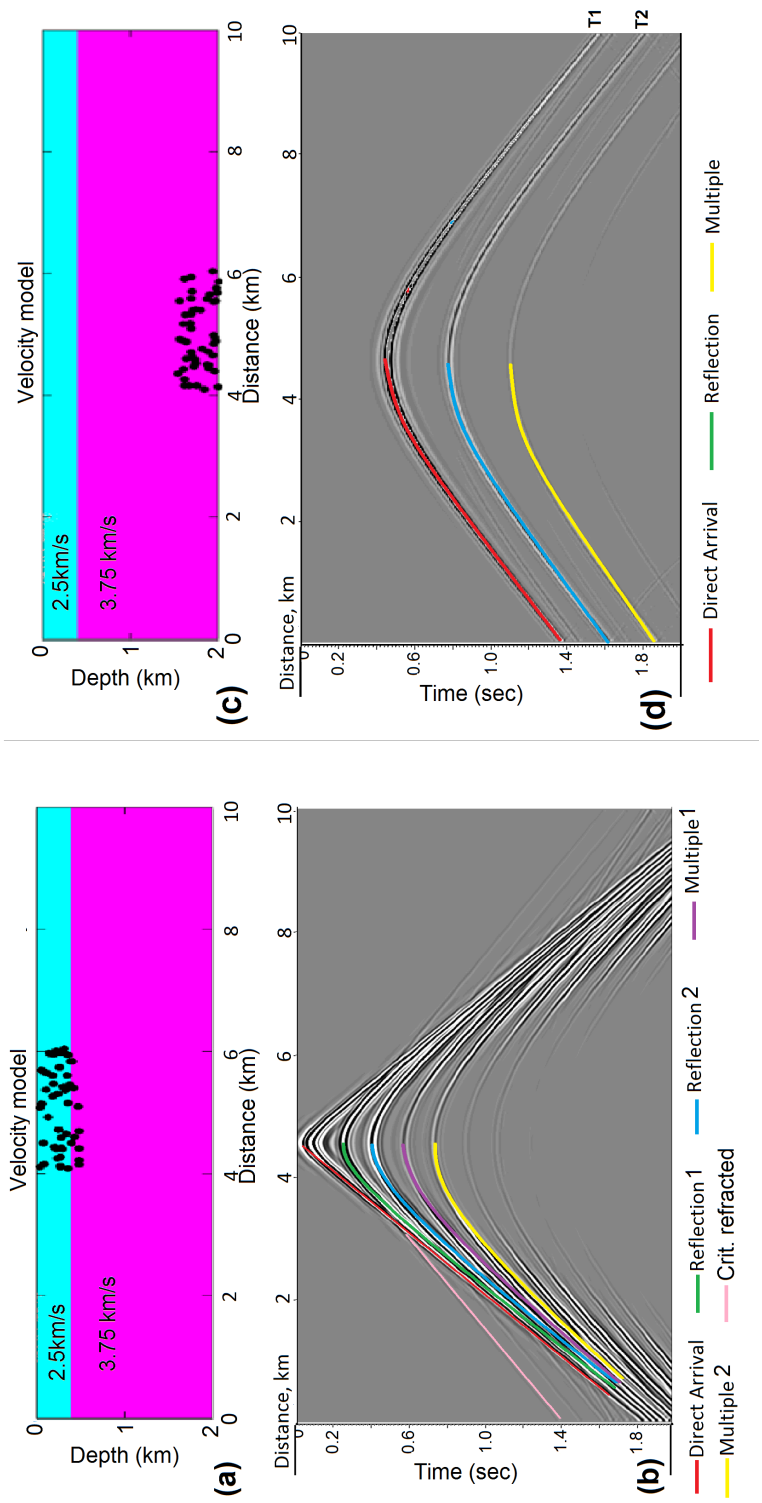

Figure 2.14: Comparison of a shot gather from a shallow and deep source (a) Input velocity model for Crewes modeling software (Margrave, 2003) for shallow sources. Black dots are locations of seismic sources(total of 50 shots); (b) Sample source record for corresponding velocity model, (c) velocity model for deep sources, (d) a sample source record for (c)

Figure 2.14 compares the surface record of a shallow source with a deep source. Arrivals are colored by same ray path seen in Figure 2.15. Note the arrivals highlighted in red and blue in both cases (T1 and T2). For the shallow receiver, there are also "extra" arrivals in between T1 and T2, which are not present in the deep source gather. These red, blue (T1 and T2) and yellow arrivals correspond to arrival and reflection of energy leaving upward from the source. In the case of shallow source, the extra arrivals are the energy traveling down from the source and reflected from the interface. Additionally, if the velocity of the underlying layer is higher, as in this case, the head wave (critically refracted wave) is a prominent arrival at offsets greater than 1 km for our source-receiver geometry. As with the deeper sources, the true reflection for a zero-offset time would be produced by the correlation between the first (direct, highlighted in red) arrival and the arrival corresponding to the direct wave energy reflected first downwards from the surface and then up from the layer (blue in Figure 2.15, where the source is drawn offset from the receiver for illustration purposes). However, in the case of shallow sources the latter is not always the second arrival, as it was for deep sources (Figure 2.14).

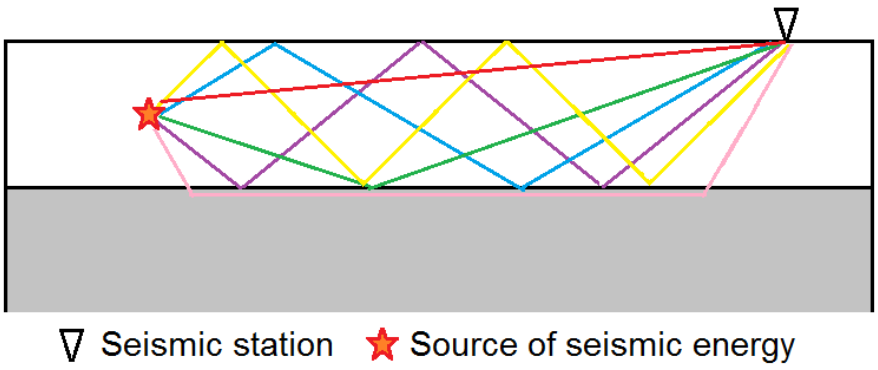

Figure 2.15: Ray paths from a shallow source within an imaged layer

Figure 2.16(a) shows the velocity model with the shallow source distribution, (b) the result of a single auto-correlation of one source record and (c) the result of an auto-correlation stack for all 50 sources within the shallow layer. Although the same number of sources was used as in the case of deeper sources, the stack shows only a weak, variable amplitude arrival for the interface reflector at 0.32 seconds. This observation contrasts with a prominent reflection at this time in Figure 2.9. Moreover, the section above the 0.32 seconds is dominated by a complex pattern of arrivals that has no clear physical relationship to the geological model.

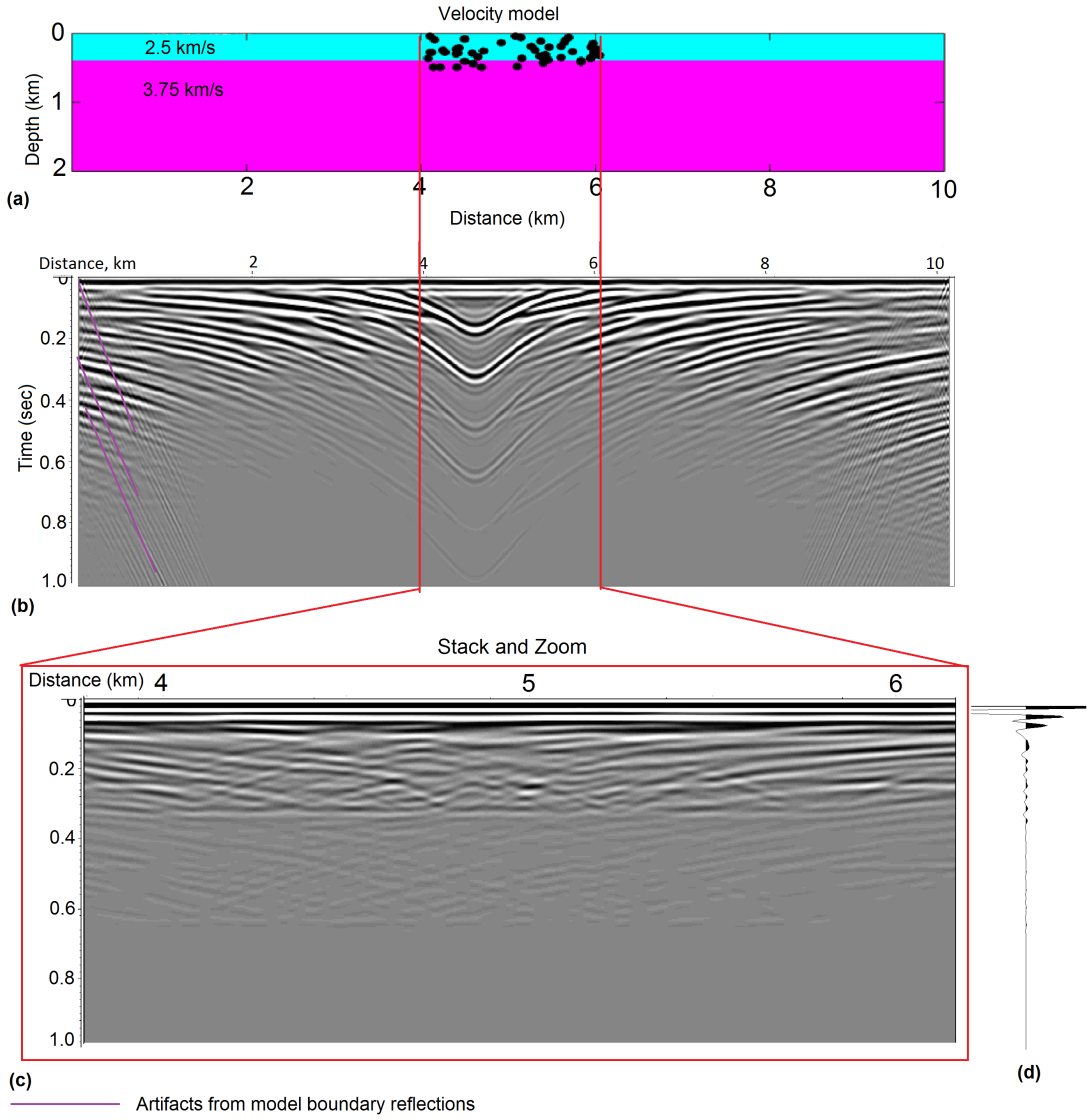

Figure 2.16: (a) Velocity model and shots (black dots) distribution within shallow depth in the model, (b) Autocorrelation of a single shallow shot (arrivals marked with purple lines are due to the side reflection from the boundaries of the model), (c) Receiver-stack of auto-correlations over all shots zoomed on offsets above the shots, (d) an example of a single trace from the receiver-stack profile.

There are two primary reasons for the difference in the reflection character retrieved by auto-correlation of the shallow versus the deep sources. The first

reason for the difference is the presence of the "extra" arrivals corresponding to reflected down-going from the source energy. This energy, which produces additional "events" after auto-correlation, is not present in the deep sources case. The second reason is that shallow sources produce arrivals with greater curvature (i.e. arrival time changes more rapidly with offset than for deep sources). Therefore there are fewer stations to contribute to the stationary phase at each source location for a shallower source compared to a deeper source.

The difference in curvature of the reflection is readily apparent in the single source auto-correlation for a shallow source (Figure 2.17a) and a deep source (Figure 2.17b). The virtual reflection with the maximum arrival time of 0.32 second (i.e. interface reflection time) is marked by the red arrow in Figure 2.17(a-b). The red curves below each profile are the traced arrival marked by the red arrow. Note the stationary phase in both red curved. There are approximately 10 receivers on the surface that are within the stationary phase for the shallow source auto-correlation. In contrast, this number is 60 for the deep source auto-correlation.

In addition to a smaller number of receivers that retrieve the reflection time of 0.32 seconds, the shallow source auto-correlation has a coherent arrival (yellow arrow) precursory to the virtual reflection. This coherent event is not present in the deep source auto-correlation. The arrival marked by the red arrow is the result of correlation of the red arrival with the blue arrival (Figures 2.14c-d) for both deep and shallow sources. The precursory arrival in the shallow source auto-correlation is the result of correlation of the red and green arrival (Figures2.14c). This green arrival is absent from the deep source record because it corresponds to the down-going energy from the source and, there-

fore, it is also missing from the auto-correlation of the this source.

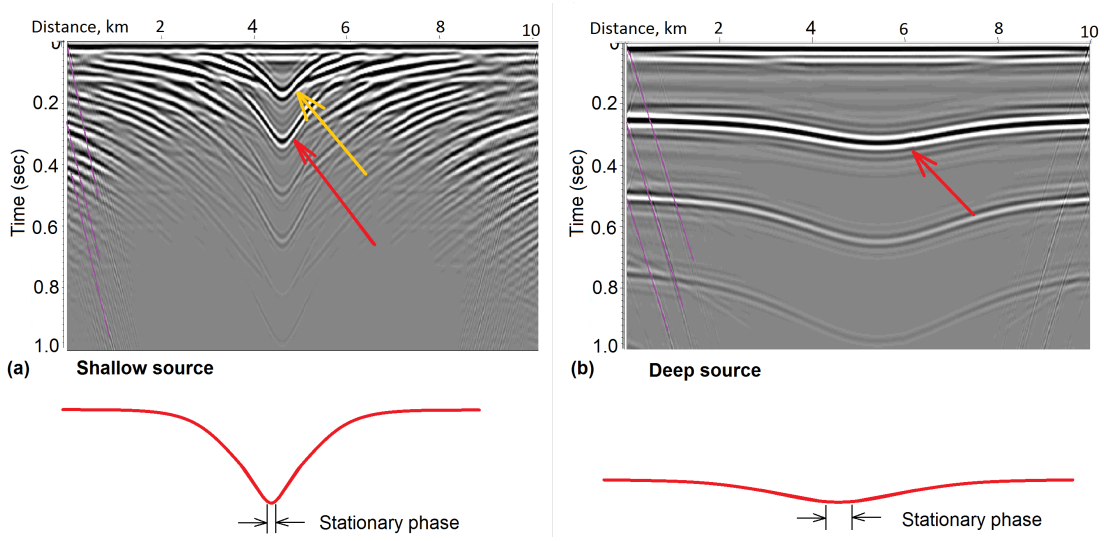

Figure 2.17: Comparison of single (a) shallow source auto-correlation and (b) deep source auto-correlation

The question naturally arises as to whether the reflection image can be improved and the artifacts suppressed by the inclusion of additional shallow sources. Figure 2.18 shows the stacked auto-correlations for 50, 100 and 200 shallow sources respectively. The larger number of sources does produce a stronger event at 0.32 seconds (average amplitude from 200 sources stack is twice that of the 50 sources). There are also fewer spurious arrivals above the virtual reflection at 0.32 seconds, which is demonstrated in Figures 2.18(d-i). Figures 2.18(d-f) are differences between Figure 2.18(a) and Figures 2.18(a-c). Figures 2.18(g-i) are differences between the absolute values of Figure 2.18(a) and Figures 2.18(a-c). The large negative numbers would correspond to an event present in the 50 sources auto-correlation and not in the 100 and 200 sources auto-correlation. Due to the fact that there are more purple (negative amplitudes) in the 200 source difference-profiles, we conclude that artifacts

above the virtual reflection decrease in amplitude with increasing number of physical sources summed.

Nevertheless, even with 4 times the number of sources (200 instead of 50), the target reflection is not nearly as coherent as that obtained using the deeper sources (Figure 2.9). Certainly, the spurious arrivals that appear within the first layer could easily be misinterpreted as complex geological structure, when in fact they are simply artifacts due to only partial cancellation of seismic energy along the paths of non-stationary phase.

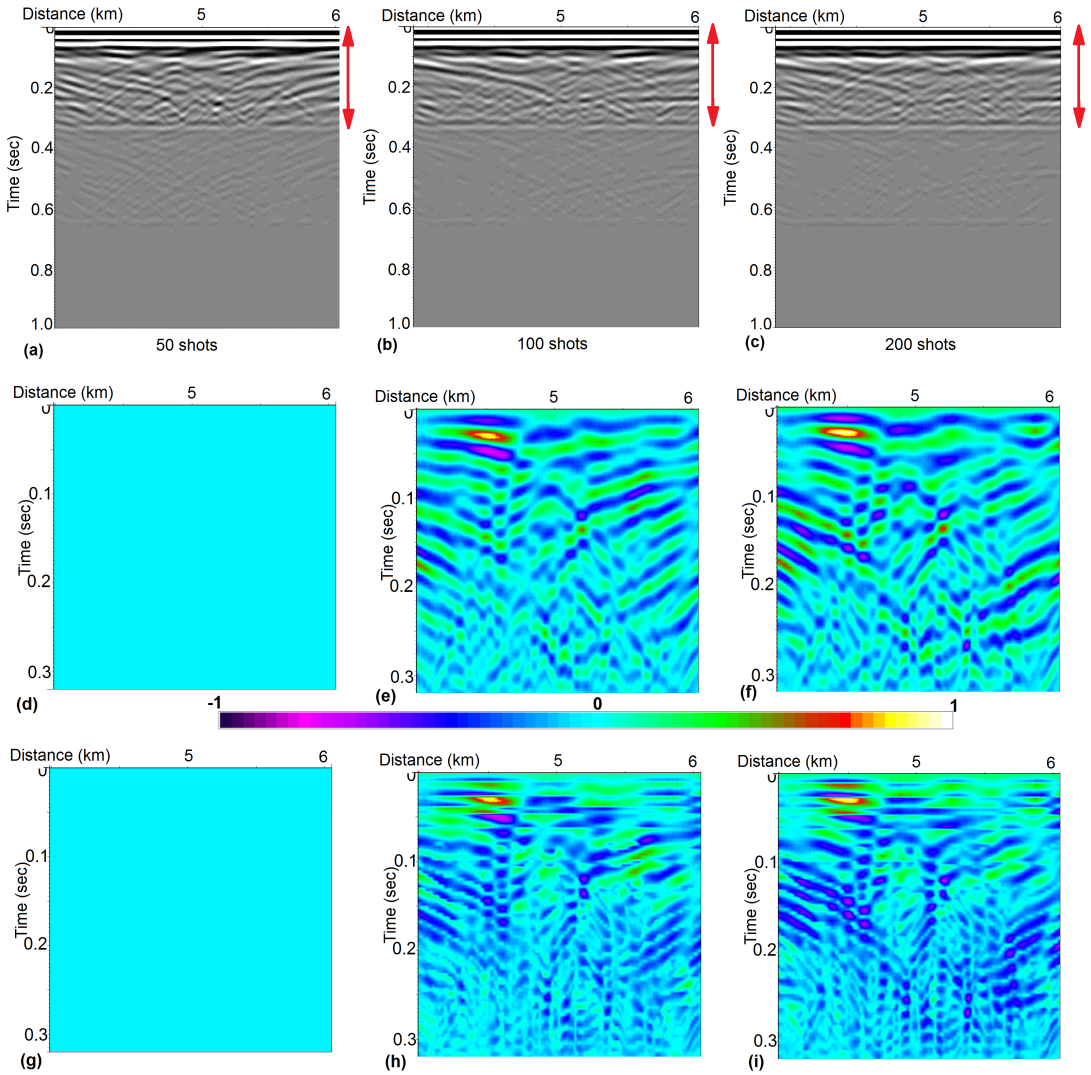

Figure 2.18: Stack of auto-correlation stacks for shallow (a) 50 shots, (b) 100 shots, (c) 200 shots

Shallow sources do not produce reflection images of subsurface reflectors as well as deep sources on zero-offset seismic sections generated by auto-correlation. One reason why this phenomenon occurs is the production of additional reflections and multiples that are not present when using deep sources. Another reason is that for a fixed station spacing, there are a fewer stations occupying positions associated with the stationary phase for a given reflector. To the

extent that ambient noise is created in the near-surface environment (Shapiro et al., 2005), interferometry using these sources is less likely to produce coherent reflection imagery. This geometrical bias can be one reason why retrieval of body wave reflection from ambient noise has been less successful than retrieval of surface waves.

2.6.4 Dipping reflector

We have repeated this same analysis for a dipping layer (Figure 2.19a) with deep seismic sources beneath it. Figure 2.19(b) shows a stacked auto-correlation section using 50 sources beneath the target interface. As with the flat layer, the dipping layer is best defined by the recording stations directly above the sources. Because we used a relatively course grid size in our synthetic generation, the dipping reflector was represented by a down-stepping interface rather than a smooth line. These artificial steps have given rise to regularly spaced diffraction hyperbolae along both the dipping reflector and its multiples. The red arrival in Figure 2.19(b) tracks one of these hyperbolae, whose curvature in fact is a measure of the velocity in the shallow most layer.

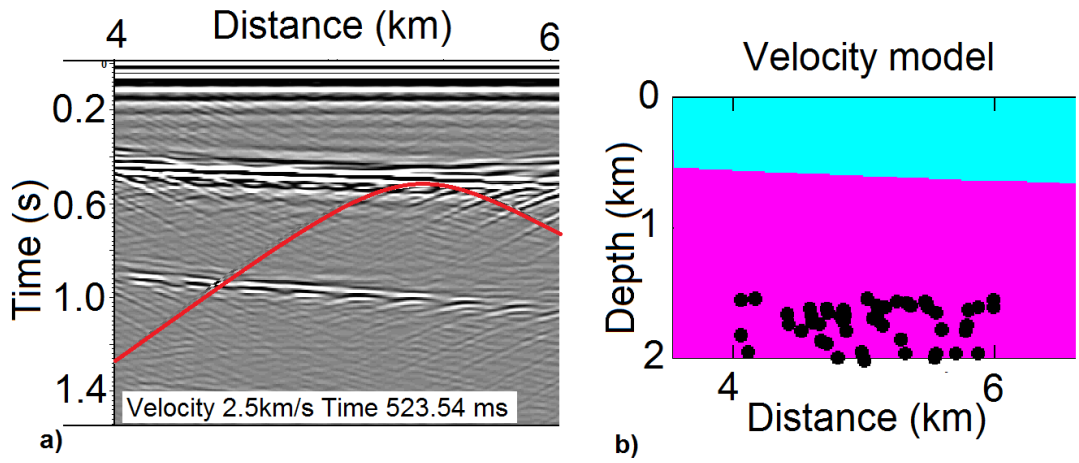

Figure 2.19: (a) Velocity model for a dipping reflector, (b) Stack of deep source autocorrelations.

Figures 2.20 shows the stacked auto-correlation seismic section for a profile line that extends well beyond the source positions to investigate the manifestation of asymmetric source distribution. The source position bias results in different artifacts down-dip (east) and up-dip (west) of the hypocenters.

The yellow line in Figure 2.20(c) indicates the expected position of the dipping interface. The misfit between the virtual reflection and the expected reflection is larger up-dip than down-dip. The region over which the virtual reflection coincides with the expected reflection is relatively small but located where the sources directly underlie the recording array.

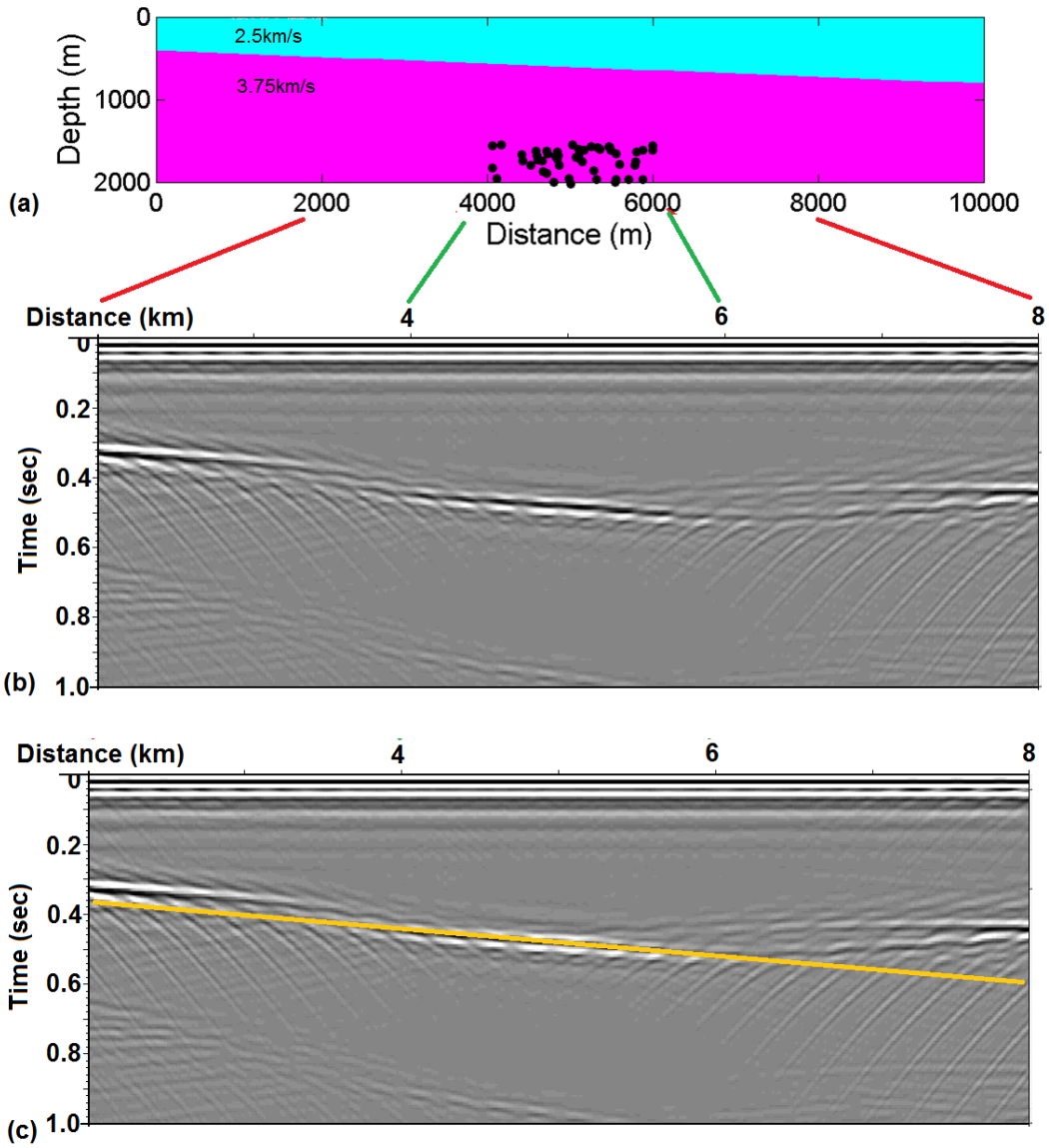

Figure 2.20: (a) Velocity model for a dipping reflector, (b) Stack of deep shots autocorrelations for asymmetrical source distribution, and (c) Same as (b) with the reflection time from surface shots zero-offset profile represented by yellow line

Thus, stacked auto-correlations can recover the dipping events provided that the source distribution extends beneath the surface recording array. If the source locations are biased, the resulting depth of the reflection is underestimated, with

the effect being even more serious on the down-dip side.

2.7 Finite-offset interferometry

We now focus on Virtual Source Gathers and the effect source distribution has on the retrieved virtual direct and reflected arrivals.

Halliday and Curtis (2008) discuss the effects of source distributions on cross-correlations for surface waves using synthetics and concluded that some source-receiver configurations result in more clear and coherent arrivals than others. However, unlike body waves, surface waves always travel in 2D with the depth of the sources effectively zero. Halliday and Curtis (2008) used a multi-layered velocity model to illustrate the importance of stationary phase in obtaining the correct surface wave velocity by means of cross-correlations (like in Figure 2.4). Here we look at similar considerations for body waves recorded out to finite virtual source-receiver offsets. We again use a simple two-layer velocity model to analyze the artifacts of poor source distribution (e.g. biased) and its role in obscuring both direct and reflected arrivals.

2.7.1 Deep and shallow sources

The velocity model used in the previous discussion (Figure 2.9) of auto-correlations is used here for computation of virtual source gathers by cross-correlations. Synthetics are computed using both deep and shallow sources. First, 50 subsurface sources records are generated for our 1000 station array, then a single station is cross-correlated with the remaining stations. Finally, all

cross-correlations are summed for all the sources (common-receiver stack). This results in a virtual source record, as opposed to the zero-offset reflectivity profile generated by auto-correlations. The virtual source gather approximates the record that would result from placing a physical source at the location of the virtual source station.

Figures 2.21(a) and (b) are the velocity models with shallow and deep sources respectively. Figures 2.21(c) and 2.21(d) are examples of the synthetic record for single source (i.e. transmission response). Figures 2.22 (c) and 2.22(d) are the gathers that result from cross-correlation of the seismic trace for the receiver at 5km with the seismic traces recorded by the remaining receivers in one source record (i.e. no summation over all sources). Note that cross-correlation shifts the traces "up" by an mount equal to the direct travel time of the source to the virtual source station.

There are a number of spurious arrivals in the cross-correlation gathers in Figures 2.22(c) and (d). One kind of spurious arrival is highlighted in red (1) in Figure 2.22(c), where some of the energy appears to be propagating linearly from the station at 4 km position rather than the virtual source position at 5 km. This effect is due to the fact that stations at 4 and 5 km are located symmetrically with respect to the physical source used to compute the virtual seismograms in 2.21(c). In other words, this source's epicenter is beneath position 4.5 km and is, therefore, centered between the 4 and 5 km stations. Therefore the first arrival from the synthetic source comes at the same time to both stations and the arrival time increases symmetrically with increasing offset from the source. The virtual events resulting from cross-correlation of these two arrival times are quasi-linear virtual arrivals propagating in the direction away from the virtual

source and symmetric (or mirrored) relative to the physical source position at 4.5km. We will refer to this effect as mirroring relative to the source (Ch. 2.7.2).

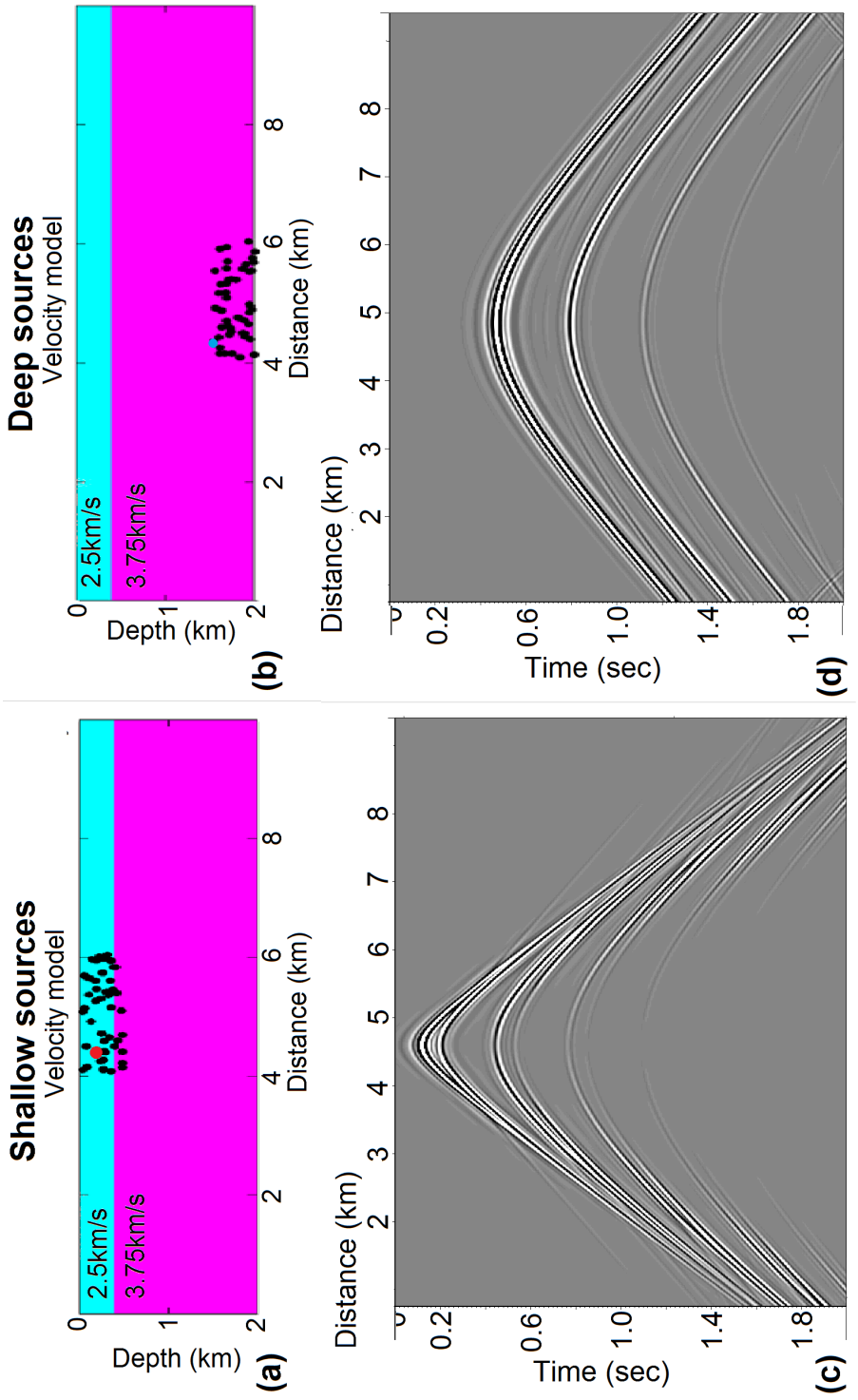

Figure 2.21: Comparison of single cross-correlation gather for shallow and deep sources: (a) velocity model for shallow sources (red dot is the shot gather displayed below), (b) velocity model for deep sources (blue dot is the shot gather displayed below), (c) and (d) are the shot gathers for shallow and deep source

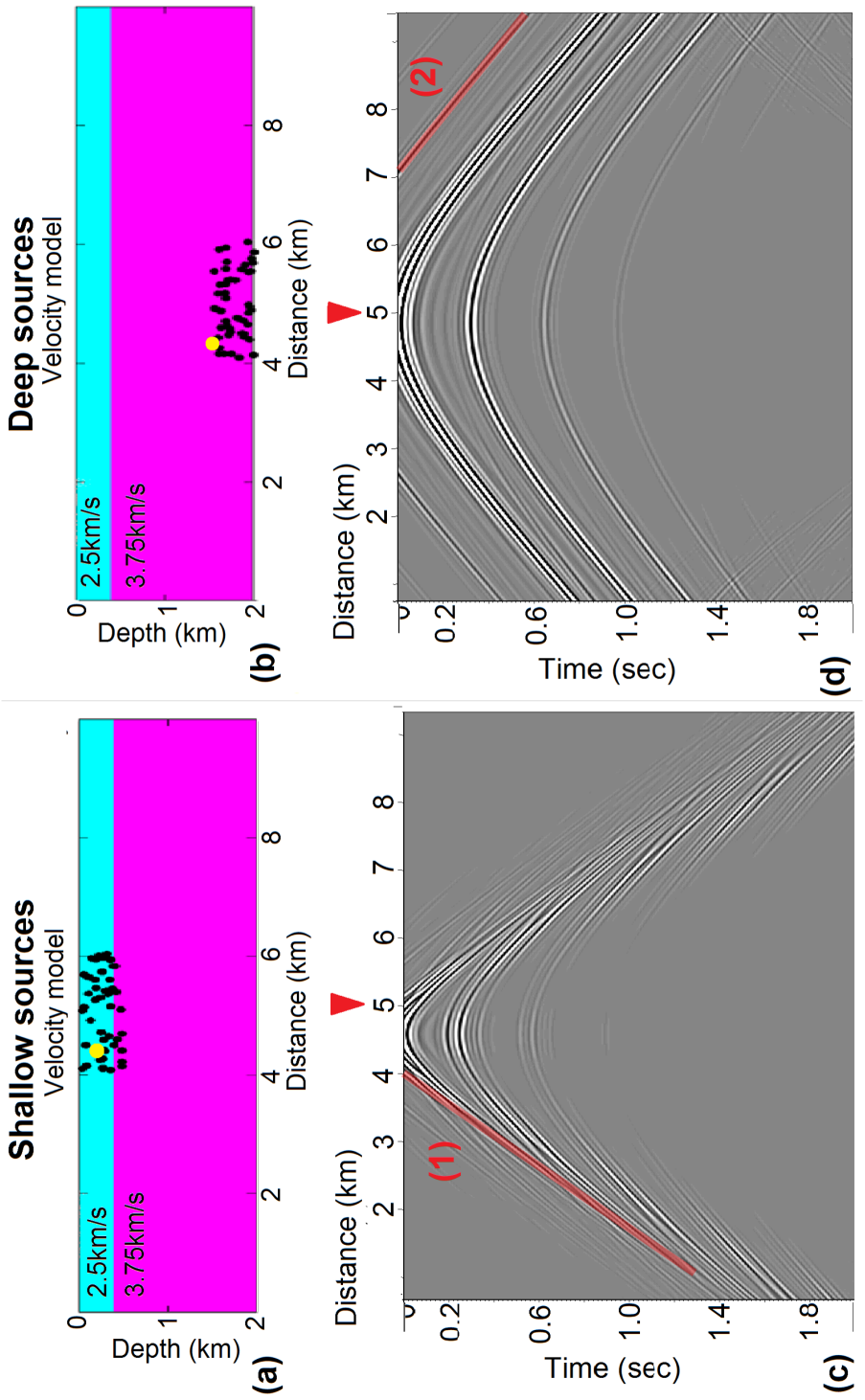

Figure 2.22: Comparison of a single cross-correlation gather for shallow and deep sources: (a) Velocity model for shallow sources (red dot is the shot gather displayed below), (b) Velocity model for deep sources (blue dot is the shot gather displayed below), (c) and (d) are single cross-correlation gathers for channel at distance 5km (marked by a red triangle) for shallow and deep sources in Figure 2.21(c) and (d)

The other kind of spurious arrival is illustrated in Figure 2.22(d), where energy is emanating from receiver at position 7km (marked in red (2)) rather than the virtual source station at 5km. If we project this arrival back to zero offset, it suggests that energy is arriving before time zero (non-causal), clearly a physical impossibility for a conventional seismic wave. This event is the result of a secondary arrival recorded by the station at 5km cross-correlating with the first arrival of stations at distances greater than 7km (Figure 2.21d). It is a clear reminder that every arrival at the station chosen to be the virtual source, not just the first arrival, correlates with all the arrivals at the remaining stations. The result is coherent energy sometimes appearing at non-physical travel times.

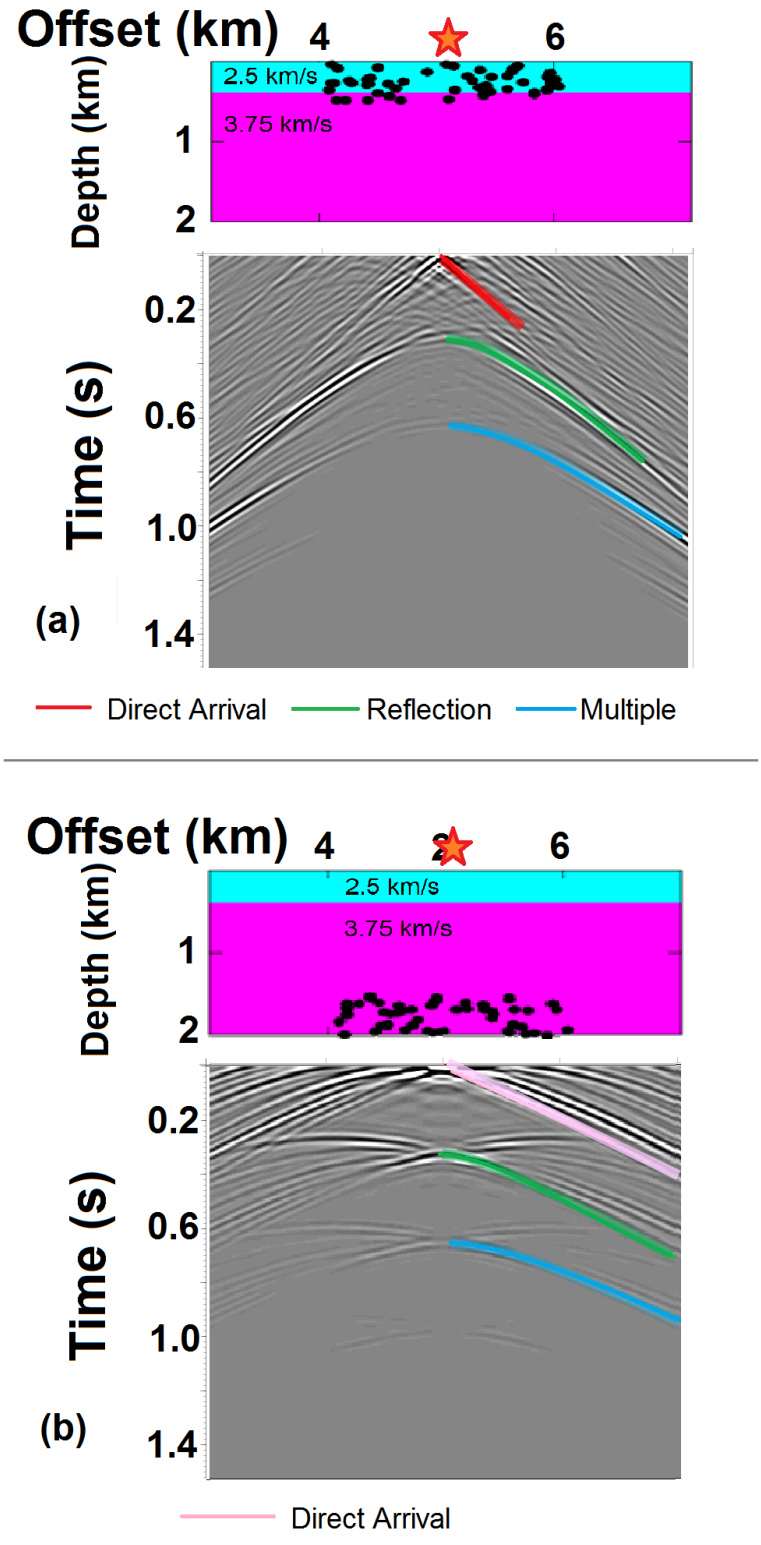

Figure 2.23: Stack of (a) 50 shallow and (b) 50 shots Cross-correlations with virtual shot location in the middle of the shot offset surface projection

Figure 2.23(a) is a virtual shot gather generated from summing cross-correlations of each source record in Figure 2.22(a). This virtual shot shows a direct arrival (highlighted in red) propagating in both directions from the virtual shot station (marked with a red star), as well as a reflection (green) and its first multiple (blue) from the interface between the layers. However, there are numerous other apparent "arrivals" that have a quasi-linear move-out but do not project back to time zero of the virtual source station. These arrivals result from incomplete cancellation of the non-causal arrivals described above.

Figure 2.23(a) is a virtual shot generated from cross-correlations of shallow sources. The virtual reflection and virtual multiples of the reflection (green and blue) are clearly visible but their amplitudes are weaker at smaller offsets. This is not due to the scaling of data during plotting (individual trace scaling is applied) but rather due to interference from unphysical energy arrivals and the smaller dimensions associated with the stationary phase of the shallow sources reflection phase (similar to auto-correlation results). Figure 2.24 compares a real surface shot with the virtual source gather from Figure 2.23(a). Individual trace scaling is applied to both gathers. The hyperbolic arrival cresting at 0.32 seconds in Figure 2.24(a) corresponds to the reflection from the model's interface. For the surface shot (Figure 2.24a) reflection amplitude decreases with increasing offset. In contrast, for the virtual shot (Figure 2.24b) the virtual reflection exhibits decreasing amplitude of the reflection with decreasing offset. Therefore, the decrease of the amplitude of the virtual reflection at small offsets is an artifact associated with the location of the physical sources.

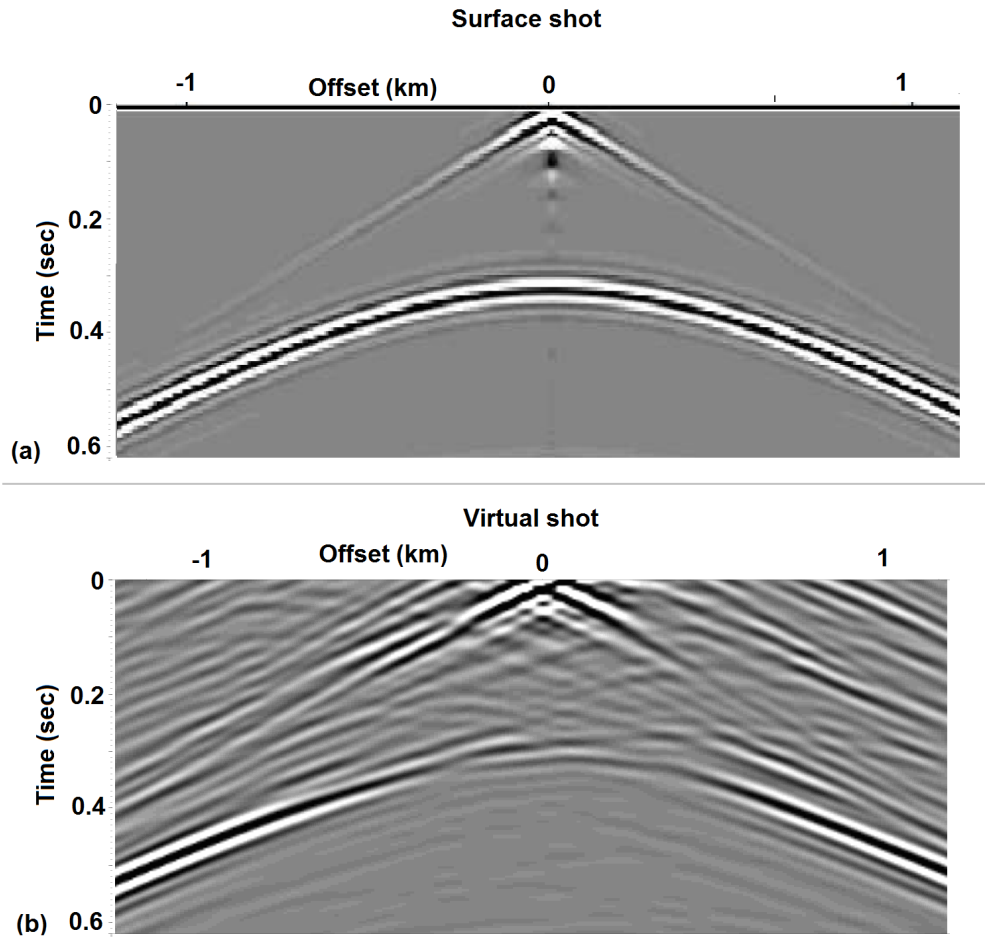

Figure 2.24: Shot gathers for (a) surface source and (b) virtual source generated from cross-correlations of shallow sources.

Figure 2.23(b) is the VSG generated from the deep sources. The arrival highlighted in pink would be a candidate for the linear direct body wave arrival. This virtual arrival is obscured by non-causal, non-linear energy and its "slope" would yield an overestimated direct wave propagation velocity. Likewise the later hyperbolic arrival, which should correspond to the reflection and multiples from the interface between the boundaries (green and blue), fail to coalesce into a simple, symmetrical hyperbola that is expected for such reflection (e.g. Figure 2.10). In fact, the reflection (green) follows the expected curvature of an

equivalent reflection from a surface source only at small offsets (similar results found by Kim et al. (2015)). Two "precursory" hyperbolae apices on both sides of the center feature corresponding to the virtual reflection, are the result of the reflected energy not focusing at the correct location for all modeled subsurface sources. However, these precursory arrivals are fainter (smaller amplitude) than the reflection itself and we attribute them to the lack of adequate lateral extent of the sources to allow the necessary cancellation of these "artifacts" and corresponding constructive interference of represented physical arrivals.

In contrast to the case for auto-correlation, cross-correlation to retrieve the virtual direct arrival seems to be more effective with shallow sources. However corresponding virtual reflections at small offsets are weak. Virtual shot gathers for deep sources result in a strong reflection (green arrival) at small offset but overestimate the normal move-out velocity at larger offsets (similarly to Kim et al. (2015)) and cannot accurately retrieve horizontally propagating (e.g. direct) arrivals. The only scenario in which deep sources can produce a linear direct arrival in a virtual source gather is if there are near-surface heterogeneities, which scatter the energy and effectively substitute shallow sources (e.g. Landès et al., 2010).

2.7.2 Asymmetric source distributions

Next, we consider the asymmetry of the source distribution for the case of shallow sources only. As described above, use of deep sources has fundamental problems, which limits their effectiveness in generating virtual shot gathers at far offsets. Figure 2.25 is a comparison of cross-correlation of a single source

(marked with yellow circle in the velocity model) for virtual shot station at 2km and at 3.5 km respectively (marked by a star) to investigate how increasing distance from the sources of energy affects the generated virtual source. For our source-receiver geometry, the station at 3.5km distance is 0.5 km from the closest source at depth, and the station at 2km is 2km away from the closest source at depth. Figure 2.26 show the summation of cross-correlations of all sources in Figure 2.25(a) and (b) respectively to produce corresponding virtual source gathers.

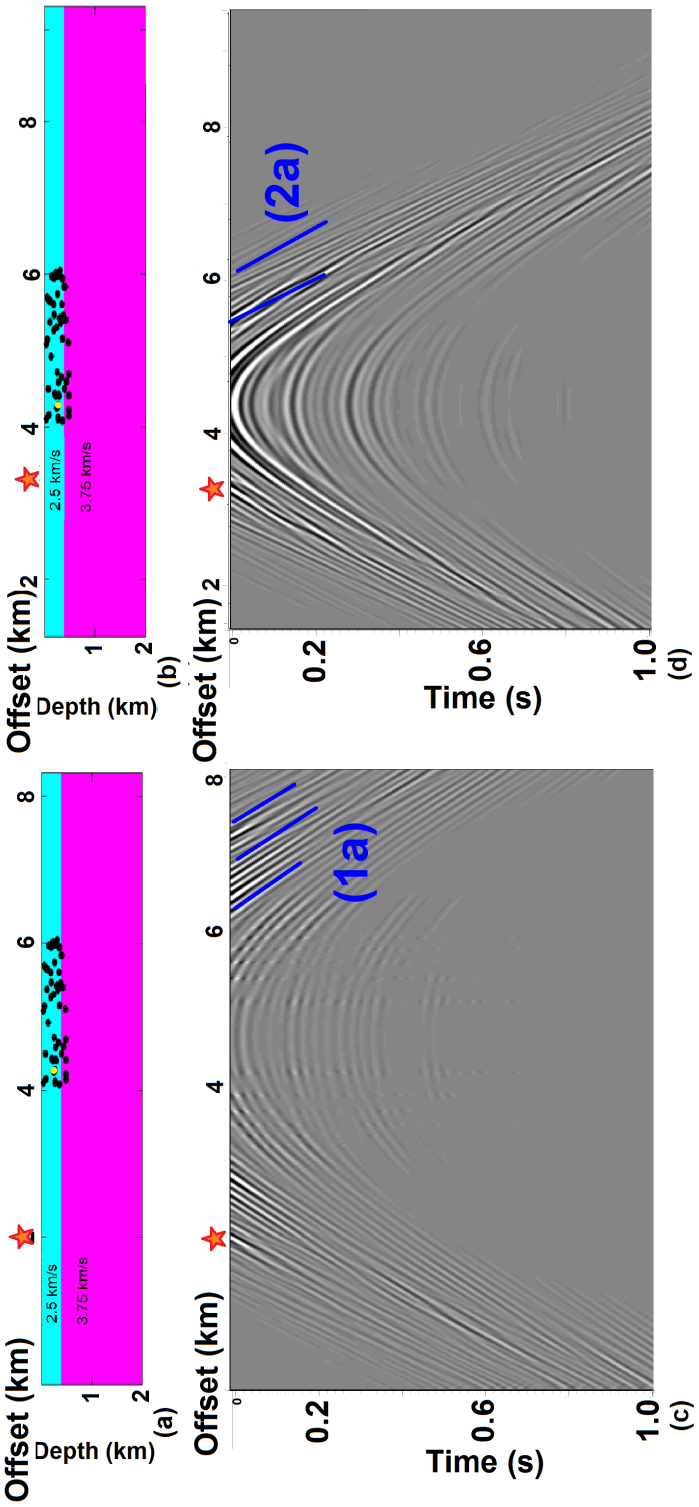

Figure 2.25: Cross-correlation example of a single source for asymmetric distribution: (a) velocity model for virtual shot at 2km, (b) velocity model for a virtual shot at 3.5km, (c) single cross-correlation of a station at 2km distance, (d) single cross-correlation of a station at 3.5km distance

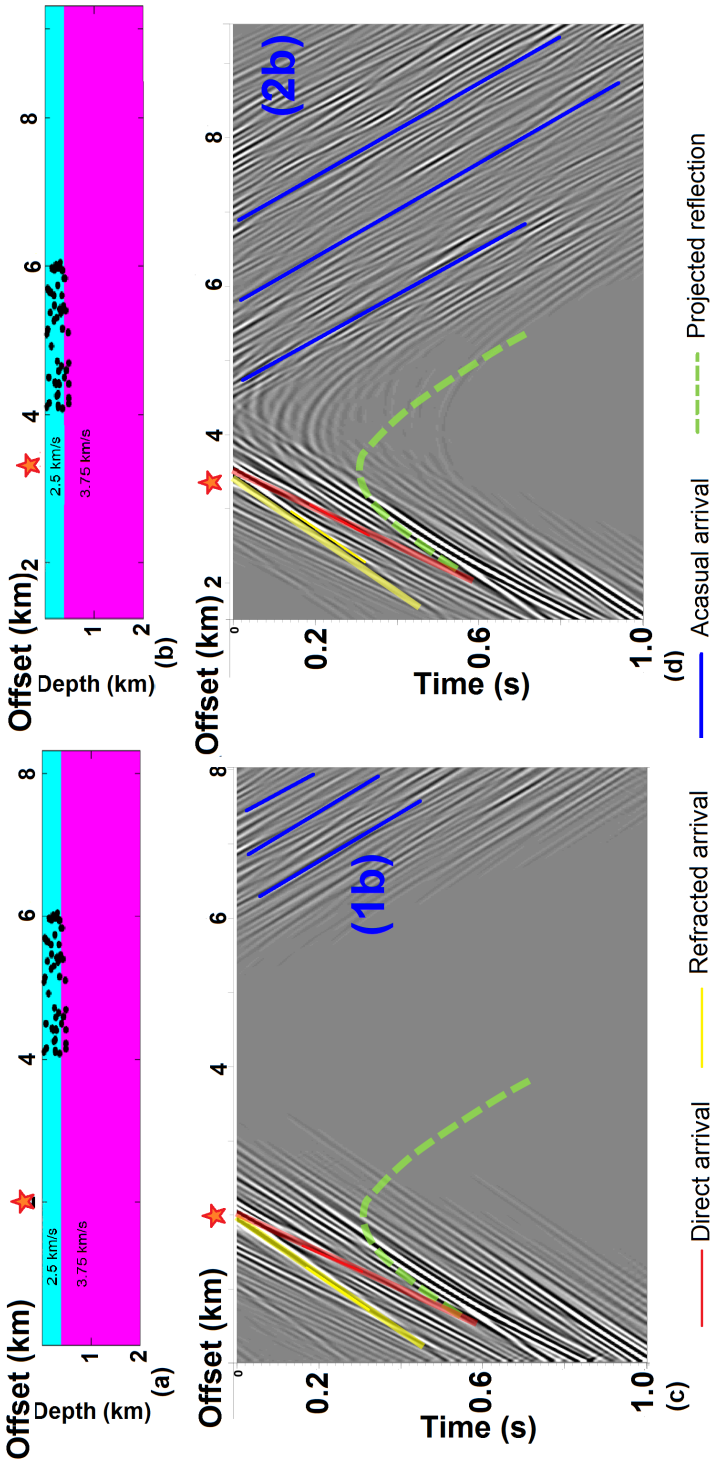

Figure 2.26: Summation of cross-correlations for asymmetric distribution of synthetic sources: (a) velocity model for virtual shot at 2km, (b) velocity model for a virtual shot at 3.5km, (c) Virtual shot gather at an offset 2km from 0 , (d) Virtual shot gather at an offset 3.5km from 0

A strong quasi-linear arrivals exists in the virtual source gather in Figure 2.26(c) and (d) (highlighted by a red line). This arrival propagates from the virtual shot in the direction away from the location of the source, but not both ways as in Figure 2.23. The velocity of this arrival is approximately 2.5km/s (offset divided by the arrival time) and is interpreted to be the direct arrival in the uppermost layer.

Compared to the previous results shown in Figure 2.23(a), a more exaggerated mirroring effect occurs ("events" marked by blue in Figures 2.25 and 2.26) for this source distribution. Figure 2.27 illustrates in more details how these "events" arise. Black circles in Figure 2.27 represent an epicenter of a source relative to the virtual shot (marked by a star) and each of the four panels represents a cross-correlation of the recording of the respective source. As the source moves farther away from the virtual shot, the axis (red dotted line) moves together with it, resulting in the mirror image relative to the red line. Therefore, the spurious arrival on the other side of the red axis also moves further from the virtual shot. After the summation of cross-correlation records, these spurious arrivals "leak though" into the virtual source record. Note that the virtual source gather in Figure 2.26(c) has effectively no arrivals at distances 5.5 to 6.5km, which is not the case for the virtual source gather in Figure 2.26(d). This lack of spurious arrivals in 2.26(c) is due to the fact that the virtual shot (star) is farther away from the source distribution than in 2.26(d) and, therefore, the mirroring axis and the events labeled (1b) are at greater offset from the virtual source.

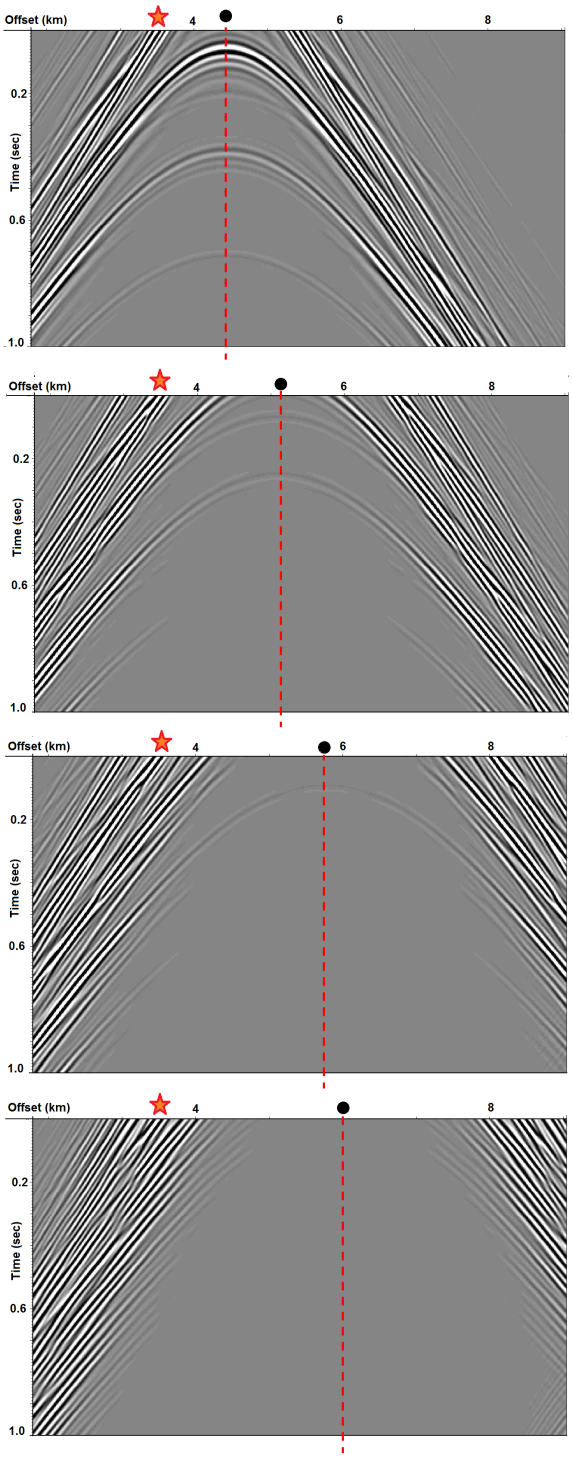

Figure 2.27: Cross-correlation as a function of virtual source - real source offset. The epicenter of the source within the array is marked by a black line, the virtual shot position is a red star and the "mirror" axis is dotted red line

Virtual source records in (Figure 2.26) resulting from the asymmetric source distribution do not retrieve the reflection phase. The green dotted curve in Figures 2.26(c) and (d) represents the location of the reflection hyperbolae expected for the surface source at the location of the virtual shots. Although there seems to be some co-linear energy with the expected hyperbolic "tails" in Figure 2.26(d), none of the energy arrives at the correct travel time and curvature to be identified as a physical reflection from the interface.

Figure 2.28 illustrates how shallow events provide energy that arrives mostly near horizontal raypaths (blue and gray lines), whereas only higher order multiples (red dotted line) from shallow sources arrive along the steeper stationary ray paths that correspond to the primary reflection. Moreover, these multiples are much weaker due to attenuation, or are otherwise completely obscured by other arrivals and recorded at later times than stronger direct arrivals. Therefore, when cross-correlating a source far away from a receiver array, there's little energy available to build a virtual reflection. However, the direct arrivals share a stationary path (gray and brown lines) with relatively little relative energy loss and are therefore are retrievable even for the biased source distribution.

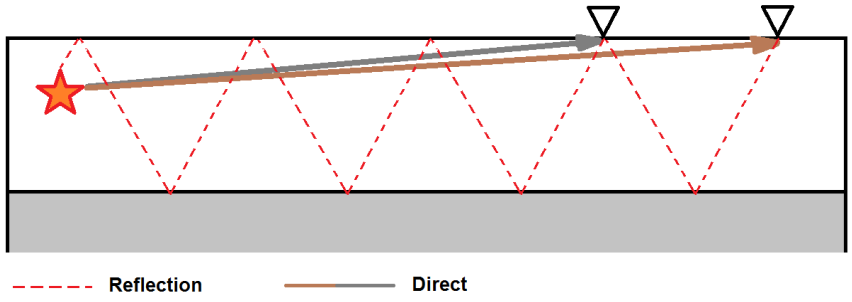

Figure 2.28: Cartoon of a far-offset source (star) from a two-station array (triangles)

As illustrated by these models, virtual source records computed from biased source distributions result in obscure and asymmetric representation of direct arrivals and distorted representation of the reflection phases (Figure 2.26), as well as strong, non-causal arrivals arising from incomplete cancellation. All of these virtual events are inherent artifacts for poorly distributed physical sources. However, if the bias is not recognized, it can lead to misinterpretation of the virtual source gathers.

2.7.3 Critically refracted arrivals

Figures 2.26(c) and (d) show that, along with the direct arrival (highlighted by red line), another strong quasi-linear arrival propagates from virtual shot in the same direction (highlighted in yellow). This second arrival corresponds to propagation velocity of 3.5km/s, which is the velocity of the bottom layer in our model. These are more clearly visible in the zoomed-in detail of the same virtual source gather shown in Figure 2.29, where the yellow line represents a linear move-out of 3.5km/s and the red line corresponds to 2.5km/s. The only physical arrival which would be expected to exhibit the higher velocity is the critically refracted wave (or head wave) from the lower layer. However, in the real shot gathers, the refracted arrivals intersect the time access at a value that scales to the depth of the refracting interfaces (e.g. Stein and Wysession, 2009, pg. 120-123). This virtual arrival, however projects back to zero distance at zero time, mimicking a direct arrival. A similar spurious arrival was noted by Mikesell et al. (2009) in their synthetic shot gather and attributed to be a critically refracted wave shifted to appear to be from the virtual shot location.

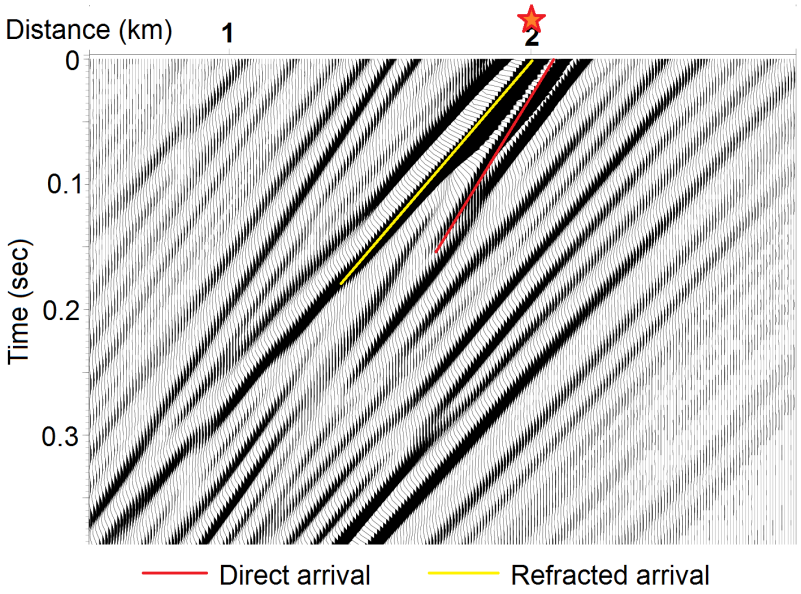

Figure 2.29: Detail of the virtual shot gather from Figure 2.26(e) (virtual shot location marked by the star)

According to Snell's law for acoustic waves (Equation 2.1) critical refraction occurs when the velocity of the overlying layer is smaller than of the layer beneath it (e.g. Stein and Wysession, 2009, pg. 120-123, illustrated in Figure 2.30).

$$\frac{\sin\theta_1}{v_1} = \frac{\sin\theta_2}{v_2} \tag{2.1}$$

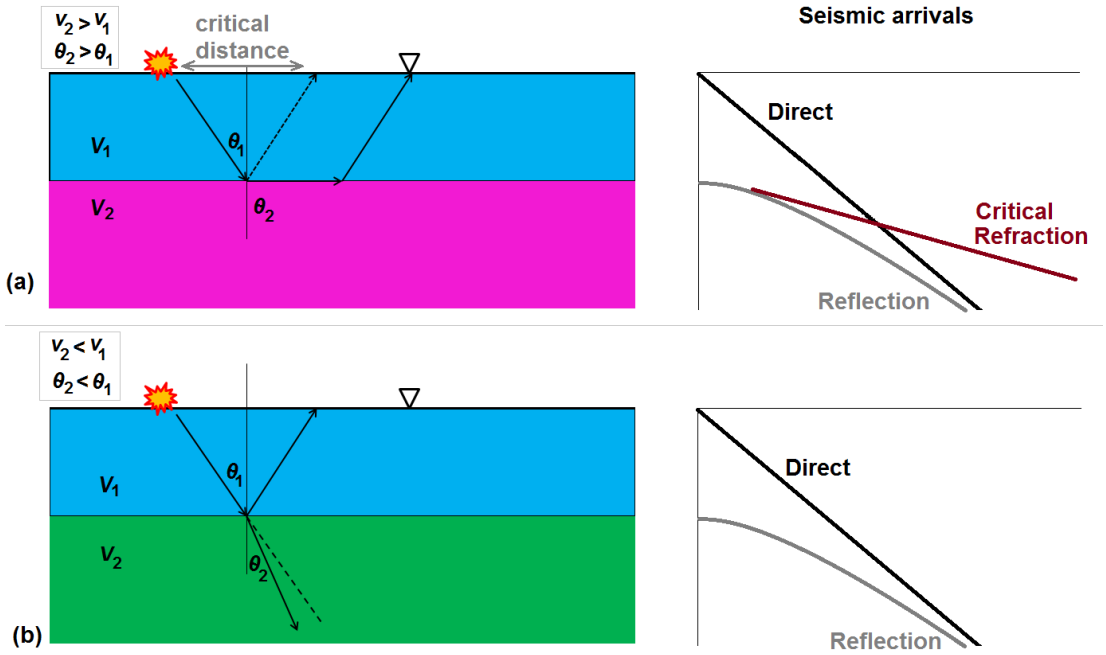

Figure 2.30: Snell's law for two layers with (a) increase in velocity at the interface (b) decrease in velocity at the interface

In Figure 2.31 we compare virtual shot gathers for the two models, one with increasing velocity with depth, the other with decreasing velocity with depth. The virtual source gather for the model with an underlying low velocity layer (Figure 2.31d) shows no spurious high velocity linear arrival emanating from the virtual source. In contrast, the virtual source gather with the underlying high velocity layer clearly exhibits this arrival (yellow in Figure 2.31c). Therefore, we conclude that critically refracted energy can appear as a spurious high velocity "direct" arrival when the sources are asymmetrically located with respect to the recording array.

We also notice that there were no strong critically refracted arrivals for symmetrical shallow source distribution used in Figure 2.23(a). We argue that this is due to the proximity of the sources to the receivers for such array configuration,

such that the majority of the stations are within critical distance and, therefore, do not record a critically refracted wave. However, for our asymmetrical source distributions, all of the sources in Figure 2.25(a) and most of the sources in Figure 2.25(b) lie beyond the critical distance for refraction in the lower layer, which is calculated for our geometry using equation 2.1 to be 0.7 km away from a surface source (smaller for sources at depth).

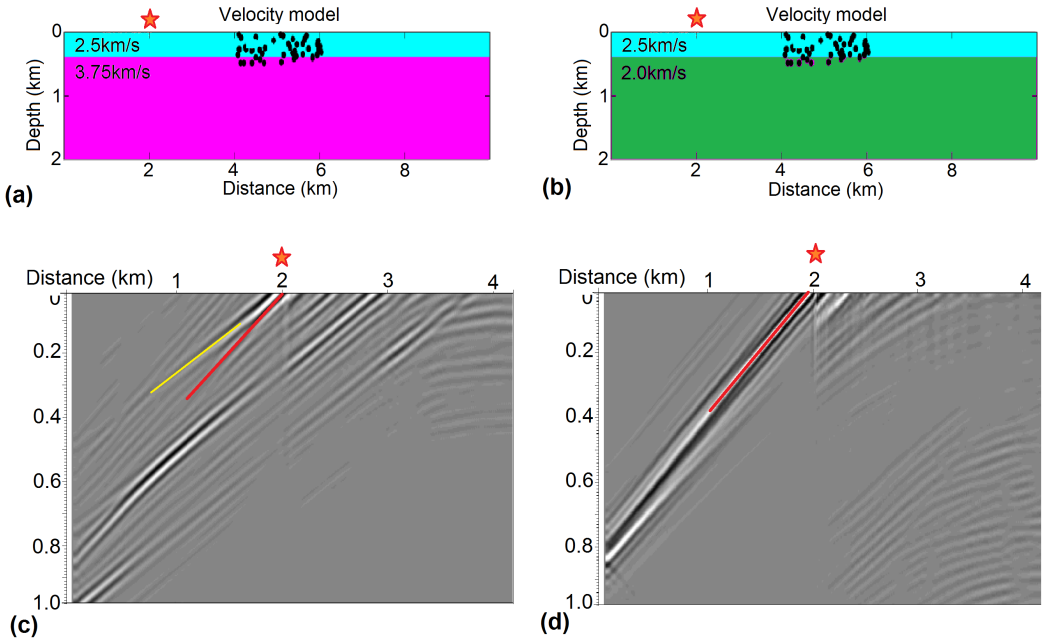

Figure 2.31: Comparison of virtual shot for 2 layered model with velocity of 2nd layer higher (a and c) and lower (b and d) than the first layer.

To further analyze how the direct and refracted arrivals map onto the virtual source record, a simple synthetic using only direct and refracted energy (i.e. no reflections) was generated. We placed 30 sources on the surface above a two-layer model (Figure 2.32) in which the lower layer has the higher velocity (3km/s and 5km/s respectively).

The arrival times of the direct and refracted waves were calculated using Snell's law for the given velocities and then convolved with a Ricker wavelet of 1Hz dominant frequency to create a record for each source.

Representative synthetic records produced by such geometry are shown in Figures 2.33 (correspond to the numbered sources in Figure 2.32) and are compared to the cross-correlation of each in Figures 2.33.

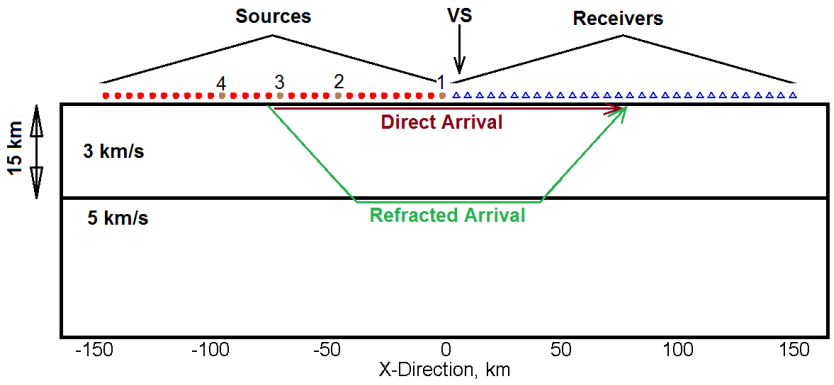

Figure 2.32: Geometry and velocity model for the synthetics in Figure 2.33. Receivers are represented by blue triangles and sources by red dots. The virtual shot station is marked by the arrow and is the closest station to the sources in the model.

Because the distance between the physical and the virtual sources in Figure 2.33(a) is smaller than the critical distance for the refraction in the lower layer, the virtual source station records only the direct wave. In this case, the virtual source gather generated by correlating this trace with the remaining traces simply shifts the traces by the direct travel time to this virtual source station. Thus, the virtual source gather (Figure 2.33b) looks very similar to the actual source gather (Figure 2.33a), no spurious events are generated and the slopes (velocities) of the direct and refracted arrivals are the same for both "real" and "virtual" gathers. However, after the source is moved far enough away for the

refracted wave to be recorded by the receiver to be used as a virtual source, cross-correlation results in four instead of the two linear arrivals. Two of these arrivals (2 and 4 in Figure 2.33d) correspond to correspond to the direct wave arrival D correlated with refracted R arrival (i.e. arrival 2) and with itself (i.e. arrival 4). However, the arrival time of this virtual wave (2) depends on the time difference between the direct D and the refracted R waves in 2.33(c), and therefore on the distance between the physical and virtual sources. As the time between D and R decreases in the record, the virtual arrival (2) "moves" closer to (4) (Figure 2.33e,f).

The other two arrivals (1 and 3) present in Figure 2.33 are result of correlation of the refracted arrival R with the direct D (i.e. arrival (3)) and itself (i.e. arrival (1)).

Virtual arrivals (1) and (4) (i.e. result of correlation of R with itself and D with itself) are independent of the time difference between D and R arrivals. Both of these virtual waves appear to emanate from the virtual source location.

Figure 2.33(g) is a record of the source 4 in Figure 2.32. For this source, the critically refracted wave R arrives at the virtual source location before the direct arrival D. Thus, the virtual arrival corresponding to correlation of D with R (i.e. arrival (2)) now comes before the arrival that corresponds to correlation of R with R (i.e. arrival (1)) in Figure 2.33(h). Similarly, the virtual arrival (4), which is a result of correlation of D with D, comes before the virtual arrival (3), which is the result of correlation of R with D. Virtual arrivals (1 and 4) again appear to emanate from the virtual source, but arrival times of (2) and (3) depend on the distance of the source from the virtual source and the difference in the velocities of the two layers.

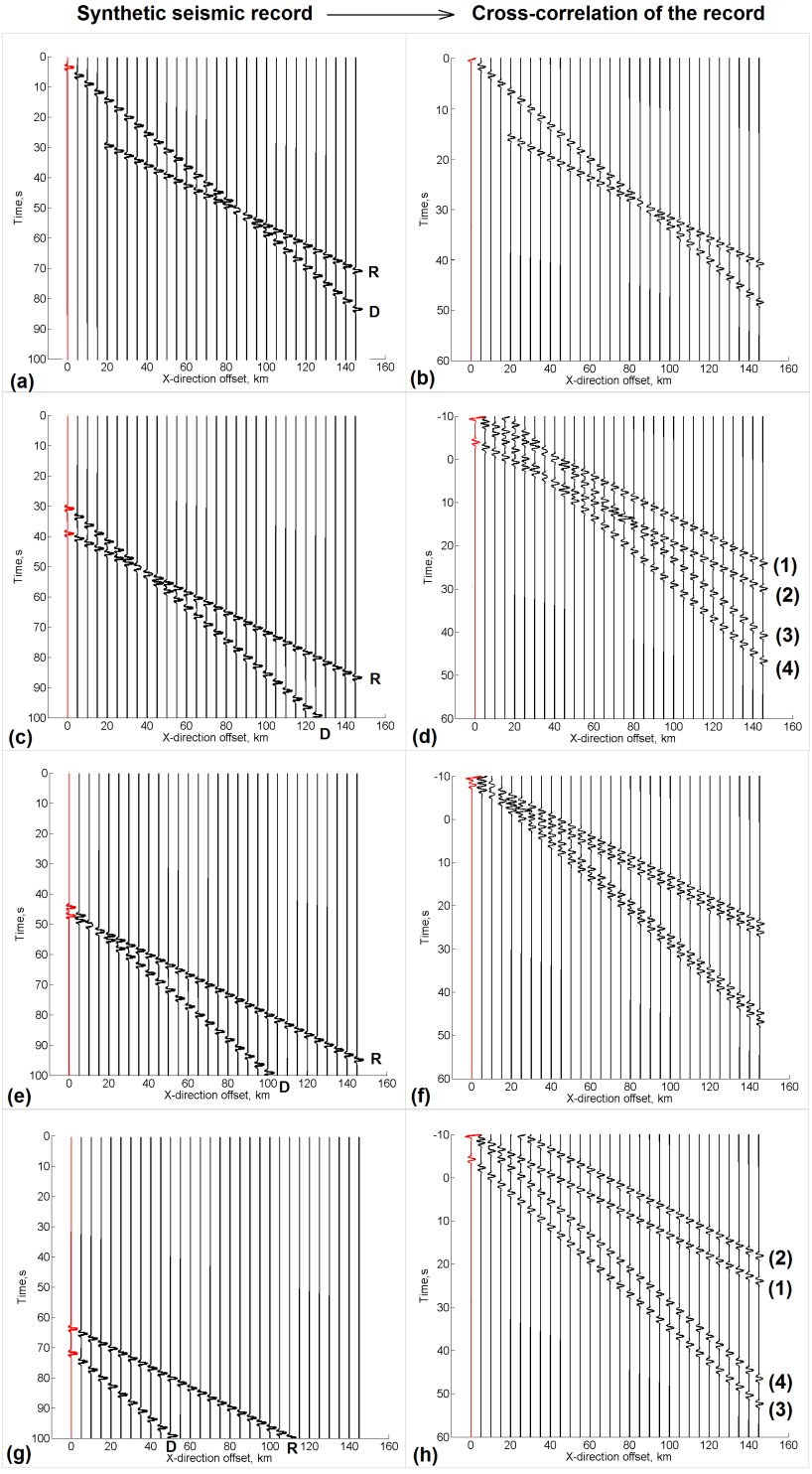

Figure 2.33: Examples of synthetic recording (left) and cross-correlation of that recording (right) for source at varying offset from the synthetic array ((a),(c),(e) and (f) are the records of the numbered (gray) sources in Figure2.32), and (b), (d), (f) and (h) are their respective cross-correlation. Red trace is the virtual source station

As a result, each cross-correlation of a more distant source produces 4 linear arrivals, two of which would always appear to emanate from the virtual shot (1 and 4), and the other two of which would project back to offset =0 at other time intercepts (including the negative intercept times).

Figure 2.34 is a virtual source record produced by summing the cross-correlations over all 30 sources in Figure 2.32. The resulting virtual gather has only two linear arrivals, with both appearing to propagate directly from the virtual shot location. The slopes of these two arrivals correspond to the apparent velocities of the "real" direct and critically refracted waves, respectively. These two arrivals are the result of the constructive interference of arrivals (1) and (4) in Figure 2.32. Arrivals (2) and (3) have been removed by destructive interference after the summation. Note that there is no observed head wave with an intercept time expected for an equivalent surface shot. Thus, we lose the information about the depth of the layer, but still retrieve the velocity. Also, because the head wave is always faster than the direct, it is the first recovered arrival in the virtual shot gather. The only location of the physical source that would yield the correct arrival time of the virtual head wave after cross-correlation is at the location of the virtual shot. However, when the cross-correlation records of the spatially-distributed sources are stacked, this "correct" head wave tends to be removed by destructive interference. Therefore, the critically refracted wave is never mapped into the expected for a surface shot arrival time in a virtual source gather.

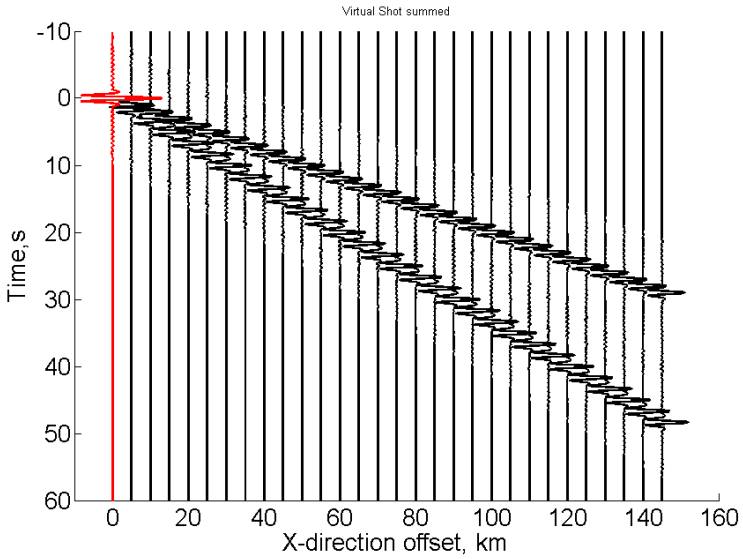

Figure 2.34: Summed cross-correlations for all shot (red dot in Figure 2.32)

2.8 Discussion and conclusions

The location of the energy sources in interferometry is critical to accurate generation of zero-offset reflectivity profiles and virtual source gathers. The main difference between shallow and deep sources of seismic energy for auto- and cross-correlations are the different "clustering" of the paths each wave follows. As with surface waves Halliday and Curtis (2008), the sources of the body waves have to be located in one of the stationary points for each station pair in order for the seismic signal to interfere constructively (Schuster et al., 2004) and produce virtual arrivals which mimic the true velocities and arrival times of a real, physical source.

In the simple case of 1D wave propagation, any source position will provide a virtual zero-offset reflection profile due to the fact that the incidence angle of

the ray is always zero for all the sources in 1D. The complications and spurious arrivals arise when going from 1D to 2D geometries.

In the 2D case, the incidence angle depends on the position of the energy source. However, the same requirement holds: the arrivals must share a stationary path in order for them to interfere constructively and produce a virtual source gather equivalent to a surface shot. The fulfillment of this requirement depends on the frequency of the signal, distance between receivers and distribution of the sources of seismic energy.

We have analyzed two distinct general geometries for the 2D case: shallow and deep sources relative to the target reflector. We demonstrate how the resulting virtual source gathers and zero-offset reflectivity profiles include different kinds of spurious arrivals (or artifacts) for variations on these two types of source distributions.

Auto-correlation of the signal from sources at depth greater than an interface of interest (deep sources) can produce an image with a strong (i.e. high amplitude and coherent) reflection at the appropirate travel time from that interface when the sources are distributed symmetrically beneath the recording array. This image is equivalent to a zero-offset surface reflection profile. Auto-correlations can also recover the dipping events for dipping interface for the same distribution of sources. If the source locations are biased, the arrival times of the virtual reflections are underestimated and, in case of the dipping interface, this effect is even more serious on the down-dip side.

Shallow sources do not produce reflection images of subsurface reflectors as effectively as deep sources on zero-offset seismic sections generated by auto-

correlation. The failure is due to the contribution of additional reflected and multiple energies that fail to cancel during summation over a limited number of sources. A contributing factor is that for a fixed station spacing, there are a fewer stations occupying positions associated with the stationary phase for a given reflector with the shallow source geometry. To the extent that ambient noise is created in the near-surface environment (Shapiro et al., 2005), interferometry using these sources is less likely to produce coherent reflection imagery. This geometrical bias can be one explanation why retrieval of body wave reflection from ambient noise has been less successful than retrieval of surface waves.

In contrast to the case of auto-correlation, cross-correlation is more effective at producing a virtual direct body wave arrival in virtual shot gathers from shallow sources than with deep sources. However, corresponding reflections at small offsets are weak. Virtual source gathers for deep sources produce a strong reflection at small offset but overestimate the normal move-out velocity at larger offsets and simply fail to retrieve direct (e.g. subhorizontal) body wave arrivals. In the case of limited spatial distribution of the sources used in cross-correlation, the virtual source gather can exhibit hyperbolic precursory arrivals offset from the main reflection hyperbola. These "artifacts" are due to incomplete cancellation of spurious arrivals.

For a biased source distribution (i.e. the physical sources are not located symmetrically beneath the recording array) the computed virtual source records result in an obscured and asymmetric representation of direct arrivals and distorted representation of the reflection phases, as well as strong non-causal arrivals arising from incomplete cancellation.

Our synthetics suggest that if a significant portion of the body wave energy

were supplied by the sources which are further than a critical distance away from the receivers (this distance depends on the depth of the layer and the velocity contrast), then the virtual source gather would have the head wave shifted such that it would appear to propagate from the virtual shot location. Both virtual direct and critically refracted arrivals will have the slopes that correspond to the velocities of the physical medium; however, the information about the depth of lower layers will be lost.

Our models show that interferometry is a powerful technique that allows the retrieval of response functions from ambient noise, but only when the distribution of contributing sources is appropriately symmetrical and distributed with depth. However, this analysis does not address a number of additional complications expected in the real world applications. One consideration that needs further study is the contribution of S-waves (direct and reflected) energy to the P-wave virtual shot gathers. Another is the spatially variable radiation pattern for both P and S waves associated with natural sources (e.g. earthquakes), which introduces an inherent asymmetry in source amplitudes during correlation and summation.

Nevertheless, the synthetics presented here provide a guide to differentiating between spurious arrivals (i.e. artifacts) and energy that accurately mimics real seismic body wave behavior. They also suggest experimental design which can optimize computation of virtual seismic profiles that provide accurate imagery of the real subsurface.

CHAPTER 3

REFLECTION IMAGING OF THE SUBDUCTING LITHOSPHERE BY SEISMIC BODY WAVE INTERFEROMETRY OF LOCAL EARTHQUAKES

3.1 Abstract

This study investigates the feasibility of generating virtual 2D reflection profiles from cross-correlation of local earthquakes in a subduction zone setting. We compute synthetic seismograms for various quasi-random distributions of subsurface sources (earthquakes) and then generate virtual reflection profiles using conventionally processed virtual source gathers. The goal is to identify acquisition strategies that favor the effective extraction of virtual P-wave reflection for robust common reflection point (CRP) imaging of subducting slabs. Our synthetics shows that while such imaging is insensitive to origin time errors. However, having an adequate lateral distribution (aperture) of sources is critical. We test these techniques using earthquakes (both zero-offset and CRP) recorded by MASE and VEOX broadband seismic lines in Mexico (MASE, 2007; VEOX, 2010). Although these resulting images are marginal at best, our synthetics suggest that relatively robust imaging is achievable with modern dense array technologies and the levels of seismicity that are characteristic of active subduction zones.

3.2 Introduction

Subduction zones are the primary location for the word's great earthquakes (e.g. Hyndman and Wang, 1995; Shao et al., 2011). In spite of great scientific interest in the subduction seismogenic zone (Dixon and Moore, 2007), high resolution reflection images of the deeper seismogenic zone of the subducting slab are very few (ANCORP, 1999; Arai et al., 2009). Yet such imaging is critical to assessing the role of fault morphology and physical properties in controlling earthquake rupture (Gulick et al., 2010).

Teleseismic earthquakes have been widely used to generate seismic images of subduction zones by exploiting such techniques like receiver function (e.g. Burdick and Langston, 1977; Ferris et al., 2003; Nábělek et al., 2009) and seismic tomography (e.g. Backus and Gilbert, 1967; Schurr et al., 2003; Yang et al., 2009; Widiyantoro et al., 1999). However, these so-called passive source images are limited in resolution due to the fact that high frequency energy from teleseismic sources is usually attenuated before reaching the station. Here, we investigate a new technique that uses local earthquakes in the proximity of the seismic array as our sources of energy. Due to this proximity, much higher frequencies are available therefore potentially providing more sensitivity to the small scale variations in the morphology and physical properties of the reflecting interfaces in the subduction system. Moreover, since this approach relies on natural seismicity rather than expensive artificial sources, it offers the possibility of more cost-effective reflection imaging than with conventional controlled sources approaches, including the potential of time lapse recovery of reflected waveforms, where subtle temporal variations in reflectivity may be detected (Bangs et al., 2011).

The subduction zone setting represents a fertile environment for the application of seismic interferometry for body wave imaging because of the high levels of local seismicity. Here we develop and test an interferometric technique which can be applied to the recordings of local earthquakes to image the slab using the larger bandwidth of these events. Such images should represent a major improvement in resolution over seismic techniques based on using teleseismic earthquakes.

Even though seismic interferometry has been most successful in surface wave imaging (e.g. Shapiro et al., 2005; Yao et al., 2006; Bensen et al., 2007; Lin et al., 2008, etc.), some advances have been made in retrieval of the body waves from natural sources (e.g. Roux et al., 2005; Draganov et al., 2007; Zhan et al., 2010; Poli et al., 2012a,b; Lin et al., 2013a, etc.), and distributed controlled sources (Schuster, 2001; Bakulin and Calvert, 2004). Here, we evaluate the same interferometric technique as it may be applied to the local subduction zone earthquakes by computing synthetic seismograms for simple models of subduction and then generating synthetic images using interferometry. Our modeling helps identify source distributions and acquisition geometries for which successful imaging is feasible. Application of these techniques to the real data previously acquired across the subduction in southeastern Mexico (MASE, 2007; VEOX, 2010) for teleseismic studies emphasizes the need for deployments better designed for effective imaging with local sources.

3.3 Subduction zone synthetics

Here we present our results of the subduction zone synthetic imaging with interferometric technique. For synthetic seismic modeling, we start with a simple 2D geometry: a dipping reflector beneath a linear surface array. Point sources of P-wave energy are distributed randomly within fixed depth and offset ranges. We then generate virtual source gathers (VSG) from these synthetic recordings. Our goal is to examine the 2D reflection profiles generated from these VSG's using conventional processing and the dependence of these reflections on the physical source distribution relative to the recording array.

The synthetics were generated using the CREWES toolbox (Margrave, 2003). We define a simple 2D velocity model with a dipping interface (e.g. Figure 3.1) to approximate a slab interface. Then the toolbox generates a rectangular grid, and places the receivers on the "surface" of the model. Stations were evenly distributed on the surface at a 200-meter spacing for a total of 1000 stations positioned above the "subduction zone". For each model 50 sources were placed randomly within a range of depth and offsets, and corresponding synthetic seismograms were generated for all receivers using the CREWES second-order finite differencing algorithm to propagate a Ricker wavelet (1.5 – 4.0Hz) from each source to the receivers. Although we expect local sources to include energy to much higher frequencies (e.g. up to approximately 35Hz; Chapter 3.4), we chose this lower bandwidth for computational efficiency.

For various scenarios we synthesized radiation from the 50 randomly distributed P-wave sources to produce recordings at the surface stations, which we then use to create virtual shot gathers by means of cross-correlation and

summation (Chapter 2). We analyzed the virtual shots and then further processed them to create 2D reflection sections using conventional processing of active seismic surveys.

The workflow implemented for all synthetics is as follows: (1) 50 shots with random locations within a specified depth range are generated within the velocity model, (2) CREWES is used to create synthetic seismic records for each of the shot and surface receivers, (3) a station (virtual source) is cross-correlated with the remaining stations for each source gather, (4) all cross-correlations are summed over all sources (stacked) to create a single virtual source gather (VSG). After several such gathers are generated for different locations of the virtual source, these gathers are processed as conventional surface source gathers to produce a Common Mid-Point (CMP) stacked reflection section. We then compare these "virtual" profiles to the 2D profiles generated using the same conventional processing of synthetic surface sources ("real" profiles).

Figure 3.1 is the synthetic velocity model for a subduction zone scenario. Black circles are the locations of the 50 randomly distributed crustal earthquakes. The red triangles in Figure 3.1 denote three separate profile segments to be discussed: up-dip from the source distribution (AB), above the sources (BC) and down-dip from the sources (CD). Stars marked by roman numerals are virtual source station location for each VSG.

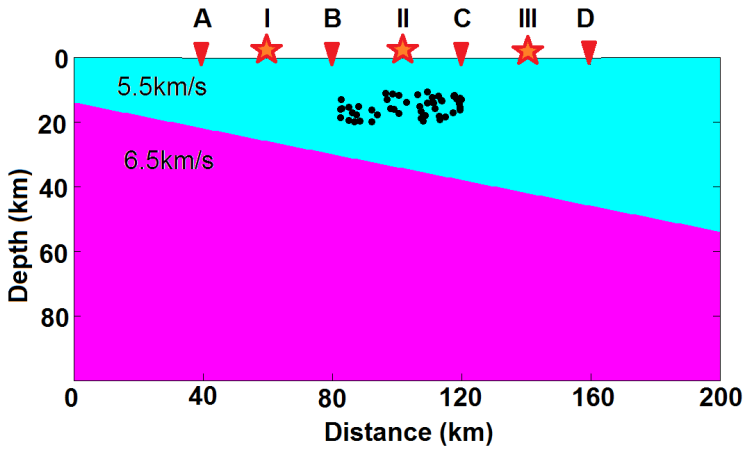

Figure 3.1: Velocity model for a subduction zone scenario where most of the earthquakes are coming from overlying continental material (e.g. the crust). Black circles are locations of 50 randomly distributed earthquakes within the overthrust material. Stations are evenly-distributed on the surface in 200-meter spacing.

Figure 3.2 is a synthetic recording of a surface shot for the velocity model displayed in Figure 3.1 at the location of star II. The magnitude of this surface source equals to the magnitude of each source distributed at depth. Direct arrival, reflection and multiple P-wave arrivals are easily identified in the record (red, green and blue). We expect to retrieve these arrivals in our virtual shot gathers. A slight asymmetry in the arrival times of the reflection phase (green; Figure 3.2) relative to the source location in the gather is representative of the tilted layer geometry.

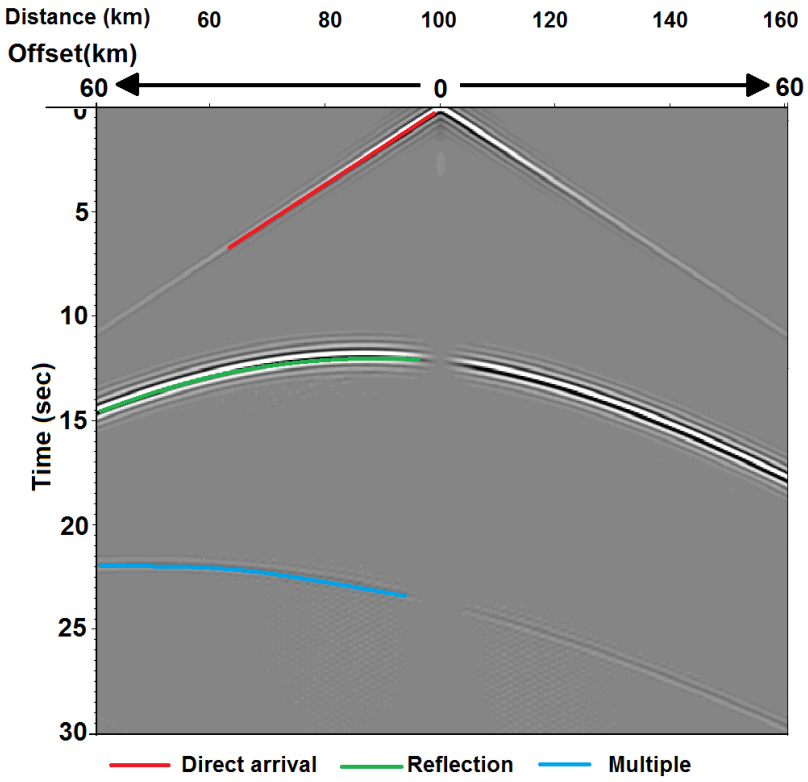

Figure 3.2: Synthetic surface shot at the location of II star in Figure 3.1. Direct Arrival, Reflection, Multiple are denoted by Red, Green, Blue.

Figure 3.3 is a single virtual source gather generated from the 50 random sources (black circles in Figure 3.1). The location of the virtual shot is in the middle of the synthetic station array, similarly to the surface shot in Figure 3.2. Even though the arrivals are not as strong as in the surface shot gather (all sections shown with same display gain settings), the same three arrivals are recovered: direct (red), reflection (green) and a hint of a multiple (blue). The normal move-out of the virtual reflection (the shape of the hyperbola) is the same as for the surface shot. The virtual reflection exhibits higher amplitudes up-dip than down-dip, which was not observed on the synthetic surface shot gather. The velocity (e.g. inverse slope of the arrival highlighted in red) of the vir-

tual direct arrival is slightly larger than that of the synthetic surface source (e.g. 6.1 km/sec vs 5.5 km/sec). This discrepancy arises from the geometry of the physical sources relative to the receivers, as illustrated in Figure 3.4. The time difference between the first arrival recorded by stations 1 and 2 is smaller for the deeper source. Cross-correlation of this arrival between these two stations results in a virtual direct arrival whose slope indicates a higher apparent velocity than a near surface source. Thus, deep sources will always produce virtual source gather that overestimate the velocity of the virtual direct arrival.

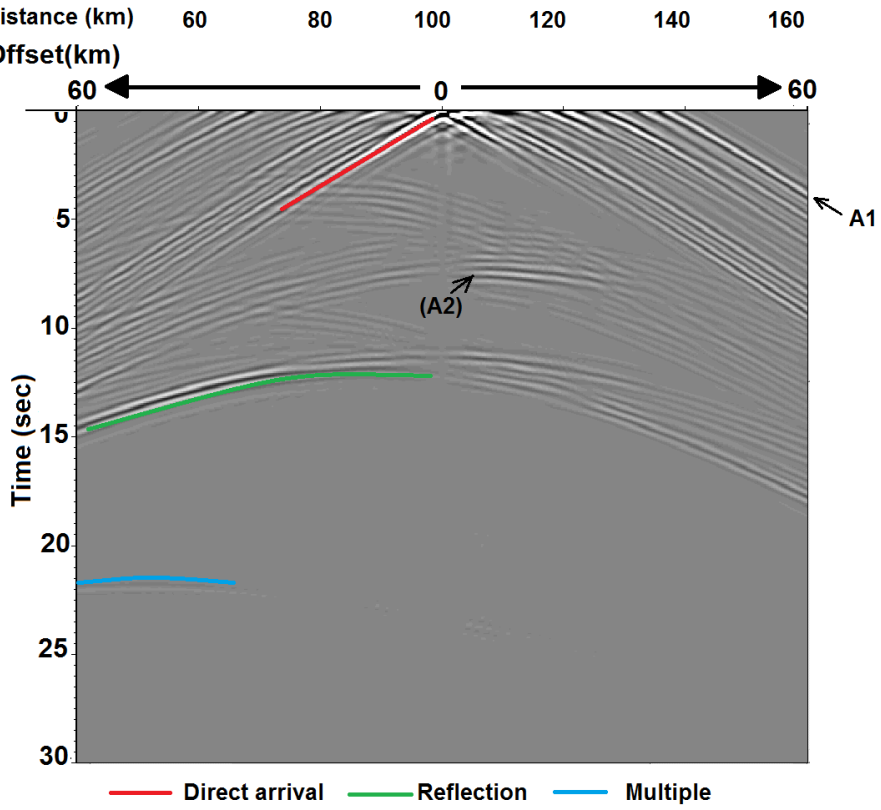

Figure 3.3: Stack of cross-correlations of 50 random shots from Figure 3.1, with virtual shot at the II star location, similarly to the surface shot in Figure 3.2.

There are numerous spurious arrivals (or artifacts A1 and A2) visible in the

virtual source gather (Figure 3.3) that are not present in the surface shot record in Figure 3.2. Artifacts like A1 are an non-causal quasi-linear arrivals that are sub-parallel to the virtual direct arrivals. Artifacts A2 are "precursory" hyperbola above the virtual reflection (green). Both result from incomplete cancellation of energy along non-stationary raypaths due to the limited number and distribution of sources (See Chapter 2).

Artifacts like A1 are caused by both a shift of the direct wave during cross-correlation of each record and its correlation with a the secondary arrival (i.e. the first reflection; see Chapter 2.7).

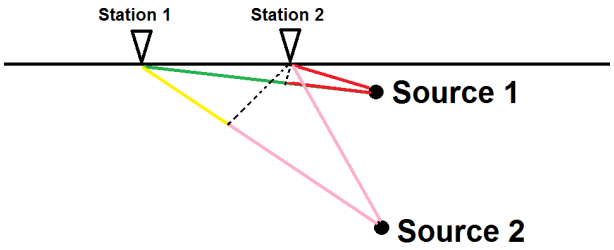

Figure 3.4: Difference in ray paths for a shallow 1 versus a deeper 2 sources

Artifact A2 is related to the restriction of the source to a narrow depth range. In our model, the depth range is only 10 km. Therefore, the depth phase of each event does not vary significantly in time from one source to another resulting in diminished cancellation of non-stationary phases. The more localized are the energy sources in depth, the more prominent this artifact can be.

Figure 3.5 is comparison of two virtual shot gathers (scaled and normalized) generated from cross-correlation of (a) 50 (from Figure 3.3) and (b) 150 distributed sources within the same depth range. Even though the virtual direct (red) and reflected (green) arrivals are stronger for the larger number of

sources, the artifacts A1 and A2 are still present in the VSG. However, since the depth range is the same for both source distributions, the A2 type artifacts are still present. It may not be possible to eliminate such artifacts completely from the virtual shot records since the source distributions are restricted in depth naturally. However, increasing the number of sources used to generate the virtual source gather clearly increases the strength and coherency of the true reflections, even for a limited depth range of the physical sources.

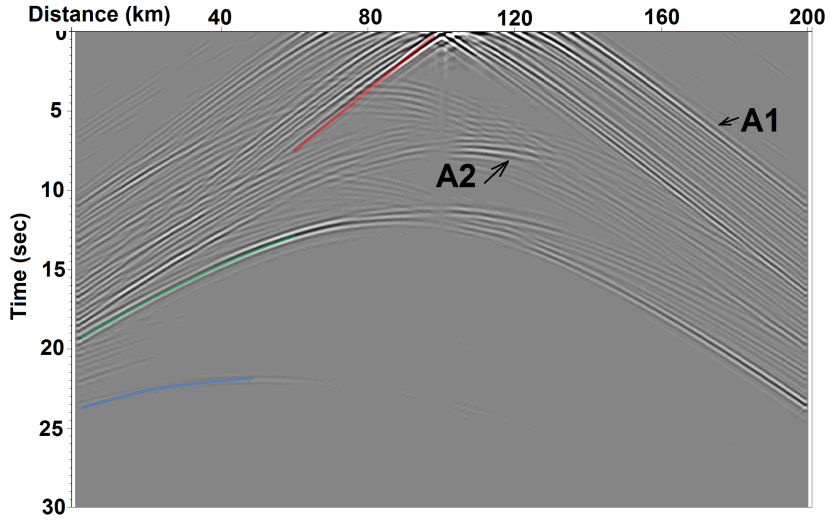

(a) cross-correlations of 50 random sources stacked (Fig. 3.3)

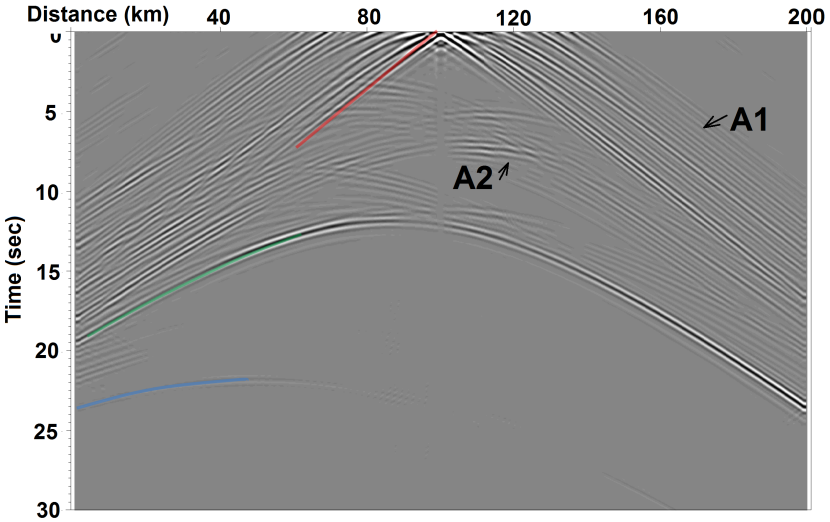

(b) cross-correlations of 150 random sources stacked

Figure 3.5: Comparison of the virtual source gathers generated by cross-correlation and summation of 50 versus 150 sources. More sources result in stronger virtual reflections, but artifacts related to the limited spatial distribution of sources remain.

Let us now consider laterally biased source distributions and their effect on the virtual source gathers. We will focus on the stations within the AB and CD sections and virtual source stations I and III respectively (Figure 3.1). Figure 3.6

is the comparison of VSG I and VSG III. Figures 3.6(a) and 3.6(b) are virtual shot gathers with the same scaling applied. Note that for Figure 3.6(a) all the sources are to the right of the stations and the virtual direct wave propagates from right to left. Similarly, for the VSG in Figure 3.6(b) all the physical sources are to the left of the virtual source (VS) station and therefore the energy propagates from the left to the right. As expected due to the asymmetry of the source distribution relative to the stations, the direct virtual wave energy appears to propagate in only one direction, i.e. away from the physical sources (Chapter 2). However, this asymmetry results in very different renderings of the underlying reflection, e.g. different arrival times of the apex of the reflection and the distorted shape of the hyperbolic arrival.

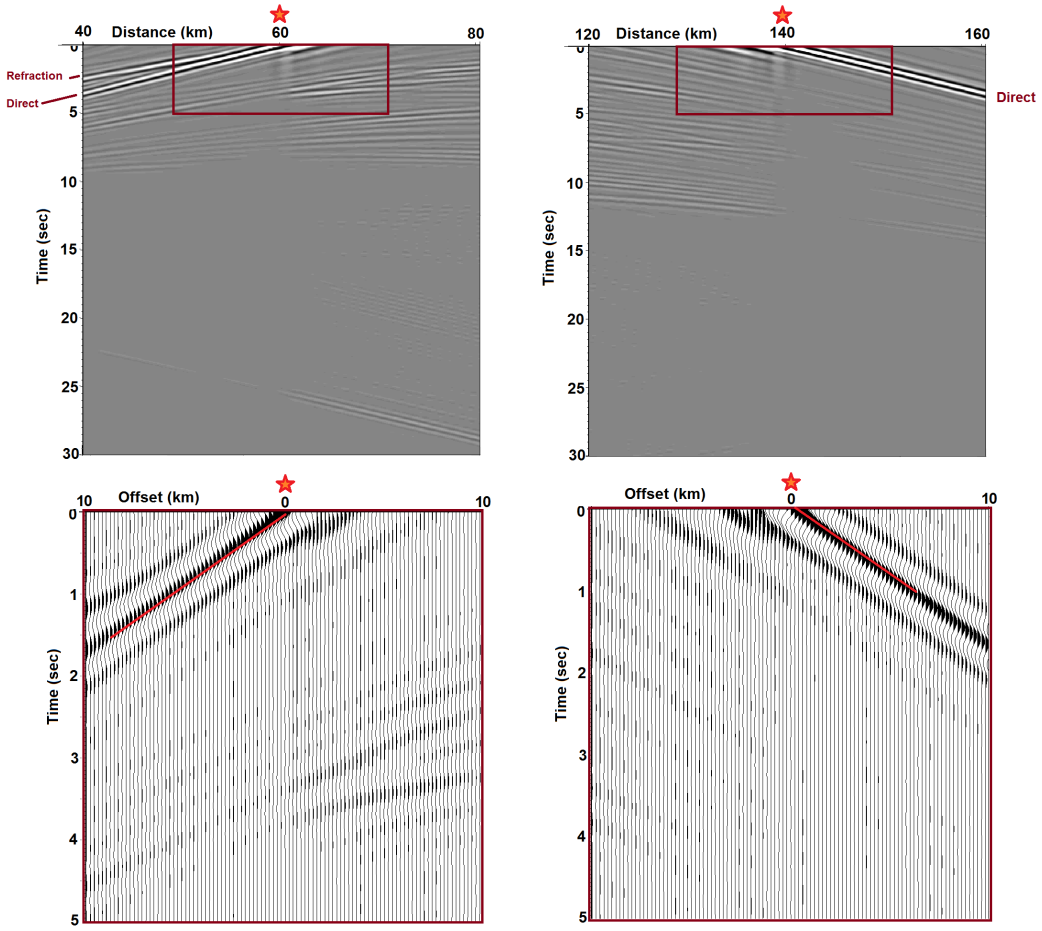

(a) 50 random sources stacked with virtual at I star at Fig. 3.1 looking at profile A-B

(b) 50 random sources stacked with virtual at III star at Fig. 3.1 looking at profile B-C

Figure 3.6: Comparison of the virtual shot gathers for biased source distribution.

Note that the virtual critically refracted wave (or head wave) is evident in the top section in 3.6(a) (emanating from the virtual shot location according to Chapter 2). However, it is not present in the top panel in Figure 3.6(b) for the down-dip stations. For the receivers located down-dip from the physical source the layer is deeper than for receivers up-dip. Therefore, the down-dip stations are within the critical distance from the physical sources of energy and the head wave is not recorded. Note that the intercept time for the head wave is at zero

virtual offset rather than the intercept time to be expected for a real head wave. This ”re-zeroing” of the refracted arrival is a by product of the cross-correlation process (see Chapter 2.7.3).

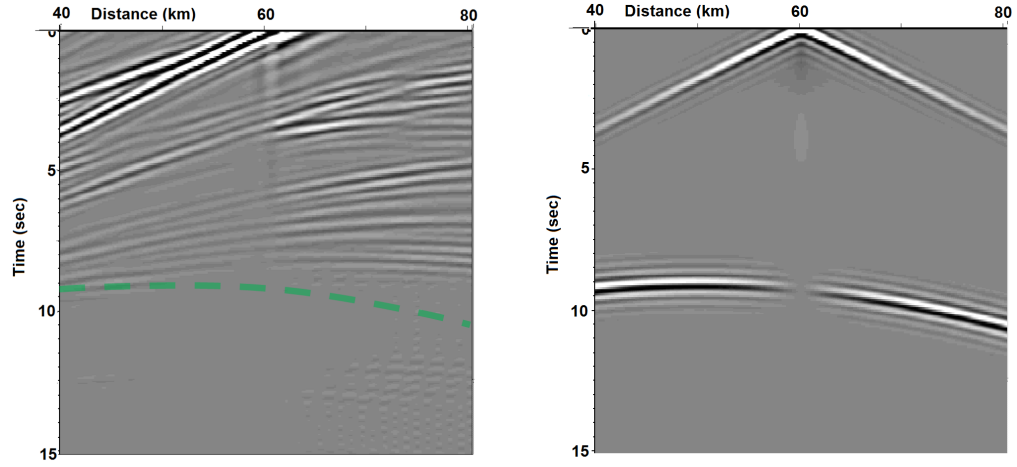

(a) 50 random sources stacked with virtual at I star at Fig. 3.1 looking at profile A-B

(b) Surface shot at location I star at Fig. 3.1 looking at profile A-B

Figure 3.7: Comparison of Virtual Shot Gather and Surface shot gather (Zoom into first 15 seconds)

Figure 3.7 is a comparison between VSG from figure 3.6(a) and the surface shot at the same location. The surface shot records a reflection hyperbola at around 8 seconds at 40km position (Figure 3.7(b)). The VSG (Figure 3.7(a)) has a faint arrival at this time with decreasing amplitude toward the center of the gather (green dotted line is a projection of the reflection from figure 3.7(b)). We will next attempt to enhance this virtual reflection by performing a common mid-point (CMP) stack used in conventional surface survey processing.

3.3.1 CMP processing of virtual source gathers

Conventional processing of an active source seismic survey takes advantage of the redundancy of the recorded data from multiple sources (e.g. Yilmaz, 1990). Figure 3.8 outlines the common-midpoint stacking technique that is the core of processing typically used to enhance reflection energy during the generation reflection profiles. The seismic data is recorded as a common shot gather and then CMP sorted. Note that for a CMP gather all of the reflected energy is imaging a single point (P) within the interface. The next step in the processing flow is to account for the increase in the travel time with the offset (Normal Move-Out or NMO correction). Finally, the NMO corrected traces are summed together (or CMP stacked) to produce a single trace with increased amplitude of the reflection from point P. The traces that image multiple points along the interface constitute the 2D reflection profile.

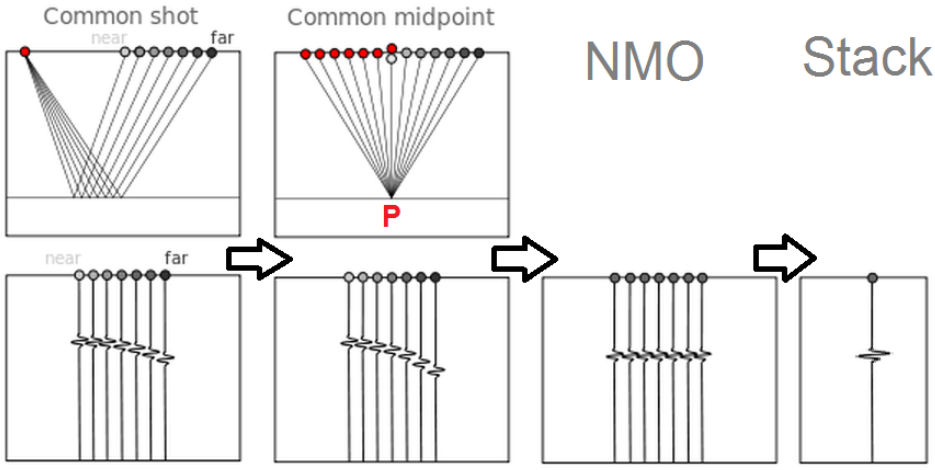

Figure 3.8: Illustration of principle of the CMP stack

Here, 11 virtual source gathers were generated at the locations marked by stars in Figure 3.9. These gathers were subsequently CMP sorted, NMO cor-

rected and stacked. Figure 3.10(a) is 2D virtual reflection profile generated after amplitude scaling and CMP stacking of the VSG within the BC section of the model (e.g. stations above the physical sources, Figure 3.9). Figure 3.10 is the same profile generated for the synthetic surface shots at the same location as the virtual sources.

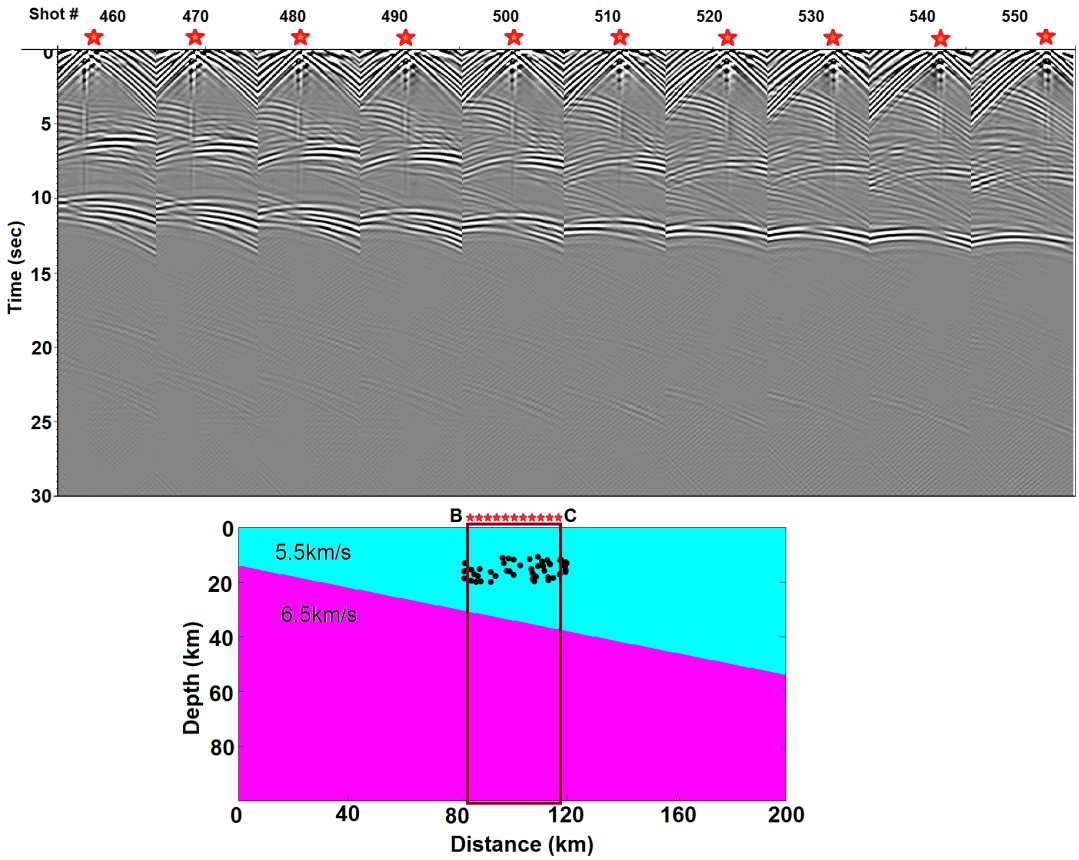

Figure 3.9: Virtual Shot gathers used for the 2D-line CMP stacking flow. The location of the shots and the extent of the stations used are shown below in the red rectangle. Virtual shot locations are marked by stars.

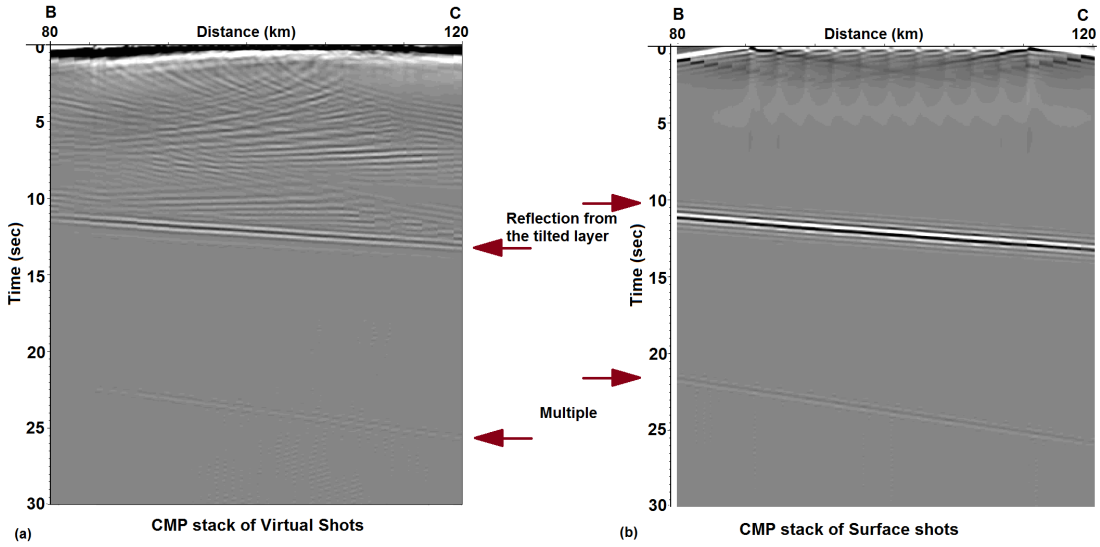

Figure 3.10: 2D CMP stack of (a) Virtual Shots, (b) Surface shots at the same location

The reflection from the dipping layer is prominent in both Figures 3.10(a) and (b). A hint of a virtual multiple is also retrieved at the correct travel time in Figure 3.10(a). Even though there are still spurious arrivals present from partial cancellation of the depth phases (see above) above the imaged virtual reflection, the target layer is well imaged, quite coherent and much larger amplitude than these artifacts.

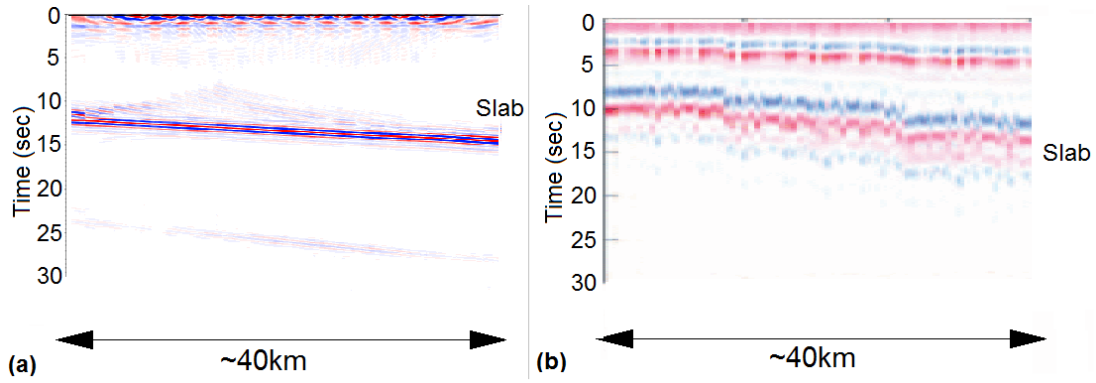

Figure 3.11: Comparison of (a) CMP stack from Figure 3.10, (b) Receiver function model of Cascadia scaled to our model (modified from (Nicholson et al., 2005))

Figure 3.11 illustrates the potential advantage of the local earthquakes interferometry over widely used teleseismic techniques. Figure 3.11 compares (1) the synthetic CMP stacked profile from Figure 3.10 with (2) a synthetic receiver function (RF) of the Cascadia subduction zone (modified from (Nicholson et al., 2005)). Note that technique recovers a virtual P wave surface reflection at the associated two-way P-wave travel time, while RF image is of the converted Ps phases (e.g. Mohsen, 2004) at a time that represents the differential arrival time of the upcoming Pp and Ps waves. Here we selected models such that these arrival times happen to be similar. Note that the number of the surface receivers is smaller for the RF synthetics, which results in lower horizontal resolution. However, the vertical resolution is limited by the effective frequencies of the respective sources. For the virtual reflection synthetics, the bandwidth was 1.5 to 4Hz, for the receiver function synthetics, a bandwidth of 0.1Hz was used. In general we can expect the effective maximum frequency of local subduction zone events to be as high as 50-100Hz (depending on the depth of the source; Figure 3.25), whereas the highest frequencies normally used in receiver func-

tions is on the order of 1-3Hz (Yamauchi et al., 2003; Gans et al., 2011).

Figure 3.12 is the same conventional CMP processing applied to VSGs of all three sections: AB, BC and CD (Figure 3.1) with virtual shot gathers created for each section separately (locations denoted by the stars, total of 11 for each section). The reflection is the strongest for the BC section (e.g. directly above the sources) and is visible in the AB section (located up-dip from the sources). However, it is not visible in the CD section which is located down-dip from the sources. This asymmetry in the reflection recovery persists in all 2D reflectivity profiles generated from cross-correlation of sources at various depth ranges (Figures 3.12, 3.13 and 3.14).

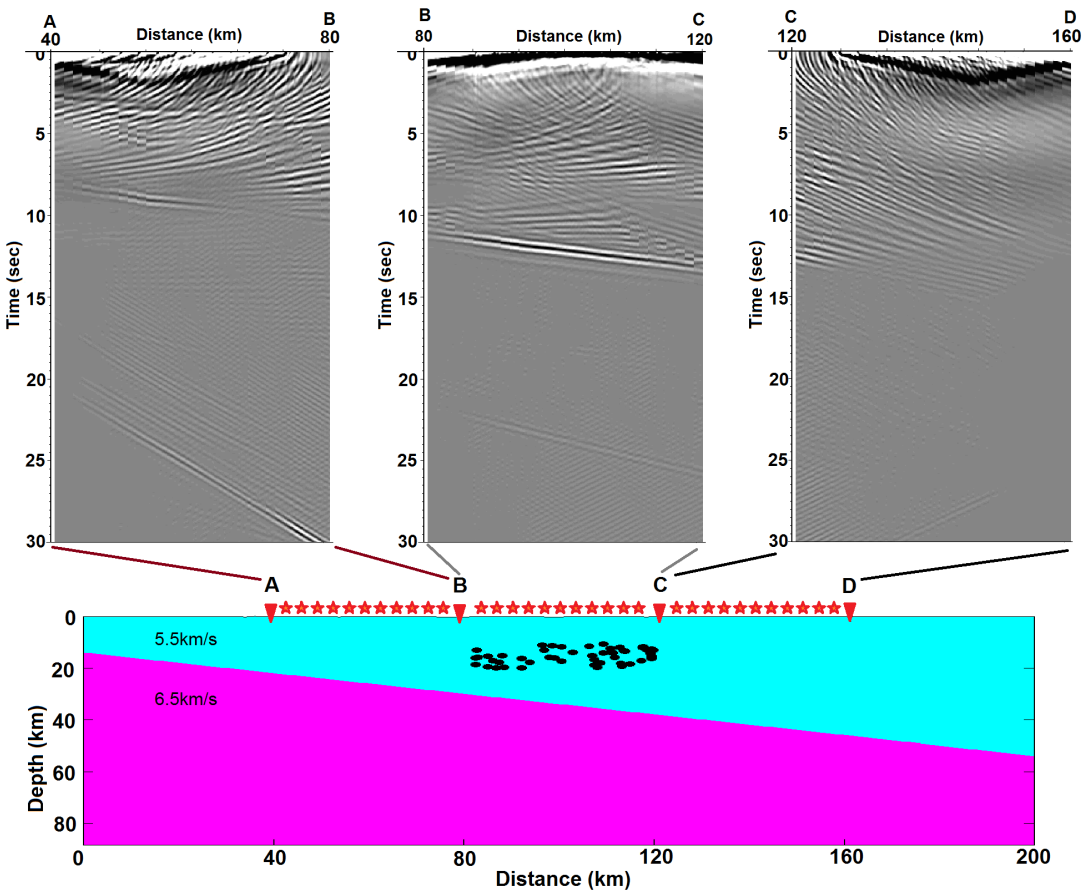

Figure 3.12: Comparison of CMP shots for laterally shifted source distribution

Figures 3.12, 3.13 and 3.14 show that deeper sources (40-60km for our model) produce a stronger and more coherent reflection, especially for the BC profile. The reasons for this improvement are discussed in Chapter 2. Note that the virtual reflection is also quite prominent in the AB section (up-dip from the sources) is very prominent for cross-correlation of the deepest sources. However, down-dip stations within CD section still cannot retrieve a coherent reflection using energy of the source below BC stations.

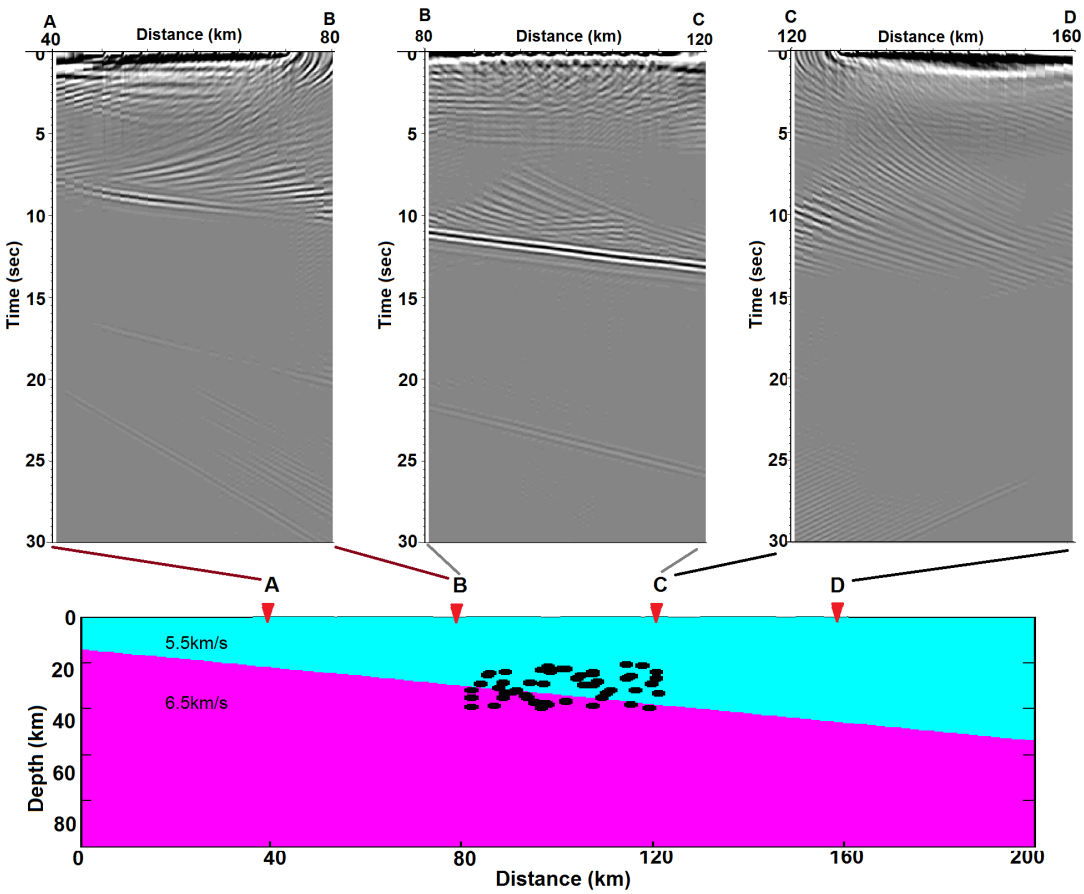

Figure 3.13: Comparison of CMP shots for laterally shifted source distribution for medium depth sources

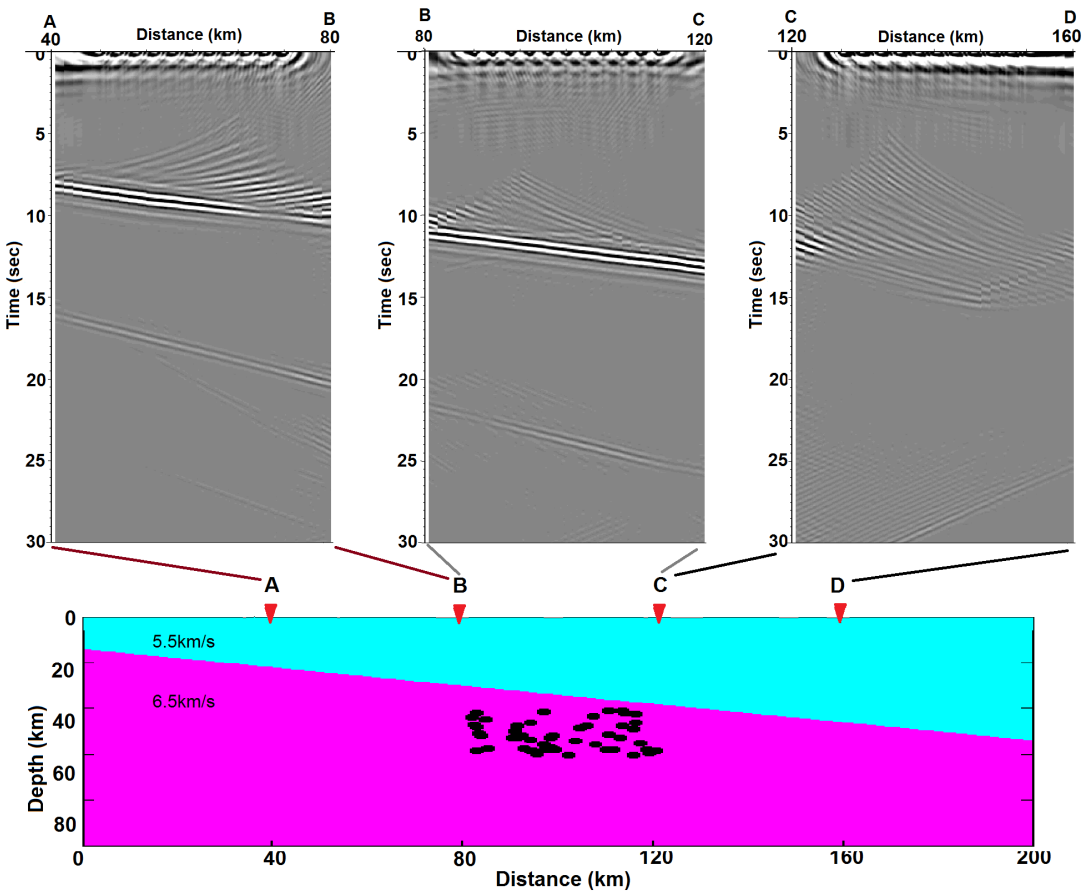

Figure 3.14: Comparison of CMP shots for laterally shifted source distribution for deep sources

Figure 3.15 helps illustrate the reason for this asymmetrical results. It compares the stationary paths for the reflection phase from dipping (red and green raypaths) and flat (orange raypaths) interfaces. For the deep sources below the interface the rays traveling from the base layer are refracted down-dip (red and green). If the stations are located slightly up-dip from the physical sources (section AB at 40-80km within our model) the direct and reflection arrivals will refracted towards the center of the model. However, for the same reflection point from a flat layer (and similarly stations down-dip from the physical sources) the reflection raypaths propagate away from the sources and the center of the

model (orange ray for the flat layer and green ray for the down-dip reflection). This bending of the raypaths down-dip results in coherent seismic image up-dip but not down-dip. The coherency of the up-dip reflection depends on the depth of the sources and the dip angle of the interface.

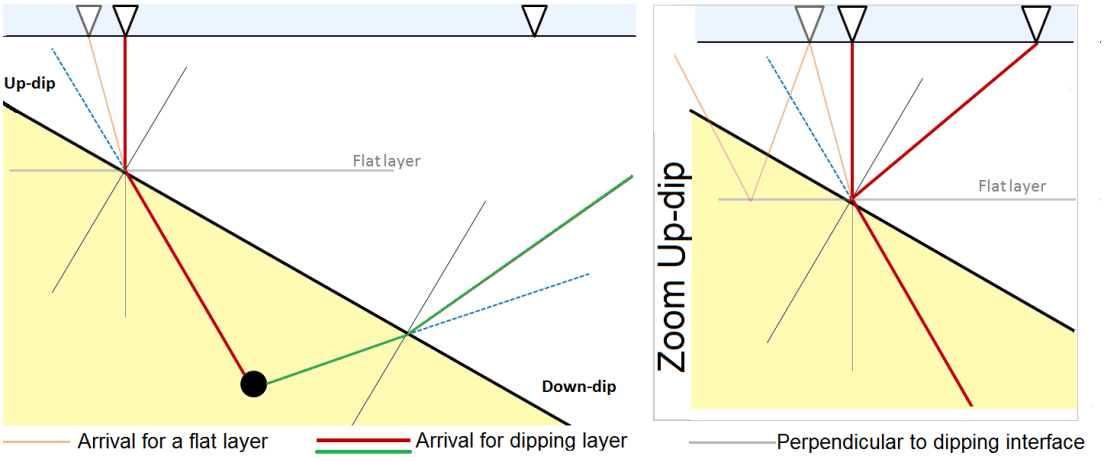

Figure 3.15: Illustration of up-dip and down-dip ray paths from synthetic sources

In reality, there are many additional factors that can negatively affect the retrieval of virtual reflections that we do not consider here. Such factors include: variations in the rupture history, focal mechanisms and magnitude of individual events, the presence of S-wave and converted phases in the recordings

In order to investigate some of these complicating issues we have modeled two scenarios: (1) combined P-and S waves and (b) varying levels of uncorrelated noise present in the recording.

3.3.2 P- and S-waves

As opposed to impulsive single mode sources used above, earthquakes generate S-waves in addition to the faster P-waves. We constructed a velocity model with sources producing two waves: a fast P-wave and slower S-wave. However, no converted phase (e.g. P to S or S to P) were considered. S-waves were approximated by a Ricker wavelet (frequency of 0.2 – 2.5Hz, as oppose to 1.5 – 4.0Hz for P-wave due to generally lower frequencies of S-waves in seismic recordings) traveling at a correspondingly lower propagation velocity (Figure 3.16c). Theoretically, both P- and S-wave reflection profiles should be extractable by interferometry, especially if these modes can be separated using three component sensors. However, we are interested here in the effect that slower arrivals can have on virtual P-wave reflection profiles.

Figure 3.16(a) is an example of sources at depth recorded by the receivers on the surface. The P- and S- arrivals are highlighted in different colors: red and pink are direct P- and S- arrivals, green and light green are reflections and blue is P-wave multiple (S-wave multiples arrive at times later than our synthetic record length). Figure 3.16(b) is a VSG (location marked by a star) generated for 50 randomly located sources distributed below the interface. Even though there are strong spurious arrivals associated with P-S cross-correlations (precursory hyperbolas above the highlighted arrivals), the virtual reflections are coherent and strong for both P- and S-waves (Figure 3.16(b) green and light green respectively).

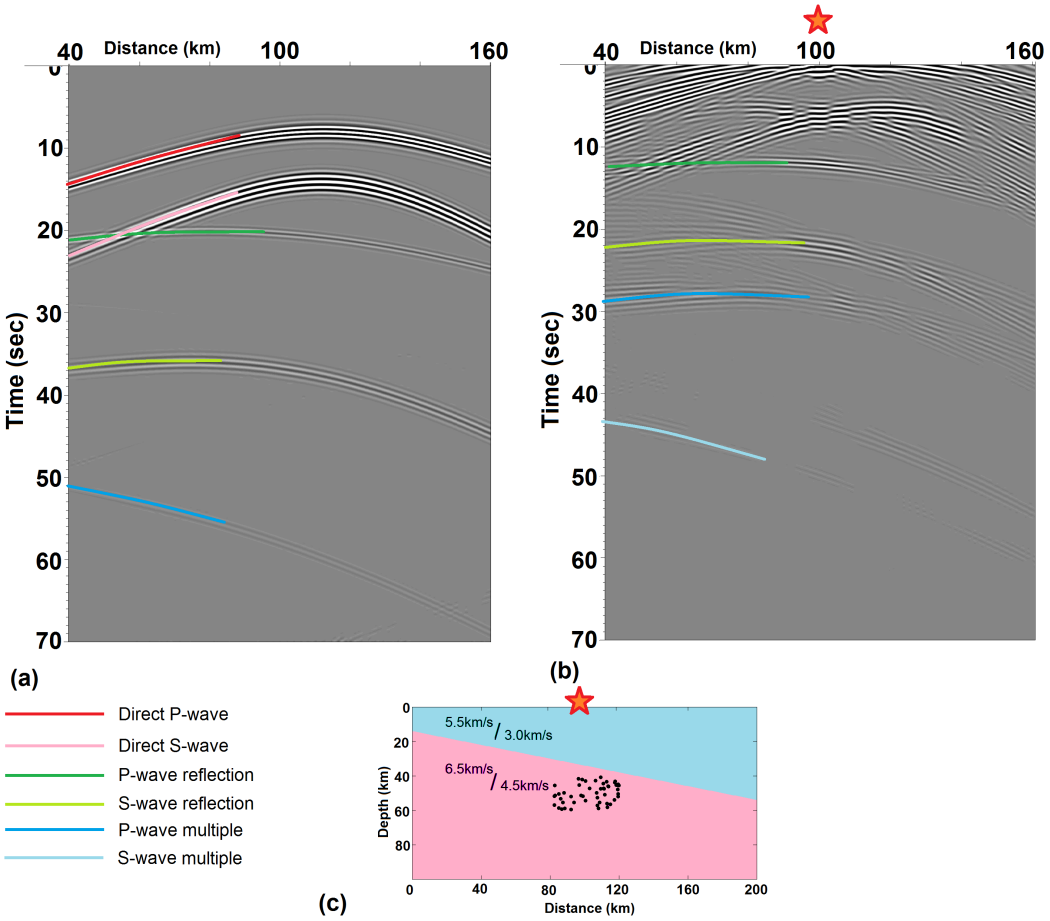

Figure 3.16: (a) Single source shot gather of P- and S- energy at depth, (b) Virtual Shot record from 50 randomly distributed sources at depth, (c) P- and S-waves velocity model (black dots are location of the shots)

Figure 3.17 is a comparison of 2D CMP stacked profiles (same scale) computed for virtual sources generated from cross-correlation of (a) deep P-wave only sources recorded by BC stations and (b) deep P- and S-wave sources. Note that the locations of the physical sources are identical in both models. The NMO correction of the P-wave velocity (6km/s) was applied prior to the CMP stack.

The P-wave reflection is recovered in both Figures 3.17(a) and (b). The CMP stack generated using virtual sources of both P- and S-waves have spurious

arrivals (A1) above the virtual P-wave reflection from the interface (R1). These spurious arrivals are result of the incomplete cancellation of energy associated with the direct P and S- wave correlation. Also, the S-wave reflection is leaking into the CMP stack (R2; Figure 3.17b). Nevertheless, even with the presence of an S-wave the virtual P-wave reflection is detectable (R1, dipping reflector at 11 seconds).

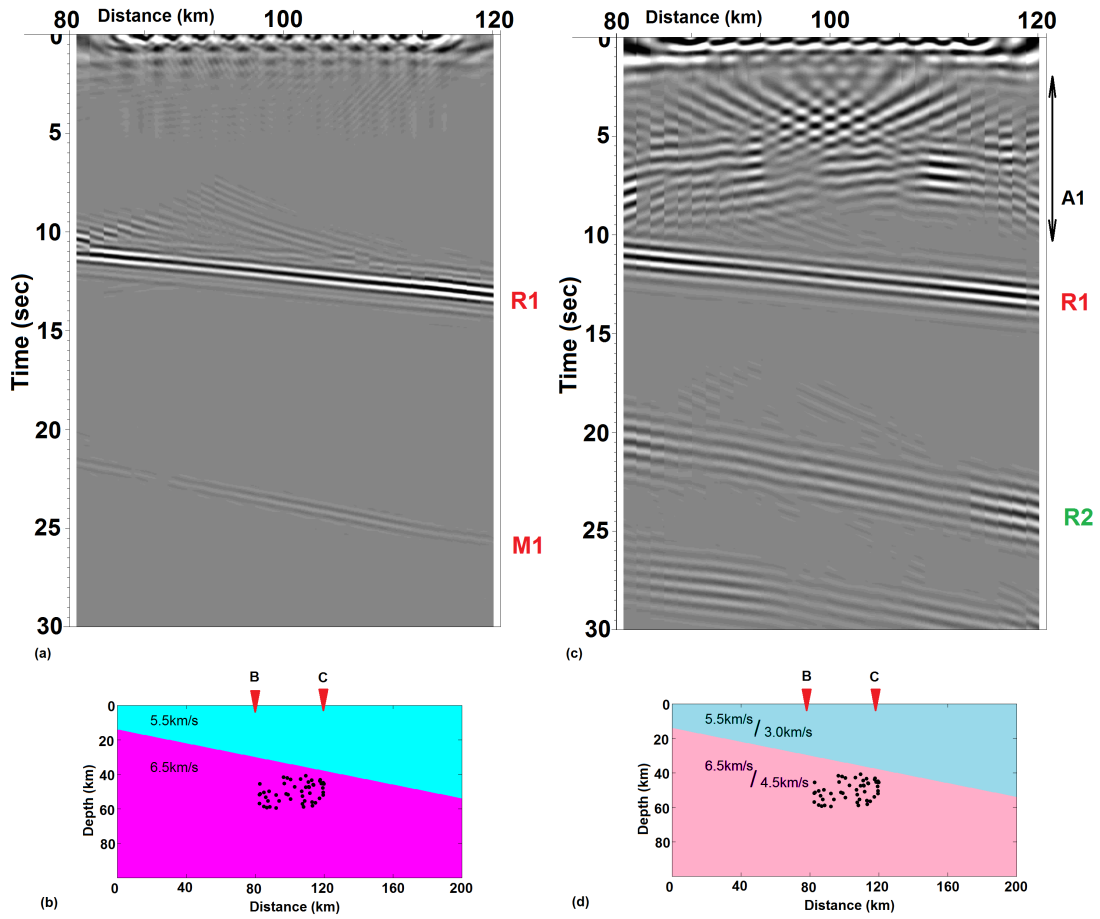

Figure 3.17: (a) CMP stack for virtual shot synthesized using energy from 50 P-wave sources, (b) velocity model and source distribution (black dots) for (a), (c) CMP stack for virtual shot synthesized using energy from 50 P- and S-wave sources, and (d) velocity model and source distribution (black dots) for (c)

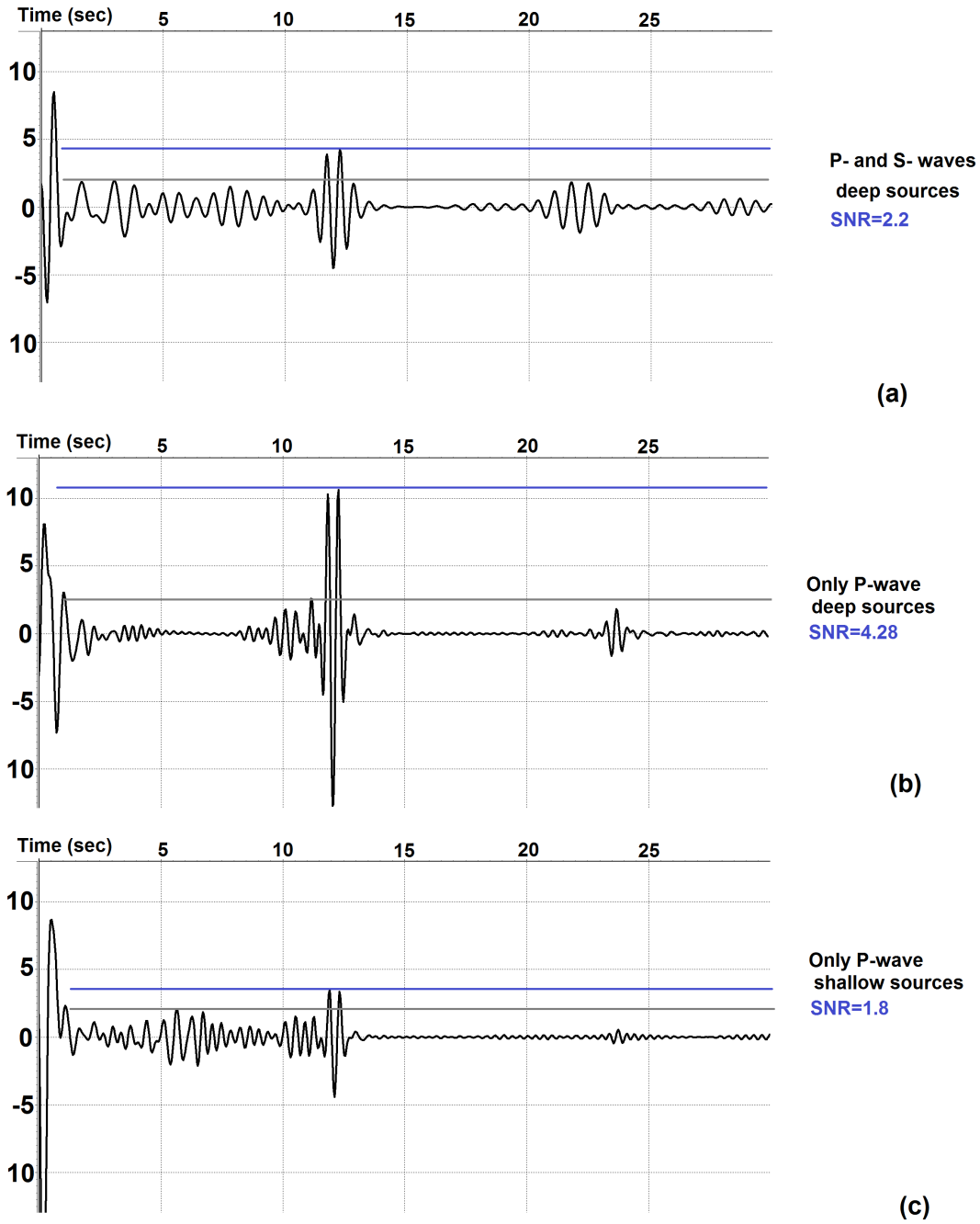

Figure 3.18: Amplitude of an average trace in (a) P- and S-waves CMP stack for deep sources interferometry, (b) only P-wave CMP stack for deep sources interferometry, and (c) only P-wave for shallow sources interferometry

Figure 3.18 is the comparison of three traces extracted from the CMP stacks generated for three scenarios: (1) P- and S-waves CMP stack from deep sources (Figure 3.17b), (2) only P-wave CMP stack for deep sources (Figure 3.17a) and (3) only P-wave for shallow sources interferometry (Figure 3.12 profile BC). The gray lines represent a maximum "noise" level (amplitudes of the spurious arrivals) and the blue line is the amplitude of the virtual reflection. The signal-to-noise (SNR) is computed by dividing the blue line by the gray line for each trace. The SNR is largest for case 3.18(b) (deep P-wave sources; SNR=4.28). Adding an S-wave to the velocity model for deep sources produces profiles with lower SNR of 2.2 (Figure 3.18a). However, using shallow P-wave sources to generate virtual 2D reflections results in even lower SNR= 1.8 (Figure 3.18c) than using P- and S-wave deep sources (Figure 3.18a).

Therefore, VSG generated by cross-correlation of deeper sources below the interface results in a more coherent virtual reflection than VSG generated by cross-correlation of shallow sources above the interface. The presence of an S-wave does not seriously hinder recovery of the P-wave reflection section. In fact it lowers the amplitude of the P-wave reflection less then relying on shallow source distribution.

3.3.3 Random Noise present in the recording

Modeling some of the factors that are expected to lower the amplitude of the virtual reflection (e.g. variations of the sources and their energy levels, focal mechanisms, complicated waveforms, topography) would require a more complicated and extensive synthetic model. Instead we introduced white noise to

the source gathers prior to cross-correlation to simulate the effect of uncorrelated noise in the image recovery.

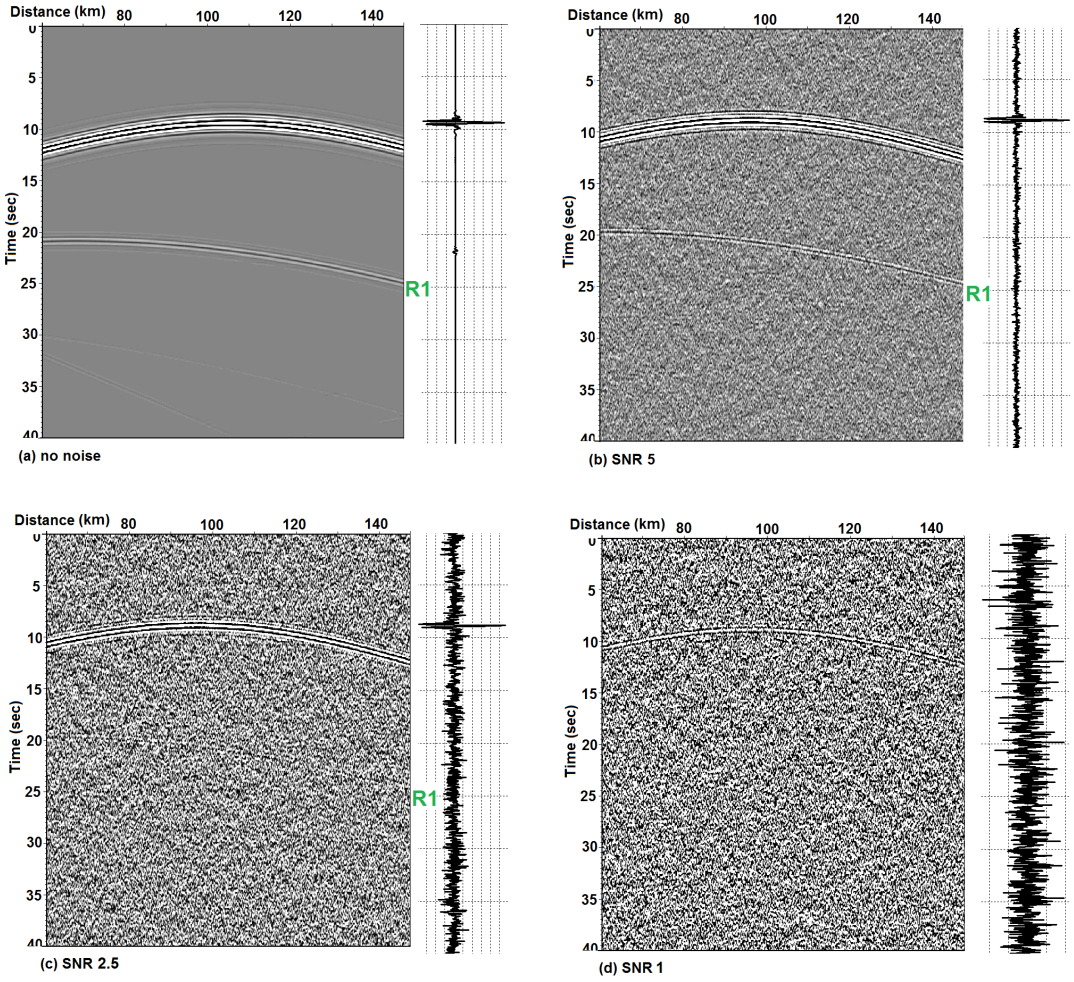

Figure 3.19: Added random noise to recording of a deep shot (a) no noise, (b) SNR 5 (c) SNR 2.5, (d) SNR 1

Figures 3.19 are recordings of a source at depth with 4 different levels of Gaussian white noise added: (a) without any noise added, (b) added noise with SNR= 5 (the amplitude of the first arrival is 5 times the maximum noise amplitude), (c) SNR = 2.5, and (d) SNR =1. The reflection phase (R1) is the second arrival after the direct (first) arrival in all four source gathers, but seriously de-

graded for SNR < 1.

Figure 3.20 is the virtual source gathers generated from cross-correlation of 50 recordings of randomly distributed sources below the interface with varying noise levels (e.g. Figure 3.19). Figure 3.20(a-b) show a coherent virtual reflection (R1), whereas the virtual reflection in Figure 3.20(c) is very low amplitude and disappears completely in Figure 3.20(d).

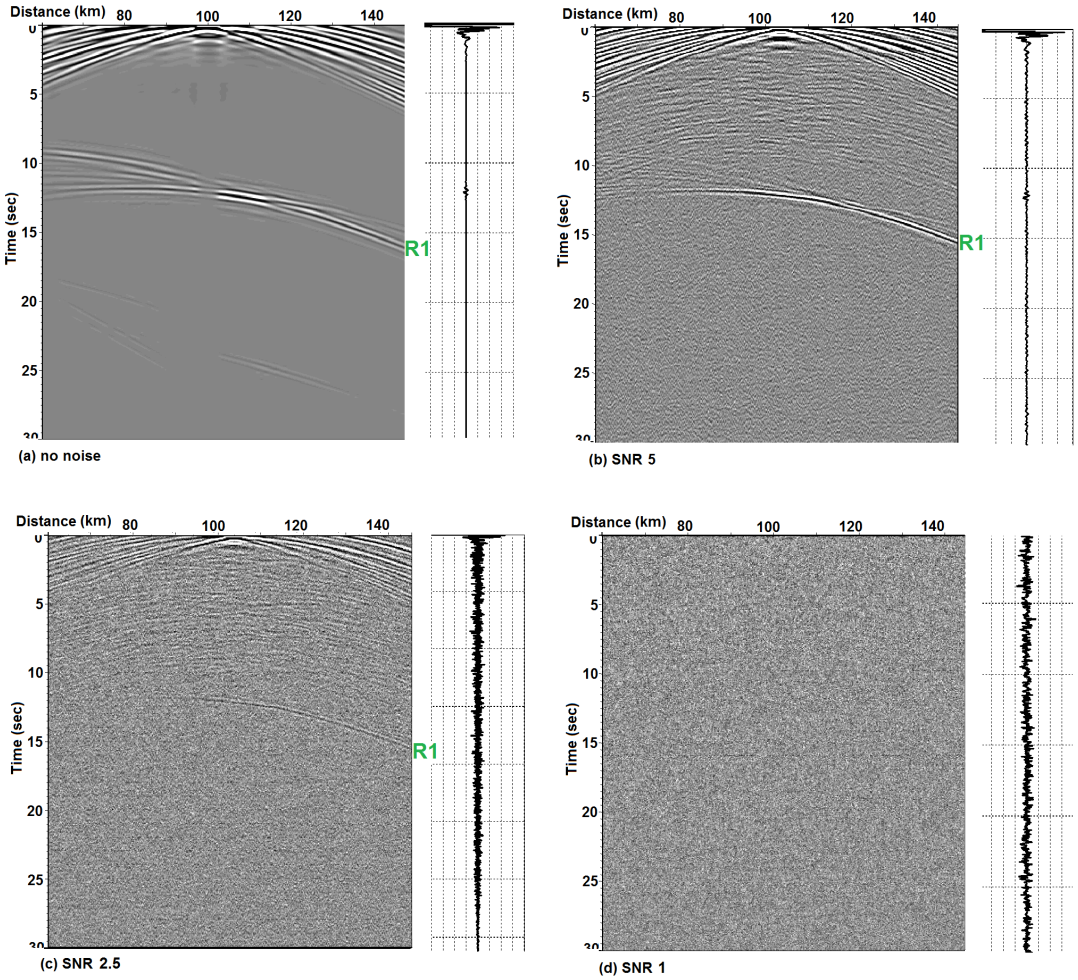

Figure 3.20: Virtual shot of recording with added random noise to recording of a deep shot (a) no noise, (b) SNR 5, (c) SNR 2.5, (d) SNR 1

Figure 3.21 are the virtual reflection profiles (CMP stacks) from VSG's in Figure 3.20 . The virtual reflection (R1) is now visible in the three out of four profiles (Figure 3.21a-c), demonstrating how CMP stack enhances the reflected phases. However, the virtual reflection is not visible in the 3.21(d) profile with the highest level of the white noise added.

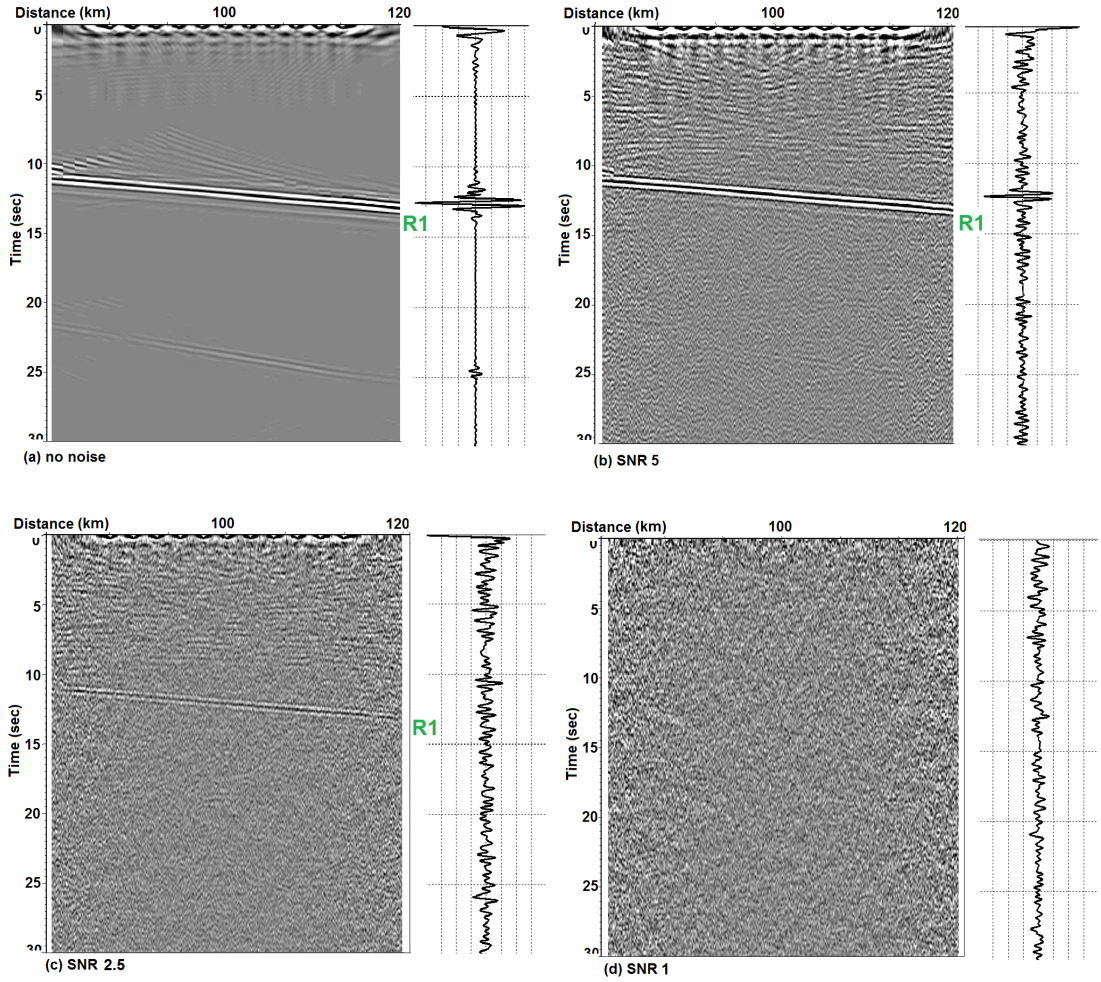

Figure 3.21: CMP stacks generated from virtual shots with added random noise(a) no noise, (b) SNR 5, (c) SNR 2.5, (d) SNR 1

Obviously the larger the SNR is in the original recording of the physical sources, the more robust the result will be after interferometric generation of

virtual data and subsequent imaging by CMP techniques. These synthetics suggest that an original SNR of 1 is at least adequate to recover useful imagery with even a modest number (e.g. 50) of sources.

3.4 Real data applications

Our modeling shows that deep sources of seismic energy should be effective in generation of virtual shot gathers and CMP stacks to image dipping interfaces like the subducting slab if the recording array and source distributions are favorable. Two existing seismic experiments were chosen to test our technique with real data, albeit collected for more conventional (e.g. tomography, receiver function) analysis: The Veracruz-Oaxaca (VEOX, 2010) and Meso-America Subduction Experiment (MASE, 2007) in southeastern Mexico (Figures 3.22 and 3.24). Both of these arrays are located above an active subduction zone (the Cocos plate subducting beneath the North American plate). The recordings from both arrays were obtained from the publicly available IRIS database.

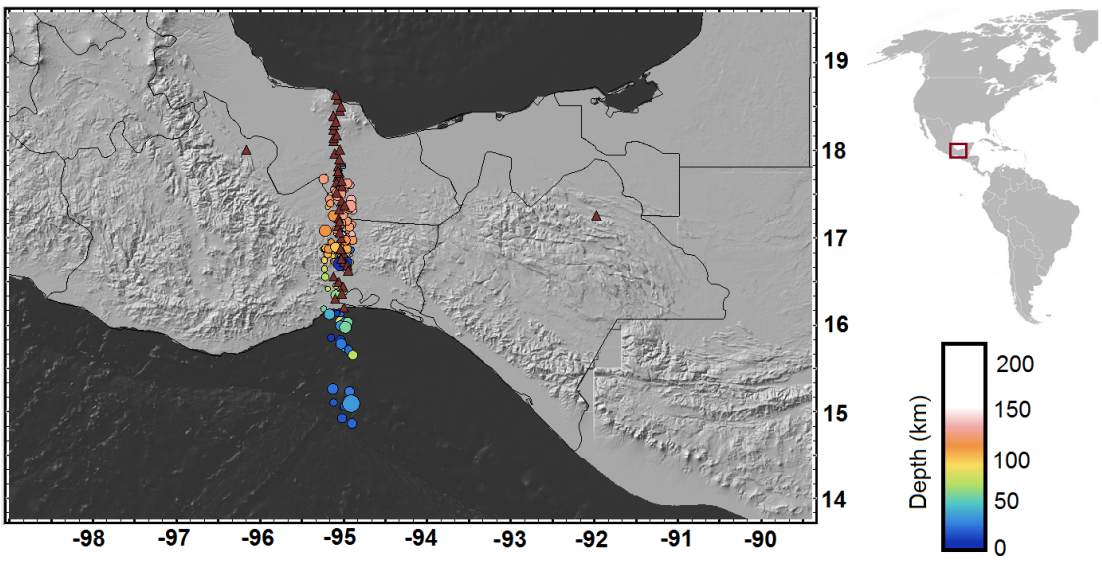

Figure 3.22: Map of earthquakes used in this analysis (circles colored by depth and scaled by size) and stations (red triangles) from VEOX experiment (VEOX, 2010)

The VEOX array consists of 45 3-component broadband stations spaced over 300 km distance (Figure 3.22). The stations recorded continuously from 2007 to 2009. During that time, 111 earthquakes of magnitude 3.5 to 4.8 were recorded by the stations and located approximately in-line with the array (colored circles in Figure 3.22). We have downloaded vertical-component seismograms of all 111 events in the form of 5-minute recording windows (1 minute before and 4 minutes after the earthquake has occurred). Figure 3.22 is a map of stations and all earthquakes used in this study, colored by depth and scaled by magnitude.

Figure 3.23 is an example of a single earthquake recording by the VEOX stations. This event has a magnitude of 3.8 and is located at 140.1 km depth according to the IRIS catalog. Figure 3.23(a) was filtered at **0.2 – 80**Hz and (b) at **0.2 –2**Hz. Both exhibit clear P and S wave energy in this example, as well as other coherent intervening phases. Not unexpectedly, we found that lower fre-

quency data (same frequency band as the models here) results in more coherent direct arrivals within the array, which translates to a more coherent virtual arrivals. This could be due to scattering in a complicated velocity and attenuation distribution above the subduction zone. Certainly the lower frequency waveforms are less affected by attenuation and are more coherent from one station to the next. Note that not all of the 111 earthquakes produce such high amplitude arrivals as shown in Figure 3.23.

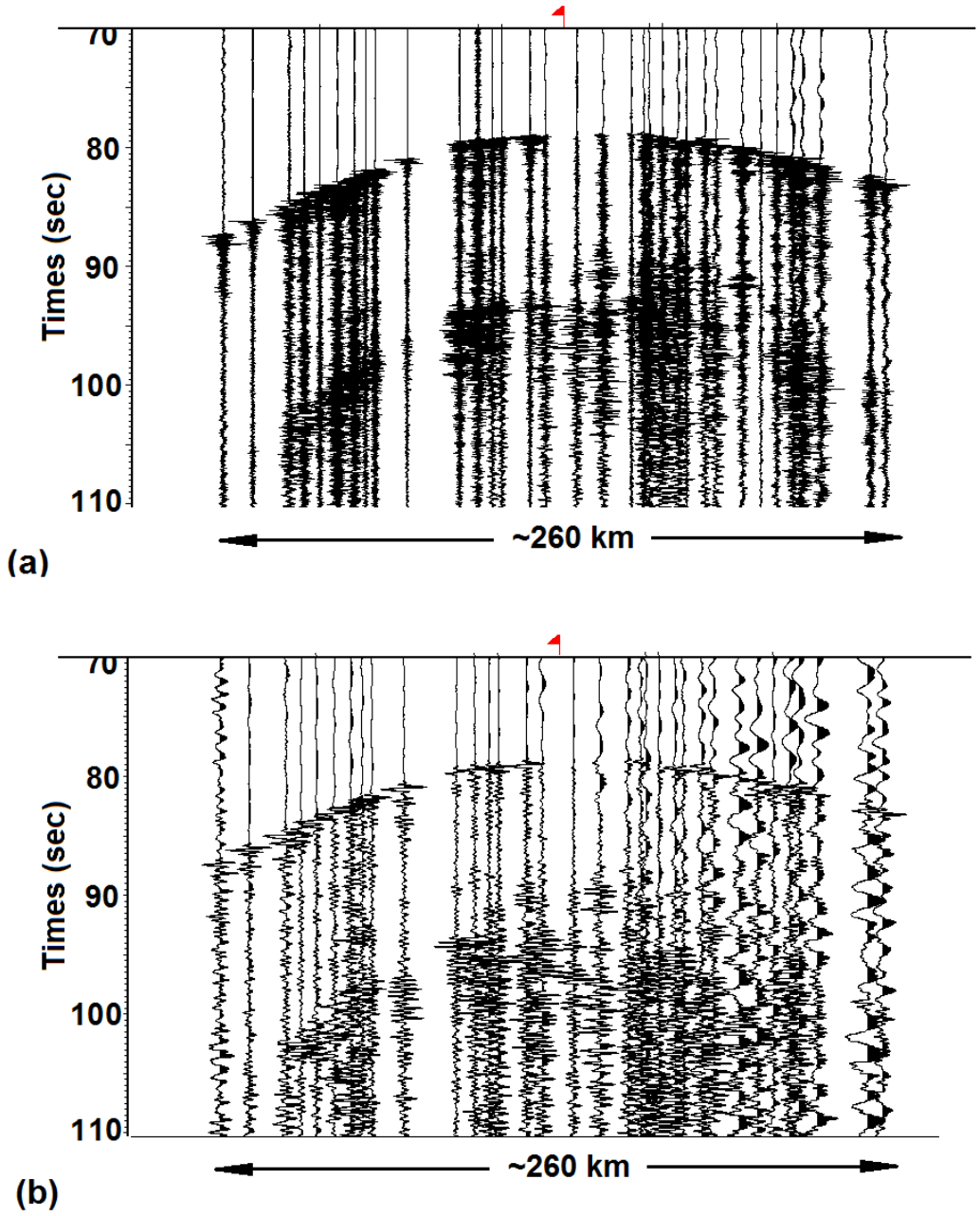

Figure 3.23: Single earthquake recoding ($M = 3.6$, $D = 140km$) (a) filtered at *0.1*/**0.2 – 80**/*160*Hz, and (b) filtered at *0.1*/**0.2 –2**/*4*Hz

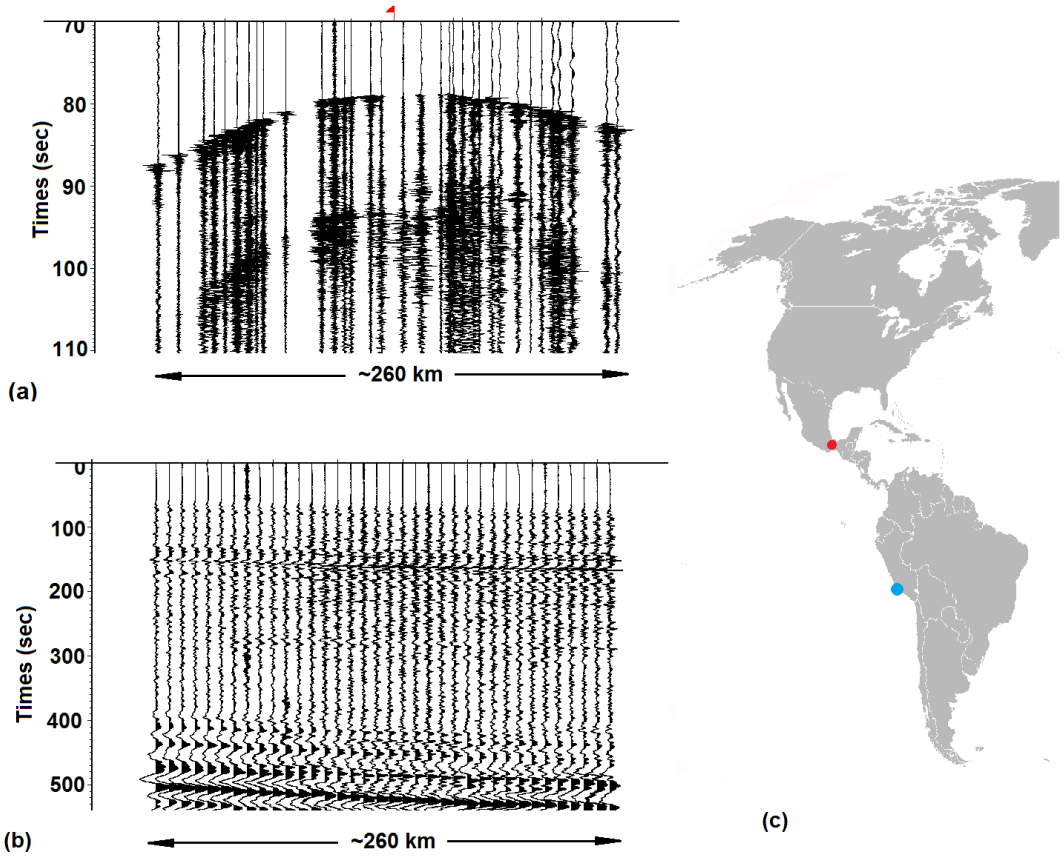

Figure 3.24: Comparison of a record of (a) local earthquake from Figure 3.23 (red dot) and (b) teleseismic earthquake (blue dot) recorded by the same stations (note the difference in the time axis)

Figure 3.24 makes clear the dramatic difference in available bandwidth from a local earthquake (same as in Figure 3.23) and a teleseismic earthquake (b) recorded by the same array. This teleseismic event occurred on a coast of Peru on August 15th, 2007 (Figure 3.24c) and it is a magnitude 8 earthquake. This earthquake was one of the events used by Kim et al. (2011) to image the subsurface beneath VEOX array using the receiver function technique. Figure 3.25 is a comparison of the spectra of the local and teleseismic event from Figure 3.24. The normalized spectra analysis demonstrates that the teleseismic event is

dominated by low frequencies ($< 1Hz$) and contains less high frequency energy when compared to the local event, in spite of the local event having a significantly lower magnitude (8.0 versus 3.8). Note that the ratio of the high to low frequency is significantly lower for the teleseismic event.

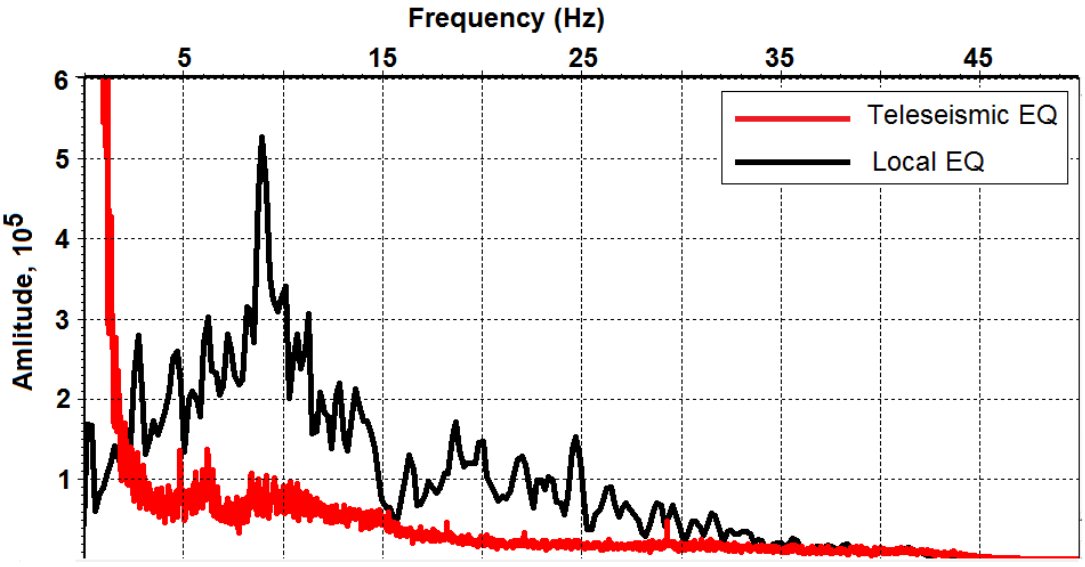

Figure 3.25: Comparison of an normalized by the number of stations frequency spectra for a local (black) and teleseismic (red) earthquakes

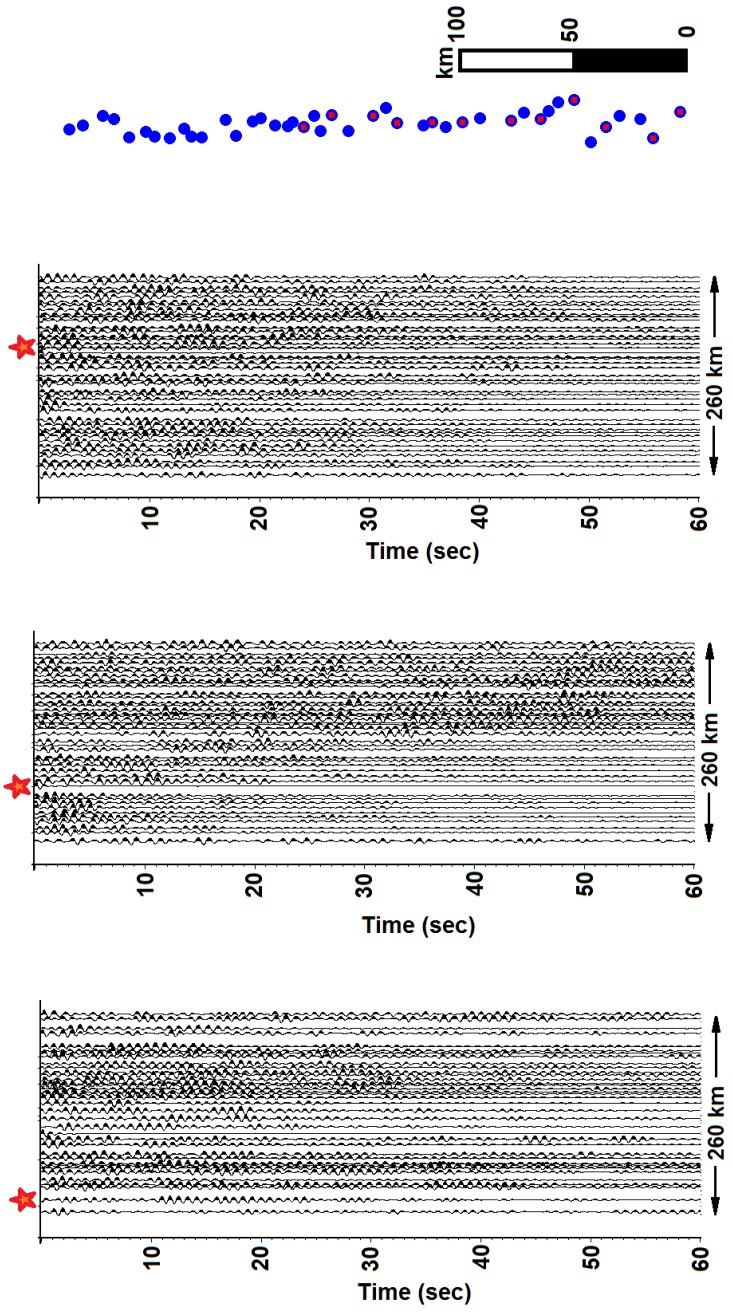

Figure 3.26: Examples of Virtual Shots produced by cross-correlation of 111 earthquakes and geometry of the station (blue circles) and VS locations (red triangles)

Figure 3.26 shows three virtual source gathers generated by cross-correlation

and summation of 111 local earthquakes. Even though the reflections are not clearly visible a CMP stack was generated in attempt to enhance and confirm any true reflections at depth. A total of 12 VSG's were generated for this line (similar number of virtual gathers as for synthetic tests; Figure 3.26d).

The resulting 2D profile is shown in Figure 3.27 with (a) mean scaling and (b) an AGC (automatic gain control used to balance the amplitudes along the whole trace) applied. Figure 3.27(c) shows the expected travel times for the P-wave reflections from Moho and Slab based on Pardo and Suarez (1995) and Kim et al. (2011), scaled to the dimensions of the seismic profiles (e.g. no vertical exaggeration).

There are several very weak but coherent virtual arrivals. Some of these arrivals (such as those highlighted in green, blue and red in Figure 3.27b) may reflect real structure. Others (e.g. dipping "fabrics" at depth) may simply be processing "noise". However, none appear to match the expected Moho or slab reflection times (Figure 3.27c) or any other "known" features inferred from previous geophysical surveys . We note however that receiver functions (Kim et al., 2011) also failed to image the subduction of the Cocos plate beneath the VEOX array. Furthermore, none of this previous work would be expected to be sensitive to all the structural variations that are within the bandwidth of the interferometric results. The eastward dip of the most prominent virtual "reflections" is consistent, in a general sense, with the convergence of subduction, and is not unreasonable to suspect that this reflection would represent structures formed above the subducted slab. If the "reflections" highlighted in blue and green (Figure 3.27b) are from the same interface in the lower crust they would appear to be offset by a subsurface fault, which happens to coincide with large elevation

gradient (plotted above the seismic profiles).

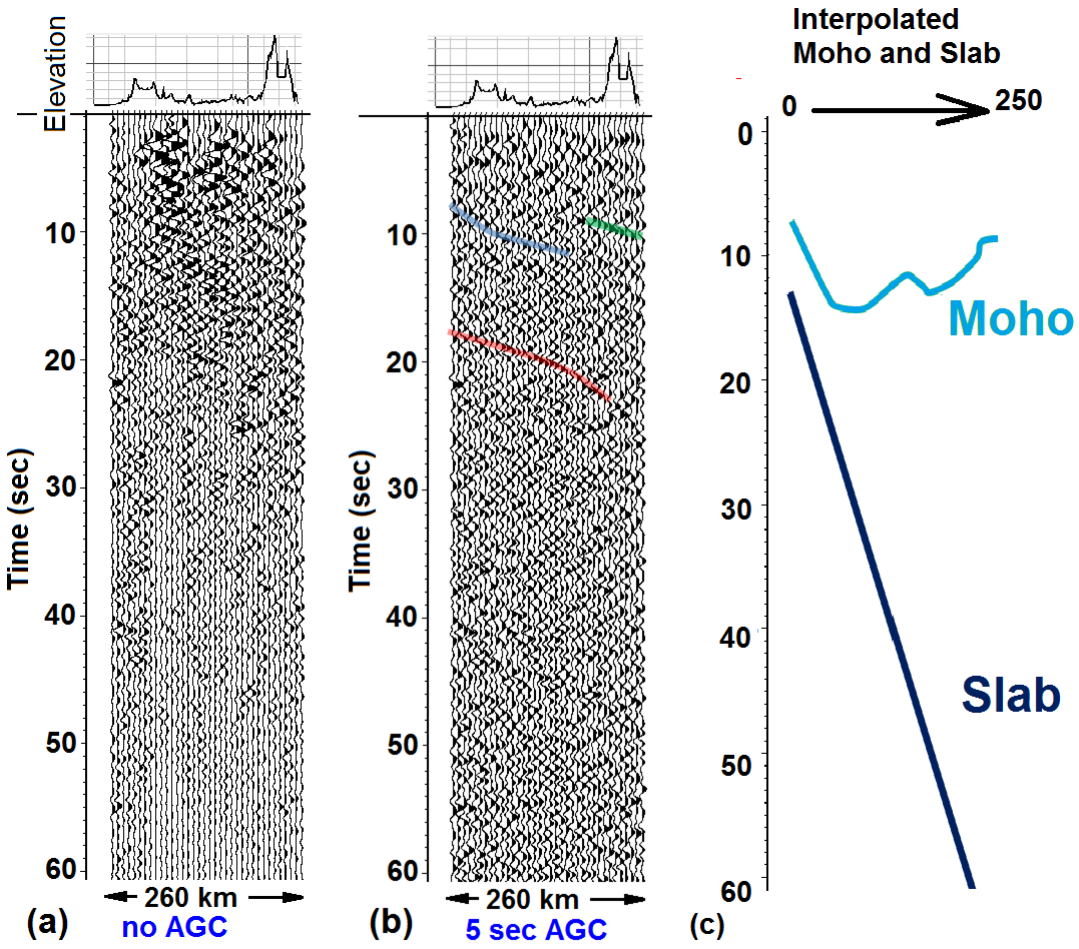

Figure 3.27: CMP stack from generated 12 virtual source gathers (no migration): (a) mean scaled, (b) AGC applied and (c) expected Moho and slab arrival times interpolated from Pardo and Suarez (1995) and Kim et al. (2011)

The complicating factor of focal mechanisms has been briefly mention, and deserves further attention here. Real seismic wave radiation pattern (Figure 3.28) are not equivalent to the impulsive source used in the synthetics above. For example, the cross-correlation of recording of station 1 and 2 in Figure 3.28 can result in either a negative (or positive) correlation coefficient depending on the focal mechanism of the earthquake relative to the position of the stations.

Note that auto-correlations are independent of the focal mechanism, as each station's recording is correlated with itself. With this advantage in mind, we have also computed zero-offset reflection profiles (Chapter 2) for the same stations of VEOX array via auto-correlation.

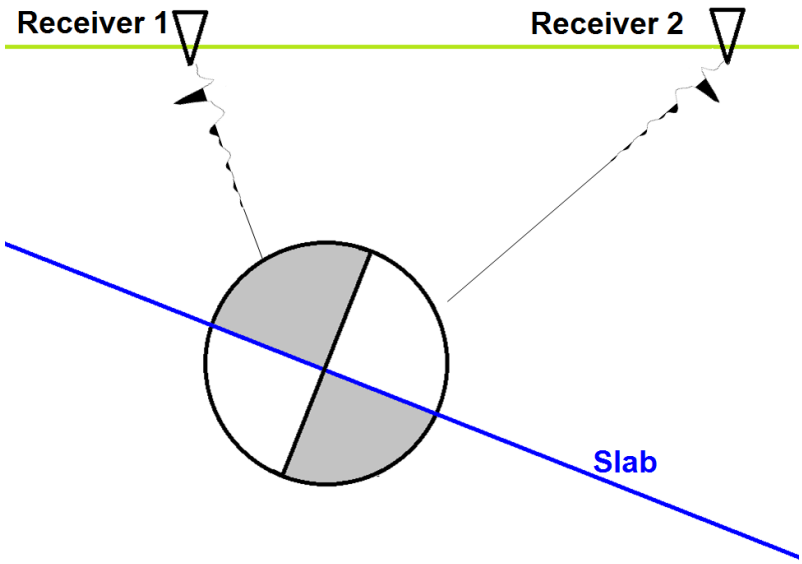

Figure 3.28: Potential polarity switch between station 1 and 2 due to the focal mechanism of a slab earthquake

Figure 3.29(a) is a zero-offset reflection section generated by stacking auto-correlations of 111 station recordings. Arguably there is coherent energy that is dipping in sympathy with subduction (e.g. to the northeast, or right in Figure 3.29) (for example highlighted in blue and green). In order to evaluate the robustness of such arrivals, and test whether they are simply artifacts associated with a particularly strong event or phase (e.g. like some artifacts observed in the synthetics) within a single earthquake, we have computed 3 partial auto-correlation stacks. These partial stacks are computed using 3 unique subsets of events, 1/3 of the total number of earthquakes each (Figures 3.29b-d). None of the partial profiles in Figures 3.29(b-d) have distinct arrivals at the same time

as green and blue energy in Figures 3.29(a). We can therefore conclude, that the virtual arrivals highlighted in Figures 3.29(a) are not an artifact of a particularly strong arrival within single earthquake record. However, neither do they support the contention that the coherencies in the full stack correspond to real reflectors beneath the survey location.

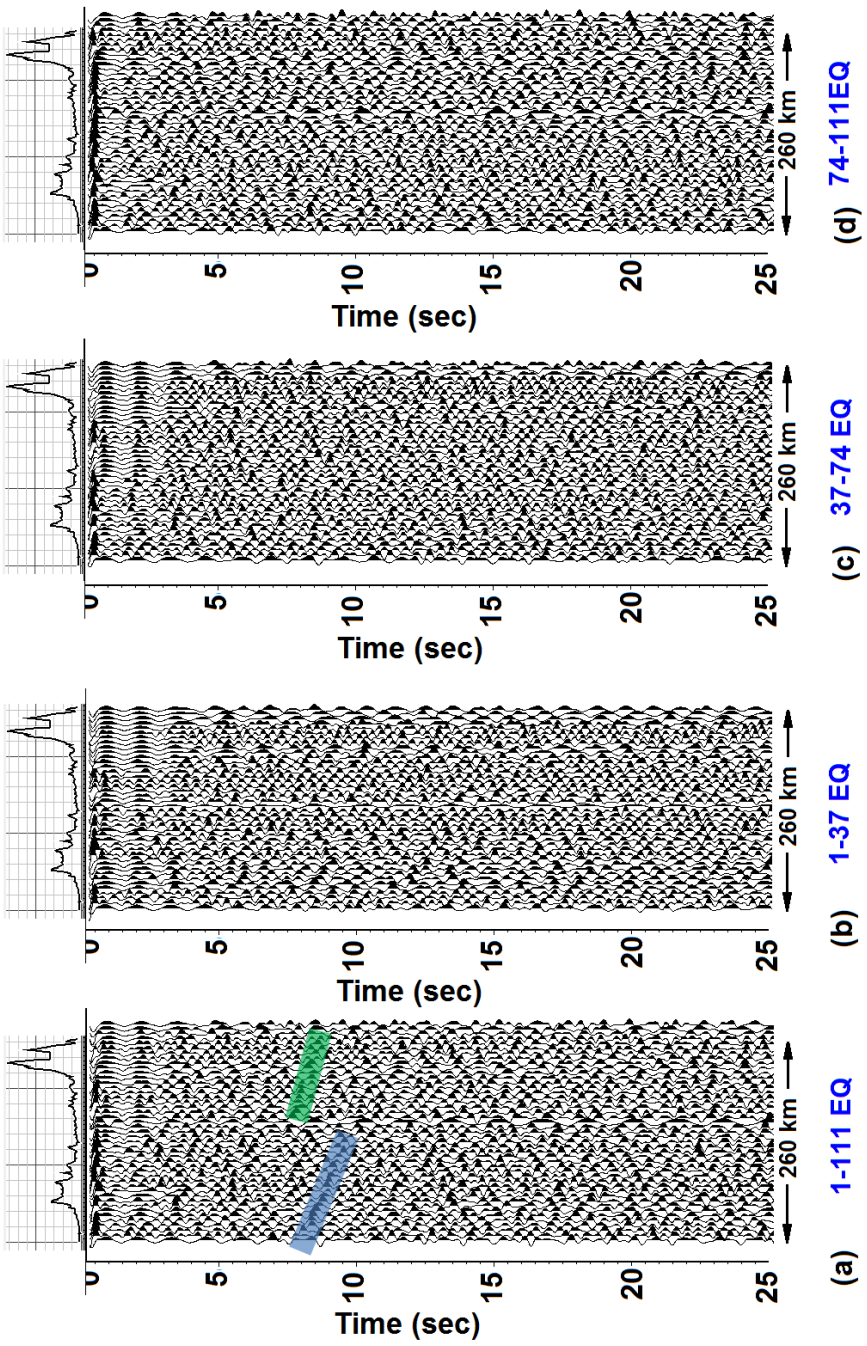

Figure 3.29: Auto-correlation of (a) all earthquakes, (b), (c) and (d) respective 1/3 of all earthquakes (no overlap)

In addition to a simple summation of auto-correlations to generate zero-

offset reflectivity profile in Figure 3.29(a), we applied a sign-bit operator (converts all amplitude to -1 or +1) before each auto-correlation. Sign-bit operator has demonstrated its effectiveness in virtual response retrieval with highly variable sources (Larose et al., 2004; Nakata et al., 2011). We tested various bandpass filters and processing sequences and based on the result chosen the following processing flow: frequency bandpass $6 - 20$Hz, sign-bit, auto-correlation and subsequent stack of the each station recording over 111 events. Figure 3.30 is the resulting virtual reflectivity profile. Additional frequency filter was applied for display as well as a 7 second-AGC. Figure 3.30(b) are expected Moho and slab arrival times from Figure 3.27(d). Again this stack hints at coherent energy, but the amplitudes are so weak that a defensible interpretation in terms of subsurface structure is questionable at best.

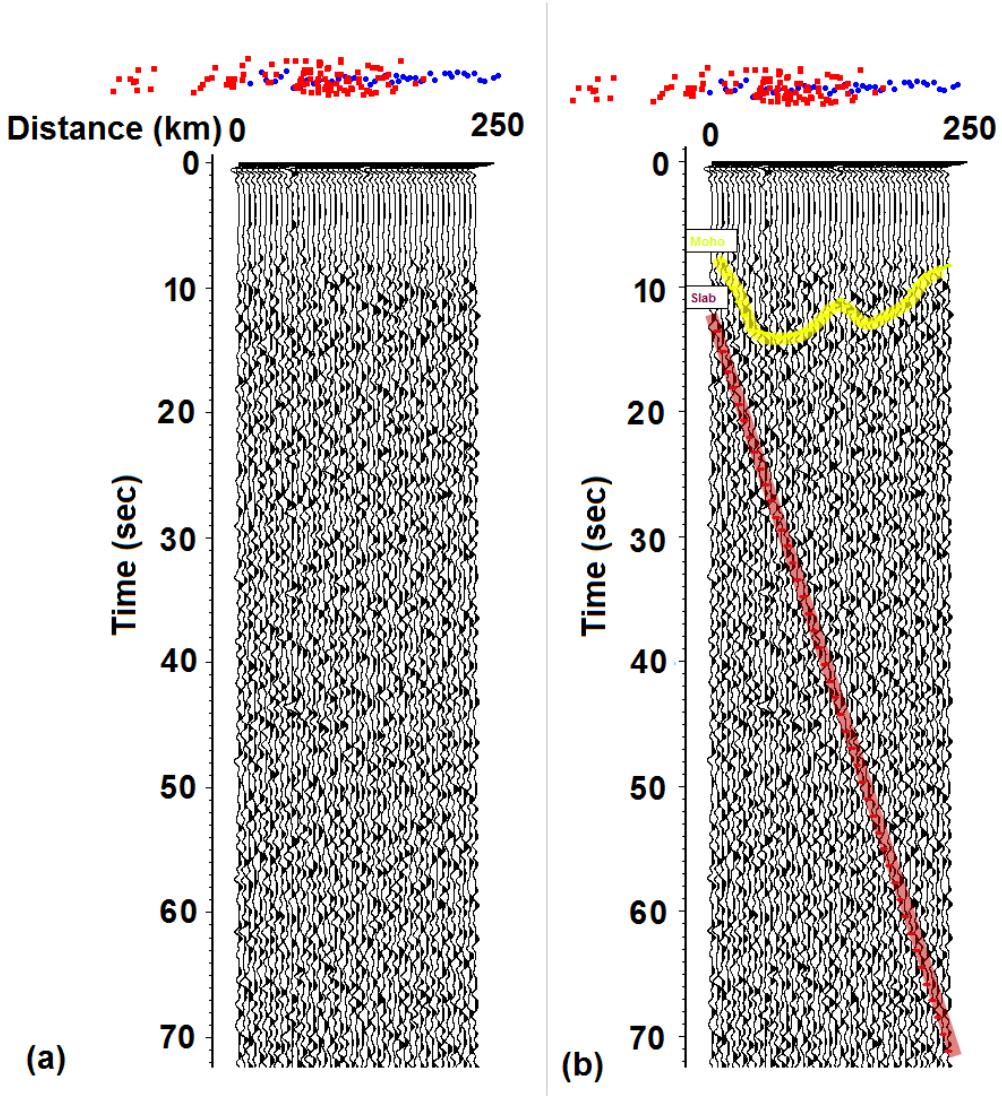

Figure 3.30: Auto-correlation of same earthquakes with sign-bit. Post-stack filter at 0.3-1Hz, AGC 7 seconds. Top panel is the geometry of the stations (blue) and the earthquake epicenters (red)

Figure 3.31 is comparison of the upper portion of the CMP stack and zero-offset reflectivity profiles (from Figure 3.27 and 3.29 respectively; marked and unmarked). One can argue that coherent energy with similar northeast dips (e.g highlighted in blue, green and red) are present in both cases, and could

plausible be related to structure associated with subduction. The SNR of these ”events” is sufficient to support any definitive interpretation as either structure, artifact or noise.

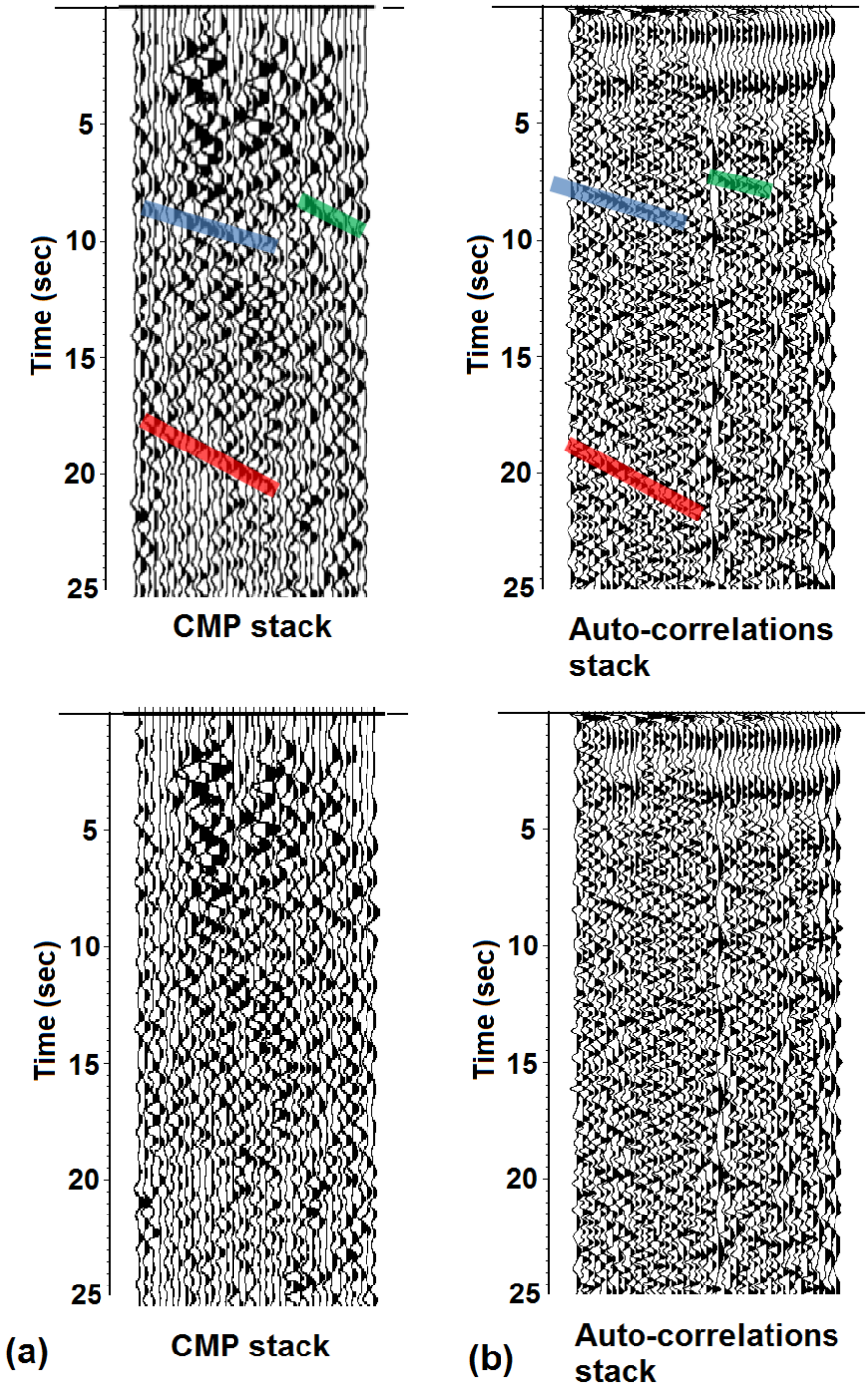

Figure 3.31: Zero-offset reflectivity from auto-correlation and summation of earthquakes from Figure 3.22

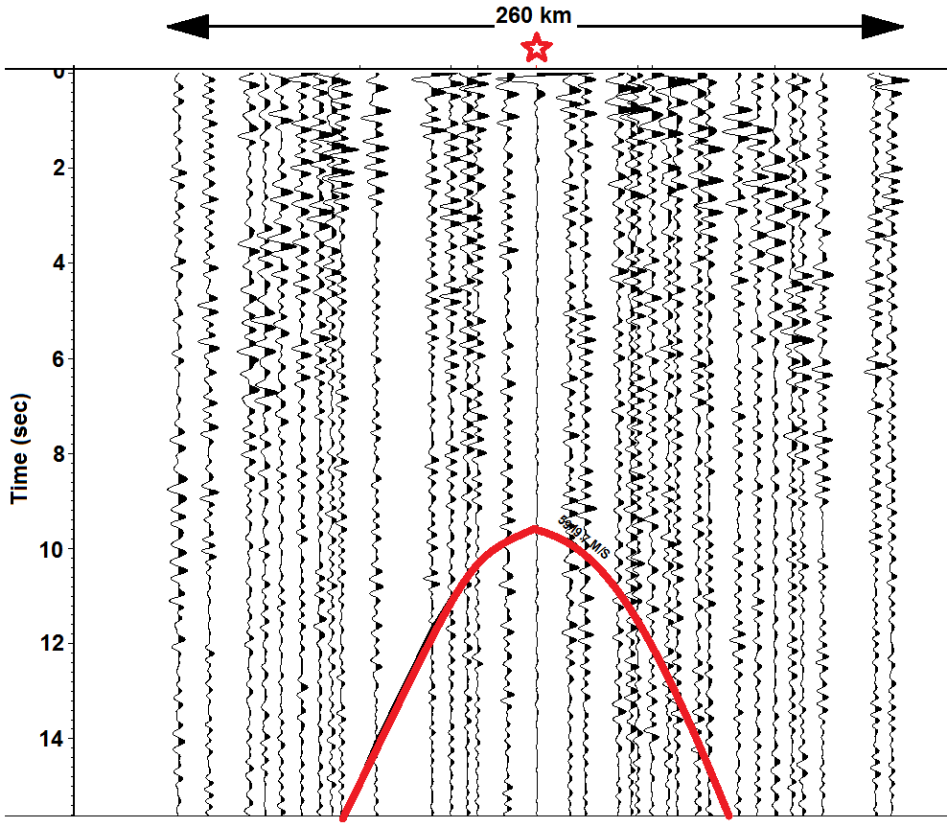

Figure 3.32: A single correlation of one trace (marked by a red star) with the remaining traces for one earthquake record.

A major difference between the synthetics and the real data discussed in this study is the spacing of stations. Since coherency is major factor in the recognition of "signal" versus noise, station spacing relative to geologic variability is a serious concern. The red hyperbola in Figure 3.32 corresponds to normal move-out of 6 km/s P-wave velocity at the expected Moho reflection time (8-12 seconds) beneath the array. Our synthetics (e.g. Chapter 2) suggest that virtual reflection are recovered only at small offsets, where the rate of differential travel time with offset is small (Ch. 3.5, less than 1 second). In the case of VEOX station spacing, 3 stations at most would contribute to the stationary signal at Moho reflection time of approximately 10 seconds. Therefore, VEOX's large station sepa-

ration can be one of the reasons why we do not retrieve a high-amplitude virtual reflection of the crust-mantle interface. There is simply insufficient redundancy for interferometry to enhance arrivals along the stationary paths versus general (true noise) paths.

As mentioned above, the receiver functions (Kim et al., 2011) also failed to image the subduction Cocos plate using VEOX array. The slab is steeply dipping and relatively deep beneath the VEOX stations (40-160km) and the number of earthquakes above magnitude 4 (blue in Figure 3.33) is relatively small. In contrast, a neighboring array (MASE, 100 broadband stations over 600km distance) recorded over 300 events during a similar deployment time (2005-2007; red in Figure 3.33), and receiver function analysis mapped a strong converted phase associated with the slab (Pérez-Campos et al., 2008). Although the MASE stations record a greater number of events, these earthquakes are poorly distributed for interferometric treatment (e.g. sources located up-dip from the stations; see Figure 3.34). Nevertheless we attempted interferometric imaging with the MASE data as well as the VEOX recordings.

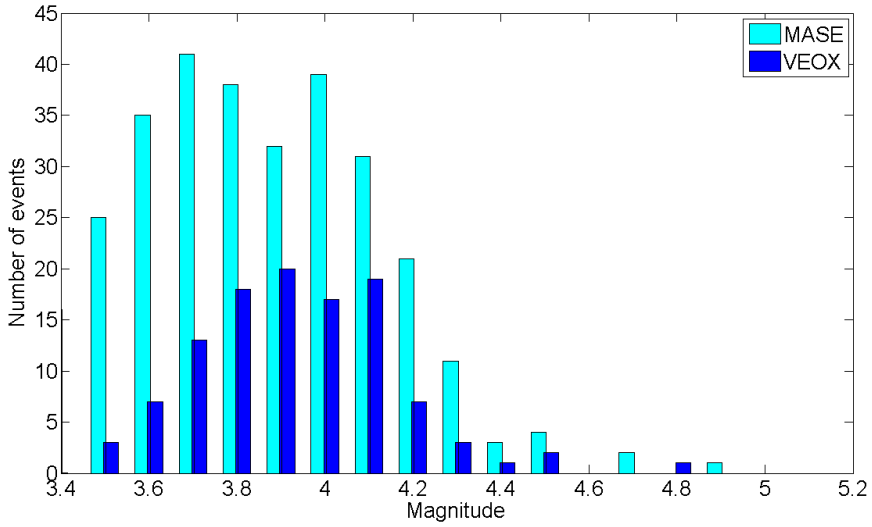

Figure 3.33: Comparison of magnitudes of earthquakes for MASE and VEOX

Figure 3.34 shows the geometry of the MASE stations (red triangles) together with the events recorded by these stations (colored by depth circles) relative to VEOX geometry (gray triangles and circles). Note that for MASE seismicity is very shallow (approximately 20 km below the station closest to the trench Pérez-Campos et al. (2008)). Recall, that according to our synthetics cross- and auto-correlation of shallow sources do not produce strong and coherent virtual reflections, but can produce good laterally propagating arrivals (directed and refracted P, S).

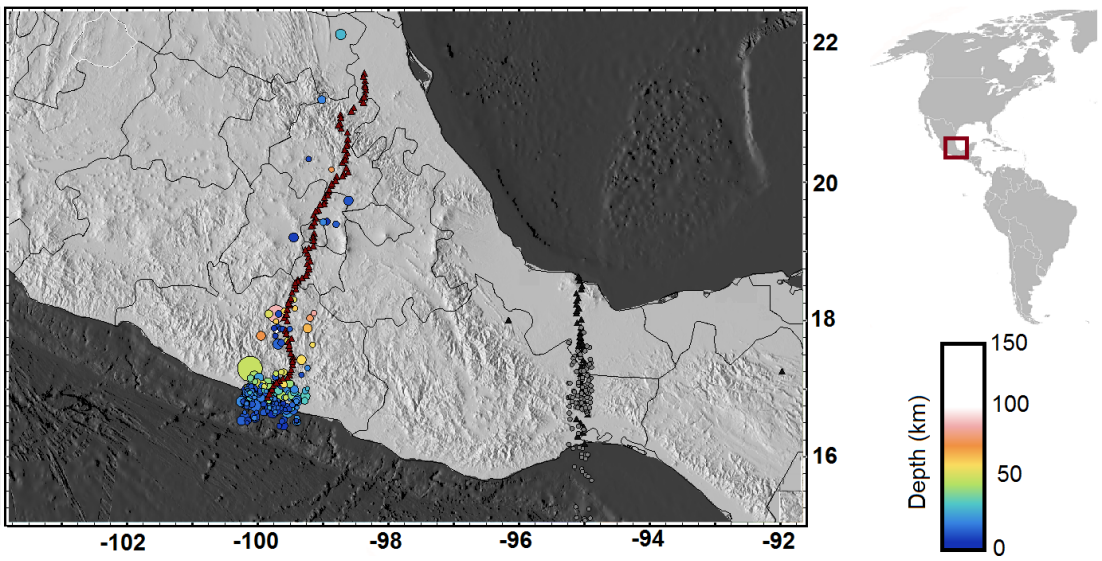

Figure 3.34: Map of earthquakes (circles colored by depth and scaled by size) and stations (red triangles) from MASE experiment (MASE, 2007) (dark grey triangles and circles are VEOX stations and earthquakes for reference)

Figure 3.35(a) is a zero-reflectivity profile generated from auto-correlation stack of 300+ earthquakes. Figure 3.35(b) is the same profile with marked Moho (yellow) and slab (red) arrival times of key interfaces inferred from from previous studies of local seismicity and receiver functions (Pardo and Suarez, 1995; Pérez-Campos et al., 2008; Dougherty et al., 2012). As expected from the poor source distribution, no strong virtual arrivals are observed in this profile. these virtual sections show little evidence of coherence that could be attributed to virtual reflections from similar structures.

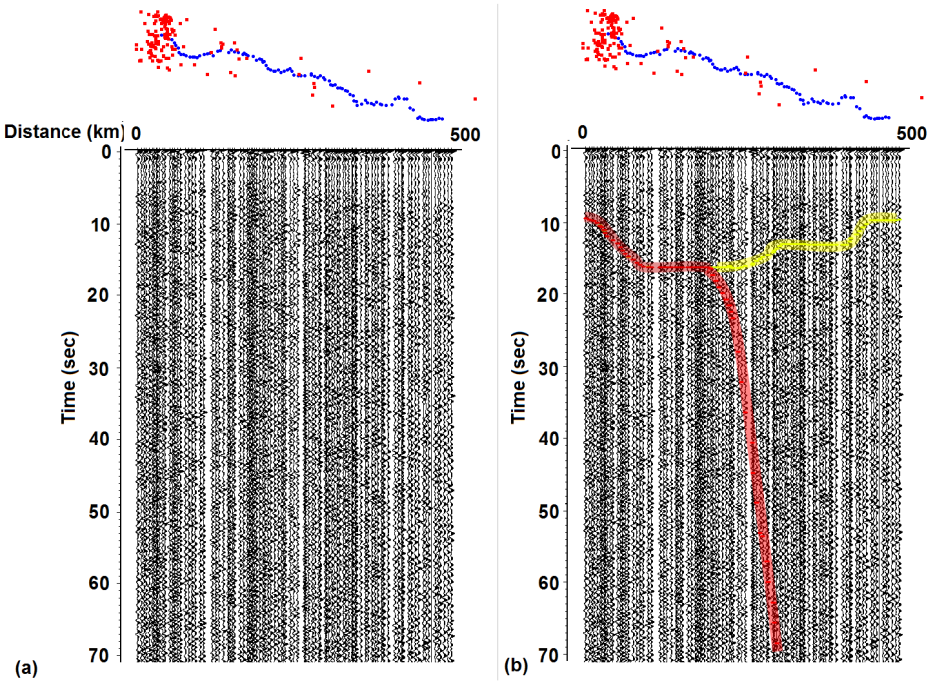

Figure 3.35: (a) Auto-correlation of MASE earthquakes from Figure 3.34 post-stack filter of 1-1.5Hz, AGC 8 seconds, (b) marked expected arrival times of Moho (yellow) and slab (red)

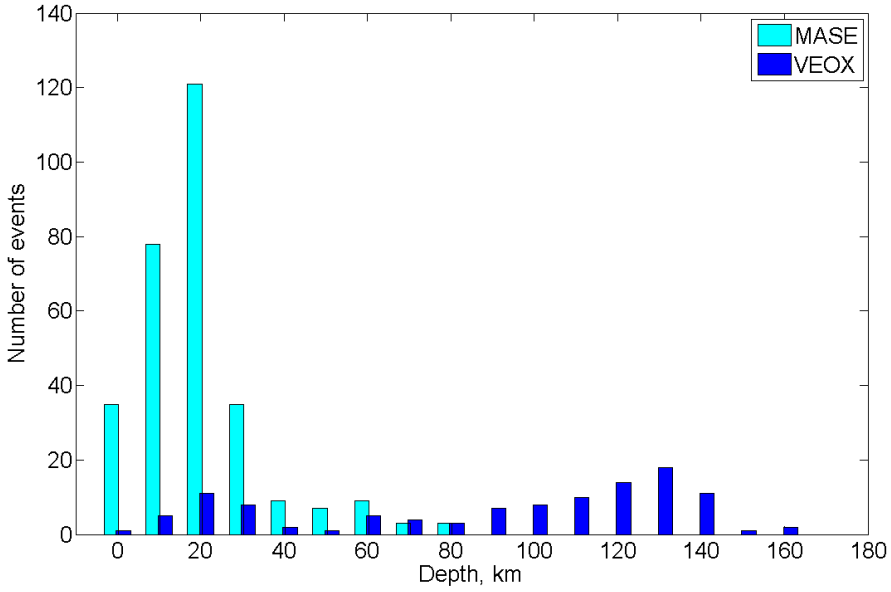

Figure 3.36: Comparison of depth of earthquakes for MASE and VEOX

The number of event above magnitude 4 recorded by MASE stations is larger than VEOX (Figure 3.33). However, distribution of the MASE events is too restricted to a smaller portion of the total length of the array (Figure 3.34) and are shallower than the VEOX events (Figure 3.36). Both factors suggest that reflection recovery with the MASE data would be less successful than with the VEOX data.

3.5 Conclusions

Our modeling suggests that a slab reflections can be retrieved by interferometric techniques applied to local earthquakes. Based on the comparison of virtual arrivals retrieved from synthetic seismograms, we conclude that cross-correlation of events located below the imaged interface produce the strongest and most coherent reflections.

Conventional CMP-stack processing can be applied to virtual source gathers generated from cross-correlation of event recordings to further enhance these reflections. However, if significant amounts of uncorrelated noise are present in the record (SNR< 2), the virtual reflection can be lost.

Selection of earthquakes to ensure the symmetric location relative to the stations is necessary to avoid artifacts in the virtual arrivals. Using sources directly beneath the stations results in strong virtual reflections, but sources down-dip from the stations can also be used. Cross-correlation of sources located exclusively up-dip from the seismic array does not produce a virtual reflection at the correct travel time.

Complicated waveforms (e.g. S-waves) decrease amplitude of the virtual reflections. However, the presence of a slower S-wave in the record is less damaging to the amplitudes of these reflections for deep sources (SNR=2.2) comparing to shallow sources (SNR=1.8).

When applied to a pre-existing real dataset, interferometry of the local earthquakes produces marginal results. Coherent energy is present on both virtual CMP stacks and zero-offset reflectivity profiles. However, none of these relatively weak arrivals correspond to expected lithospheric structures (Moho and slab).

Cross- and auto-correlation of local earthquakes clearly has tremendous potential to produce reflectivity profiles with higher resolution than those based on teleseismic earthquakes. However, to be successful this approach requires an adequate number of well-distributed earthquakes large enough to be recorded by a dense array of seismic stations.

CHAPTER 4

3D PASSIVE SOURCE INTERFEROMETRY USING CONVENTIONAL OIL EXPLORATION EQUIPMENT (BRADFORD, PA)

4.1 Abstract

This study evaluates methods of extracting unconventional body and surface wave information by applying interferometry to the results of a 3D recording experiment using conventional oil exploration equipment. The seismic survey consisted of approximately 400 vertical component stations deployed in a 2D surface array, with 225 stations at 880 feet (268 meters) spacing (sparse array) and smaller inset of 220 feet (67 meters) spacing between the stations (dense array) near Bradford county, Pennsylvania. The data corresponds to 6.5 days of continuous recording, as well as the record of a dynamite shot to be used for calibration. Following tests of various pre-processing sequences, we successfully recovered virtual surface waves which appear to originate from two geographically different areas with distinct frequency contents. We have concluded that there are two separate sources of ambient noise, one with higher (**7-14**Hz) and the other with lower frequency (**0.1-0.8**Hz) content. The low frequency source appears to be in the direction of the Atlantic ocean. The high frequency source appears to be close to or within the array and distributed over a wider range of azimuths. We found only hints of direct body (P wave) arrivals at the higher frequencies and weak evidence of critically refracted arrivals in the virtual records. The lack of body waves in the virtual records may be due to the lack of ambient sources or the relatively short observation period of the array. Given the limited azimuthal distribution of the surface wave energy, velocity estimation based

on dispersion of the surface waves is problematic. However the results we obtained are consistent with the geology of the area of nearby seismic observations with artificial sources at this site.

4.2 Introduction

The Bradford seismic experiment was carried out by Geokinetics near Bradford, Pennsylvania (Figure 4.1) in mid-December, 2009. It was located at the site of an industry seismic reflection survey which was augmented by a special deployment to investigate ambient noise. The stations were deployed for a maximum of 6 and a half days, with the recordings susequently cut into 1 minute files for the analysis reported here. The test deployment consisted of approximately 400 stations in a 2D surface array, with 225 stations at 880 feet (268m meters) spacing, here referred to as the sparse array, and smaller inset of 220 feet (67 meters) spacing between the stations (referred to as the dense array) near Bradford county, Pennsylvania. Vertical component ground motion was continuously recorded by 10 Hz geophones (OYO GeoSPace GS-30CT) at a sampling rate of $2ms$. Figure 4.1 is a location map of the Bradford experiment showing the geometry of all stations. The ambient noise recordings made with this array were provided to the Earth and Atmospheric Sciences (EAS) department at Cornell University for application of interferometric methods. Here, we present the results of our analysis using cross-correlation to generate virtual sources using this 3D dataset.

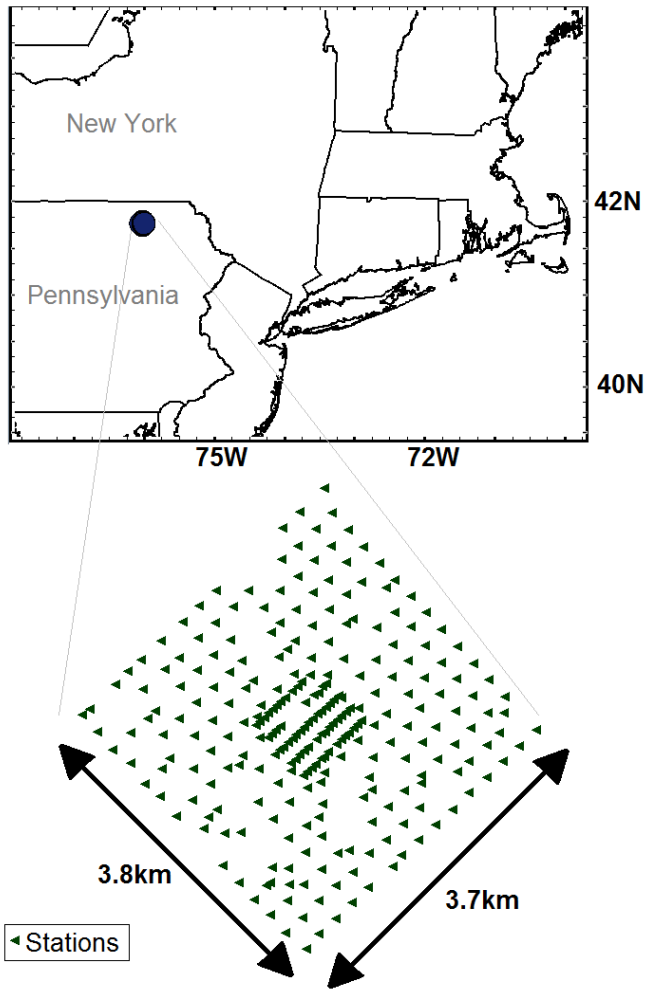

Figure 4.1: Bradford survey. Triangles represent stations of the sparse array (spacing= $880ft \approx 268m$) and the dense array (spacing= $220ft \approx 67m$)

4.3 Geology of the survey site

The Bradford survey was located on a plateau with elevation of approximately 3-4,000 ft (0.9-1.2km). The geology beneath the site consists of intermittent glacial deposits overlying Paleozoic sandstones, siltstones and shales sitting on

a Precambrian basement (Hills, 1985). The depth of the basement is approximately 16-18,000 ft (5-5.5km) below the sea level (Dietrich and Colton, 1967; Hills, 1985).

4.4 Dynamite recording by Bradford stations

A recoding of an explosive source (Figure 4.2) was helpful for calibration and interpretation of our interferometry arrivals. This shot is located within the array (red dot in Figure 4.2).

Figures 4.2 and 4.3 show the first 5 and 2 seconds of the explosive shot gather respectively. The most prominent linear arrivals, from slowest to fastest, are: the air wave (red in Figure 4.2), with a slope corresponding to a velocity of approximately 300m/s, a surface wave (green in Figure 4.2) with an apparent velocity of approximately 2.5km/s and a body wave (P-wave, yellow in Figure 4.2) with an apparent velocity of 4.5km/s. A very clear reflection is present at around 500 ms at zero offset (Figure 4.3). Converting to depth using the direct P-wave velocity puts this reflector at approximately 1.3 km, which is well within the sedimentary cover. There is no obvious reflection on this shot gather that can be associated with the basement, which would be expected at 2-3 seconds (Dietrich and Colton, 1967; Hills, 1985). Even re-scaling the gather (mean scale, Automatic Gain Control (AGC), etc.) did not visually increase the amplitude of a potential reflection at this arrival time.

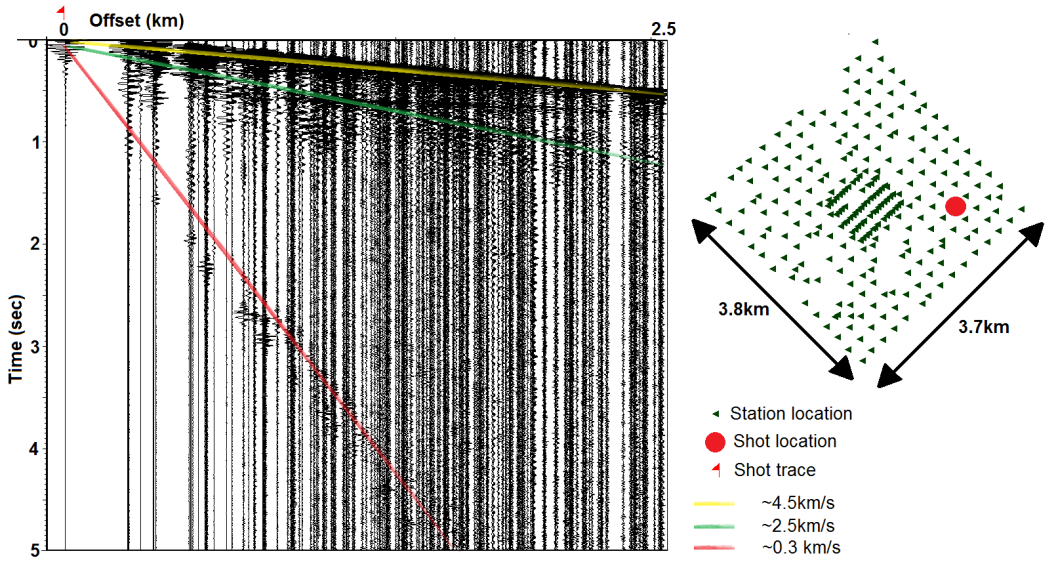

Figure 4.2: Shot gather at the location of 30430 station, sorted by offset and filtered at $10/15 - 55/80Hz$. The green triangles are geophone locations and the red dot is the shot location. The most prominent linear arrivals are marked with red, green and yellow (discussed in the text)

Note that the surface waves in Figure 4.3 appear to be more prominent at larger offsets from the shot regardless of the scaling of the record.

Figure 4.3 (bottom panel) shows an average frequency spectrum of the explosive source record. Most of the energy is contained between 5 and 30 Hz, which includes both body and surface wave energy. Lower frequencies, however, are presumably attenuated by the response of the 10Hz geophones and/or not generated by the dynamite shot itself. In general surface waves recovered using interferometry with broadband seismometers tend to correspond to frequencies lower than 1Hz (Lin et al., 2013b; Gutenberg, 1958), with virtual body energy often below 6Hz (e.g. Roux et al., 2005; Bonnefoy-Claudet et al., 2006; Poli et al., 2012b). Thus, the difference in the spectra has to be taken into consideration when comparing the virtual arrivals with the dynamite recording (Draganov

et al., 2007).

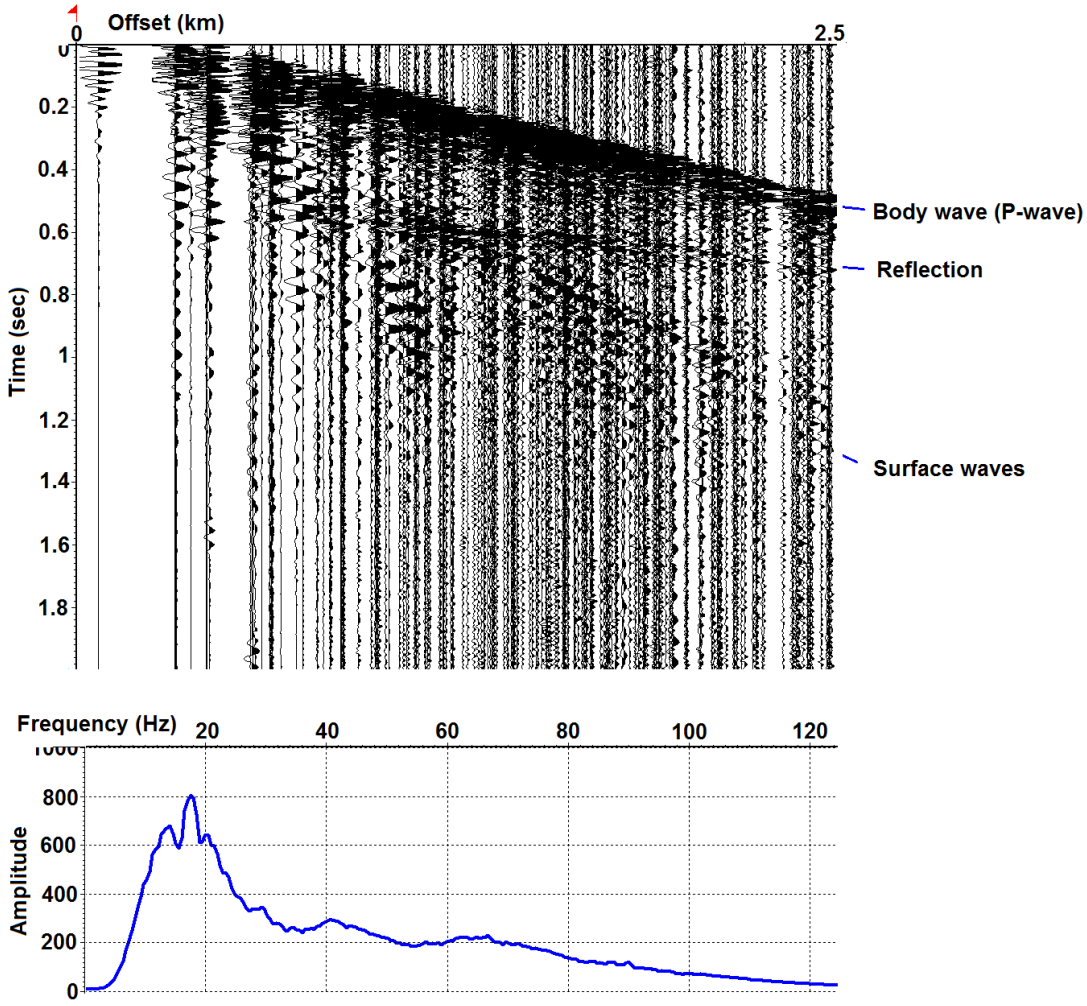

Figure 4.3: First 2 seconds of the shot gather in Figure 4.2. The reflection at around 600 ms zero-offset time is prominent across the array. The bottom plot shows the frequency spectrum of this shot record

4.5 Processing

The stations for both sparse (880 ft) and dense (220 ft) arrays were deployed for over 7 days; however the overlap between most of them is around 6 days.

The continuous recordings were cut into 1 minute segy files with a sampling frequency of $2ms$.

The pre-correlation processing and cross-correlations of these files were carried out using Matlab Software and Seismic Toolboxes. SegyMat (publicly available Matlab toolbox for segy file import and export) was used to export results of correlations as segy files for data analysis using the Vista (TM Schlumberger) seismic processing package. The sparse and dense arrays were processed separately in Matlab but following the same steps. First all of the stations were sorted by the time of recording and gain balanced (scaled) to ensure the same average amplitude is recorded by all geophones. Then all recording were cross-correlated and summed over the entire duration of the experiment (relevant Matlab codes and functions are presented in appendix C).

The goal of the subsequent analysis was to evaluate current methods of surface and body wave extraction using interferometry with this type of data. We started with surface wave retrieval and then moved to the issue of body waves extraction.

Several processing routines were applied in our attempt to enhance the recovery of the surface and body waves using interferometry in addition to simple correlations, taking advantage of cross-correlations in both time and frequency domains. These routines included: (a) frequency clipping to minimize monotonic-frequency dominance on the final stack (discussed in more detail later in this report), (b) 2D mixing (or array synthesis (Capon et al., 1967)), (c) FK filtering and (d) sign bit before cross-correlations.

4.6 2D Seismic Interferometry results

Our analysis began with a treatment of selected individual lines (Figure 4.4) of the sparse array: Line 2033 (red), Line 2049 (orange) and a cross-line (blue). These lines were chosen for the analysis to help inform the subsequent 3D processing.

In order to create a virtual source (VS) record we followed a conventional technique (Claerbout, 1964), where a single station is cross-correlated with the rest of the receivers for the entire duration of the experiment. That is, all the cross-correlations of the minute windows were summed (i.e. stacked) together for each station pair (i.e. common - receiver stack) to create a virtual source gather with the location of the shot at the chosen station (Schuster, 2001).

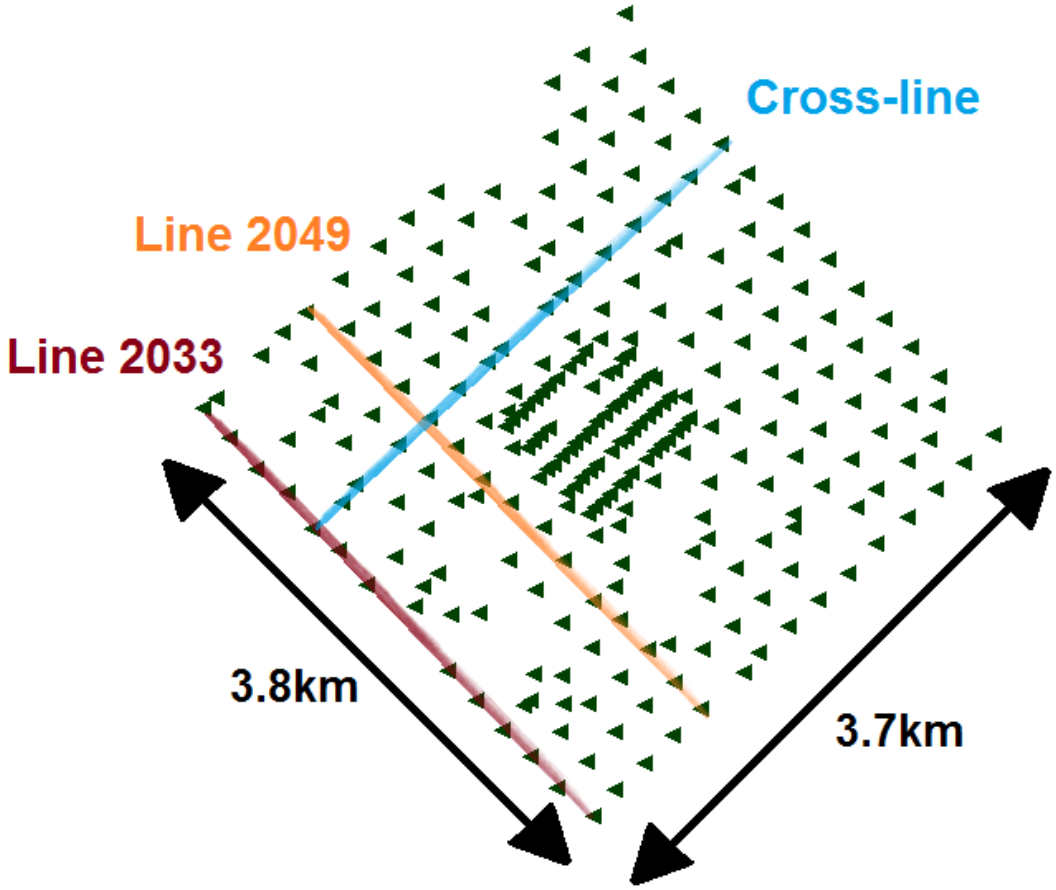

Figure 4.4: A map of Bradford arrays with Lines 2033 (red), 2049 (orange) and the selected crossline (blue) highlighted

Band-pass filters were applied after virtual source gathers (VSG) were created, and no processing was applied prior cross-correlations other than trace normalization.

We began looking for virtual arrivals by systematically scanning the virtual source data at different frequency bands. Figure 4.5 shows a virtual source gather for a single 2D line (Line 2049) filtered after virtual source generation followed by bandpass filering in three frequency bands: a low frequency band of 0.05/**0.10 – 0.60**/1.00Hz, a mid frequency band of $1Hz$/**2Hz – 4Hz**/8Hz and a

high frequency band of 5/**6 - 14**/17Hz. All stations were sorted by offset from the virtual source, whose position is denoted by the red star. High and low frequency panels show coherent arrivals with quasi-linear move-out from the virtual source. However, the low frequency gather shows a very clear unidirectional arrival (top right to bottom left in Figure 4.5(a)), which corresponds to SE to NW wave propagation. The high frequency virtual gather shows a more symmetric arrival. This arrival does not seem to propagate far from the virtual source station, i.e. it is not observed by receivers farthest from the virtual source station (Figure 4.5(c)). By contrast, no signal is evident at the mid-frequencies. We will refer to this pattern as a "discretization" of virtual arrivals in frequency. Two possible explanations for "missing signal" are (1) ambient energy is simply not available at these frequencies, or (2) it is not recorded by the hardware (e.g. geophone response).

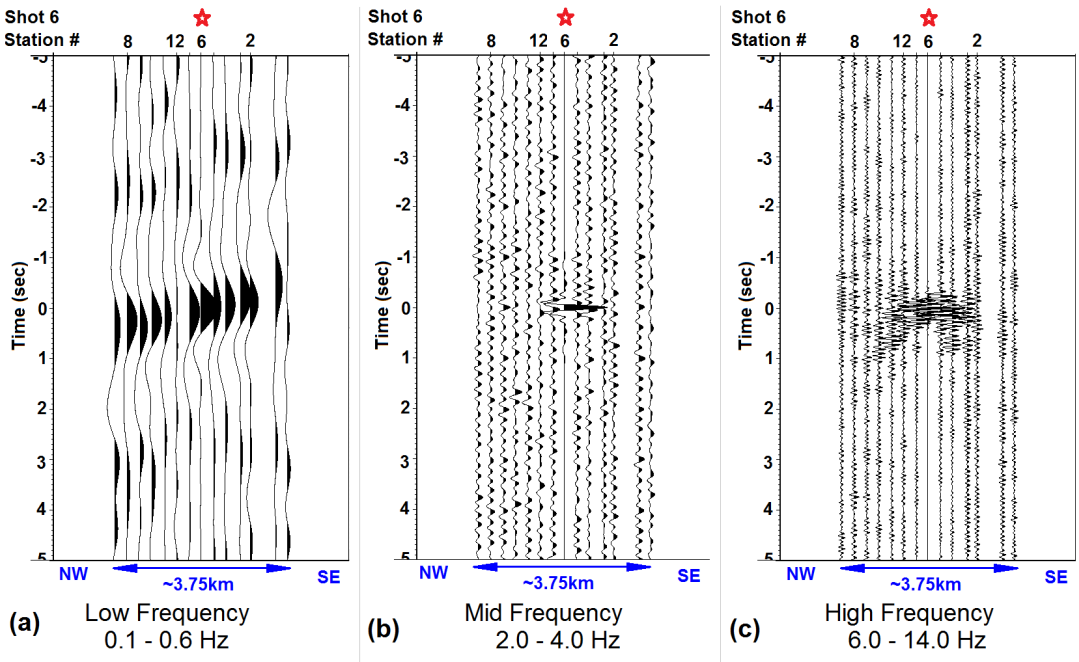

Figure 4.5: Virtual source record for Line 2049 filtered at: (a) 0.05/**0.10 – 0.60**/1.00Hz, (b) 1Hz/**2Hz – 4Hz**/8Hz, and (c) 5/**6 – 14**/17Hz sorted by the offset from the virtual source (red star is virtual source location)

The geophones used in this study (OYO GS-30CT with response function shown in Figure 4.6) have a natural undamped frequency of 10Hz. Despite the decrease in the sensitivity of the instrument below the natural frequency, we appear to have recorded virtual arrivals at frequencies well below 5Hz (Figure 4.6). However, the geophones' response does not provide an explanation why the station would preferentially filter our the mid-frequencies and not affect the low frequencies. Thus we argue, that the absence of the signal in mid-frequencies is not due to the hardware response but is probably related either to the spectra of ambient noise sources.

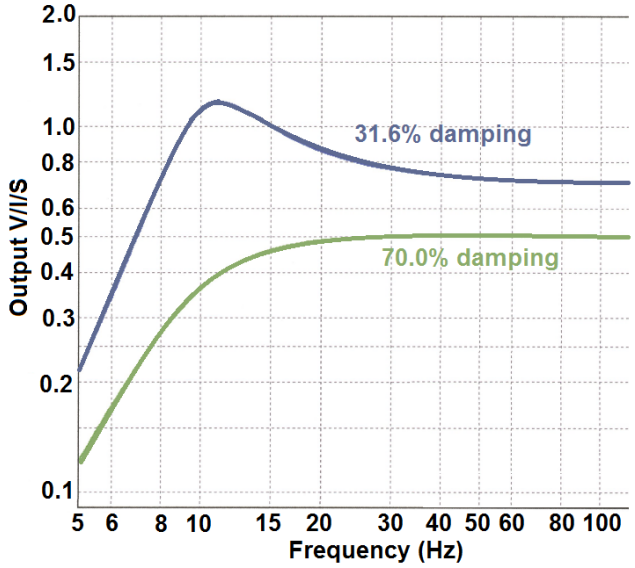

Figure 4.6: OYO GS-30CT geophone response function. Natural frequency is $10Hz$

In order to confirm that the virtual arrivals are coherent within the line for multiple virtual source positions, as well as to look for a systematic variations that may relate to the source energy, we have examined all 15 (number of stations in single line of receivers) virtual source gathers generated for Line 2049. An example of 4 such VSGs (virtual source gather) is shown in Figure 4.7 (the position of virtual source is denoted by a red star in each panel). The virtual source location is propagating from South-East to North-West. Note, that only a positive lag of cross-correlation (as oppose to Figure 4.5) is shown here, which would correspond to a virtual energy emanating from the virtual source position at time 0. The first arrival has a linear move-out velocity of approximately 2.7km/s (red line), which makes it a good surface wave candidate based on the velocities recorded from the dynamite shot (Figures 4.2 and 4.3). Similar results are obtained for several shot gathers, where the strength of the surface waves varies but are detectable in all gathers. As the virtual source moves to the right,

the signal gets weaker to the left of it, indicating the that physical source of energy is positioned somewhere to the left of the red star (SE, Figure 4.7).

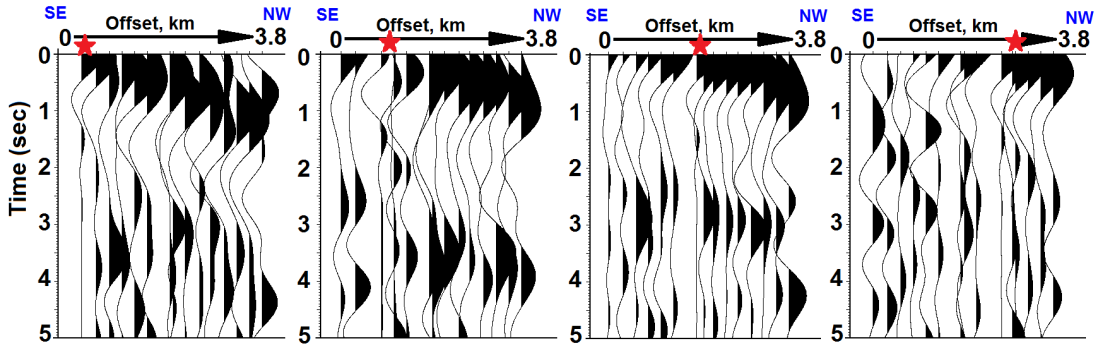

Figure 4.7: Virtual source filtered at 0.05/**0.1 – 0.60**/1.00Hz with different panels corresponding to a different virtual source Location within the line (star)

4.7 Comparison of virtual source and explosive source recordings

Before a more complex analysis of the arrivals apparently recovered by interferometry, we compared them with the explosive source recording. We have chosen a single virtual source (VS) with coherent linear arrivals as the focus of this comparison. There are several things to consider when comparing the explosive source gather and VSG: (1) the locations of the shot is known with an uncertainty of approximately ±100m; (2) the surface wave in the dynamite shot record are not strong at smaller offsets due to a finite distance needed for the surface waves to develop fully (this effect was first noted by Gutenberg (1945)). The comparison is done within the frequency bands, which produced coherent virtual arrivals discussed previously.

Figure 4.8 compares the explosive and virtual source recordings, both filtered for high frequencies (6/**7 – 14**/17Hz). The shot gathers look most similar to each other at these frequencies due to an overlap in spectra between ambient and the explosive sources (e.g. Figure 4.3). The top panel in Figure 4.8 shows the real and virtual source records unmarked. The lines corresponding to slopes indicating particular velocities are added in the bottom panel. Both virtual and explosive shot records exhibit similar surface wave velocities of 1.8 (yellow) and 2km/s (green). Finally, the explosive source record has a weak body wave arrival (blue) at these frequencies. However a similar body wave arrival is unrecognizable on the virtual source record.

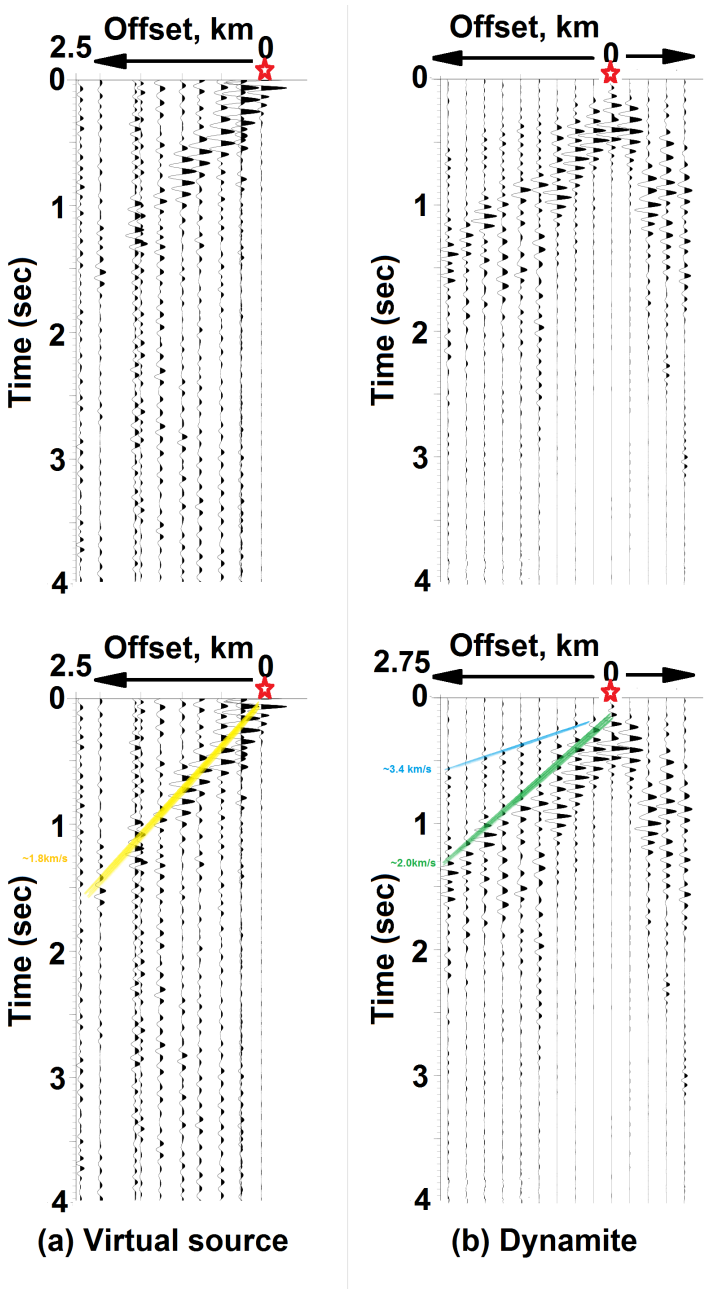

Figure 4.8: Comparison of (a) virtual and (b) dynamite shots for a single 2D line filtered at high frequency 6/**7 – 14**/17Hz

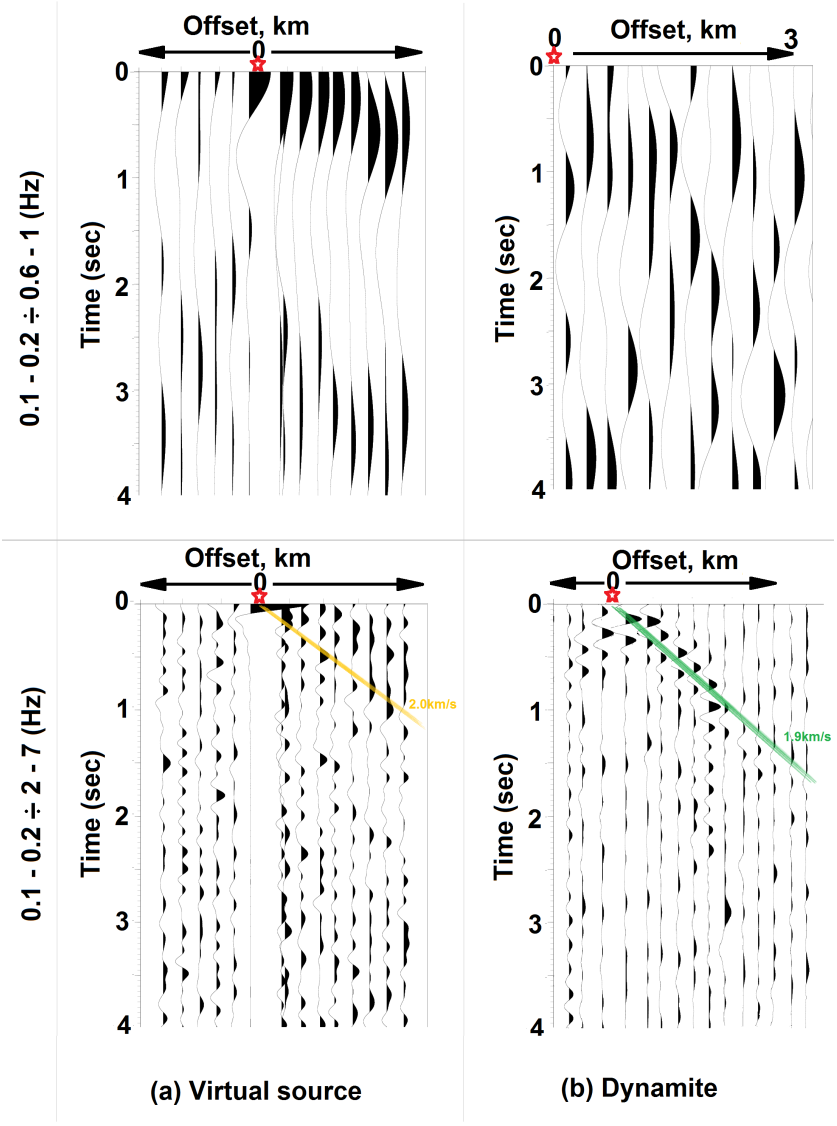

Figure 4.9: Comparison of virtual and real source records for a single 2D line filtered at two different frequency bands: *0.1*/**0.2 – 0.6**/*1.0*Hz (top) and 0.1/**0.2 – 2.0**/7.0Hz (bottom). (a) virtual source record, (b) dynamite shot.

Figure 4.9 shows (a) a VSG and (b) explosive source both filtered at two frequency bands: *0.1*/**0.2 – 0.6**/*1.0*Hz on the top and *0.1*/**0.2 – 2.0**/*7.0*Hz on the bottom (the locations of the shots are marked with a star). The reason for choosing the low frequency pass band is that energy is more coherent on the VSG.

However, these low frequencies (**0.2 – 0.6**Hz) are not present in the explosive source record. Therefore, slightly higher frequencies were analyzed as well (**0.2 – 2.0**Hz) in order to compare lower frequency surface wave on both gathers. This issue of non-matching spectra of virtual and artificial source recording was also recognized by Draganov et al. (2007).

There is a clear linear arrival (green) on the dynamite shot with an apparent velocity of approximately 1.9km/s (Figure 4.9 (a) and (b) bottom panel) with only a hint of the surface wave on the virtual record (yellow line with an apparent velocity of 2.0km/s). The difference in quality of the virtual and explosive source arrivals is presumably due to the difference in the frequency content of the ambient noise vs. active source and the absence of intermediate frequencies in the virtual source gathers.

None of the virtual arrivals exhibit move-out velocities consistent with P-wave on the explosive source record. We therefore interpret these arrivals on the virtual source gathers as surface waves in both frequency bands.

4.8 Directivity of retrieved arrivals

In order to better characterize the physical sources of energy, we analyzed VSG generated for three individual lines: Line 2049, Line 2033 and cross-line. We focused on (a) the directivity of observed signal, (b) the coherency of retrieved arrivals between the lines, and (c) frequency characteristics of the recovered signal.

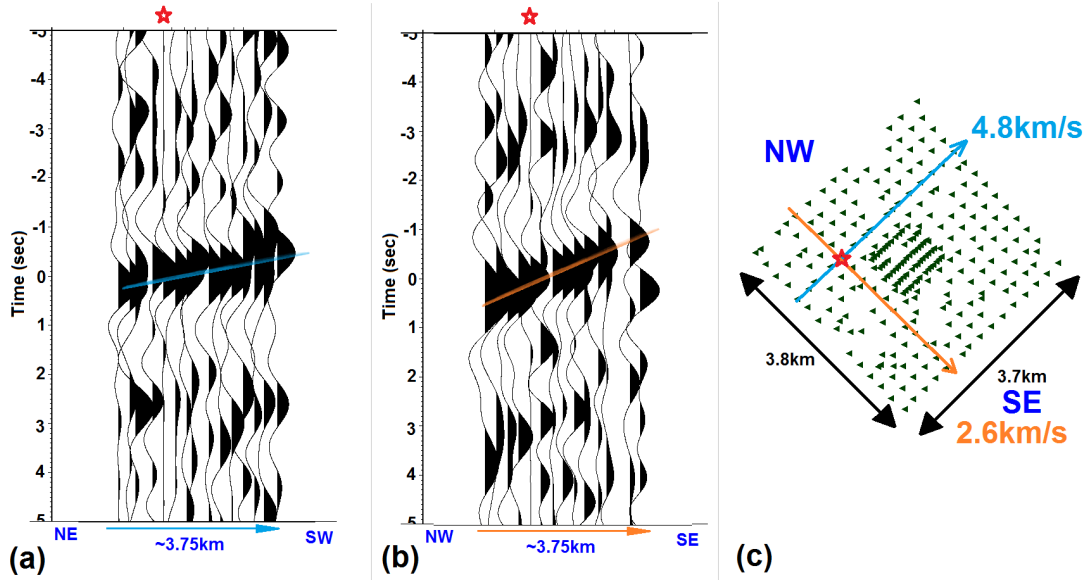

Figure 4.10: Comparison of arrivals and linear velocities of Line 2049 and its cross-line, filtered at **0.10 – 0.60**Hz

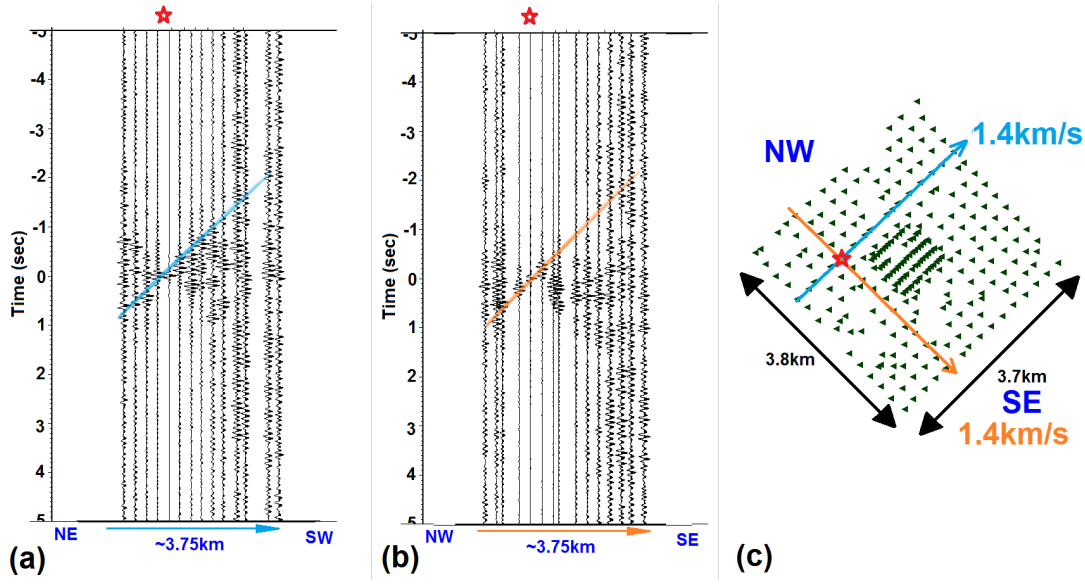

Figure 4.11: Comparison of arrivals and linear velocities of Line 2049 and its cross-line, filtered at **6 – 14**Hz

Figure 4.10 shows the difference in the move-out of the retrieved arrivals filtered at low frequency for Line 2049 (or in-line) (Figure 4.10(b)) and its cross-

line (Figure 4.10(a)). The apparent velocity estimated by a visual fit of a straight line for the cross-line is approximately $v_1 = 4.8$km/s, whereas it is only $v_2 = 2.6$ km/s for the in-line. Solving equations 4.1 and 4.2 simultaneously (Figure 4.12) implies the true velocity (v_t) of approximately 2.3km/s from the east-southeast. The velocity of 2.3km/s suggests that this arrival is a surface waves, as it is too slow to be a P wave (velocity of approximately 4.5km/s from the dynamite shot in Figure 4.2).

$$v_t = v_1 \cdot \cos\alpha \tag{4.1}$$

$$v_t = v_2 \cdot \cos\left(\frac{\pi}{2} - \alpha\right) \tag{4.2}$$

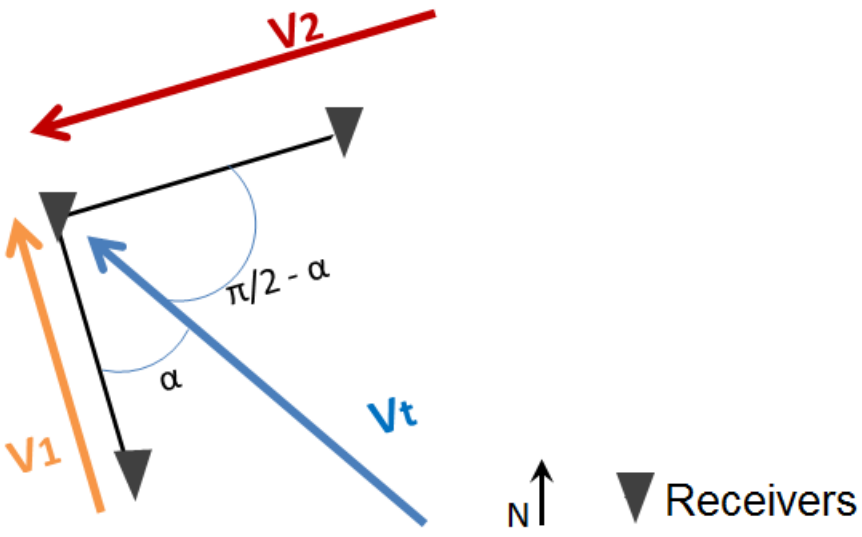

Figure 4.12: Geometry of the incident wave and measured velocities

The VS gathers in Figure 4.11 correspond to the same lines in Figure 4.10 filtered at high frequency band. Visual identification of coherent arrivals is more

difficult for high frequency arrivals, but the two picks shown in Figure 4.11 indicate apparent velocities of approximately 1.4km/s for for cross- and in-line. Similar apparent velocities on both lines indicate the component of the motion along each direction is the same. This similarity could be a result of a more homogeneous source distribution, which enables interferometry to recover the true velocity of the subsurface. However, the high frequency arrivals attenuate rapidly with distance from the virtual source. We suggest that the rapid decrease in amplitude with offset indicates that ambient sources at these frequencies are close to the stations. In addition, the lack of the variability in the apparent velocity with the direction implies the physical sources are uniformly distributed with respect to azimuth.

Directionality of low frequency arrivals has also been reported in other locations in (Toksöz and Lacoss, 1968; Horike, 1985; Satoh et al., 2001; Pedersen and Krüger, 2007). Our interpretation of the azimuthal variations of the virtual surface waves is that the Atlantic coastline is the source of the low frequency energy, and that human activities in the area of the survey may be the high frequency source. This interpretation is also supported by the fact that natural noise tends to be lower frequency (< 0.5 Hz; (Bonnefoy-Claudet et al., 2006; Gutenberg, 1958)) than anthropogenic seismic noise (> 1Hz; (Bonnefoy-Claudet et al., 2006)).

Figure 4.13 confirms that similar apparent velocities correspond to two parallel lines Line 2033 (red) and Line 2049 (orange), supporting our interpretation of the previous velocity differences being due to azimuthal variations at low frequencies.

However, Figure 4.14 shows that the Line 2033 (red) did not retrieve any vir-

tual arrivals at high frequency band, while Line 2049 (orange) did. This contrast suggests that the high frequency sources are near the center of the array.

Overall, when comparing high and low frequency arrivals for all virtual sources within the lines, the high frequency virtual arrivals seem to ehibit less coherency, attenuate fast and do not appear in all virtual source gathers.

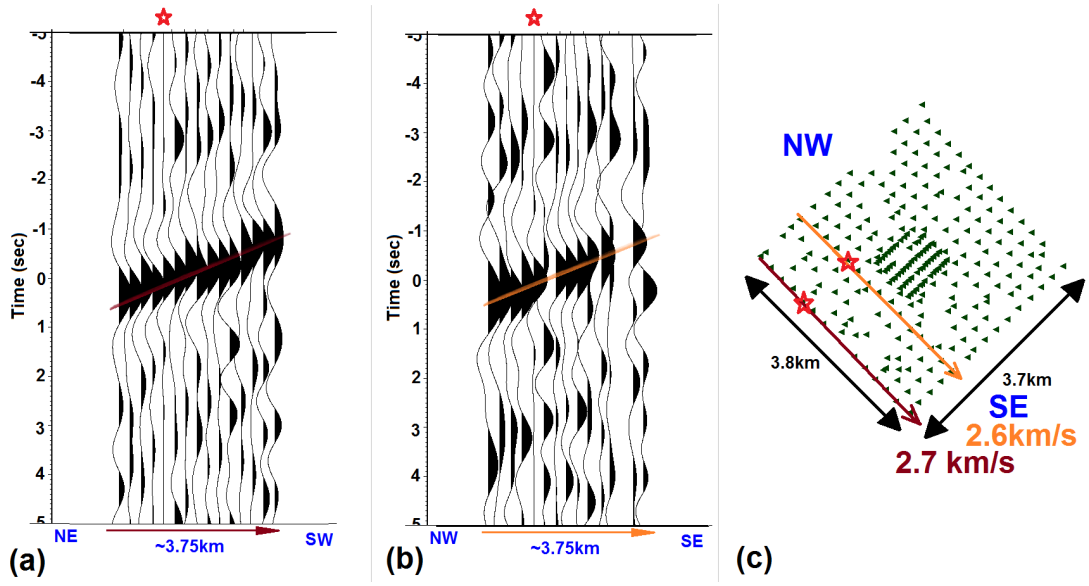

Figure 4.13: Comparison of arrivals for Line 2033 (red) and Line 2049 (orange), filtered at **0.1 – 0.6**Hz

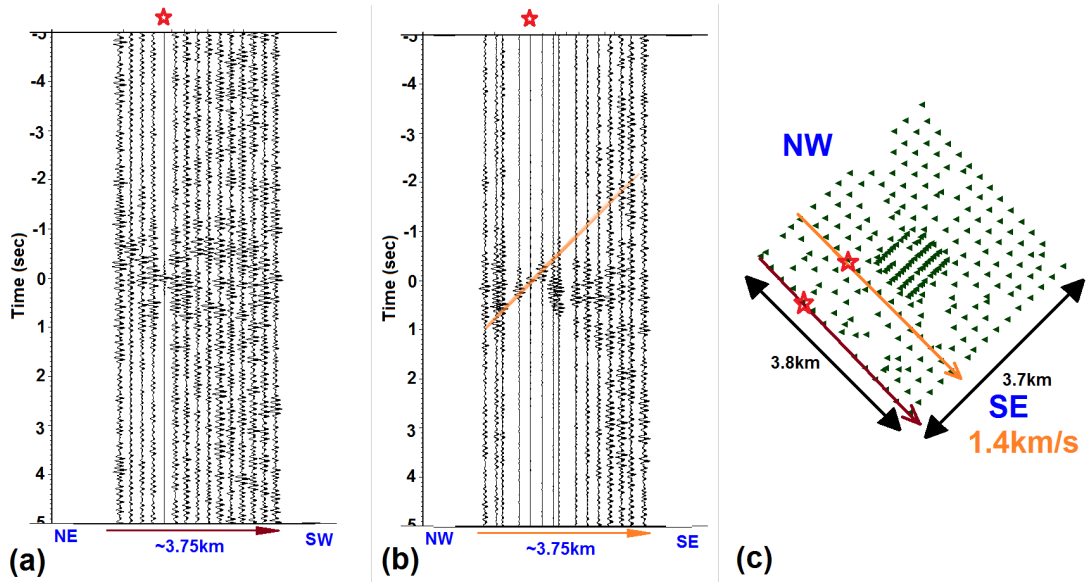

Figure 4.14: Comparison of arrivals for Line 2033 (red) and Line 2049 (orange), filtered at **6 – 14**Hz

4.9 Surface wave Dispersion

Most studies on interferometry focus on retrieval of surface waves and their subsequent inversion for subsurface velocities (Shapiro et al., 2005; Bensen et al., 2007; Harmon et al., 2008; Lin et al., 2013b,a). Dispersion (velocity dependence on frequency) is one of the main characteristics of surface waves and is the basis of the inversion. We first examine the VS arrivals for evidence of dispersion by looking at apparent velocity as a function of frequency within the two distinct frequency bands where the signal is concentrated: low (below 1Hz) and high (6-14Hz).

Figure 4.15 shows a virtual source gather filtered at different pass bands within the low-frequency range. Visual arrival picks for each panel are high-

lighted with red lines and corresponding velocities are noted under each panel. The shot location is the same for all five panels and is denoted by a red star. This line of stations is trending from SE to NW. The linear move-out velocity seems to decrease very slightly between the first and the second panel from 3.1km/s to 2.8km/s with increasing frequency. This is consistent with velocity increase with depth (Dobrin, 1951). However the coherence of the interpreted first arrival decreases with increasing frequency, which undermies the significance of this observation.

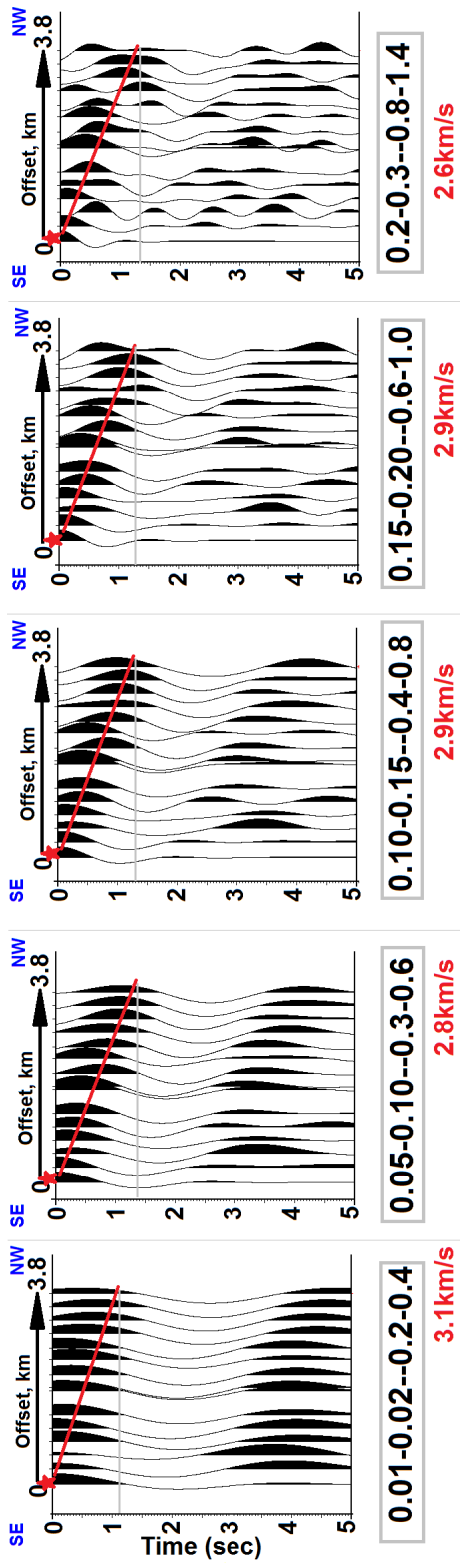

Figure 4.15: Virtual source record filtered at 5 different frequency bands (gray box) for low frequency arrival

Figure 4.16 shows similar analysis for the higher frequency range. There is a suggestion of velocity increase with frequency, which would be more consistent with a low velocity layer in the sedimentary cover. However the arrivals are not very prominent or coherent, again casting some doubt on the significance of this velocity variation. Nevertheless, these velocities are smaller (e.g. 1.7 versus 2.9 km/s) than those measured for the lower frequency range of **0.02 – 0.8**Hz, which is indicative of an increase in velocity with depth.

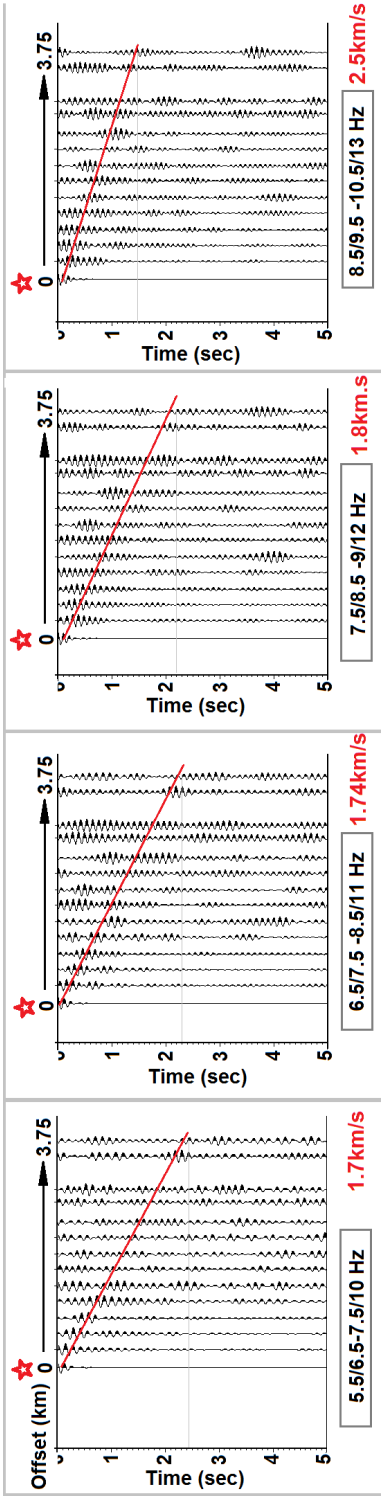

Figure 4.16: Virtual source record filtered at 5 different frequency bands (gray box) for high frequency arrival (zoom out)

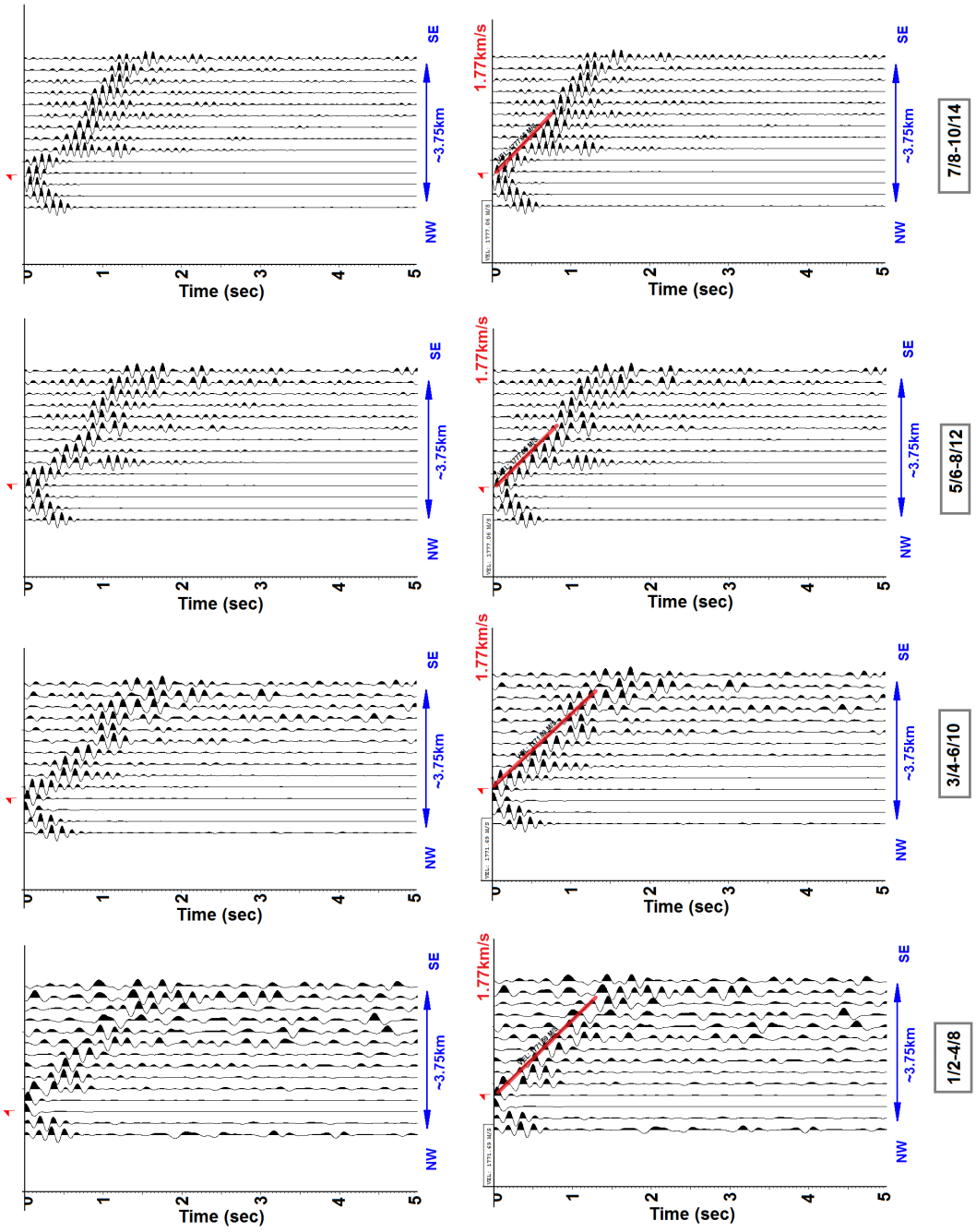

Figure 4.17: Explosive source record filtered at 4 different frequency bands (gray box) to show virtually no variations in velocities (approximately 1.8km/s for all 4 panels)

Similar analysis of the explosive source record is shown (Figure 4.17). Note

that frequency bands for the dynamite shot analysis are similar but not identical to those used for VSG. This is due to the fact, that dynamite record does not contain lowermost frequencies (i.e. < 2Hz) recovered from interferometry. Based on these visual picks, there does not appear to be any variation with frequency for this record, and the velocity of 1.78 km/s is essentially identical to that obtained for the high frequency range of the VS. This match leans considerable support to our interpretation of the virtual arrivals as due to real surface wave energy.

Dispersion analysis and inversion was run on the VSG and explosive source gathers in order to compute dispersion curves and access what additional information the virtual surface wave may have to provide in addition to the active source recordings.

First we generated velocity histograms, or dispersion plots, for the unfiltered virtual source gathers used to produce Figures 4.15 and 4.16 (Figure 4.18). This dispersion plot was calculated using the Geopsy Linear FK-analysis toolbox (MASW) (Wathelet et al., 2008; Giulio et al., 2006). Two versions of this dispersion plot are shown in Figure 4.18: (a) is plotted on log frequency scale to best represent the low frequencies and (b) is plotted on linear frequency scale to better represent higher frequencies. Black lines correspond to the expected limits of non-aliased space corresponding to the spacing within stations and total length of the Bradford 2D array (k_{min} and k_{max}, as well as $k_{min}/2$ and $k_{max}/2$; See (Asten and Henstridge, 1984; Wathelet et al., 2008) for derivation).

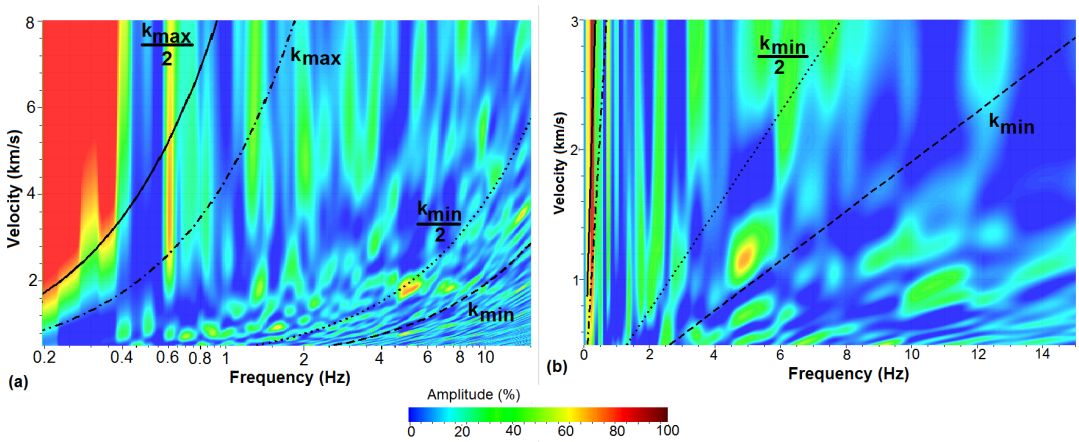

Figure 4.18: Dispersion plot for a single unfiltered virtual source gather (a) log frequency axis (b) linear frequency axis

Similarly we have generated dispersion plot for the dynamite shot in Figure 4.17. As previously noted from the filtered shot gathers, there is no distinct energy at frequencies below 2Hz present in the explosion dispersion curve.

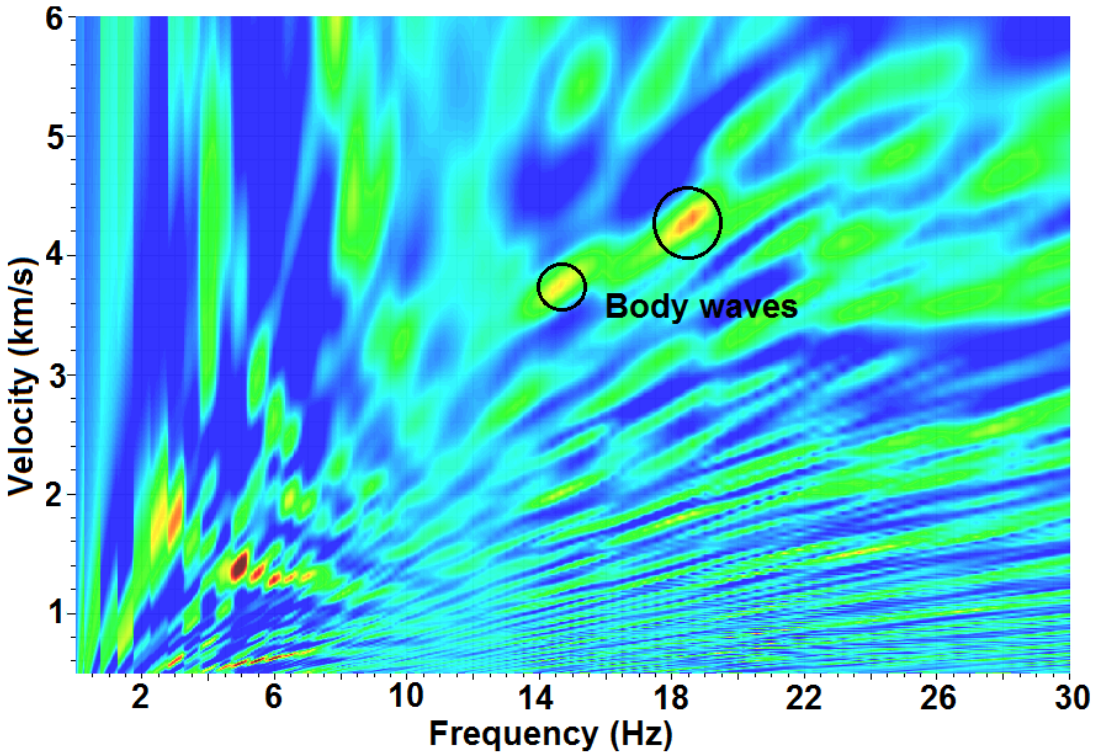

Figure 4.19: Dispersion Curve generated for a single 2D explosive source shot gather

A comparison of the virtual and explosion dispersion plots in Figure 4.20 suggests similar surface wave velocities ranging from 1.5-1.8 km/s between 4-6Hz. However, the explosive source dispersion curve exhibits better continuity across these frequencies. Recall that no coherent energy between 1-5Hz was found in the virtual source, which is not to be the case for the explosive source recoding. Perhaps most significant is that the virtual source gathers were able to retrieve a lower frequency signal that was not recorded on the explosive source gather. In this case the virtual source provides important bandwidth not available in the conventional record.

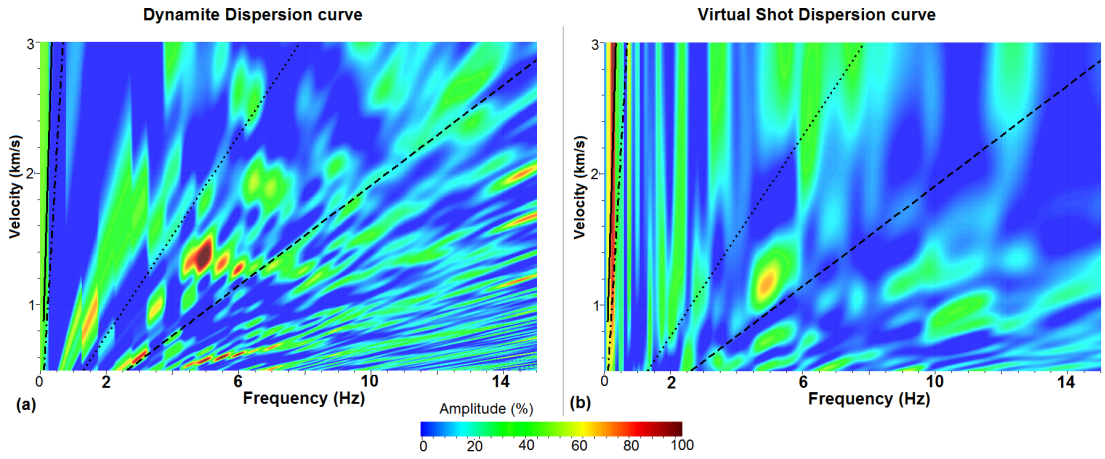

Figure 4.20: Comparison of explosive source dispersion curve with body wave energy and virtual source (lower frequency range due to monotonic frequency pollutions at 16Hz and higher) dispersion curves

A surface wave inversion experiment was performed in the area near our survey by Roy (2013) using active sources. Roy (2013) analyzed a 2D line trending NW to SE with 96 3-component seismometers at approximately 110 ft (33.5m) spacing. The total length of the profile was 1 mile (1.6 km). A total of 17 in-line and 20 slightly off-line dynamite shots, and 12-31 stations recorded each shot. The resulting vertical component dispersion plot is displayed in Figure 4.21. Although these controlled sources produce a smoother and more distinct dispersion pattern, the resulting velocities are largely consistent with those from our analysis of the virtual sources. The "real" surface waves do not display any significant changes in velocities with increasing frequency, and even have a slight increase between $12Hz$ and $14Hz$. However, unlike the virtual source dispersion curves, there is no energy evident at frequencies below 5Hz on the active source dispersion curve (Figure 4.21).

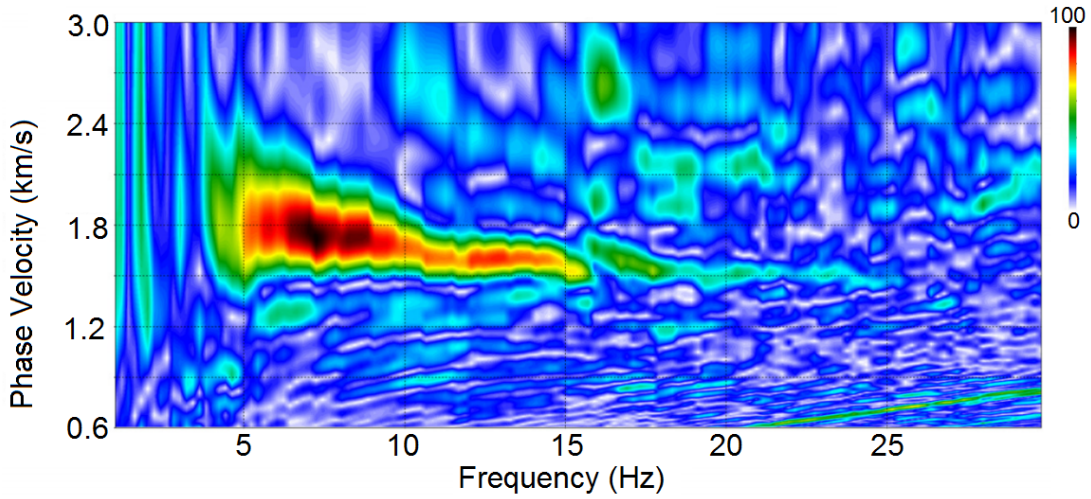

Figure 4.21: Velocity histogram generated (dispersion) in a survey near Bradford, PA (Roy, 2013)

Due to the much smaller station spacing and shorter length of Roy's (2013) array, we expect the results of this array to have less penetration to depth. Station spacing and the total length of the array limits the minimum and maximum wavelength of the signal recorded without aliasing (Asten and Henstridge, 1984; Wathelet et al., 2008). The total length of the array equals to the maximum wavelength that the array can confidently record without aliasing. For the sparse array $L = \lambda = 3.75km$ for a single line of receivers. For the surface wave velocity $v = 1.6km/s$, the minimum frequency we can recover is $f_{min} = v/\lambda = 0.4Hz$, or for the faster surface wave velocity $v = 2.6km/s$, the recoverable frequency $f_{min} = 0.69Hz$. According to the same calculations for the dense array ($L = 1km$), the minimum frequency is $1.6Hz$. The station spacing determines the maximum recoverable frequency. For the sparse array ($dl \approx 0.26km$) the maximum frequency of reliable signal is $f_{max} = v/dl = 10Hz$, whereas for the dense array ($dl = 0.06km$) $f_{max} = 26Hz$.

Therefore, Bradford array with larger station spacing and total length of the

line of stations corresponds to generally lower frequency recoverable signal and, thus, a larger penetration depth compared to Roy's (2013) stations. In Figures 4.22 and 4.23 we attempt to test the consistency of our results with a hybrid geological model by merging the result of Roy's inversion for shallow structure (1D S-velocity, table 4.1) with a geological model that includes an addition of a basement interface at 6km with appropriate seismic P- and S- velocities and densities of an average granitic basement (Coussy, 1987). We then computed synthetic surface waves using Herrmann (2013) code for 2D array with a station spacing of 300m and a total line length of 4,500m to approximate our geometry.

Figure 4.22 shows the resulting synthetic surface waves filtered at 4 frequency bands which span those of the virtual source data discussed in this report, including the intermediate frequencies which were absent from our virtual source. An f-k analysis was performed on these synthetics to produce a dispersion plot comparable to those derived from the VS and artificial sources (Figure 4.23).

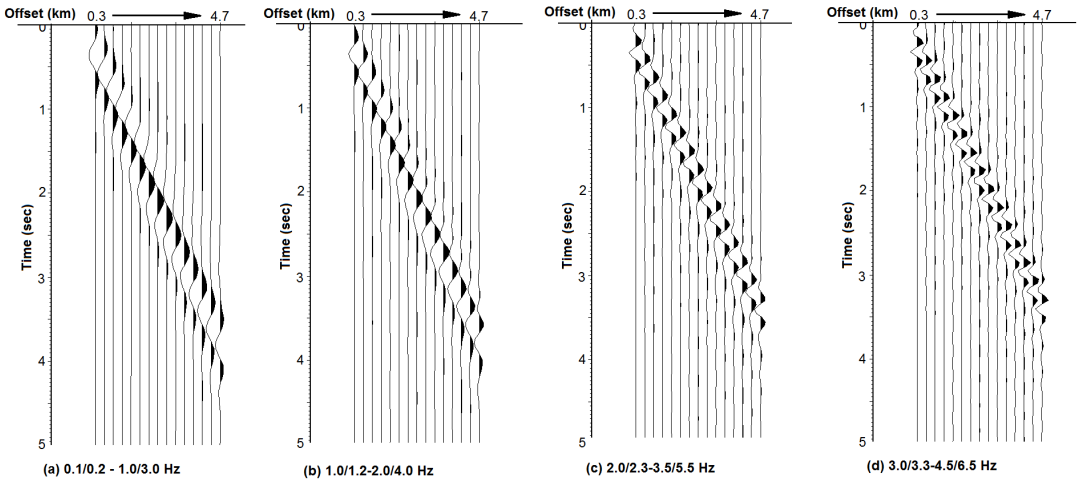

Figure 4.22: Synthetic Surface wave generated for a synthetic dynamite shot using (Herrmann, 2013) with distances between stations 300m total of 4km linear array filtered at 4 frequency bands (a) $0.1/0.2 - 1.0/3.0Hz$ (b) $1.0/1.2 - 2.0/4.0Hz$ (c) $2.0/2.3 - 3.5/5.5Hz$ (d) $3.0/3.3 - 4.5/6.5Hz$

H(km)	VP(km/s)	VS (km/s)	Density(gm/cc)	QP	QS
0.060	3.0	1.58	2.0	600	300
0.100	3.5	2.90	2.3	600	300.
6.000	4.5	3.54	2.5	600	300.
below	6.0	4.00	2.7	600.	300.

Table 4.1: Thickness (H), P- and S- wave velocities (VP and VS) and attenuation factors (QP and QS) for synthetic surface wave in Figure 4.22. S-waves are taken from (Roy, 2013)

The first order observation is an overall similarity of the retrieved velocities in appropriate frequency bands. However, the continuity of the dispersion plot for the virtual source is not as high as for synthetics, which we attribute to the aforementioned absence of the real energy at frequencies between 0.8 and 4Hz. We interpret the increase in phase velocity at around 2Hz to be due to the effect of the crystalline basement (Figure 4.23(b)). The VS dispersion curve appear to have detected this high velocity contrast, which is absent completely in curve by

Roy (2013). This supports our previous assertion that the virtual source results provide information that does not exist in the controlled source data.

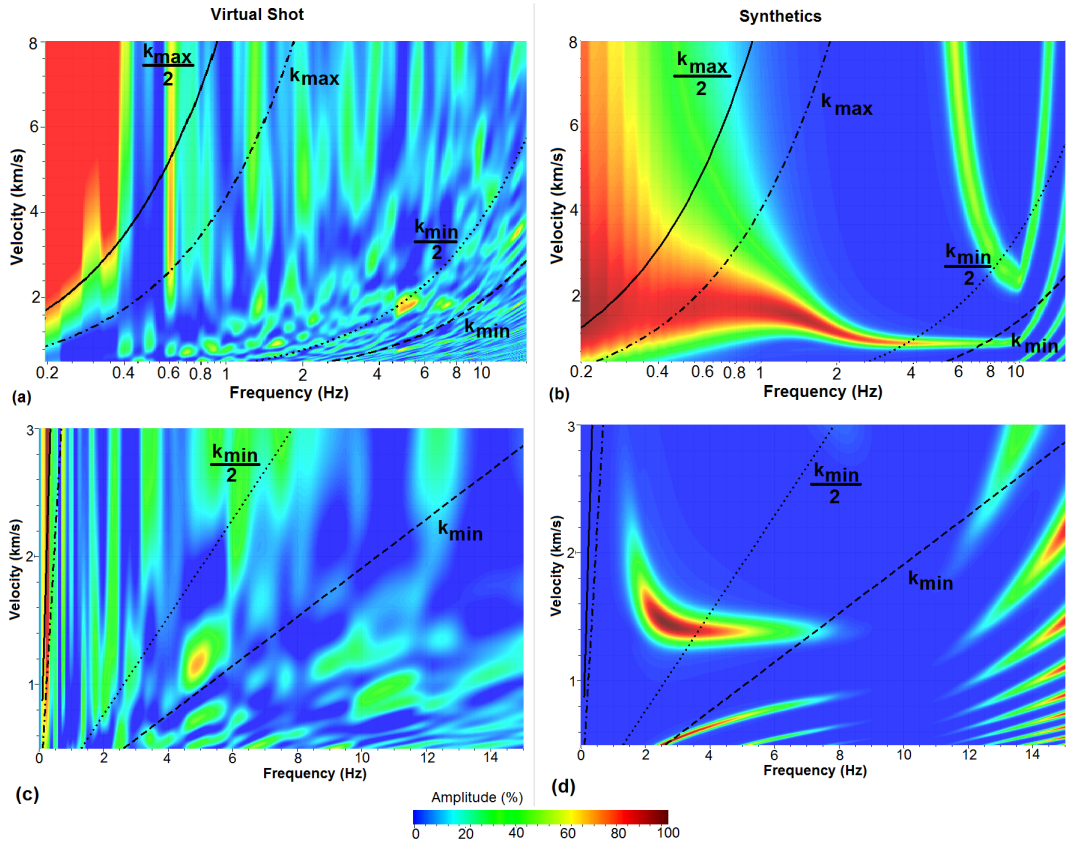

Figure 4.23: Comparison of (a)(c) virtual source and (b)(d) synthetic dispersion curves

The poorer quality of the dispersion curve for the virtual source data, compared to that for the synthetic model may be attributed to: (1) the poor quality of the surface waves generated from interferometry either due to limited total time of the station deployment or the influence of monotonic noise in the record (to be discussed), (2) the velocity of the subsurface at the depth to which our array is sensitive without aliasing (approximately 3 - 6km for k_{max} and $k_{max}/2$ assuming 2km/s velocity) does not exhibit strong variations at the frequency bands recorded by the array, and (3) a combined effect of subsurface heterogene-

ity and elevations statics distorting the seismic data and affecting coherency of the recorded arrivals (as observed by Roy (2013)), (4) the limited spectra of the ambient noise sources used to create the virtual sources, rather than being an artifact of the hardware, station geometry or subsurface model. Overall, we cannot conclude that the station geometry is not adequate for successful surface wave dispersion curve generation, however due to overall poor quality of dispersion curve when compared to Roy (2013) dispersion, we argue that velocity heterogeneity and elevation static probably has a significant effect on the results of interferometry, as well as the dynamite shot dispersion. We also suggest that a longer ambient noise recording period would be more effective for this area in generating the virtual surface wave retrievable by interferometry.

In spite of discontinuous nature of the dispersion curves derived from virtual source data, we attempted to invert for velocity with depth using Geopsy software. We picked two simple dispersion curves shown in Figure 4.24 using Geopsy software. Each curve has only three points, and only the low frequency pick is different. The boundary conditions for the inversion were based on the results from (Roy, 2013) and are displayed in table 4.2.

Depth	VP(km/s)	VS (km/s)	Density(gm/cc)
0-100m	0.2-5	0.15-5	2.0
0-200m	0.2-6	0.15-5	2.3
0-10km	0.2-6	0.15-5	2.5
0.000	0.2-6	0.15-5	2.7

Table 4.2: Input parameters for the Curve 1 and Curve 2 inversion

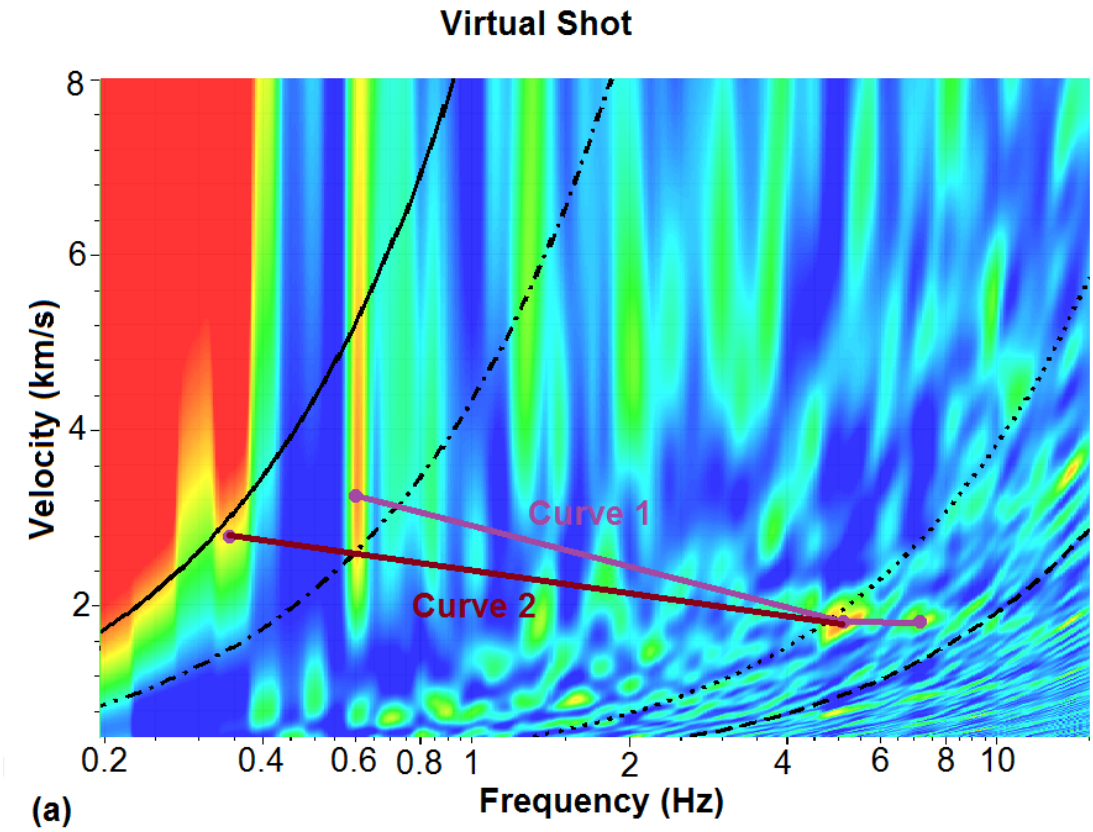

Figure 4.24: Dispersion curves 1 and 2 picked on Bradford virtual source data

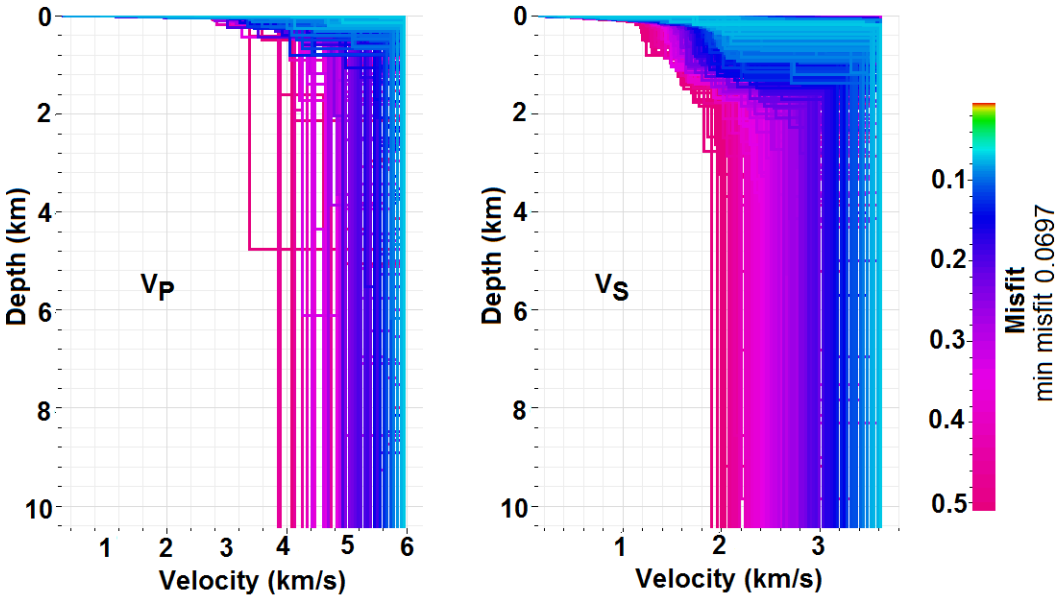

Figure 4.25: Dispersion curves 1 and 2 picked on Bradford virtual source data

Figure 4.25 shows the results of inversion (P- and S- waves) of dispersion curve 1. Different colors represent multiple iterations and in the case of this inversion, blue lines are the best fit models (minimum misfit of 7%). However, due to limited number of points comprising the dispersion curve, a large number of models would fit the f-v (frequency-velocity) measurement with equal misfit.

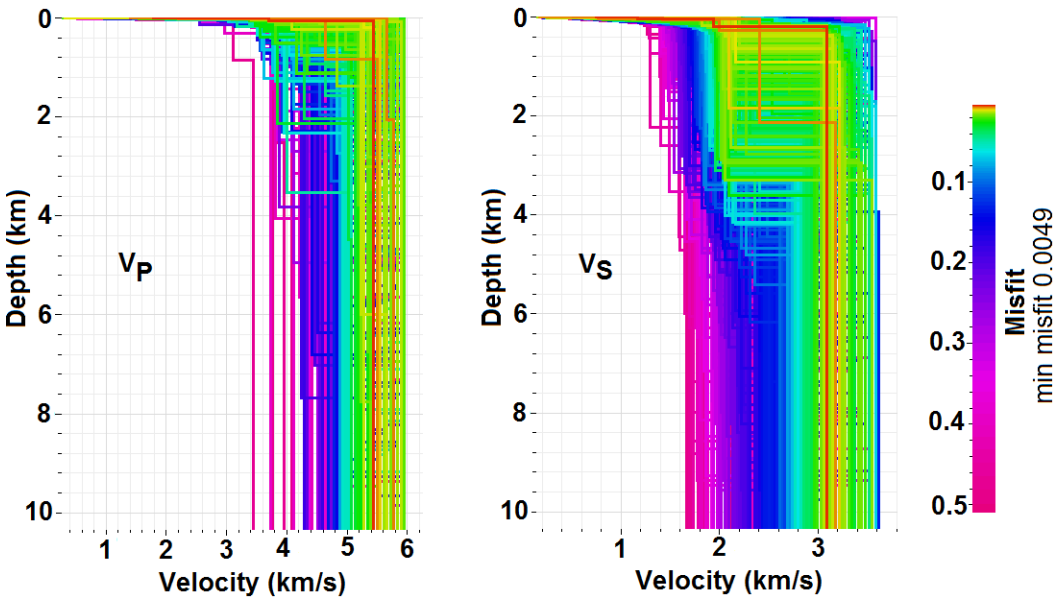

Figure 4.26: Dispersion curves 1 and 2 picked on Bradford virtual source data

Figure 4.26 shows the inversion results for dispersion curve 2. It has a smaller misfit of approximately 0.5% (red lines), and the P and S velocities are more consistent with Table 4.1. However, none of the low misfit inversions resolves the depth to the expected basement interface at 5.5-6km depth this area (Dietrich and Colton, 1967; Hills, 1985). We suggest this is due to the lack of ambient energy in the intermediate frequency range that we have previously described. Nevertheless, in contrast to Roy (2013) conventional active source surface waves, the virtual surface waves pick up the underlying higher velocity layer (Table 4.3).

Depth	V_R (km/s) (Roy, 2013)	V_R V.S. (km/s)	V_P V.S. (km/s)
shallow	1.8	1.8	4.0
deep	-	2.2	5.5-6.0

Table 4.3: Comparison of (Roy, 2013) and our inversion

4.9.1 Temporal variability

In order to assess the temporal variation in the strength and coherence of virtual arrivals with time, six 24-hour virtual gathers were produced for the two frequency ranges in which significant ambient energy has been identified (Figures 4.27 and 4.28).

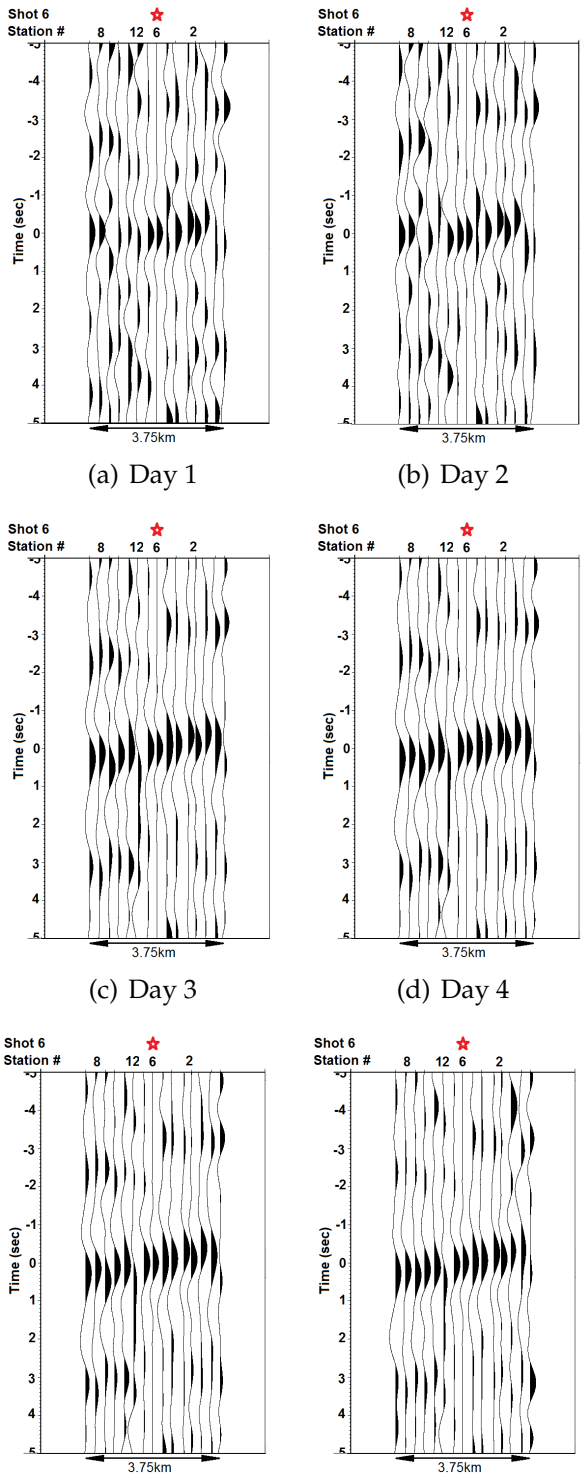

(a) Day 1 (b) Day 2

(c) Day 3 (d) Day 4

(e) Day 5 (f) Day 6

Figure 4.27: Daily variations of cross-correlated data, Low Frequency Filter (Line 2049, Figure 4.4) filtered at *0.01*/**0.02 – 0.6**/*1.0Hz*

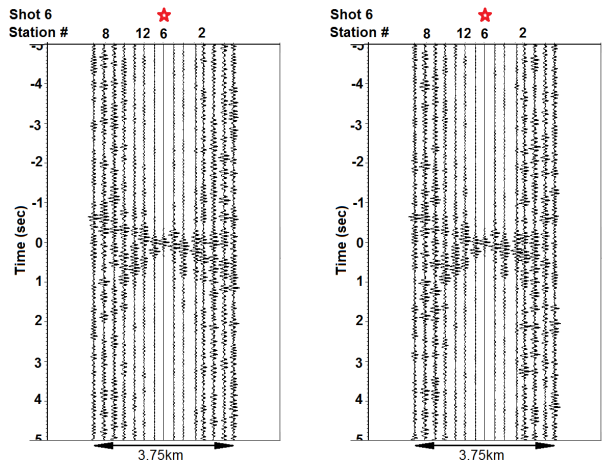

(a) Day 1 (b) Day 2

(c) Day 3 (d) Day 4

(e) Day 5 (f) Day 6

Figure 4.28: Daily variations of cross-correlated data, High Frequency Filter (Line 2049, Figure 4.4) filtered at *5.5*/**6.5 – 10**/*14Hz*

Figures 4.27 and 4.28 are virtual source gathers generated for 24-hour period, starting with the deployment of the station (Day1) throughout the duration of the entire experiment (for Line 2049, all stations were deployed for approximately six and a half days). The virtual source gathers shown here stack the same amount of time. Therefore any difference of the strength of the virtual arrivals should be due to the daily variations of available energy.

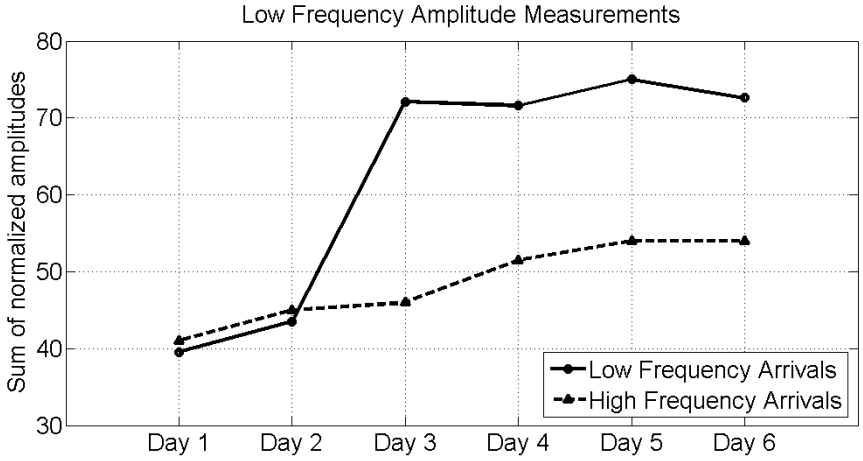

Figure 4.29: Amplitude variations of velocity picks for high and low frequencies

The amplitudes of the arrivals in Figures 4.27 and 4.28 are shown in Figure 4.29. These amplitudes were computed as follows: we have picked the maximum amplitude and time of the retrieved surface wave for Day 5, transferred the pick times to the remaining days and then measured and summed the amplitude at these picks for each day (Appendix E). The resulting variation is shown in Figure 4.29 for high and low ranges separately.

For the low frequency range, the amplitudes are relatively low for days 1 and 2, but then increase dramatically on Day 3 and continue high for days 4-6. In contrast, the amplitudes of the virtual energy in the higher frequency range

shows a much less variable behavior, thought it too shows an increase in time. This difference in behavior is consistent with two distinct energy sources. If the low frequency energy is related to wave activity along the Atlantic coast, the rapid increase from Day 2 to Day 3 could be weather related (e.g. arrival of a storm).

In contrast, the high frequency source appears to be more uniform with time, as well as being more local (see above). We suspect that these high frequency sources are associated with human activity.

4.10 Body Waves from interferometry (2D)

Despite seismic noise being generally dominated by surface waves due to this energy's proximity to the surface (Shapiro et al., 2005), a growing number of authors have now recovered virtual body-wave energy from ambient noise recording (e.g Gerstoft et al. (2008); Draganov et al. (2007, 2009); Ruigrok et al. (2011); Lin et al. (2013a)). Landes et al. (2008) found a large portion of body-wave energy in the frequency band $0.6 - 2.0Hz$, whereas Draganov et al. (2009) found reflection energy in $6 - 27Hz$ frequency band. Seismic arrivals recovered for the Bradford stations by means of interferometry are within this range of frequencies.

According to our previous velocity analysis of low and high frequency bands, we do not detect a signal with the move-out that would be consistent with body waves for the low frequency band. Therefore, we here focus on high frequency band to look for body wave arrivals. Even though the strength of the arrivals is variable and not coherent for all virtual sources, we were able to de-

tect quasi-linear arrivals with body wave velocities (Figure 4.30). Blue and red lines (1 and 3) correspond to body wave of 3.1 and 4.5 km/s velocity. In contrast the green line (2) is only 1.8 km/s and is interpreted as a surface wave. Without a 3-component data we cannot confirm wave type from particle motion. However, the explosive source record suggests that the higher velocity arrivals are body waves. Even though the 3.1 km/s velocity is smaller than the ones recorded by the explosion recording, we note that Roy's (2013) surface wave inversion suggests P-wave velocities within first 100 meters are 3.0-3.5km/s, increasing to 4.5km/s at depth.

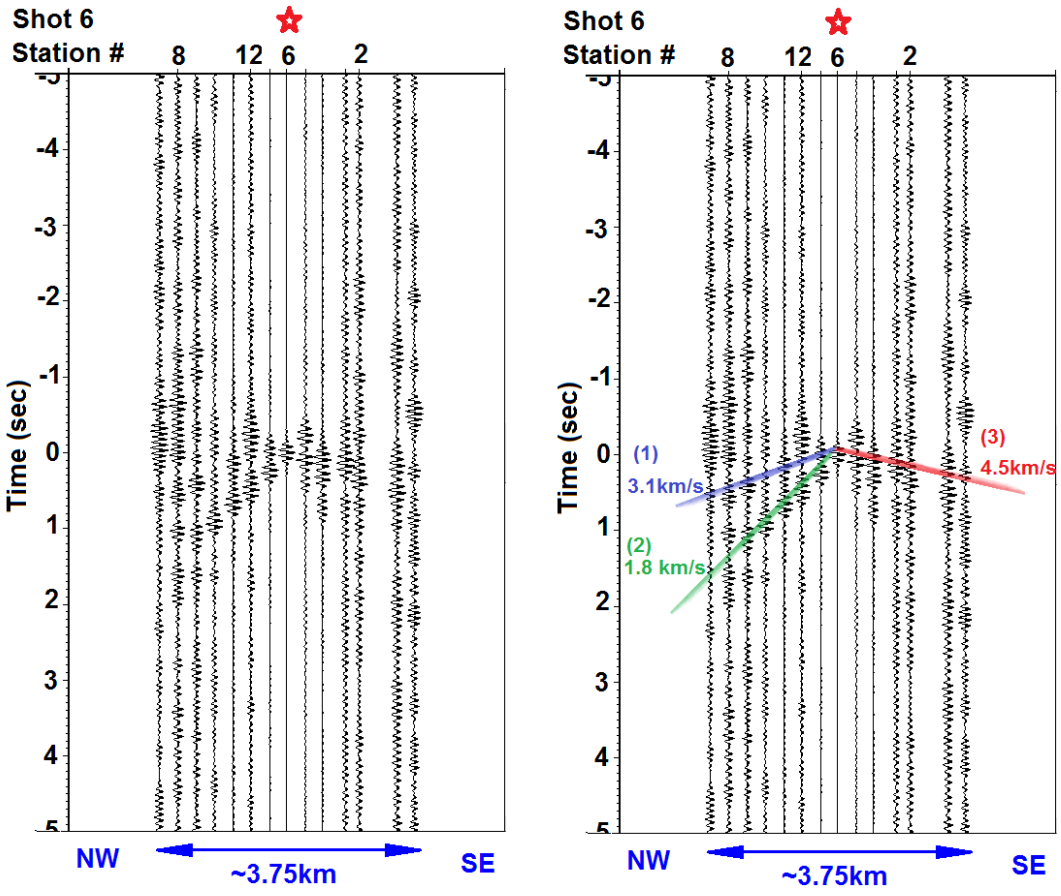

Figure 4.30: Virtual source for Line 2049 filtered at *9*/**11 – 14**/*17*Hz with and without reference lines that correspond to velocities 1 (blue) of 3.1km/s, 2 (green) of 1.8km/s, and 3 (red) 4.5km/s

Only a few VS gathers display visually recognizable arrivals with body wave velocities. However, on the virtual gathers that exhibit such arrivals, energy propagating to the NW from the selected virtual source position tends to have a lower velocity than that propagating to the SE (Figure 4.31, blue and red lines). This asymmetry can be related to poor quality of the virtual gathers However it might be due to a dipping layer. In case of the latter, this effect can be explained by a dipping layer. The higher velocity would correspond to shifted refracted wave (Mikesell et al., 2009) (Chapter 2) with lower velocity corresponding to the direct wave. The reason for the asymmetry is that larger offsets are required to generate a critically refracted wave down-dip vs. up-dip, which is illustrated by a synthetic model below in Figure 4.32.

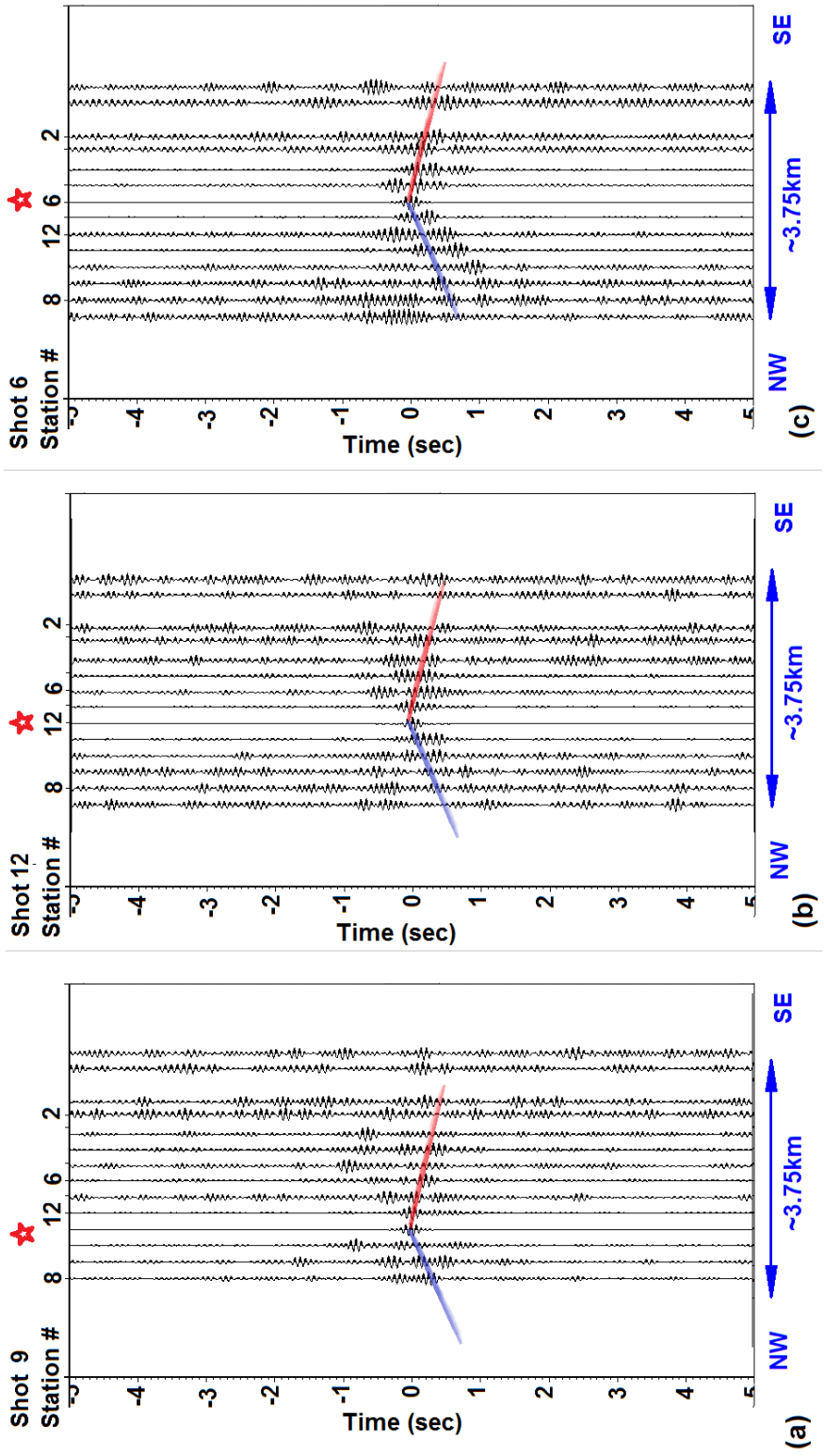

Figure 4.31: Three virtual sources generated for Line 2049 filtered at 9/**11 – 14**/17Hz; blue line corresponds to velocity around 3.1km/s, and red line corresponds to velocity 4.5km/s

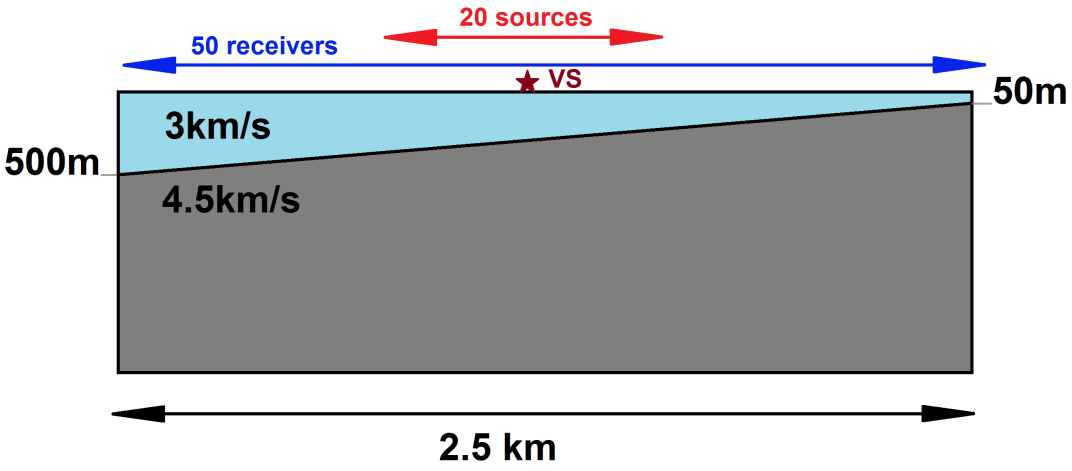

Figure 4.32: Synthetic model for the dipping layer direct and refracted waves

The synthetic record for the geometry in Figure 4.32 is shown in Figure 4.33. It was computed for 20 surface sources and 50 receivers above a dipping layer. Snell's law was applied to calculate the arrivals times for direct and critically refracted waves and then convolved with a 14Hz Ricker wavelet.The virtual source gather in Figure 4.33 was created by cross-correlating a receiver (red trace in Figure 4.33) for each shot gather and subsequently receiver-stacking all cross-correlations. In Figure 4.33(b) (3) and (5) are the virtual direct waves and (4) is the virtual refraction. Note that for this VSG both direct and critically refracted waves appear to originate at the VS location and stations to the left of the VS do not recover the faster arrival (4). There is no constraint on the depth aof the reflector in the VSG model, although the synthetic indicates the interface would have to be dipping to NW.

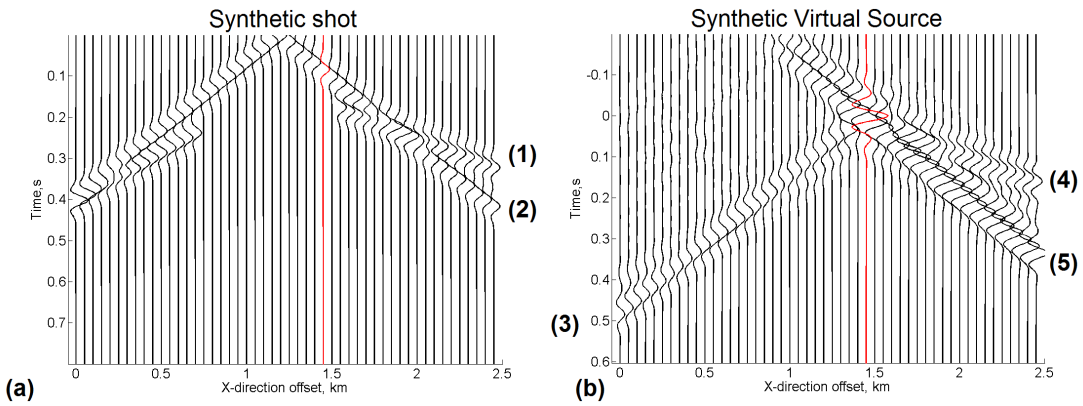

Figure 4.33: (a) Synthetic record for direct and refracted arrivals above a dipping layer, (b) virtual source record created by summing the cross-correlations for 20 such synthetic shots

4.11 Monotonic frequencies

We have found a significant monotonic energy present in both raw data and cross-correlated spectra (the peaks in Figures 4.34 and 4.35) for the Bradford recordings. These spectra were computed on de-biased and mean-scaled data, without any frequency filtering applied and are normalized by the number of traces used in computing the spectra. Comparing the spectra of the raw data (Figure 4.34) with the explosive source spectra in Figure 4.3, the monotonic frequency peaks are weak (max amplitude $1.4 \cdot 10^{-4}$ vs. 800). However, after cross-correlation and stacking, these spectral peaks often dominate the signal (Figure 4.35).

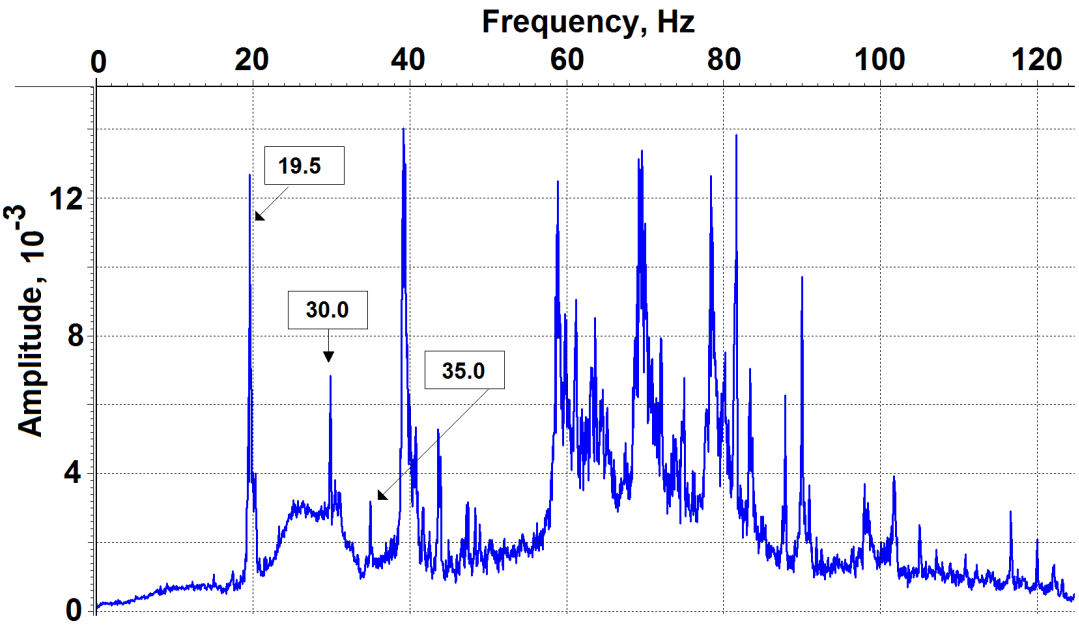

Figure 4.34: Average frequency spectra computed for 50 traces picked randomly within a 60 second window of input raw data

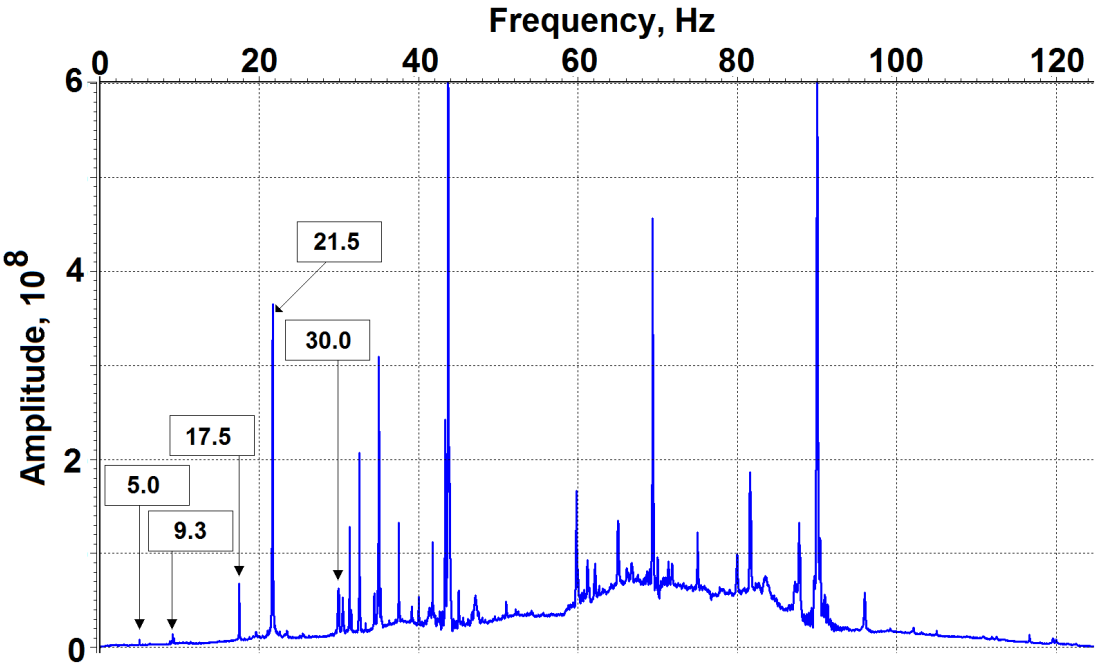

Figure 4.35: Average frequency spectra of a single virtual source within a 120 second window of output correlated data

The effect of including monotonic frequencies within the bandwidth filter of the final virtual source is shown in Figure 4.36. The first panel is filtered below 17.5Hz and shows a clear arrival propagating from the virtual source station (marked by a red star). The same arrival in the second panel, where 17.5Hz monotonic frequency peak is included within the pass band, is barely visible, and disappears completely when the monotonic 21.5Hz peak is included as well (Figure 4.36).

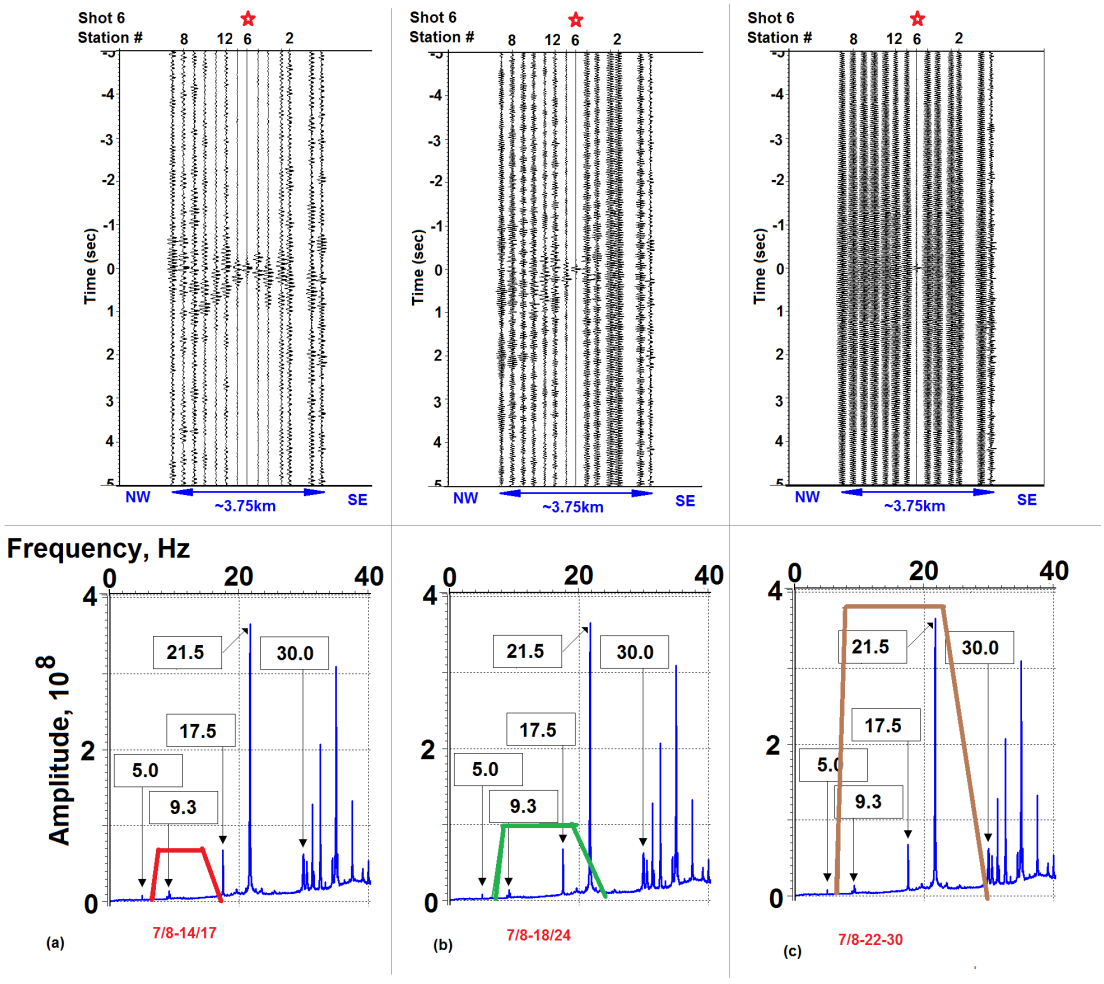

Figure 4.36: Virtual gather filtered at three frequency bands shown below each panel: (a) 7/8 – 14/17Hz, (b) 7/8 – 18/24Hz, (c) 7/8 – 22/30Hz before correlation. Corresponding spectra and pass-bands shown below each panel

Note that not all frequency peaks in the raw data sample (Figure 4.34) are transferred to the VSG spectrum in Figure 4.35. This is due to temporal variations of the ambient noise spectra. These variations result in long- and short-lived frequency peaks (Figures 4.37 and 4.38; each color represents an average spectra of 100 1-minutes traces measured at different days).The more persistent monotonic noise will tend to increase in amplitude after cross-correlation summation, but also destructively interfere with less persistent frequency peaks, removing them from the final VSG.

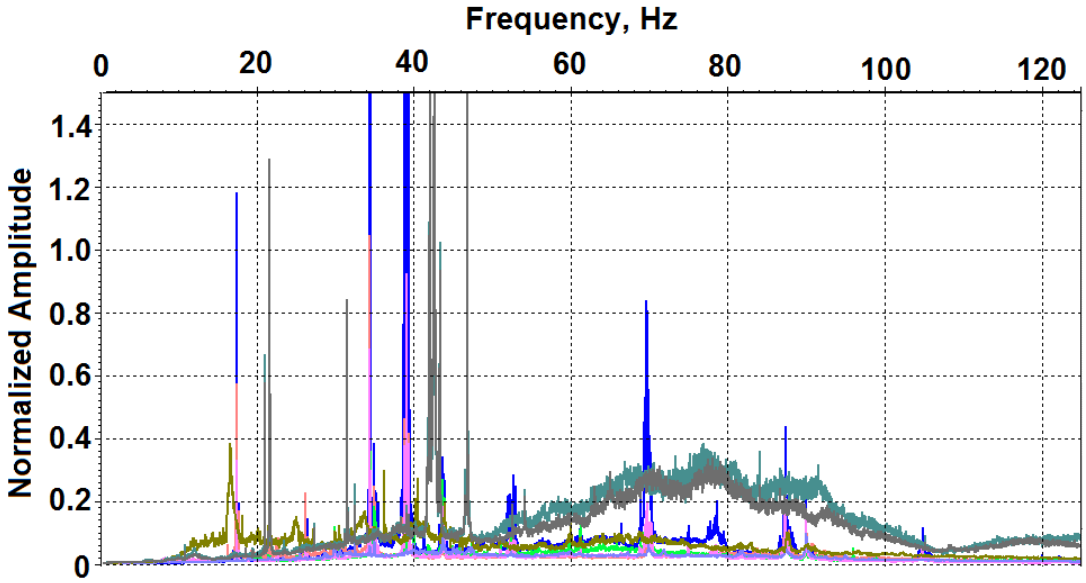

Figure 4.37: Average frequency spectra 100 randomly picked traces within an hour of recording for different days of input raw data

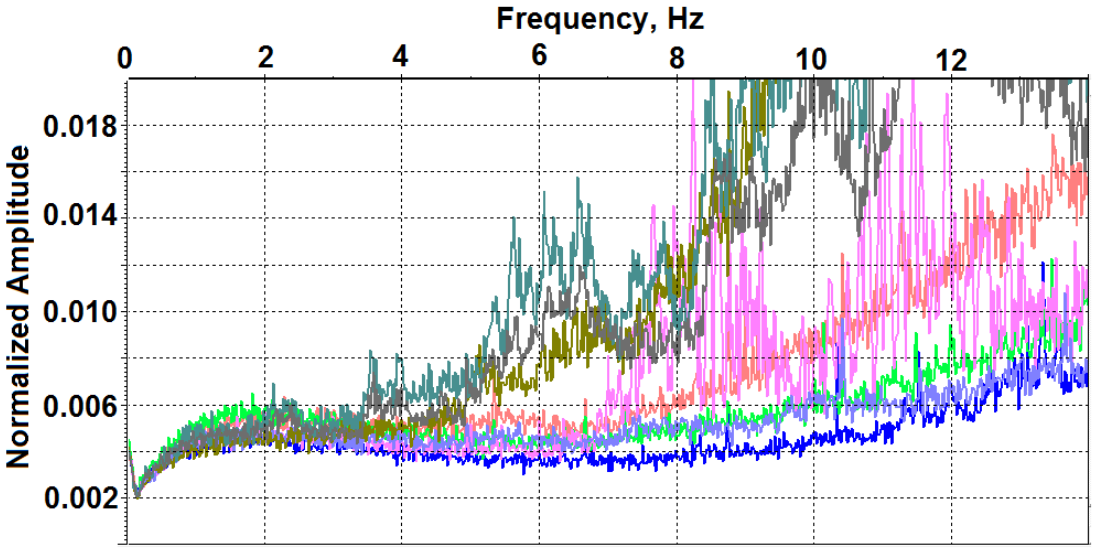

Figure 4.38: Average frequency spectra 100 randomly picked traces within an hour of recording for different days of input raw data, zoom-in of low frequencies

Frequencies below $1Hz$ do not display evidence of monotonic noise in the spectrum before and after correlation, which may help explain why high amplitude coherent virtual arrivals are recovered in these frequency range in spite of the geophone response. The VSG spectrum in Figure 4.35 also does not show significant monotonic energy presence in the intermediate frequency band (1 – 4Hz) identified earlier. Thus the lack of virtual arrivals at these frequencies is most likely due to the lack of available energy sources operating at these frequencies.

Although the monotonic noise negatively affects virtual body and surface waves (Figure 4.36), notch filtering (narrow frequency band-pass filter) did not prove to be effective in reducing its contribute. We suspect that removing the more persistent frequency peaks simply enhances the contribution of shorter-lived monotonic noise at nearby frequencies.

4.11.1 Frequency clipping

To decrease the effects of monotonic noise on VSG, we have attempted to limit its contribution by amplitude clipping in frequency domain.

Clipping of amplitudes in time domain has been shown to diminish dominance of strong but poorly distributed sources, like earthquakes (Bensen et al., 2007). However, monotonic noise is expressed by high amplitudes in frequency domain, not in time domain. Therefore, we have attempted to apply amplitude clipping techniques to our data's spectrum instead of the time series.

The difference in time and frequency domain clipping is shown in Figure 4.39, where blue is the original data and red is a clipped trace. The time domain clipping is intuitive: the amplitudes higher than a threshold are limited, producing a flat cutoff (Figure 4.40(b)). Frequency clipping is the same technique applied to the spectra, where the contribution of sporadically dominant frequencies are reduced while the remaining frequencies are left intact.

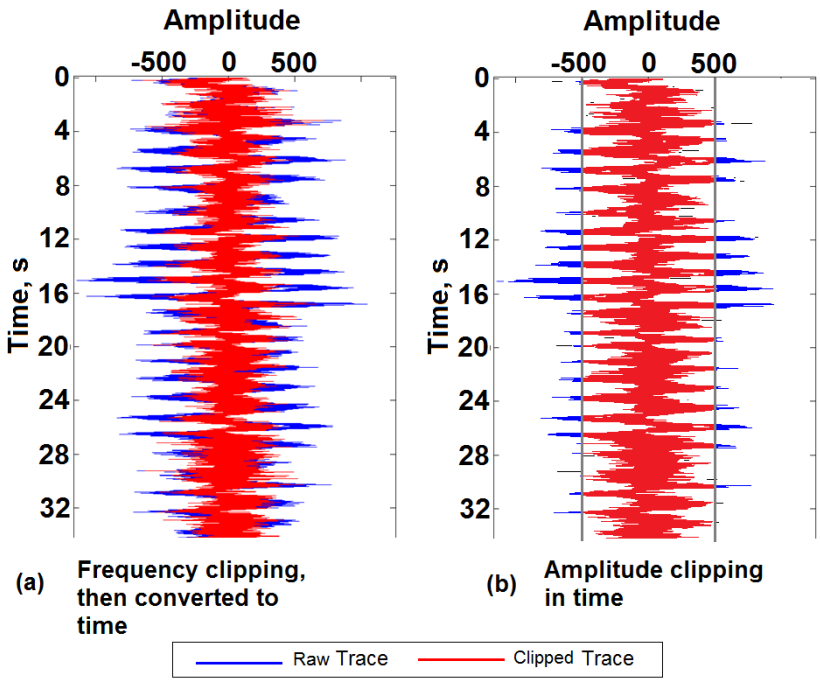

Figure 4.39: Comparison of trace in time domain that was clipped in (a) frequency domain, and (b) in time domain

Comparison of raw data frequency spectra vs. same spectra clipped at two different levels is shown in Figure 4.40, where blue is original spectra and is referred to as "0 clipping", red is clipped at level 4, and green at level 2.

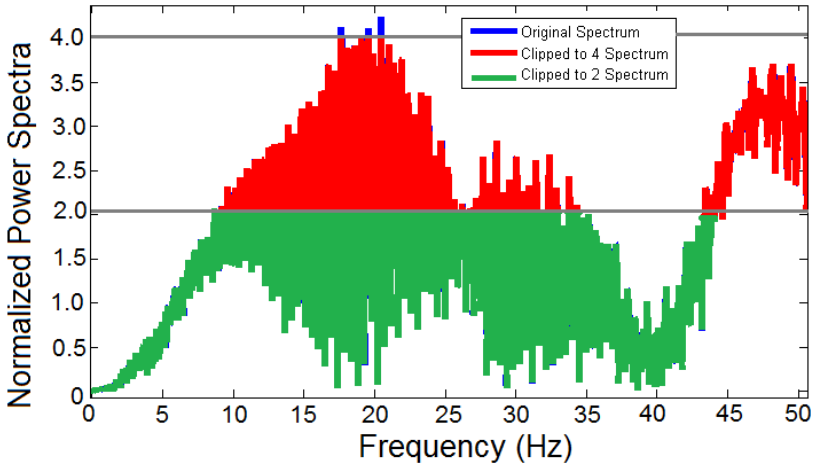

Figure 4.40: Frequency Spectra of a single trace. Blue,red and green together are the power spectra of raw data, red and green are clipped spectra to a power of $4 \cdot P_{average}$ ("clip 4") and green is clipped spectra to a power of $2 \cdot P_{average}$ ("clip 2")

Frequency clipping at various thresholds was applied to raw 2D data (cross-line in Figure 4.4) before correlation, then virtual source gathers created. Figures 4.41 - 4.43 are the results of different levels of clipping at three different frequency bands: low (**0.02 – 0.6**Hz),intermediate (**2 – 4**Hz) (intermediate) and very high (**12 - 40**Hz). Figure 4.40 suggests, that no signal is affected by f-clipping below 9Hz for level "2" and below 20Hz for level "4", therefore we should not expect to see any difference in the amplitudes of the virtual arrivals due to clipping in low and intermediate bands. This is what we observe in Figures 4.41 and 4.42. Thus frequency clipping in this case has little to contribute to enhancing surface wave recovery.

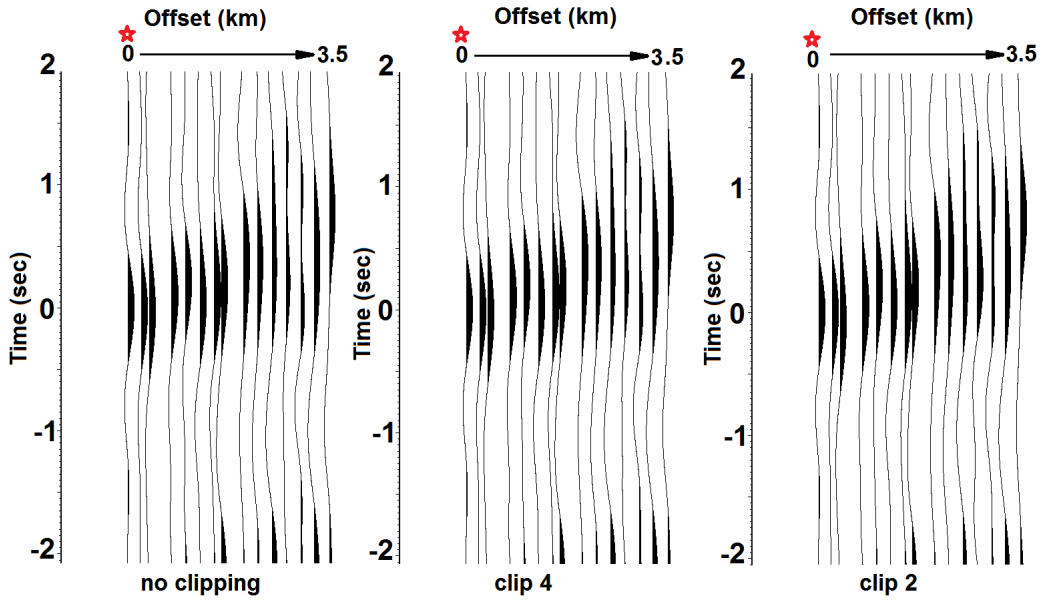

Figure 4.41: Cross-line (Figure 4.4) virtual source gather comparison of clipping levels filtered at *0.01*/**0.02 – 0.6**/*1.0*Hz for a 2D cross-line(location of the shot marked by a star)

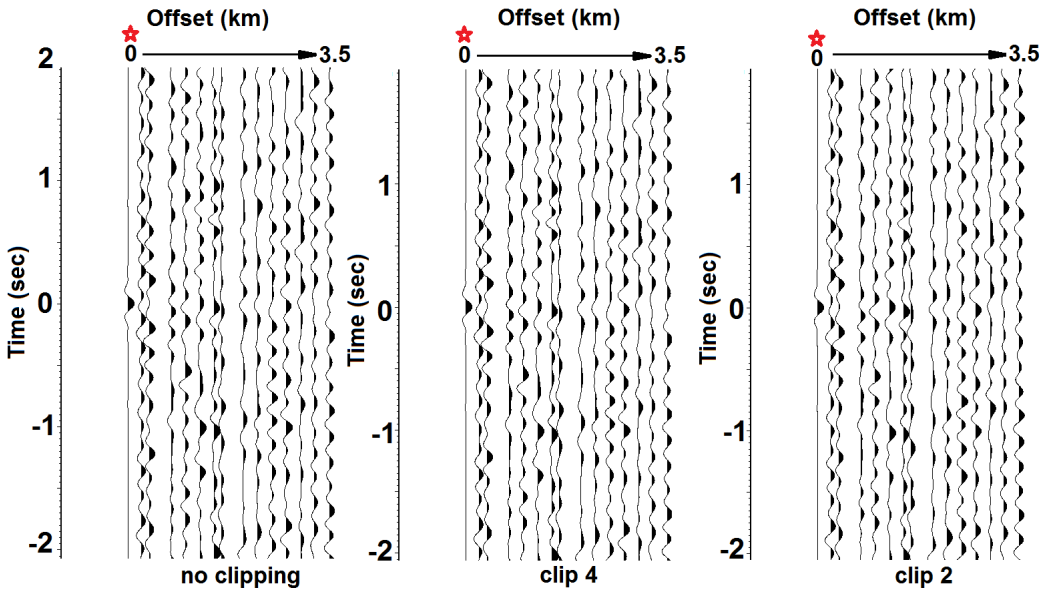

Figure 4.42: Cross-line virtual source gather comparison of clipping levels filtered at *1*/**2 – 4**/*8*Hz for a 2D cross-line (location of the shot marked by a star)

At the very high frequency band both "Clip 4" and "Clip 2" (Figure 4.43) resulted in increased amplitude of linearly propagating energy in the VSG (Figure 4.43). However, the apparent velocity of this arrival is 7km/s, much too fast for a real body wave propagating in the sedimentary cover. We suggest that this energy (which is quite reverbatory in character) could represent an off-line source, or alternatively could be a deeper crustal refraction "re-zeroed" by cross-correlation. In any case, it suggests that frequency clipping might be a viable technique for signal enhancement during virtual source generation.

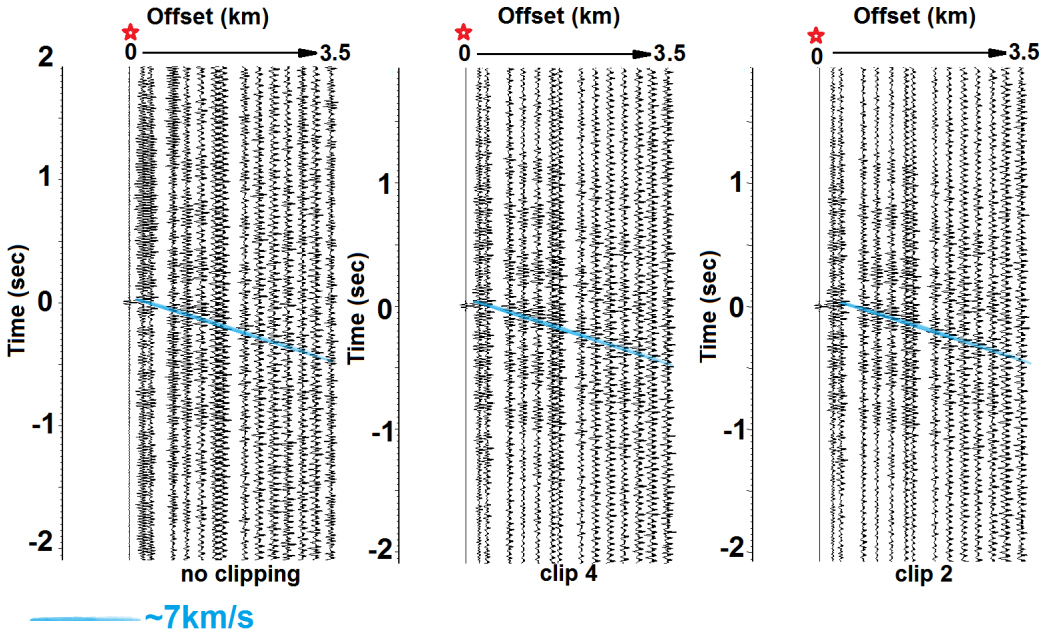

Figure 4.43: Cross-line virtual source gather comparison of clipping levels filtered at $10Hz/12Hz - 40Hz/80Hz$ for a 2D cross-line (location of the shot marked by a star)

Furthermore, even though frequency clipping was apparently not effective at removing the prominent monotonic noise peak at $f = 21.5$Hz, it minimized the effect of the 17.5Hz frequency peak to reveal a strong air-wave signal (Figure 4.44), which is very sensitive to the frequency pass band. The apparent velocity

of this virtual air-wave is 360m/s and it seems to propagate from the NW as it appears only in the positive lag of the cross-correlation. Further analysis (automatic gain control, scaling, etc.) of this virtual record at this frequency band did not reveal the presence of body wave energy in the same gather. We suggest that body wave energy is limited in this location, therefore cannot be enhanced by the clipping. Nevertheless the enhancement of the air wave in this narrow band after clipping shows the potential of enhancing the signal masked by monotonic energy.

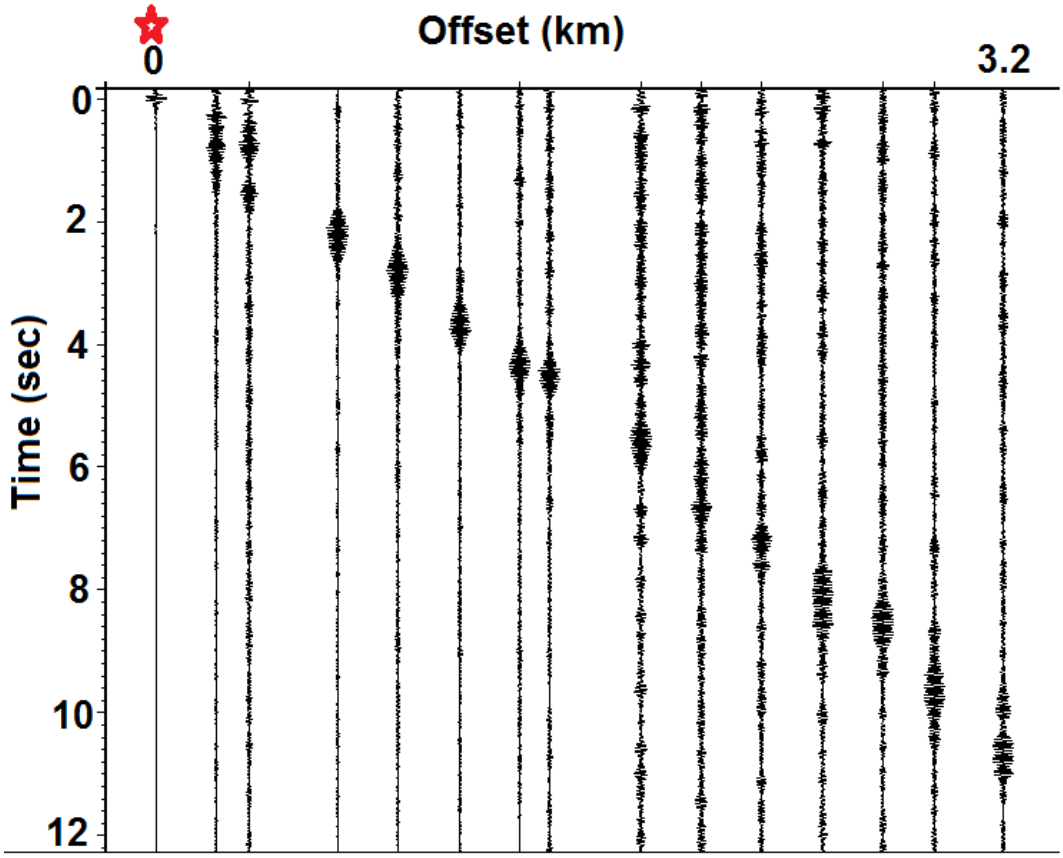

Figure 4.44: Virtual air-wave, at frequencies **6-18**Hz with frequency clipping level "2"

4.12 Spatial filter for body wave interferometry

Array synthesis (also referred to as wavenumber filtering or mixing) is a known technique that helps distinguish signals based on their apparent propagation velocity (e.g. Capon et al., 1967). It is often used in seismic processing to enhance near-vertical arrivals and reflections and minimize surface waves. We have applied wavenumber filter to our data in attempt to enhance body wave energy at the expense of surface wave energy that may be present in the VSG.

The wavenumber filter (or mixing) is equivalent to averaging seismic data recorded by n neighboring stations. We chose $n = 3$ in combination with a bandpass filter (*6*/**7 – 14**/*17*Hz) based on trial filtering of the explosive source record to remove surface wave energy.

Two different wavenumber filter flows were tested: (1) first apply a bandpass filter to the raw data, subsequently cross-correlating , then mixing followed by the summation over the entire duration of the survey (Figure 4.45(c)) and (2) same as the first flow but mixing is applied prior to cross-correlation (Figure 4.45(b)). Scaling and normalization is applied to all traces after each step. The results are compared to a "no mixing stack", where data was filtered, cross-correlated and stacked without applying the wavenumber filter (Figure 4.45(a)).

Figure 4.45(b) shows lateral smearing of the energy, which is especially evident for the first three traces. The apparent coherency of the arrivals does not extend beyond any 3 neighboring traces. Thus any increased coherency would seem to be merely an artifact of the mixing filter.

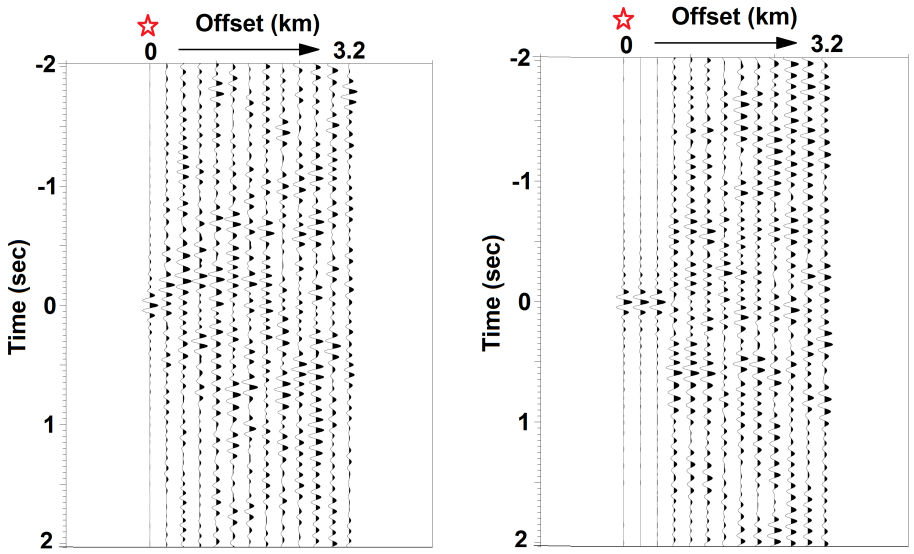

(a) High Filter → Correlation → Stack

(b) High Filter → Mixing → Correlation → Stack

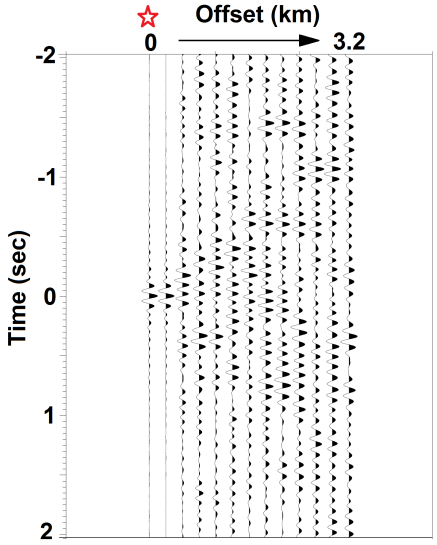

(c) High Filter → Correlation → Mixing Stack

Figure 4.45: Comparison of mixing traces before and after correlations

Figure 4.45(c) also exhibits some apparent smearing to a lesser extent than Figure 4.45(b). As shown in the zoomed Figure 4.46, mixing after cross-correlation appears to have slightly enhanced the faster arrival (3.1 km/s velocity; potentially a P-wave), while degrading an interpreted surface wave (green,

1.8km/s). Mixing does not appear to have enhanced any body wave energy with the hyperbolic arrival time that would characterize any reflected energy from depth.

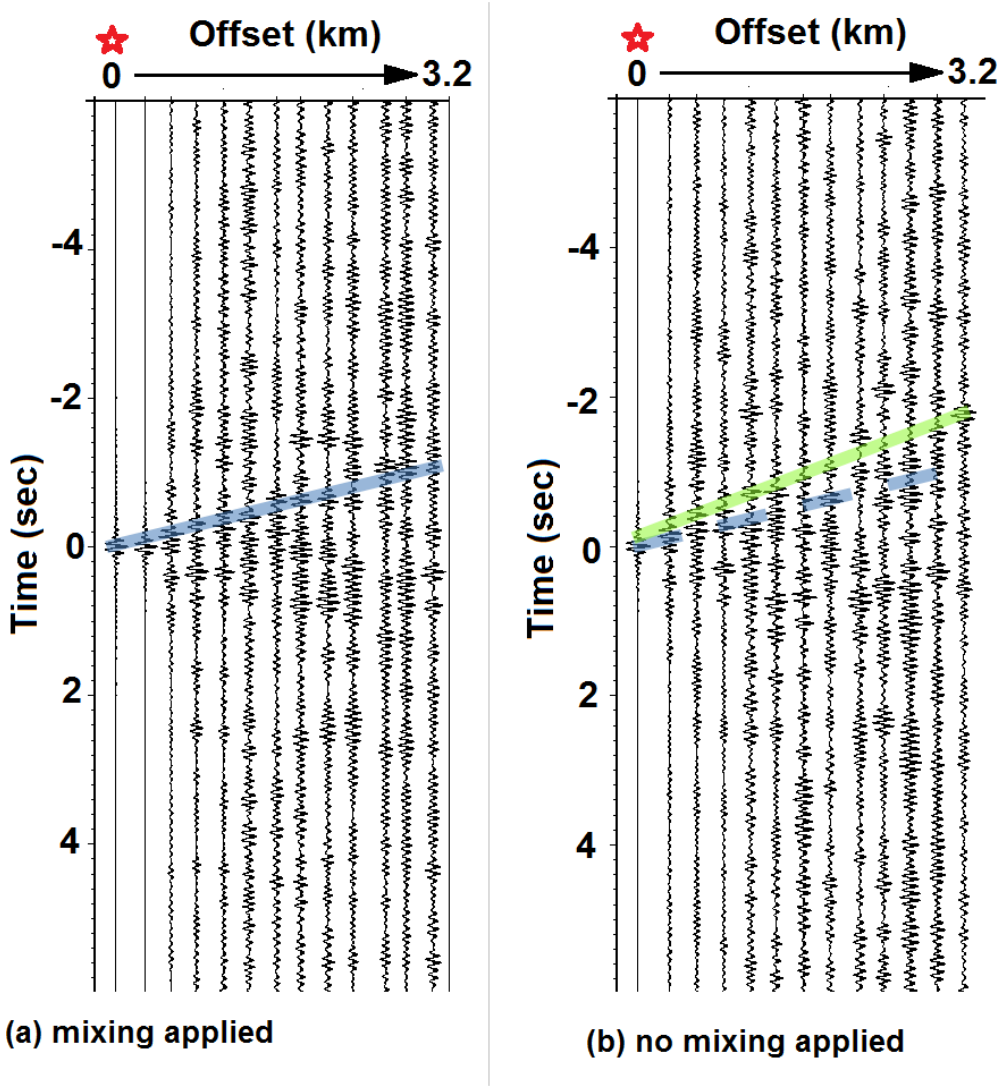

Figure 4.46: Comparison of VSG (a) with and (b) without spatial filtering (blue line corresponds to velocity 3.1km/s and blue line corresponds to velocity 1.8 km/s)

4.13 Frequency-Wavenumber (f-k) filter

F-K filtering applied prior to cross-correlations has also been used to enhance virtual reflection energy (e.g. Draganov et al., 2013).

Figure 4.47 shows the f-k domain of a synthetic dataset for Bradford single line geometry with two arrivals: 2km/s (two steep slopes below two seconds propagating from the opposite directions) and 3.5km/s (two steep slopes above two seconds) (the propagation direction and the arrival times of the synthetic arrivals are different to illustrate that the filter does not discriminate against the location of the source but only the propagation velocity). These synthetic arrivals are used exclusively to determine the shape of the filter (i.e. the masking area in Figure 4.47(b)). These arrivals are mapped onto f-k space as two lines with slopes corresponding to these velocities. We then designed a f-k filter to minimize the arrivals that come at velocities less than 3.2km/sec (e.g. corresponding to the slower surface wave energy)(Figure 4.47(b)). After the filter is applied, only the faster arrival remains in the synthetic record record (Figure 4.47(d)).

This f-k filter (Figure 4.47) was then applied on raw data (Line 2049) prior to cross-correlation. Note, that due to our station spacing we are not affecting any signal at frequencies higher than approximately 8Hz, which is evident from the Figure 4.47(a-b).

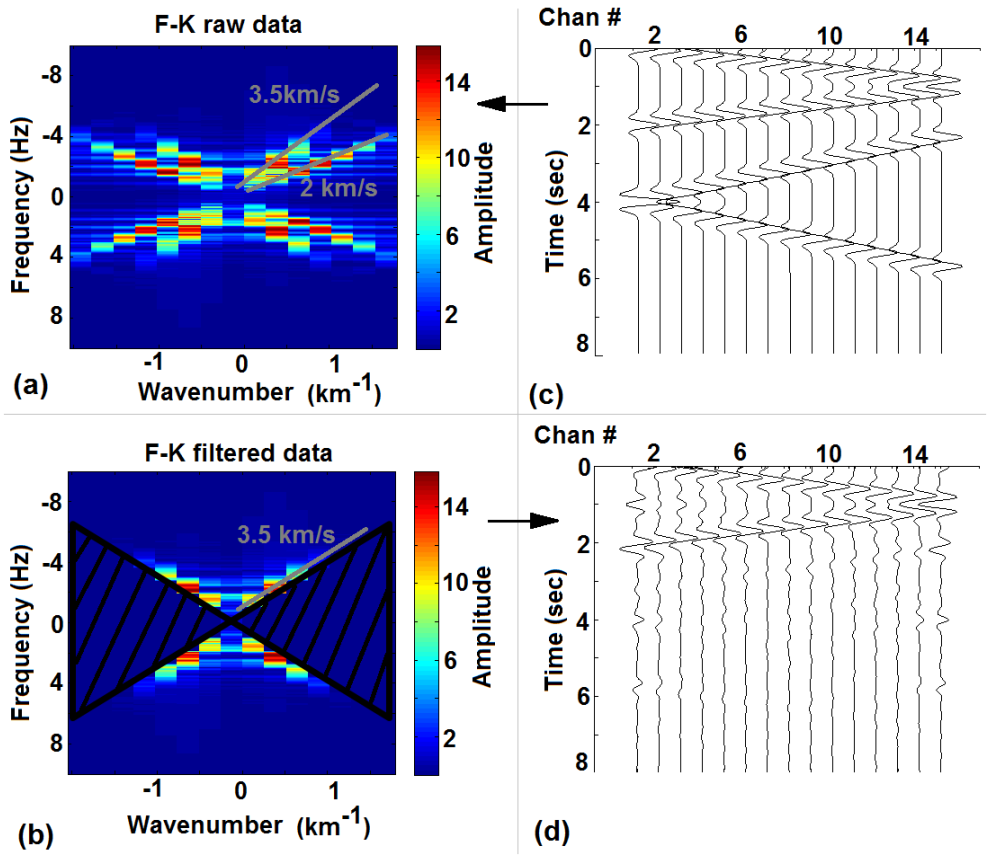

Figure 4.47: f-k filter designed to remove energy propagating at velocities less than 3.5 km/s. Synthetic shot gather (top) and f-k filtered synthetics (bottom)

Figure 4.48(a) is virtual sources gather without f-k filter and 4.48(b) is virtual source gather generated with the f-k filtered data. There is no significant difference in the two, thus we are going to compare them in separate frequency bands.

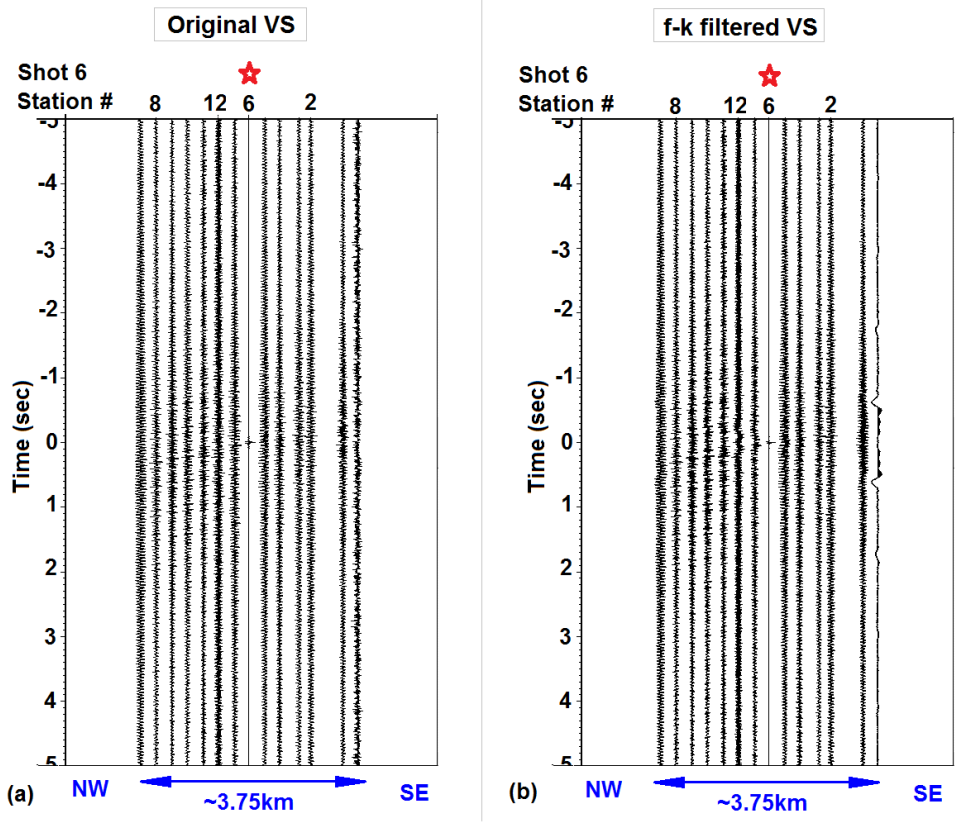

Figure 4.48: (a) Original virtual source, and (b) virtual source created after f-k filter in Figure 4.47 was applied

Figures 4.49 and 4.50 are Figure 4.48 filtered with two pass-bands: high frequency (**7 – 14**Hz) and low frequency (**0.2 – 1**Hz). The higher frequency (above 7Hz) are not affected by the filter (outside of the shaded region in the f-k space in Figure 4.47(b)). However, the low frequency virtual shot gather is dominated by what appears to be zero lag arrival, which bifurcates at further offsets. We interpret it to be an artifact generated by the f-k filter. The arrivals responsible for this artifact are highlighted in Figure 4.51 below 2 seconds. These arrivals are amplified during cross-correlation and stacking. Since the f-k filter did not appear to produce any enhancement of body wave energy at the lower frequencies, we suggest that this is further evidence that body wave energy simply did

not exist in the ambient energy at these low frequencies.

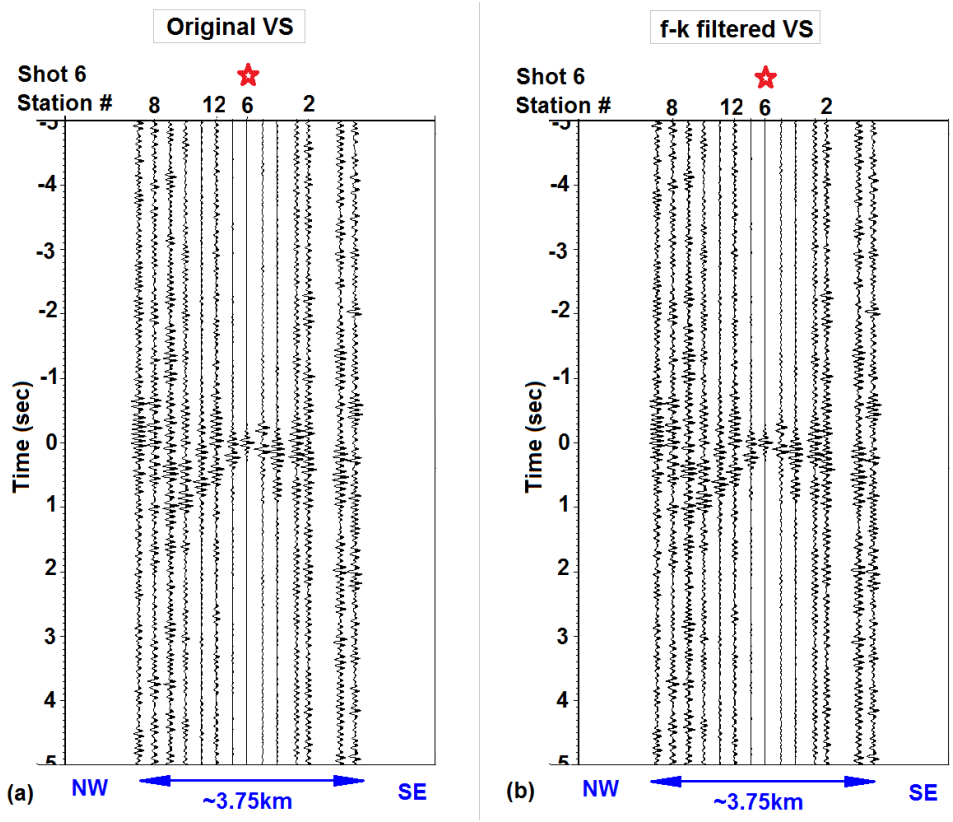

Figure 4.49: (a) Original virtual source, and (b) virtual source created after f-k filter is applied (Figure 4.47), filter post-stack at *6*/**7 – 14** */17*Hz

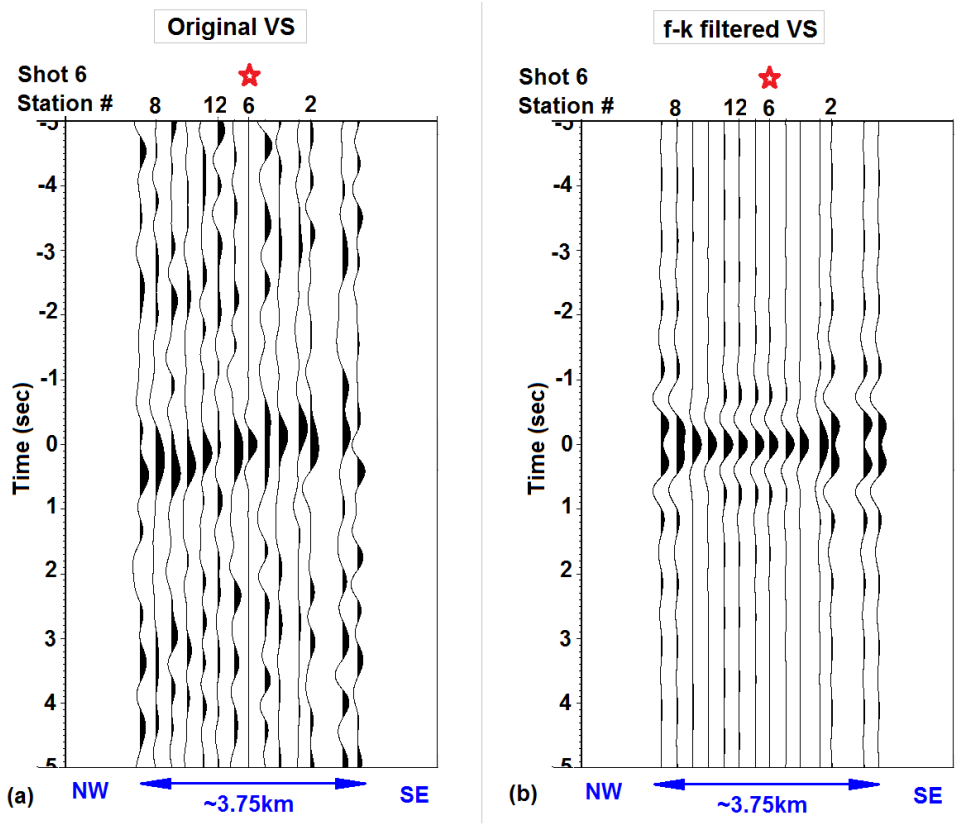

Figure 4.50: (a)(a) Original virtual source, and (b) virtual source created after f-k filter is applied (Figure 4.47), filter post-stack at *0.1*/**0.2 – 1** /2Hz

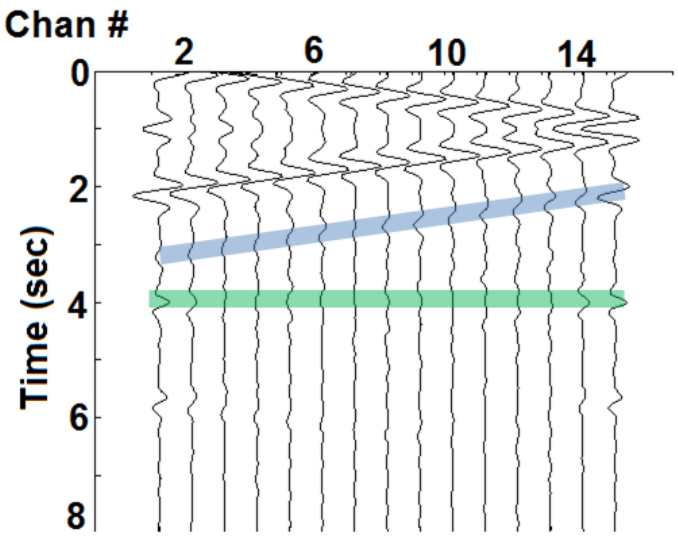

Figure 4.51: Artifacts from the f-k filtered synthetics in Figure 4.47(d) highlighed in blue and green

4.14 3D interferometry

Up to this point we have been looking at VSG created for 2D lines. Informed by these results, we processed the entire 3D array without only gain balancing and normalization was applied to the data prior to cross-correlation.

The total of 226 receivers were used to create 3D virtual source gathers, which can be viewed in a 3D cube or in a 2D line sorted by the offset from the virtual source station. Generating 3D cubes provided help in determining the directivity of ambient energy, while the 2D views helped let us assess how far from the virtual source the virtual arrival appears to propagate.

Figure 4.52 is a virtual source gather created for the sparse array sorted by the offset, where one station was cross-correlated with all the rest in the 3D

array and then summed over the entire duration of the experiment (geometry is shown in Figure 4.52(c)). As with the to 2D results, all of the extracted signal appears to be contained in the two frequency bands: low (*0.01*/**0.02 – 0.6**/*1.0*Hz, Figure 4.52(a)) and high (*6*/**7 – 14**/*17*Hz, Figure 4.52(b)).

Figure 4.52(a) makes clear that low frequency signal tends to be coherent over the entire array, whereas the high frequency signal (Figure 4.52(b)) attenuates rapidly with distance from the virtual source and are not identifiable beyond approximately 2km offset. This again supports the interpretation that the high frequency sources are located within the array and are not as strong as the low frequency energy.

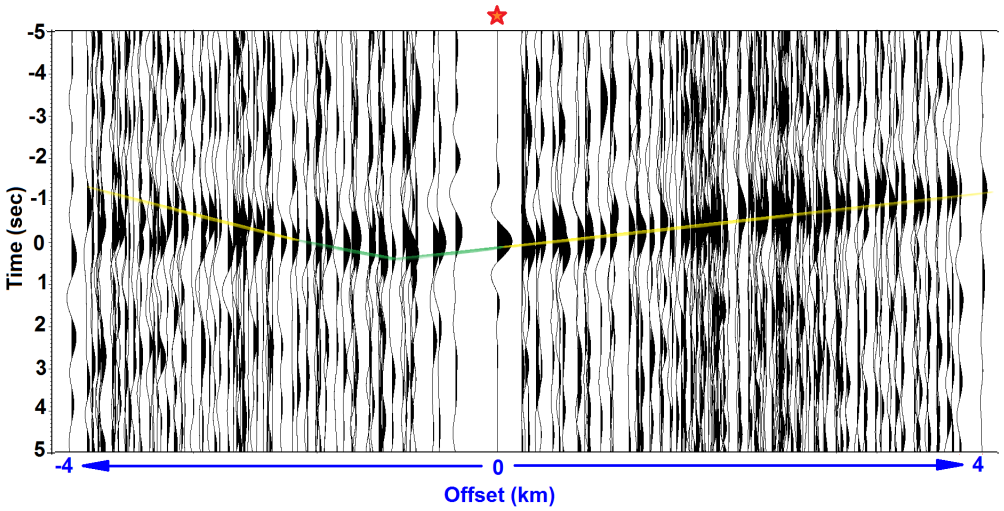

(a) Filtered at *0.01*/**0.02 – 0.6**/*1.0*Hz

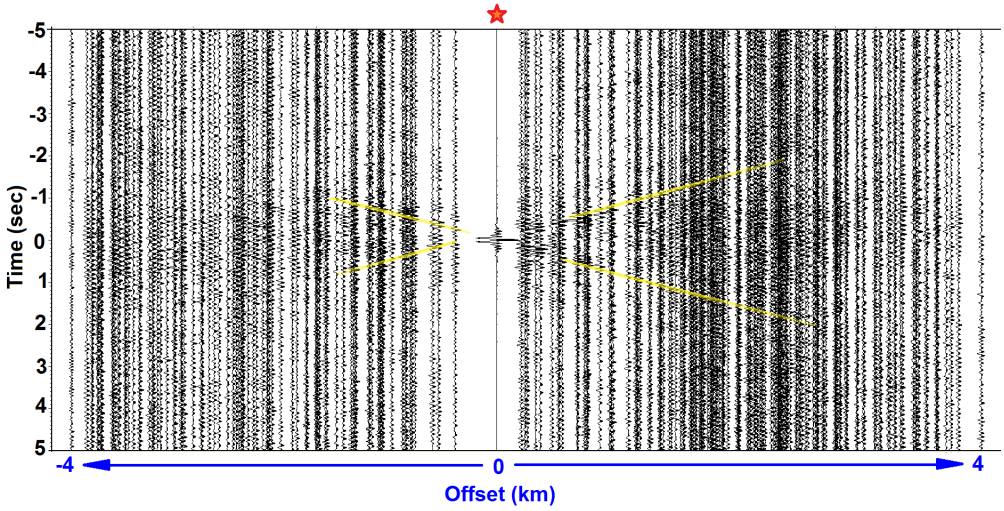

(b) Filtered at *6*/**7 – 14**/*17*Hz

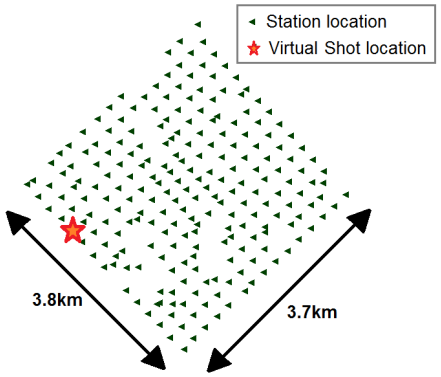

(c) Geometry of the stations

Figure 4.52: An example of a single virtual source gather shot for all stations ordered by the shot-stations offset

The virtual arrival in Figure 4.52(a) is almost entirely in the negative lag (yellow line, as opposed to green line for the positive lag). This is consistent with our previous conclusion that the low frequency source is located east - south-east of the array.

Figure 4.52(b) shows coherent virtual arrivals in both directions and both lags (yellow line) in high frequency band. This is also consistent with our previous conclusion that high-frequency sources are homogeneously distributed due to the symmetry of the arrivals in positive and negative lags (Snieder and Wapenaar, 2010).

Figure 4.53 shows 3D time slices of the virtual source gather used in Figure 4.52 at **0.02 – 0.6**Hz. The time slices for each panel are moving from negative lags down to the positive lag from (a) to (d). As the time slice moves down, the high positive amplitudes (red) appear to shift from East/South-East to West/North-West confining the source location E/SE of the array.

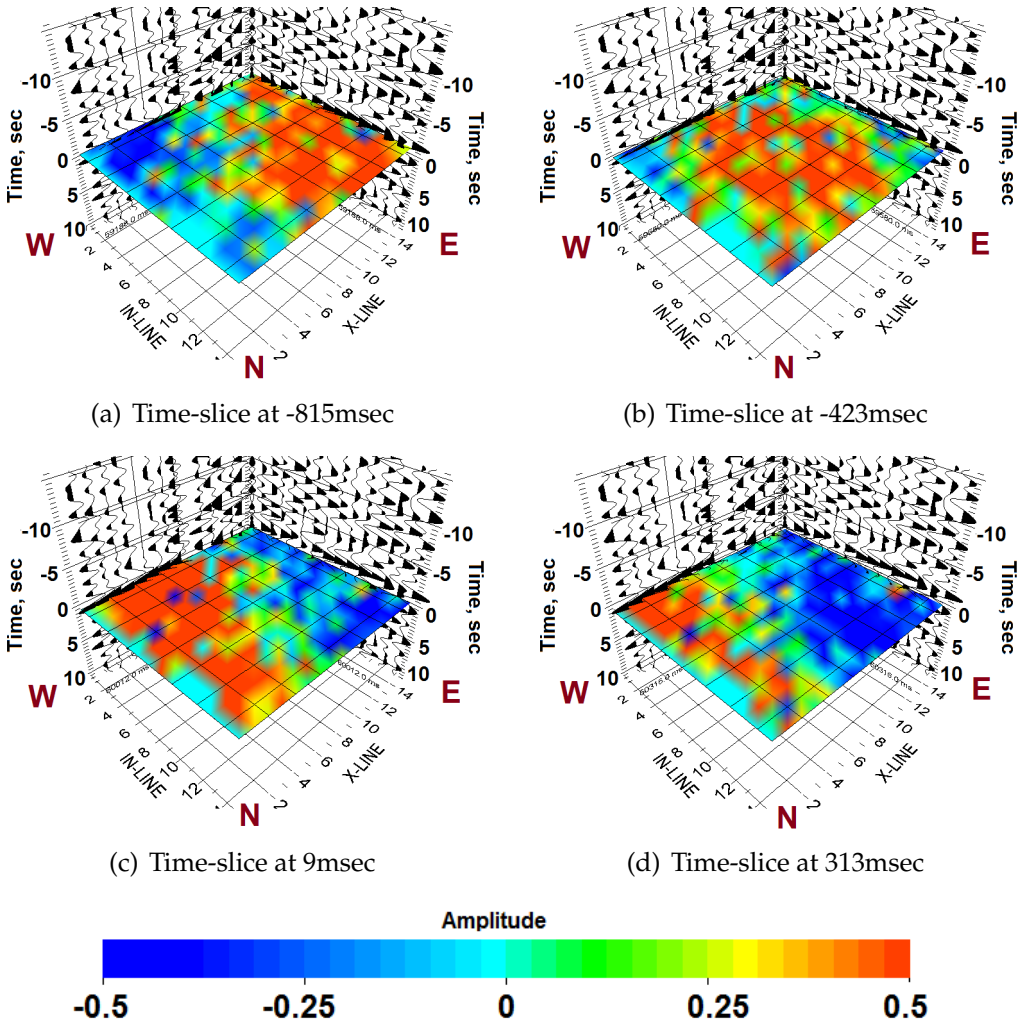

(a) Time-slice at -815msec

(b) Time-slice at -423msec

(c) Time-slice at 9msec

(d) Time-slice at 313msec

Figure 4.53: 3D shot gather with propagating time slice (star denotes the location of virtual source: In-line 1, X-line 5) filtered at *0.01*/**0.02 – 0.6**/*1.0*Hz

Figure 4.54 shows the high frequency (**7 – 14**Hz) time slices. The time slices at this frequency band look dramatically different from the low frequency band. High frequency virtual arrivals are not as coherent as in the low-frequency band, and cannot be clearly identified as propagating though the time slice.

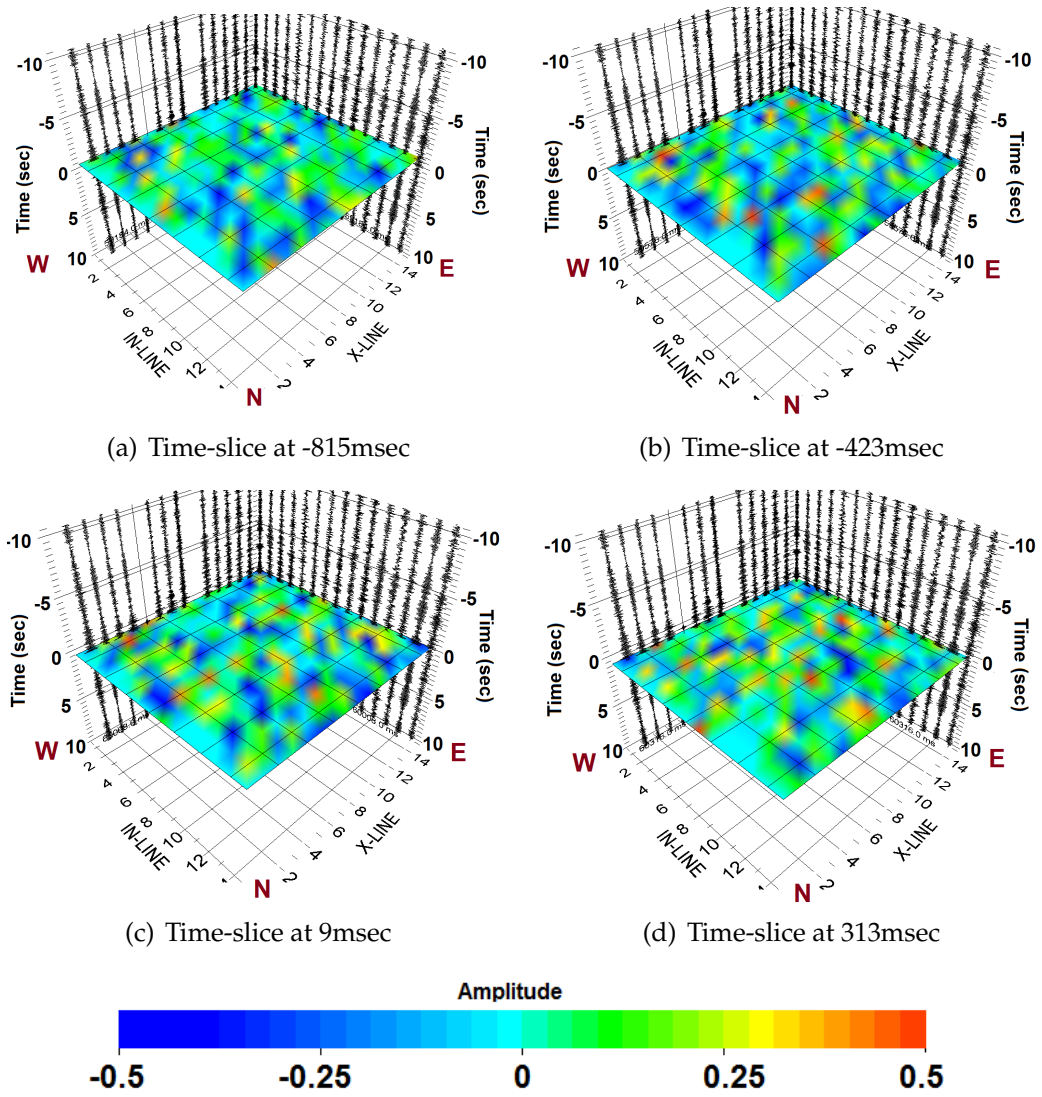

(a) Time-slice at -815msec

(b) Time-slice at -423msec

(c) Time-slice at 9msec

(d) Time-slice at 313msec

Figure 4.54: 3D shot gather with propagating time slice (star denotes the location of virtual source: In-line 1, X-line 5) filtered at *6*/**7** – **14**/*17*Hz

In summary, 3D analysis of virtual sources confirms a clear distinction between high and low frequency arrivals, which agrees with our earlier interpretation from the 2D analysis of different sources for these frequency bands.

4.15 3D Synthetic Seismic

A simple 3D seismic synthetic was created to examine the affect of heterogeneous source distribution on a virtual shot gather . Only one impulsive source is used in these synthetics, whose response was computed for all the stations and then cross-correlated to produce a synthetic virtual source gather. Here, all synthetics were produced assuming a fixed velocity of 2.5km/s to calculate arrival times ($t = d/v$) of the signal from a source to all the stations. These arrival times were then convolved with a Ricker wavelet of 0.6Hz dominant frequency to create the synthetic record. A recording from single station can then be cross-correlated with the remaining stations within this record to generate a virtual source gather.

Figure 4.55 is a synthetic record with the source located within the array (station marked by a star). This arrival radiating from the synthetic source should match any virtual arrival derived from cross-correlation and summation over homogeneously distributed sources (Claerbout, 1964) for the equivalent virtual source location. However, the virtual arrival from the real data (Figure 4.53) does not exhibit the same amplitude pattern in the time slices as the synthetic surface shot. Therefore, we generated a record with a source offset from the synthetic 3D array (red dot in Figure 4.56).

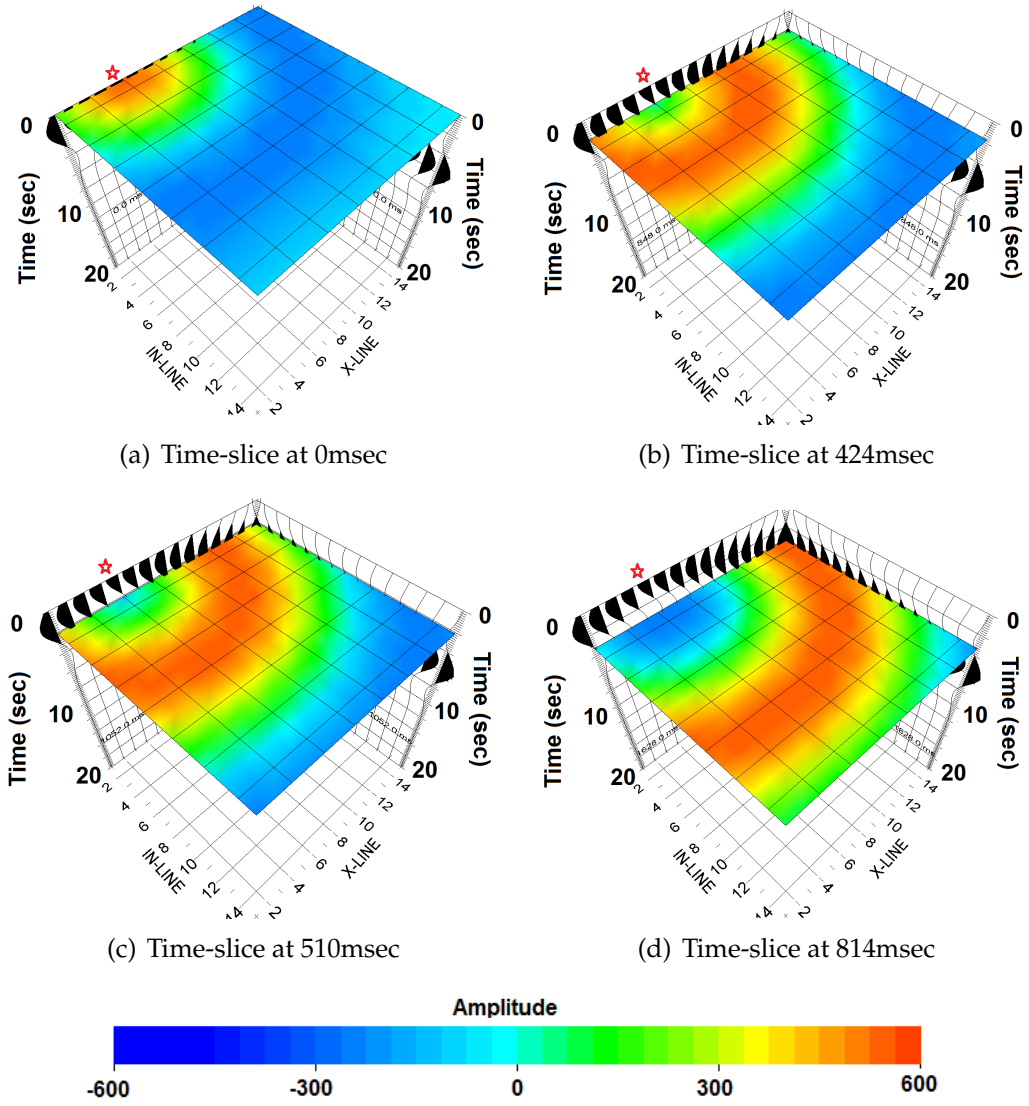

(a) Time-slice at 0msec

(b) Time-slice at 424msec

(c) Time-slice at 510msec

(d) Time-slice at 814msec

Figure 4.55: 3D syntehtic shot gather with propagating time slice (star denotes the location of virtual source: In-line 1, X-line 5)

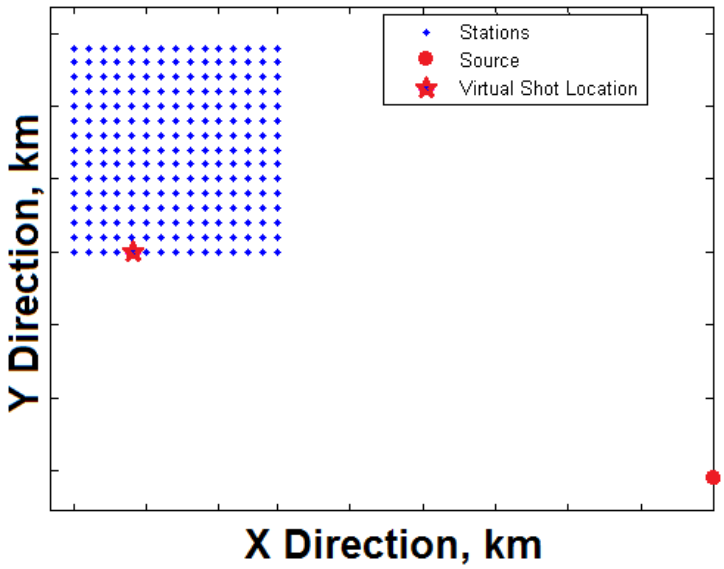

Figure 4.56: Station, source and virtual source geometry for synthetic seismic survey

Figure 4.57(a) is the synthetic surface record of s synthetic source located at some offset from the 3D array (red dot in Figure 4.56) displayed for a line of stations within the array (highlighted in green, Figure 4.57(a)). Figure 4.57(b) is a virtual source gather created from this record by cross-correlating a trace (marked with a red star) with the remaining traces. Note, that for this source-receiver geometry most of the signal is recovered in the negative lag (Figure 4.57(b), gray),), as was the case with the Bradford virtual records (Figure 4.5).

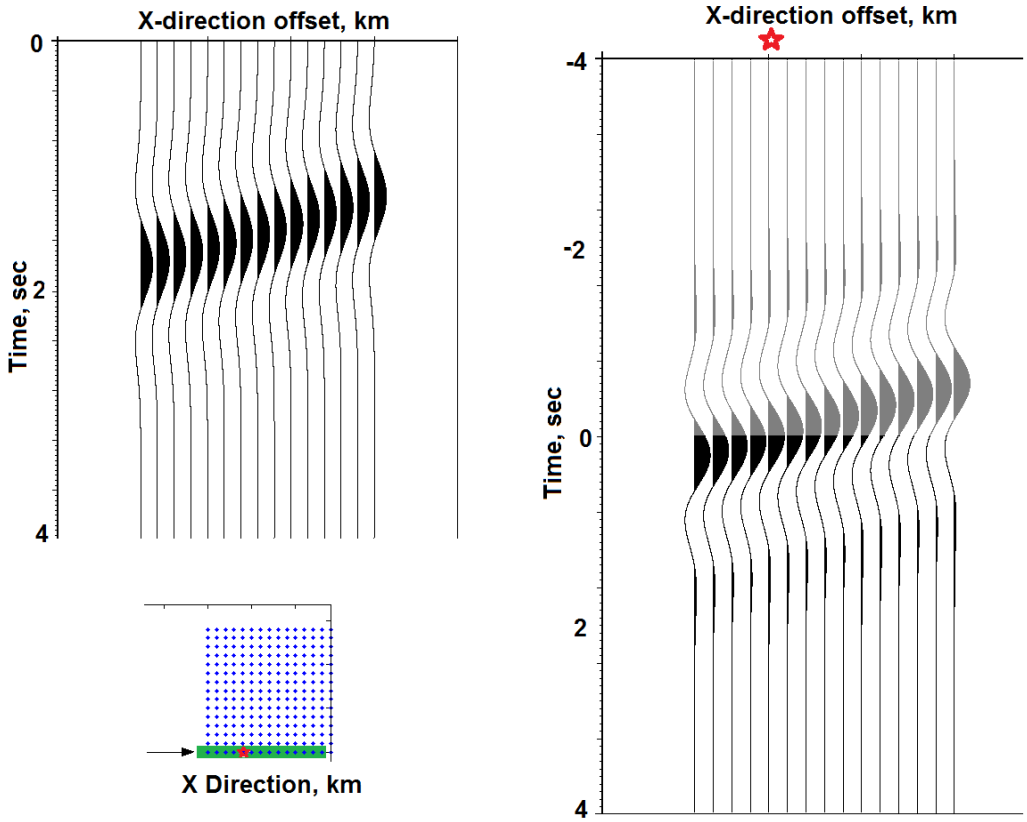

(a) First arrival from the synthetic seismic source, and the geometry from Figure 4.56

(b) Cross-correlation of the first arrival

Figure 4.57: Synthetic first arrival for a single line of receivers and same profile symmetrically cross-correlated (star denotes the virtual source trace, colored in gray represents the negative lag)

Figure 4.58 shows the 3D time slices through the synthetic virtual source gathers corresponding to the line result shown in Figure 4.57(b). The time slices show energy moving down from negative (a) to positive lags (d). The virtual arrival is moving from east to west in both synthetic and the real VSG (Figure 4.59) and does not appear to radiate from the virtual source station like in Figure 4.55. These patterns are similar to those seen for the Bradford virtual data (Figure 4.53), thus supporting our inference that there is a strong bias in the direction to the source of ambient energy recovered as virtual surface waves.

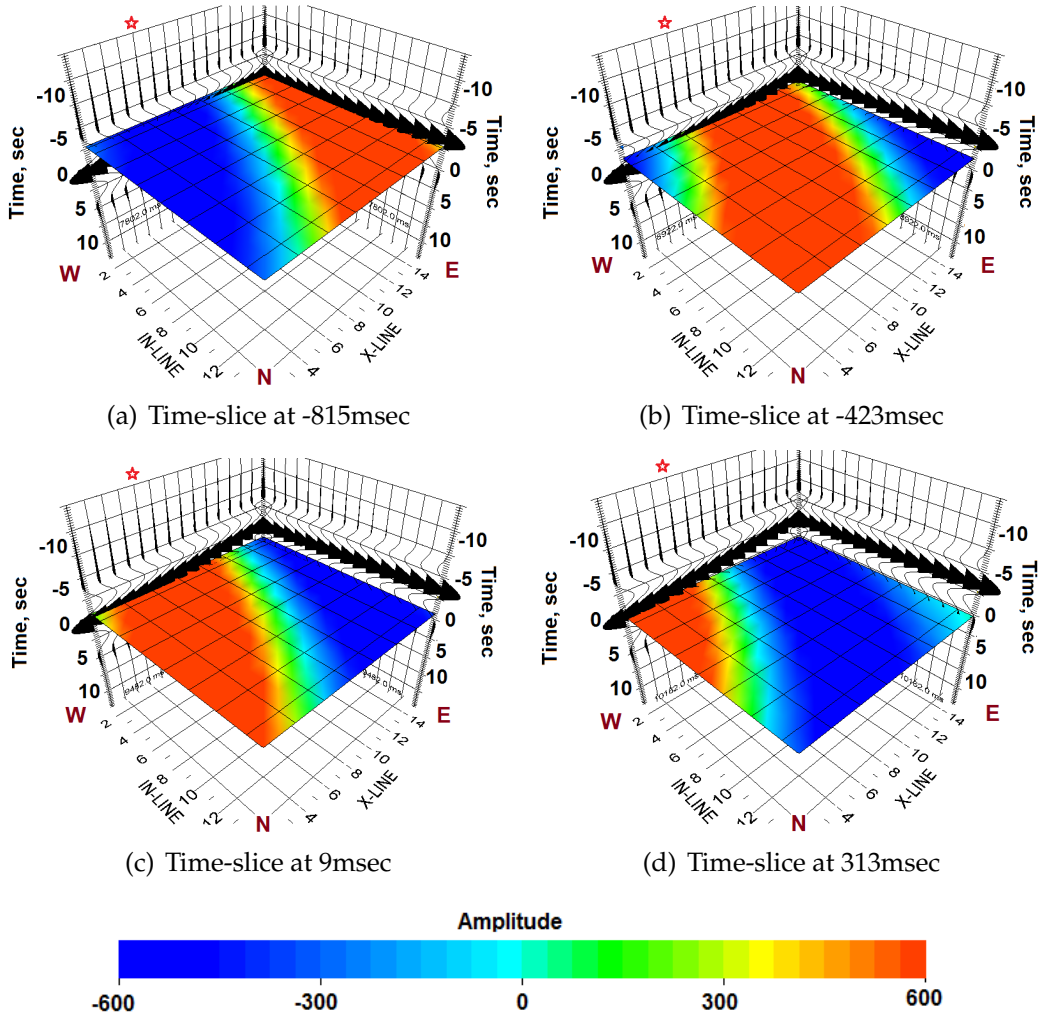

(a) Time-slice at -815msec

(b) Time-slice at -423msec

(c) Time-slice at 9msec

(d) Time-slice at 313msec

Figure 4.58: 3D synthetic shot gather with propagating time slice (star denotes the location of virtual source: In-line 1, X-line 5)

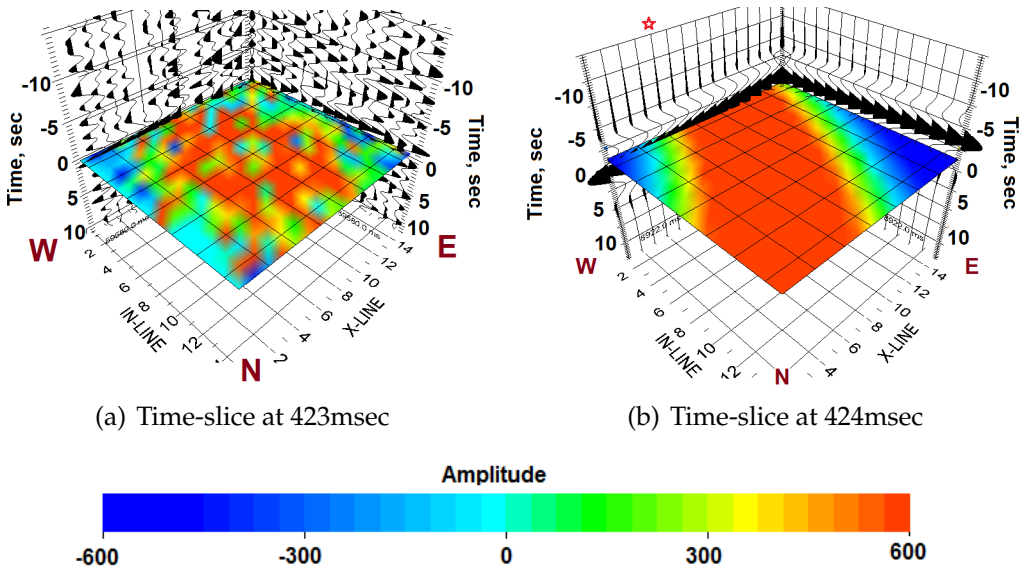

(a) Time-slice at 423msec

(b) Time-slice at 424msec

Figure 4.59: Comparison of synthetic real (a) and synthetic (b) seismic with a time slice at 423 msec (star denotes the location of virtual source: In-line 1, X-line 5) for both cubes

Our synthetics support our conclusion that the low frequency source of ambient energy available for recovery of virtual surface waves is located at a distance from the array and primarily in the E/SE direction (Figure 4.59). Most of the low frequency seismic energy is coming from the direction of the Atlantic coast and therefore azimuthally biased, resulting in "asymmetric" virtual arrivals relative to the virtual source. Only virtual source gathers azimuthally aligned along this azimuth (black line in Figure 4.60) will produce estimates of the true velocity of the subsurface.

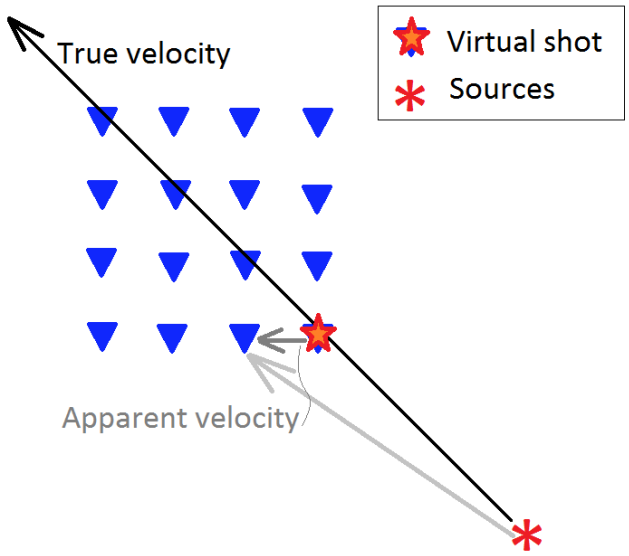

Figure 4.60: 3D true velocity vs apparent velocity

According to Figure 4.60, the location of the sources of the ambient noise will affect the move-out of the virtual arrival across the 3D array. Figure 4.61 illustrates virtual sources computed from the synthetic sources located at different offsets from the array. Note that for the sources further away from the array, the energy arrives approximately as a plane wave (a,c). For closer sources, the spherical radiation pattern can be distinguished. A subsequent sum of virtual sources in Figures 4.61(a-c) (Figure 4.61(d)) illustrated how VSG can provide a very biased estimate of propagation velocity.

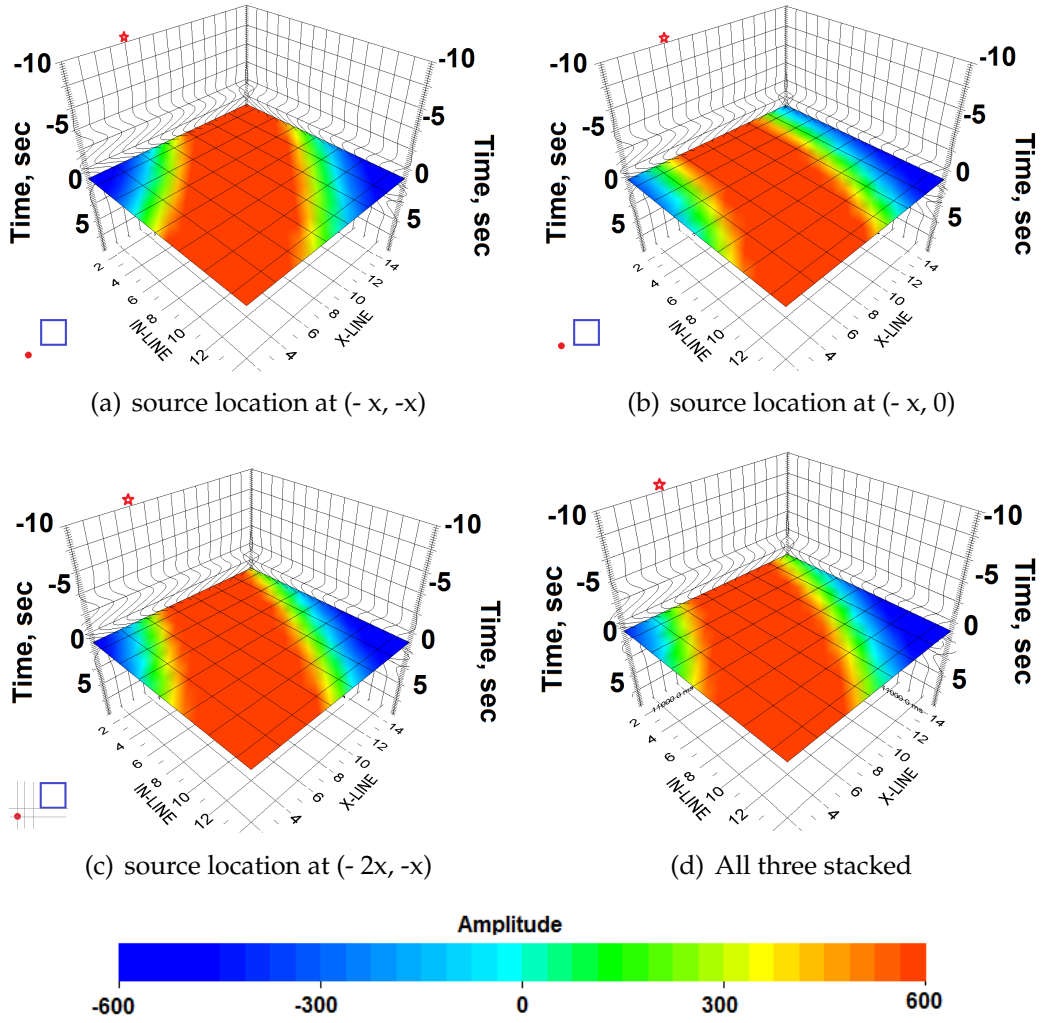

(a) source location at (- x, -x)

(b) source location at (- x, 0)

(c) source location at (- 2x, -x)

(d) All three stacked

Figure 4.61: Dependence of synthetic seismic on the location of the source of ambient seismic energy at a 0.25Hz dominant frequency

Frequency variations among ambient sources can also distort a subsequent virtual shot gather based on summation over these sources. Figure 4.62 illustrates the effect of stacking virtual source gathers derived from different frequency sources in different positions. The last panel (4.62(d)) is a stack of all three virtual sources in Figures 4.62(a-c).

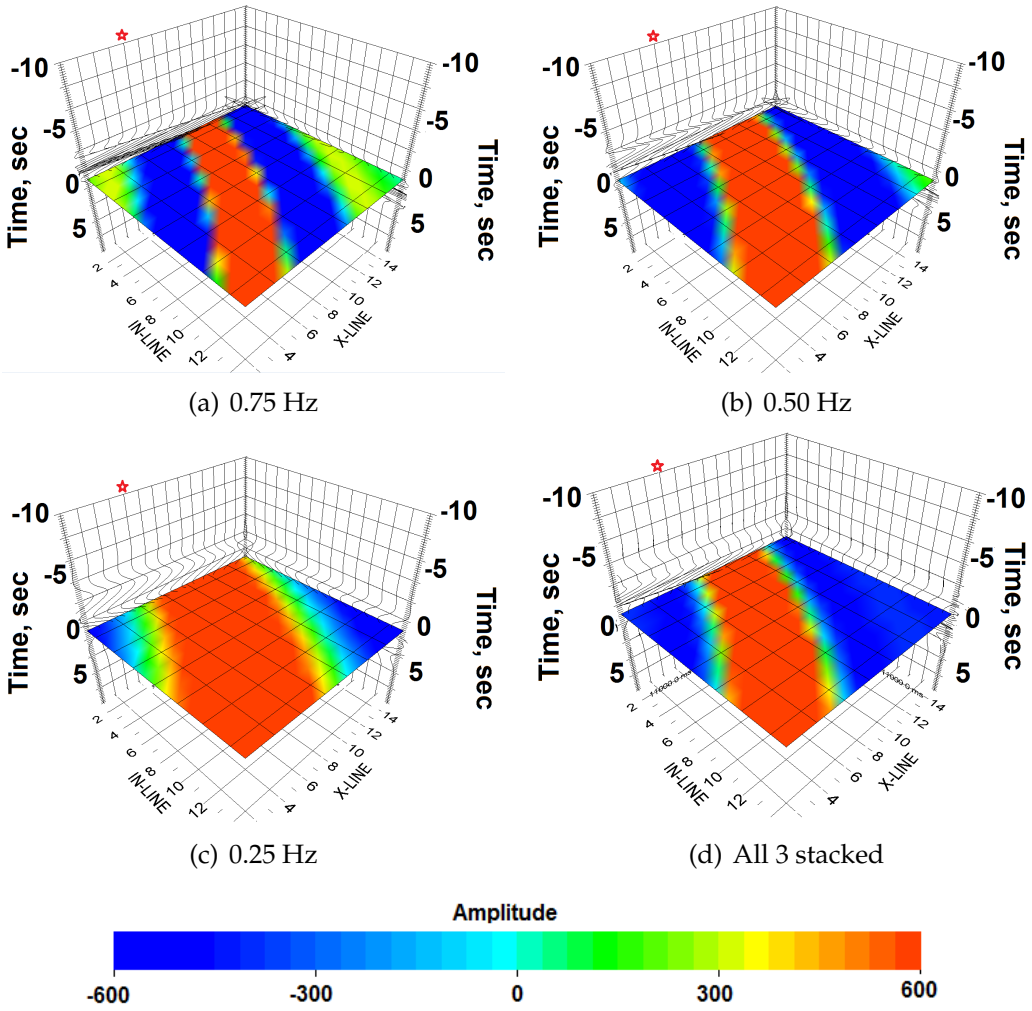

(a) 0.75 Hz (b) 0.50 Hz

(c) 0.25 Hz (d) All 3 stacked

Figure 4.62: Dependence of synthetic seismic on the center frequency of the Ricker wavelet at time lag of 423 msec for a source at (-2x, x)

4.16 Dense 3D array results

We generated the virtual source gathers for the 3D dense array (Figure 4.63) following the same procedure as for 3D sparse array. Figures 4.64(a-c) are virtual source gathers derived by displaying the entire 3D dense array sorted by the offset from the virtual source station, and successively filtered at same pass

bands as the sparse array: low (**0.02 – 0.6**Hz), intermediate (**1.0 – 4.0**Hz) and high (**6.5 – 14.0**Hz) frequency bands. We do not show the analysis of individual receiver lines for the dense array because of the small number of stations within each line, which makes visual identification of virtual arrivals difficult.

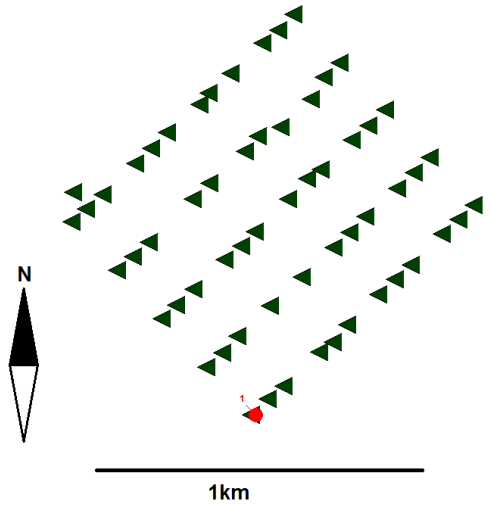

Figure 4.63: 3D geometry of the Virtual Source (red circle) within dense (220ft spacing) array

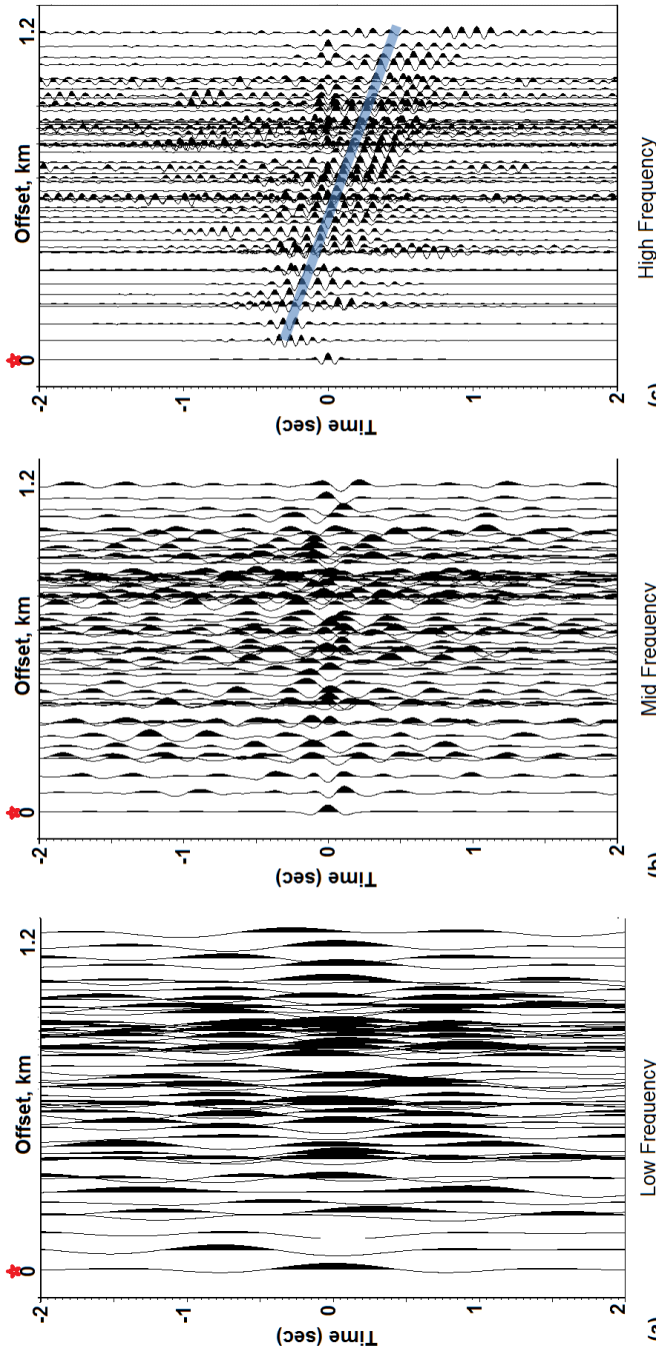

Figure 4.64: Dense array VSG filtered at frequencies: (a) low (*0.01*/**0.02 – 0.6**/*1.0*Hz), (b) intermediate (*0.6*/**1.0 – 4.0**/*7.0*Hz) and (c) high (*5.5*/**6.5 – 14.0**/*17.0*Hz); red star denotes the virtual source station, blue line corresponds to velocity of 1.6km/s

Figure 4.64(a-b) does not retrieve any coherent virtual arrivals. The absence of mid-frequency arrivals 4.64(b) is consistent with our interpretation from the sparse array that sources at these frequencies are simply lacking in the environment. However, the low frequency coherent signal that was present in the sparse array VSG is missing in the dense array results. Therefore, we attribute the missing low band virtual arrival in the dense array to aliasing due to smaller station spacing (see 4.9).

Figure 4.64(c) shows a striking virtual arrival with a corresponding velocity of the 1.6km/s. Note that similar velocities were retrieved by the sparse array and were identified as the virtual surface waves. The directivity of this arrival (i.e. mostly in the positive lag) indicates that the sources of this high frequency energy are not distributed homogeneously around the dense array. We infer a location for this source that is west of the dense array, but still within the sparse array, because. These sources cannot be far from the densely spaced stations due to a very strong virtual arrival at these frequencies regardless of rapid attenuation inferred from the sparse array analysis. The interpreted location of these sources would also explain why this arrival is not present in all VSG's in the sparse array, as they seem to be localized in the west portion of the sparse array.

The high frequency virtual arrival (Figure 4.64(c)) is very strong and appears to have dispersive characteristic. However, a more careful analysis of this virtual energy reveals that virtual arrivals are not coherent within the entire array and no dispersion is present (Figure 4.65). First, note the red lines that correspond to 1.6 km/s propagation velocity. It appears that the side-lobes of this virtual arrival constitute parallel arrival picks and do not all originate from the

virtual shot location, as would be expected in case of the dispersion. Next, the coherent arrival at zero lag highlighted in blue would correspond to a infinite velocity and is also present in Figure 4.64(b). We interpret this arrival to be non-physical. Finally, the green rectangle shows the low coherency stations. This low coherency of the virtual arrival at these stations complicates the velocity picking and therefore we cannot be confident in the dispersive nature of this arrival.

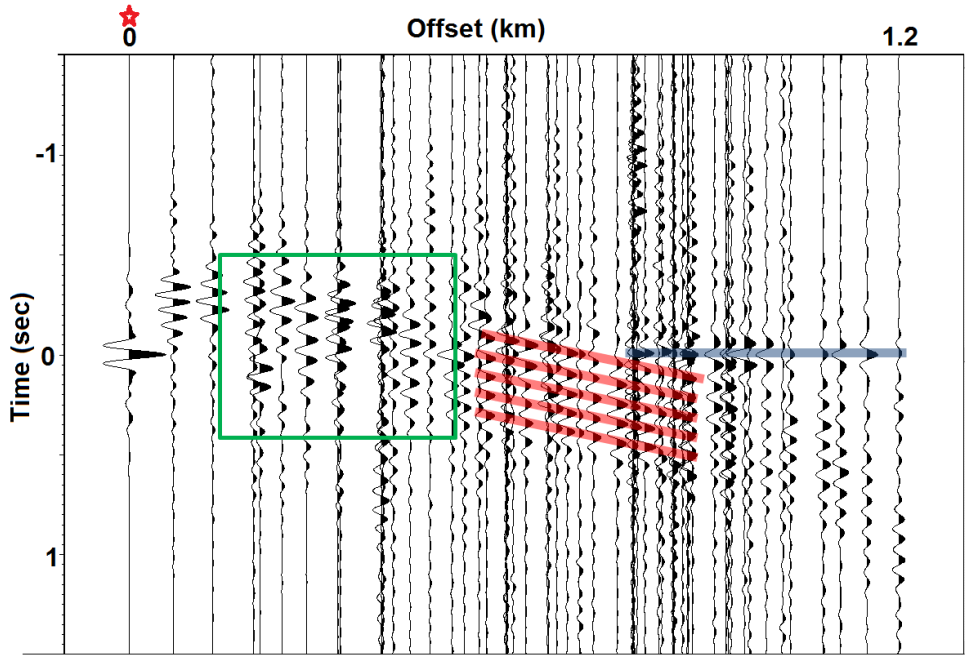

Figure 4.65: VSG from Figure 4.64(c). The red lines represent velocity of 1.6km/s, blue line marks vertical arrivals, and green rectangle highlights an area of low coherency of the virtual signal

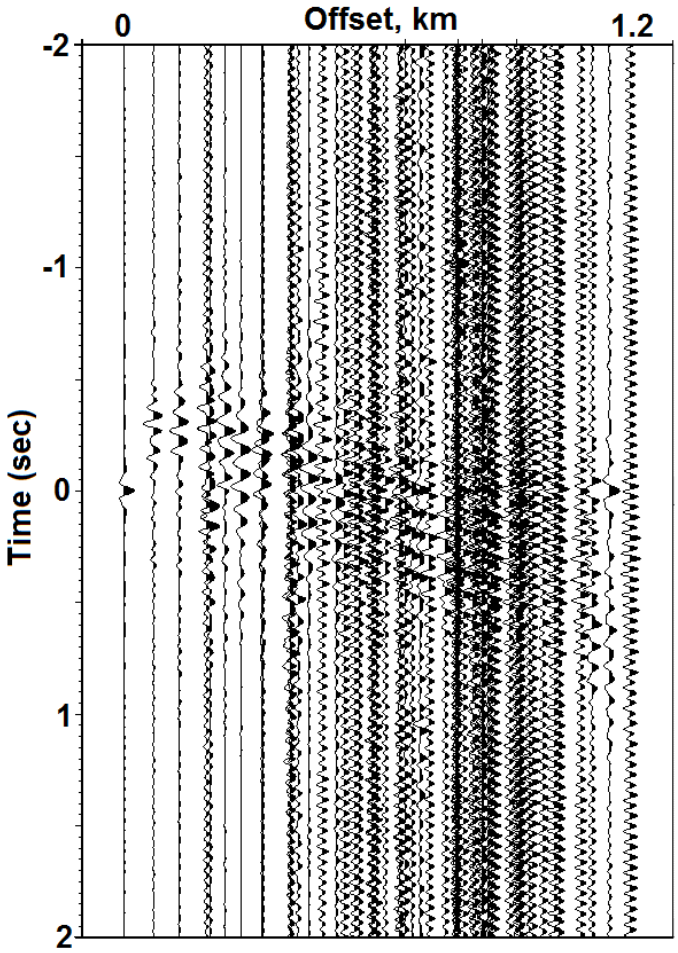

Figure 4.66: VSG from Figure 4.64 filtered at *5.5*/**6.5 – 20.0**/*28.0*Hz)

In Figures 4.66 we have expanded the range of higher frequencies ($> 17.5Hz$) included in the pass band. However, as was the case with the sparse array, the inclusion of higher frequencies has introduced interference from monotonic sources.

Overall, the dense array results are consistent with the sparse array.

4.17 Conclusions

Our analysis of 6.5 days of ambient noise recording by sparse (880ft=265m) and dense (220ft=67m) vertical component seismic arrays in Bradford, PA, has demonstrated that both virtual surface waves and (weak) body waves could be recovered in spite of the relatively short recording period.

However, the virtual surface waves were only observed in the two frequency bands: low (**0.6 – 1.0**Hz) and high (**6.5 – 14.0**Hz). We interpreted this discretization of the signal in frequencies to two separate band-limited sources of seismic energy: Atlantic ocean for the low and anthropogenic for the high frequencies. The low frequency virtual arrivals exhibit slightly faster move-outs than the high frequency arrivals (2.8km/s vs. 1.7km/s). Two distinct sources of ambient surface wave energy is also indicated by analysis of the directivity of virtual surface arrivals across the 3D array.

High frequency virtual arrivals appear to attenuate rapidly and be less coherent from one virtual source gather to another when compared to the low frequency arrivals. However, the amplitude variation analysis showed that high frequency signal is less variable with time, whereas the low frequency arrivals are too weak to be detected during the first two days of station deployment.

Even though the measured velocities of the virtual surface waves from low to high frequency bands are consistent with the general increase of velocity with depth, dispersion analysis of these arrivals was problematic due to missing intermediate frequency signal. However, our synthetics suggests that the surface waves at these frequencies (< 10Hz) are not sensitive to small variation within the sedimentary cover. Instead, the basin and basement can be approximated

by a two layer case with lower sedimentary velocities overlying higher granitic velocities. The virtual surface wave inversion provided the correct velocity expected for the granitic basement, which could not be achieved with the previous active source surface wave analysis. However, due to the absence of virtual signal at the intermediate frequency band, our inversion could not confirm the 5.5-6km basement depth.

Possible body waves recovered by interferometry are interpreted as a direct P wave and a refracted P wave from a dipping subsurface interface. Attempts to enhance P wave energy at the expense of the stronger virtual surface wave energy by various filtering schemes proved in effective, suggesting that the environment contained insufficiently large body wave sources to be recoverable over the relatively short period of ambient noise recording used here

Monotonic noise was ubquitious at higher frequencies, compromising attempts at interferometric body wave recovery. Application of a novel "frequency clipping" filter proved to have limited, but promising, effect.

In summary, althought coherent virtual surface waves and body waves are recoverable with arrays typically use for conventional seismic surveys, the utility of the resulting data can be highlyl biased by spatial and temporal variations in the ambient energy sources that contribute to the virtual signals. The recording period should be long enough average over, or at least better characterize, this source variability in order to obtain more robust and useful results

4.18 Acknowledgment

I thank Lee Bell, Christof Stork and Dace Yacco from Geokinetics for graciously providing Bradford, PE survey recording for our ambient noise interferometry study.

Also, thanks to Robert Herrmann for his software and guidance in surface wave modeling, which is a included in 4th chapter of this dissertation.

CHAPTER 5

3D BASEMENT STRUCTURE IN SOUTHEASTERN NEW MEXICO FROM NORMALLY DISCARDED PORTIONS OF CONTINUOUSLY RECORDED OIL EXPLORATION SURVEYS

5.1 Abstract

Due to advances in recording capabilities, seismic data for land oil-industry surveys is now often recorded continuously. A large portion of these data is usually discarded since it is not directly used for conventional imaging purposes. However, there is a growing consensus that these "surplus" recordings contain a variety of useful information about the subsurface, especially for academic seismologists but also for oil explorers. This paper presents an example of extraction of 3D information about the deep crust from such recordings. In this case the deep information was retrieved from a post-harvest but pre-correlation dataset by means of extended correlation. Although signal penetration in this particular area is limited by an extremely thick ($> 20,000$ ft) overlying sedimentary cover, the exercise demonstrates the tremendous potential of systematically mining the rapidly expanding database of continuously recorded oil exploration data, and the clear need to preserve rather than discard the unconventional portions of those records.

Cabolova, A. and L. Brown (2015, October 22). 3D reflection imaging of the deep basement in southeastern New Mexico from normally discarded portions of a vibrosesis oil exploration survey, Extended Abstracts Publication.

5.2 Introduction

The oil and gas industry performs on average 200-300 3D seismic surveys per year (McFarland, 2009). Although their interest is limited to the part of the record that probes sedimentary rocks that lie above crystalline basement, they often record information about greater depths, but these are normally discarded (e.g. Okaya, 1986). Shared with academia, these data can be used to study deeper geology, such as inter-basement reflections and even the base of the crust, without undermining the confidentiality of the shallow part of the data. The expanded use of continuous, "nodal" recording in modern industry surveys (Lin et al., 2013b) has greatly increased the likelihood that information about the deeper crust has been routinely collected in 3D. This paper is a case study of a recently acquired industry dataset collected with continuous nodal instrumentation with which we attempt to extract 3D imagery of the crystalline basement from a portion of the data that would normally be discarded.

The survey examined here is a large N (number of recording channels), vibroseis dataset acquired in southeast New Mexico in 2014 and provided to Cornell's Department of Earth and Atmospheric science by Fairfield Nodal. The dataset consists of uncorrelated records harvested for a conventional reflection survey, cut into 21 second shot gathers for conventional correlation with a 16 second, 4-76 Hz upsweep to produce a 5 second correlated shot gathers. Ideally our analysis would have been carried out on data harvested specifically to allow full correlation to the crustal depths of interest, this shorter conventional harvest was more quickly available at this point, and serves to illustrate that even these conventional harvests can be productively used. The additional correlated data lengths were obtained by the technique of extended correlation (Okaya, 1986)

in which bandwidth is sacrificed for greater correlated record length.

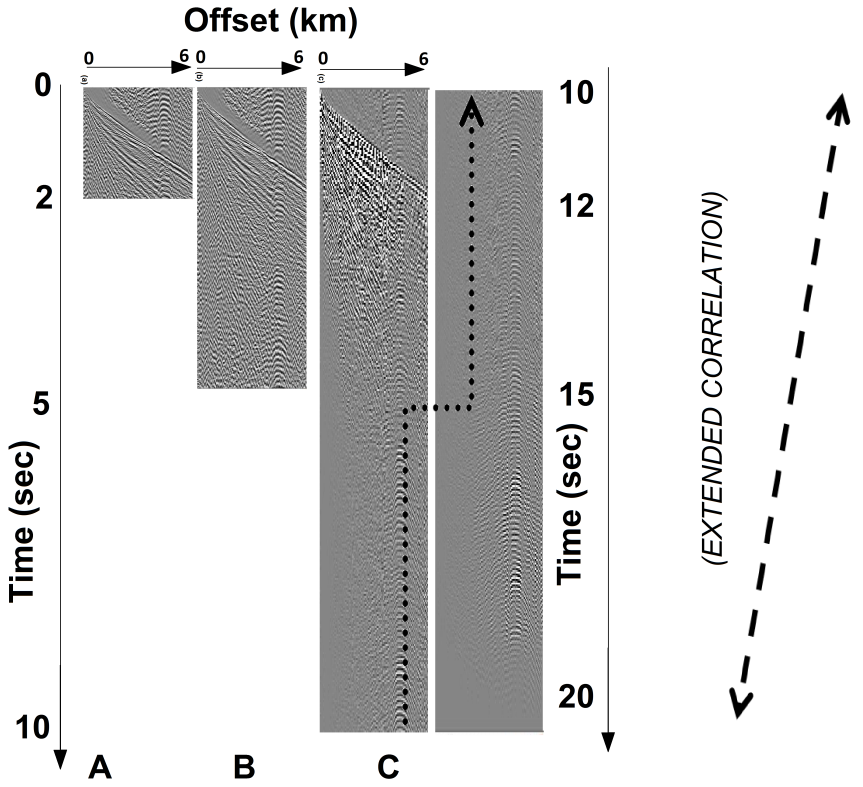

Figure 5.1: (a) Correlated shot gather truncated to time length corresponding to reflections above the basement in this area, (b) conventional, full correlation that is the default for this survey, (c) "self-truncating" extended correlation to recover reflection energy from depths well below the original target depth of this survey.. Note the "wraparound" of the display to show the full 21 seconds of the extended correlation.

Figure 5.1 compares various lengths of data that could be recovered from this dataset: (a) a data length that would focus on the sedimentary rocks that are of exploration interest in this area, (b) the default, full-bandwidth conventional vibroseis correlation, where the time of the output = time of the recording - sweep duration, and (c) a "self-truncating" extended correlation, where bandwidth is sacrificed to obtain longer data recording. Since a vibroseis upsweep

was used for this survey, the frequencies lost with extended depth correspond to the high end of the sweep. Note that these frequencies are less likely to penetrate to greater depth anyway.

5.3 Dataset and Geology

The survey was designed to explore the Delaware basin (Keller et al., 1980), which is a part of Permian basin in South Lea County New Mexico (Figure 5.2). Shallow beds of Delaware Basin (Willis, 1929) are the deepest compared to the shallow beds of the other portions of Permian Basin (Galley, 1955) (i.e. Central basin (Cartwright, 1930) and Midland basin (Sellards, 1932)). The thickness of Paleozoic sedimentary rocks in Delaware basin can reach 7.5km (25,000ft) (Hills, 1984). The top of the Pre-Cambrian basement in Delaware basin, deepest in central Texas, is estimated to be approximately 6.0-7.0km (20,000-23,000ft) deep below the surface beneath our station array (Ward et al., 1986; Flawn et al., 1967). The base of the crust, or Moho discontinuity, is estimated to be approximately 40km (Allenby and Schnetzler, 1983).

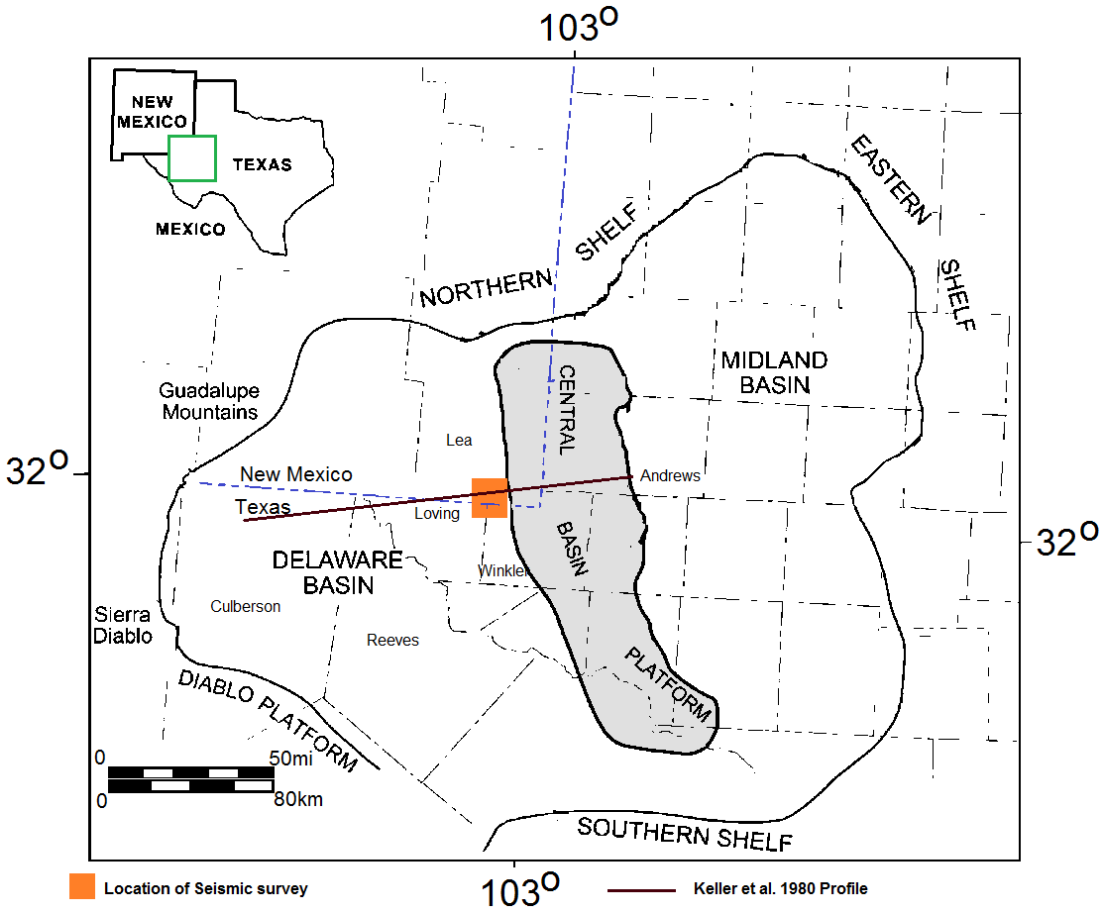

Figure 5.2: Paleogeographic map of the west Texas and southeastern New Mexico area during the middle Permian showing the location of the dataset relative to the major sedimentary basins (modified from Ruppel and Jones (2006) and Ruppel and Ward (2012)). The orange square is the location of the survey from which data were obtained for this study. The dark red line is location of the geological profile derived from borehole data Keller et al. (1980) and used here to constrain our interpretation of the seismic data

The shot and receiver geometry of the data analyzed here is shown in Figure 5.3.

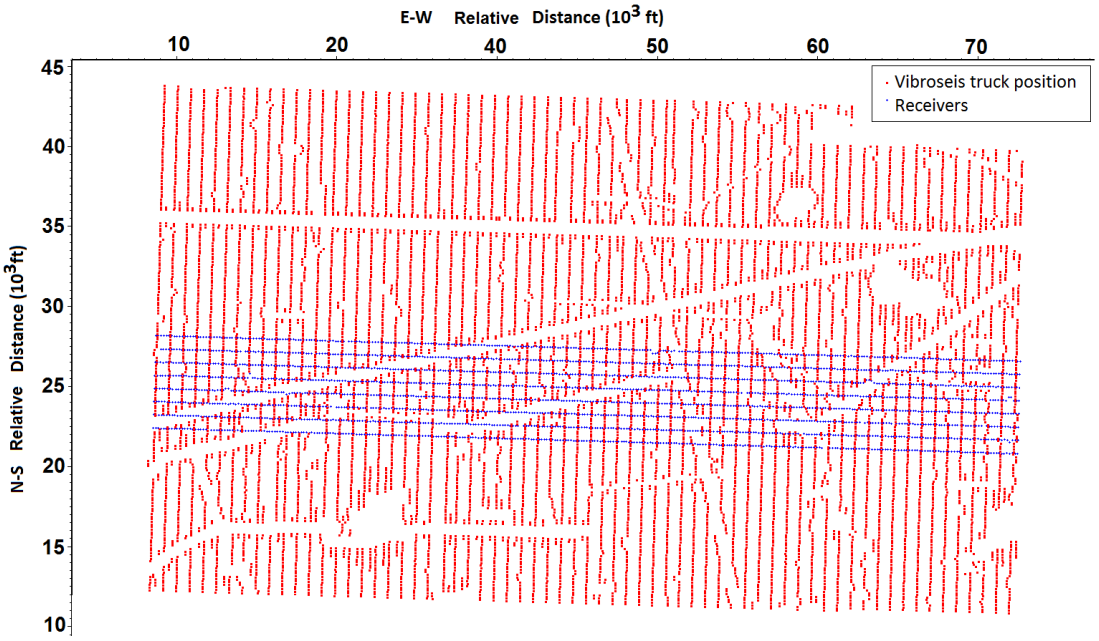

Figure 5.3: Geometry of the seismic dataset used in this study. Red squares are the source (vibroseis) positions and blue crosses are the positions of vertical component geophones

The thickness of Paleozoic Delaware basin sediments is the largest in Lea county, NM and the basement decreases in depth to the east and west of it. The sediments consist mostly of carbonates and sandstones (Galley, 1955; Ward et al., 1986). Two well measurements in the general area of our survey indicate that the depth to Precambrian basement is around 21,000 ft (6.4km) below the sea level (Keller et al., 1980, Figure 5.4). Adams and Keller (1996) predict a similar total thickness of Paleozoic Sediments with gravity measurements over a larger area, but argue that there is a granitic intrusion 5-15km thick between Cambrian sediments and granitic Precambrian basement (Bickford et al., 1986).

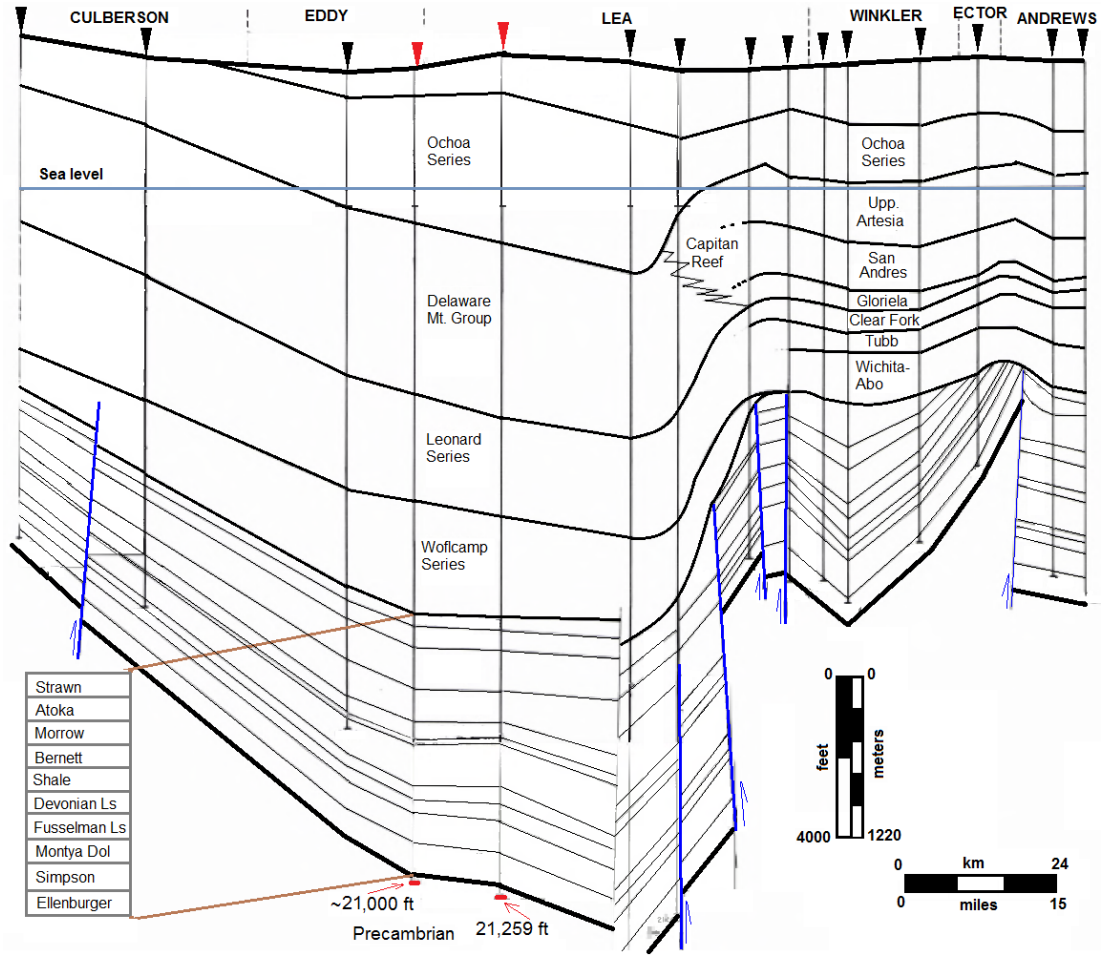

Figure 5.4: E-W geological profile of Delaware and Central Platform modified from Keller et al. (1980). Black triangles represent surface location of the wells, based on which the profile was generated, red triangles represent wells that penetrated into the Precambrian basement, blue lines are faults with the sense of upward direction noted with an arrow.

5.4 Extended Correlation

The length of the output of conventional vibroseis correlation equals the difference between the length of the uncorrelated data and the length of the sweep. Correlation with a shorter sweep results in a longer (deeper) record. Extended

correlation is a technique by which a shorter sweep, retaining sufficient bandwidth to produce an interpretable record, is applied to produce a longer recording. There are two approaches to extended correlation. In "fixed-bandwidth" correlation (e.g. Oliver et al., 1976; Oliver and Kaufman, 1977), the sweep itself is truncated to a fixed length, making the correlation result longer by sacrificing a fixed portion of the bandwidth of the original sweep. An alternative approach is "self-truncating" correlation (used here), in which the uncorrelated record is padded with zeros at the end resulting in a correlated record length equal to the original uncorrelated recorded length but one in which the bandwidth decreases linearly with increasing record time below the conventionally correlated portion ((e.g. Okaya, 1986); Figure 5.5). Here we use the self-truncating method, padding the original 21 second uncorrelated record with 16 seconds of zero amplitudes. The final result of extended correlation is a 21-second record, which preserves the full band-width above 5 sec while adding 16 sec of correlated data with linearly diminishing bandwidth. Since it is likely that much of the higher frequency range is lost to attenuation in the ground, the shrinking bandwidth is not such a handicap as it might seem.

Note that at 11 sec of extended correlation our records retain a bandwidth of 4-32 Hz (based on the upsweep frequencies), essentially equivalent to that used by the COCORP program in its deep seismic reflection studies in this area (Oliver et al., 1976).

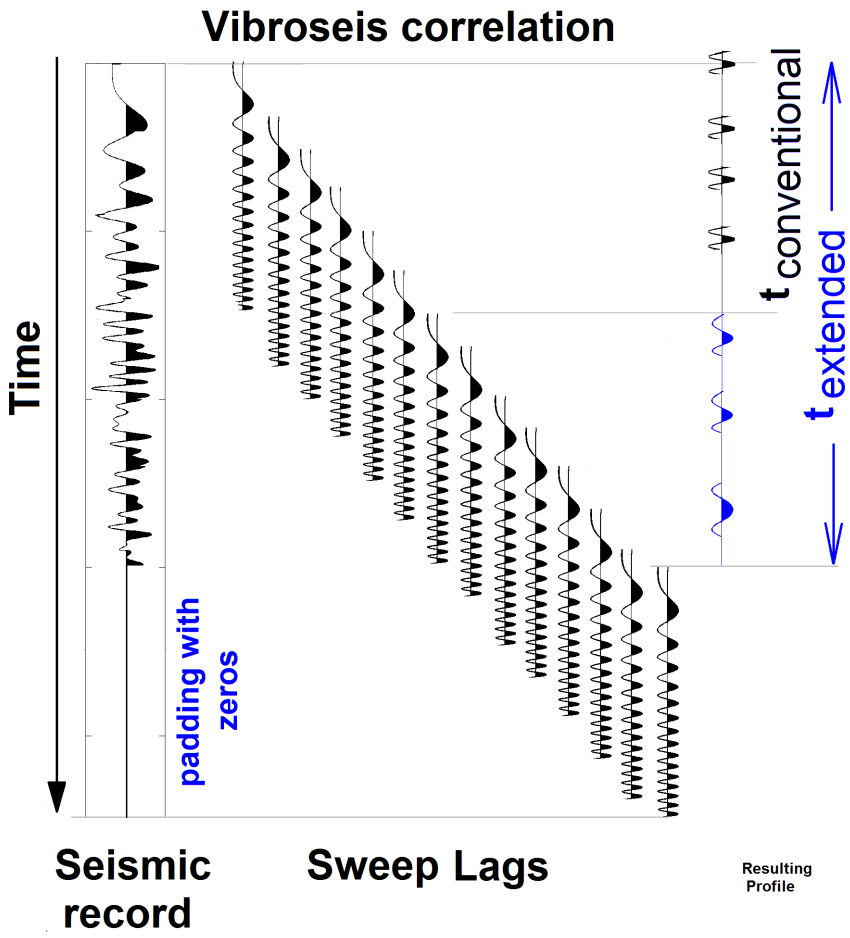

Figure 5.5: Conventional vibroseis correlation (black) vs. extended correlation (blue), the latter resulting in a longer correlated recorded with reduced bandwidth (modified from (Okaya, 1986))

Clearly signal penetration depends on the correlated length of the recording, but it is also limited by the input energy of the seismic source and subsequent attenuation losses (anelasticity, transmission losses) along the seismic ray path. The amplitudes of the correlated records (Figure 5.6) computed here show logarithmic decay down to a correlated travel time of approximately 6-7 sec, below which the average amplitudes remain constant, presumably defining the ambient background noise level. Since the top of basement in this area is expected to

lie at approximately 2.5-3 sec travel time, this plot suggest that the sources used in this survey are adequate to penetrate well into uppermost Precambrian basement (e.g. Mayer and Brown, 1986), but may not have provided enough energy to reach the Moho discontinuity at approximately 13.3 sec, assuming average 6km/s velocity for the crust.

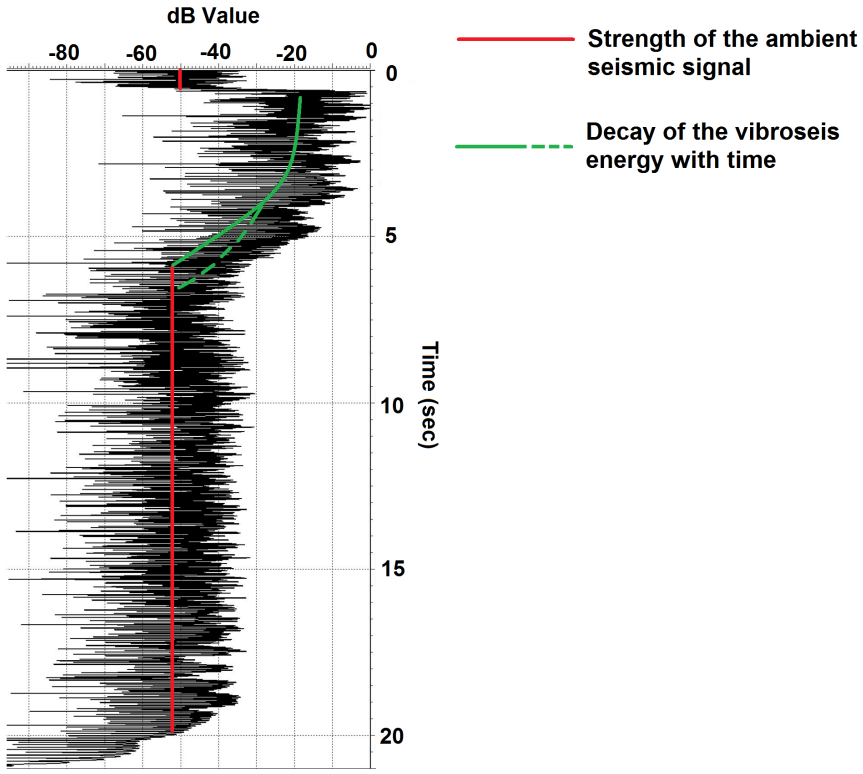

Figure 5.6: Log (amplitude) vs. time for a single extended correlated trace slightly offset from the vibroseis source

5.5 Processing and Velocity Analysis

Figure 5.7 shows the first 5 seconds of a typical extended correlation of relatively wide range of source-receiver offsets. All of the signal processing reported here was performed using Vista 3D Seismic Processing Software (TM Schlumberger).

The general workflow is shown in Figure 5.8. We removed the traces for offsets greater than 10.7 km (35,000 ft) since the data shot gathers at larger offsets show little evidence of any reflected energy (Figure 5.7).

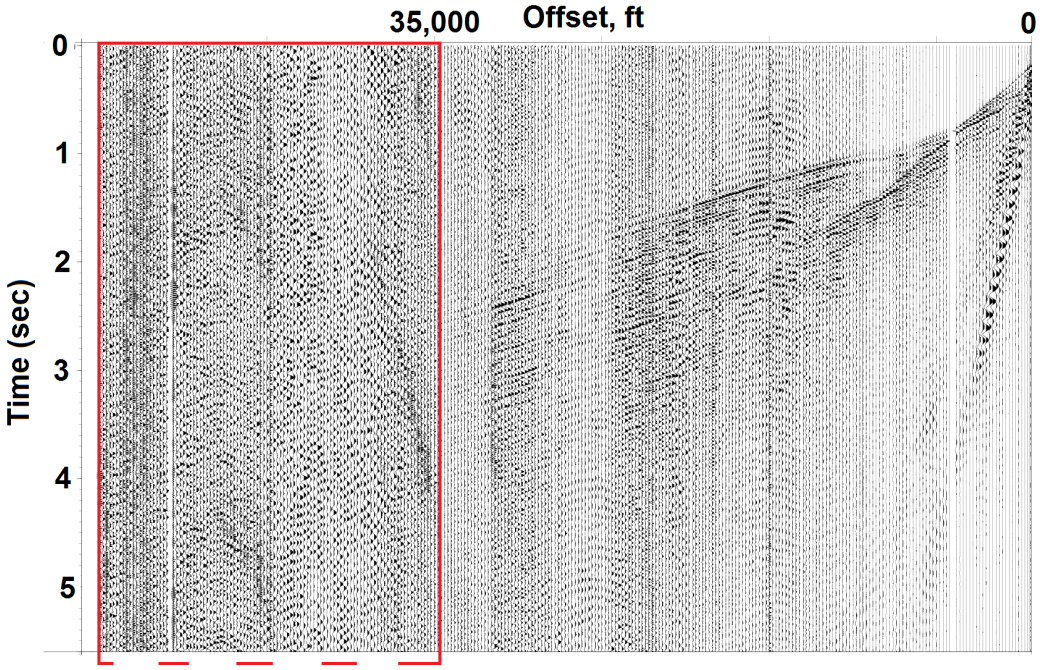

Figure 5.7: First 5 seconds of a typical extended correlation. Note the domination of the far offsets (e.g. > 10.7 km) by noise. These offsets (red rectangle) were not included in the CMP stacks

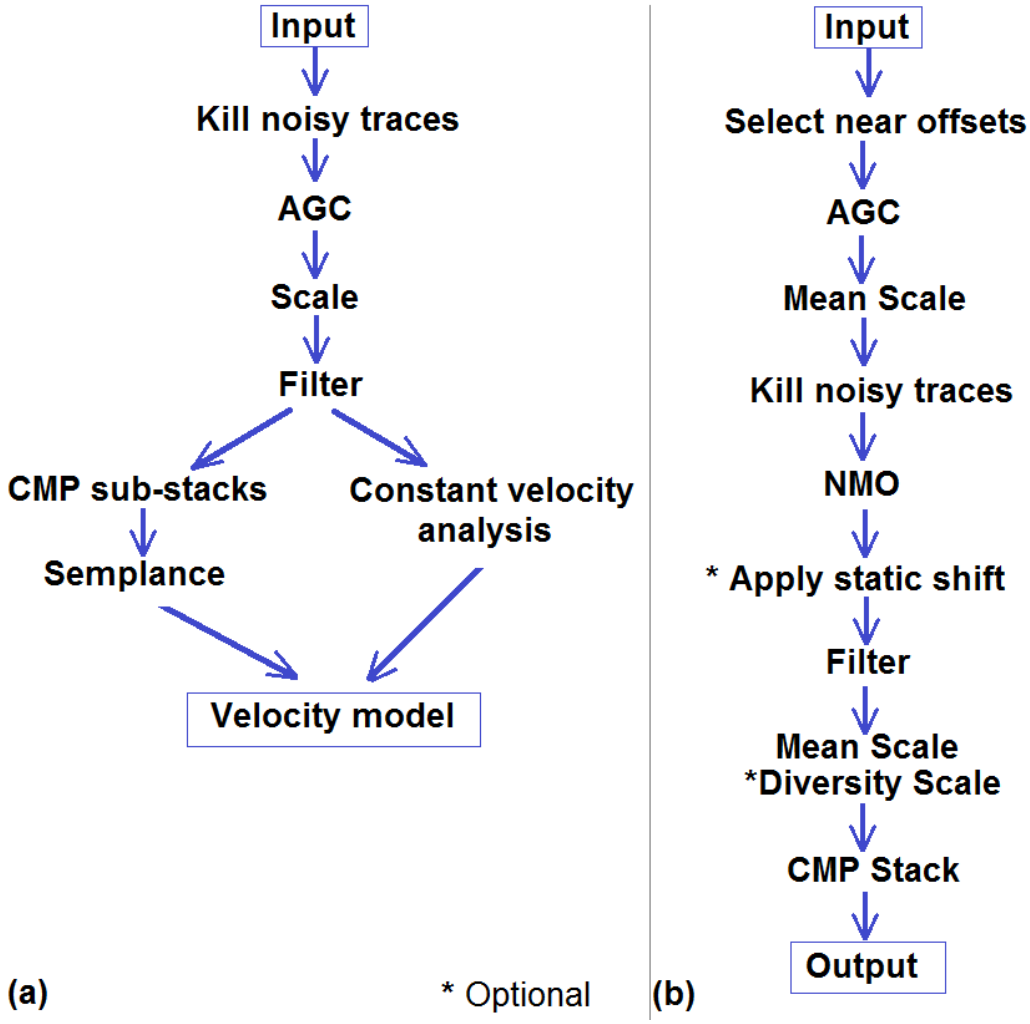

Figure 5.8: Work flows for (a) velocity analysis, and (b) CMP stacking

Conventional velocity analysis was performed on the well-defined, relatively shallow reflections that presumably represent the sedimentary cover (Figure 5.9). Following development of a velocity model using the prominent sedimentary reflectors, velocities variations for the deeper portions of the data were explored with constant velocity stacks. Given the aperture of data used ($<$ 10.7km), normal move-out below 5 seconds is both expected and found to be relatively insensitive to reasonable velocity variations, thus a constant 6 km/s was used for stacking the deeper data (Figure 5.10). Two velocity models

were generated: (1) using velocities picked for every 10th out of 352 CMP gathers (Figure 5.10(b)), and (2) a constant gradient velocity for all CMP's (Figure 5.10(a)). Both velocity were used to generate stacked 2D profiles in time and depth, with the results compared to assess the dependence of the CMP stack quality on velocity. The profiles generated by these two velocity models show few differences in time and only slight variation in depth.

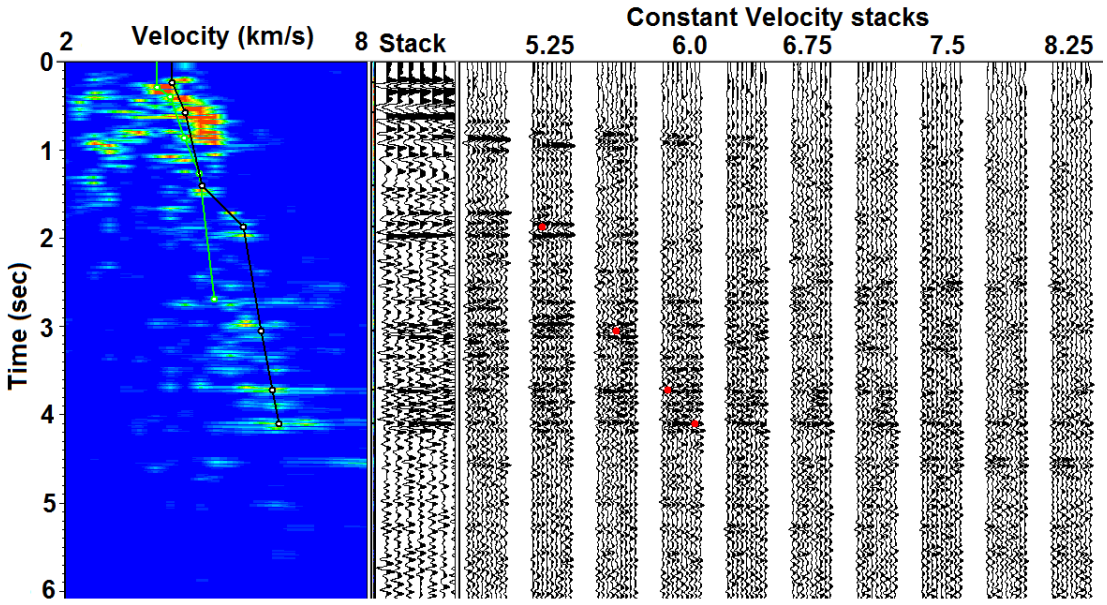

Figure 5.9: Velocity picks - semblance on the left, partial stack and panels of constant velocity stack

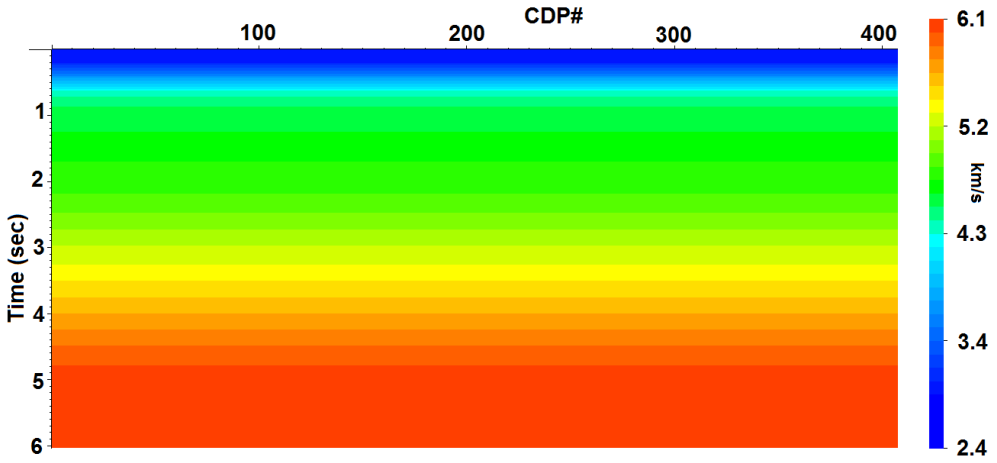

(a) Constant gradient velocity

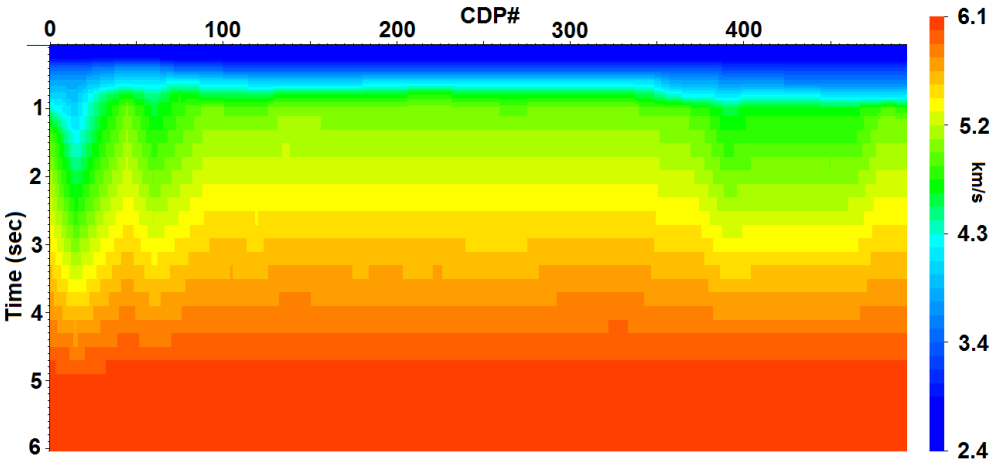

(b) Picked velocity model

Figure 5.10: (a) Constant gradient layered velocity model, (b) Picked velocity model

The first two seconds of a single CMP gather are shown in Figure 5.11. Apart from the direct P wave and the surface waves (at least those that survived the 14-74Hz bandpass filter that was applied to reduce their interference) and the air-wave, a number of hyperbolic reflections are obvious. The most prominent is at about 0.8 seconds (zero offset travel time), although coherent energy is clear down to at least 3-4 sec on both shot point and CMP gathers.

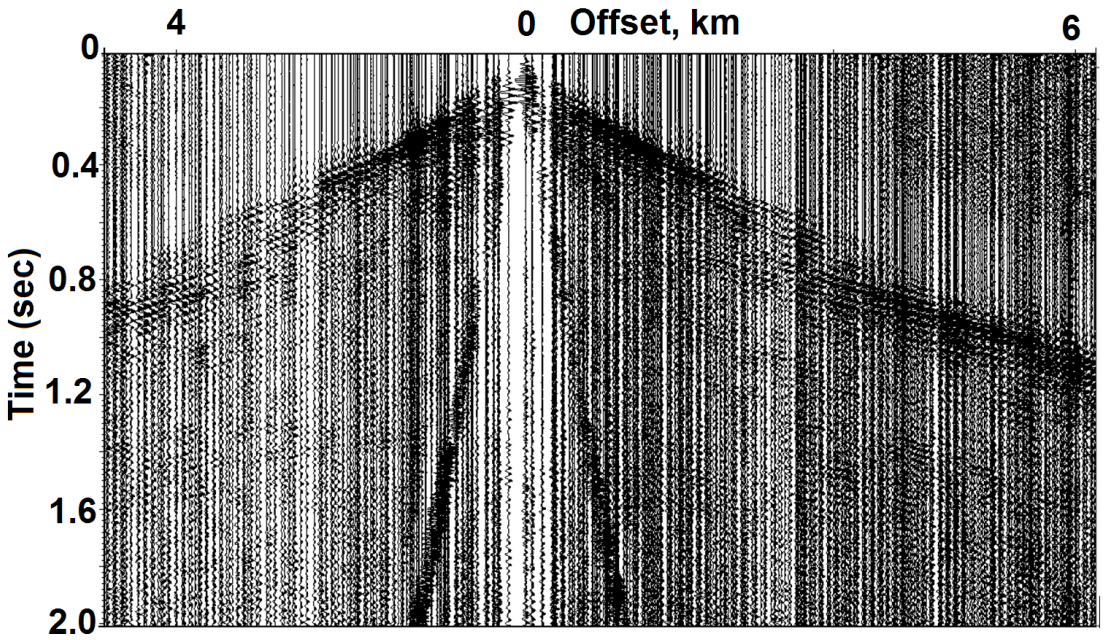

Figure 5.11: A sample CMP gather with AGC filter of 800ms length applied

The data processing was divided into 3 stages: (a) 2D analysis for quality control and initial work flow establishment, (b) 3D sub-array analysis to extend and modify the workflow from 2D to 3D, and finally (c) full 3D processing. Results from all three are discussed below.

5.6 Results and Discussion

Figure 5.12 is a comparison of stacked profiles in time using a constant gradient velocity model (5.12(a)) vs. picked velocity model (5.12(b)). Even though there is a slight variation in the quality and continuity of the reflectors, the basic reflection character does not depend strongly on slight variations in the velocity models used here for normal move-out corrections.

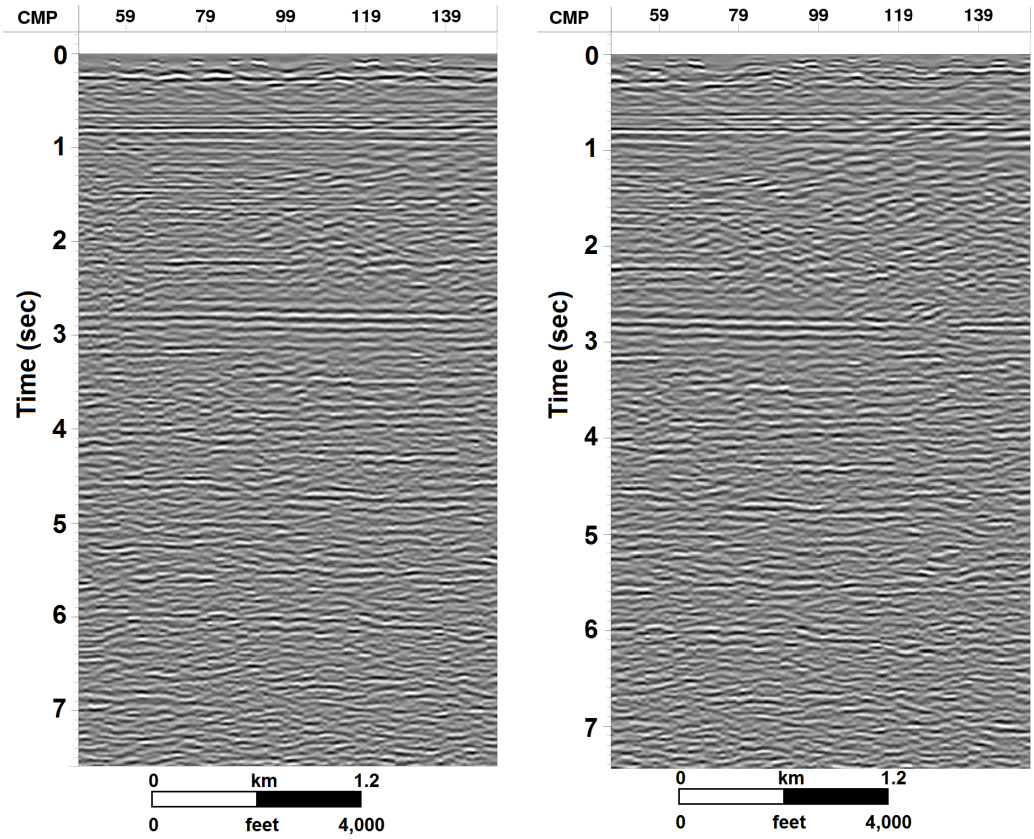

(a) Constant gradient velocity stack (b) Picked velocity model stack

Figure 5.12: (a) Constant layered velocity stack on the left, (b) Picked velocity stack on the right

A 2D west-to-east trending depth section of the processed seismic data (Figure 5.13) is dominated by a series of sub-horizontal reflectors down to a time of about 3.1 sec, or 9 km using the stacking velocities derived from our analysis. The most prominent reflector (0.8 sec, Figure 5.12(a-b)) lies at approximately 1.5 km depth (Figure 5.13) and is interpreted to be from the Delaware Mountain Group (also referred to as Guadalupe series) based on a stratigraphy report from well measurements across Lea county by Keller et al. (1980). The base of the overlying Ochoa series is mostly salt and anhydrite, whereas the top of the Delaware Mountain Group formation is blocky limestones, shales or

sands. This difference in the geological units provides a good contrast in acoustic impedance and therefore a very prominent reflector in seismic profile (0.8 seconds in Figure 5.12). Resistivity logs from Taylor County east of the Ector County show high resistivity contrast at similar depths (approximately 1.4 km).

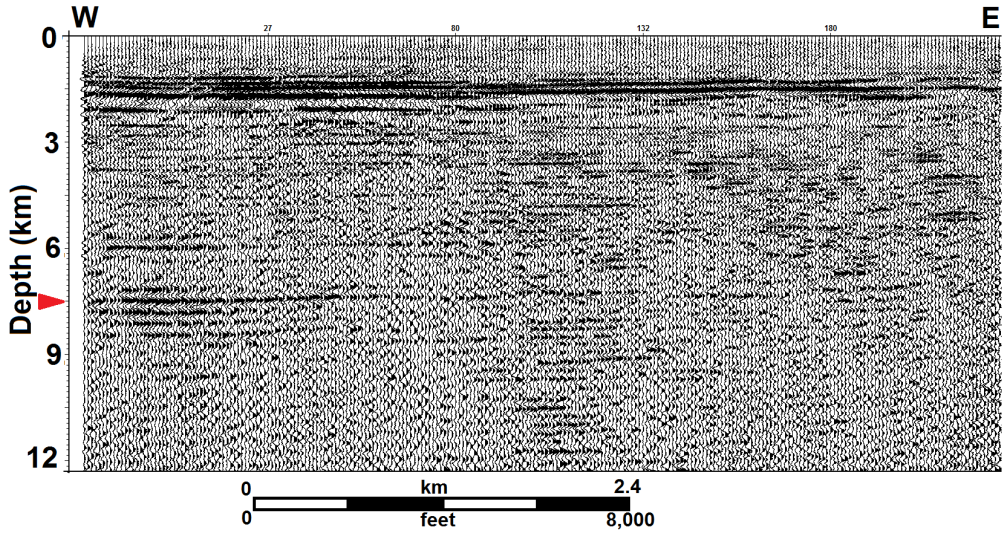

(a) Depth profile

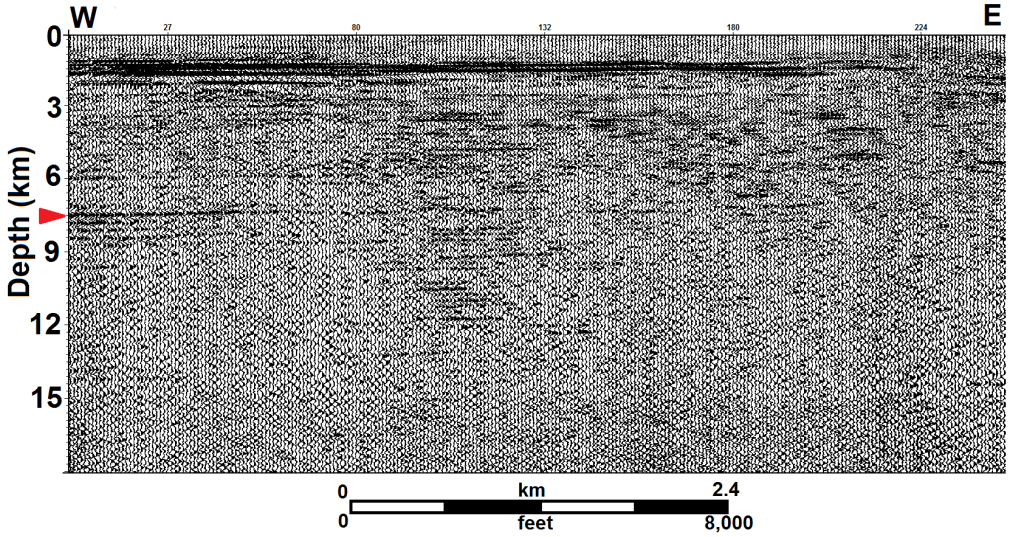

(b) Depth profile, zoom out

Figure 5.13: 2D Depth Profile stack and generated using picked velocity model

Key to our interpretation is the identification of the top of the Precambrian basement. Extrapolating the well information reported by Ward et al. (1986), Keller et al. (1980) and basement topography map by Hills (1984), we expect the base of the Paleozoic sedimentary section to consist of mostly dolomite (Hills, 1984) and lie at a depth of about 6-7.2 km (Figure 5.4; red triangle) from the surface. The strong reflection at about this depth (7.2-7.5km) under the west end of the profile is interpreted here to make the top of the basement or a stratigraphic unit near the basement. The depth and amplitude of this reflector decreases toward the East as it approaches the central basin, which is consistent with the Ward et al. (1986) and Keller et al. (1980) well log interpretations.

There is coherent energy at travel times corresponding to greater apparent depths on Figure 5.13 (e.g. within Precambrian basement). However, with the exception of short patch near the center of the profile, it is generally weak and continuous only in short segment. The sub-parallelism of much of coherent energy between 9 and 16 km raises the possibility that these are simply multiples that have "leaked" through the CMP stack. On the other hand, COCORP surveys from northeastern Texas found that the Pre-Cambrian basement was characterized by extensive layered reflection sequences (e.g. Oliver et al., 1976; Brewer et al., 1983). We note that the relatively high stacking velocities (e.g. 5.2 to 6.0 km/sec) for travel times between 3 and 5 sec (9 and 15 km), are consistent with both the carbonate lithologies of the lower Paleozoic (and presumably any multiples they generate) as well as suspected Precambrian basement rocks. Based on the well data from Hills (1984), these reflectors, if not multiples, would correspond to inter-basement depth. At travel times corresponding to the deeper crust (e.g. depth $> 15km$) energy is coherent at best for only a few traces. This character on the depth section is arguably as consistent with noise

as with basement heterogeneity.

Shot gathers and CMP gathers from the east and west parts of the survey receivers seems to exhibit different reflectivity patterns (Figure 5.14) and therefore may have different limit in depth penetration. We attribute the lateral changes in the image quality to the lateral changes in sedimentary geology (Figure 5.4).

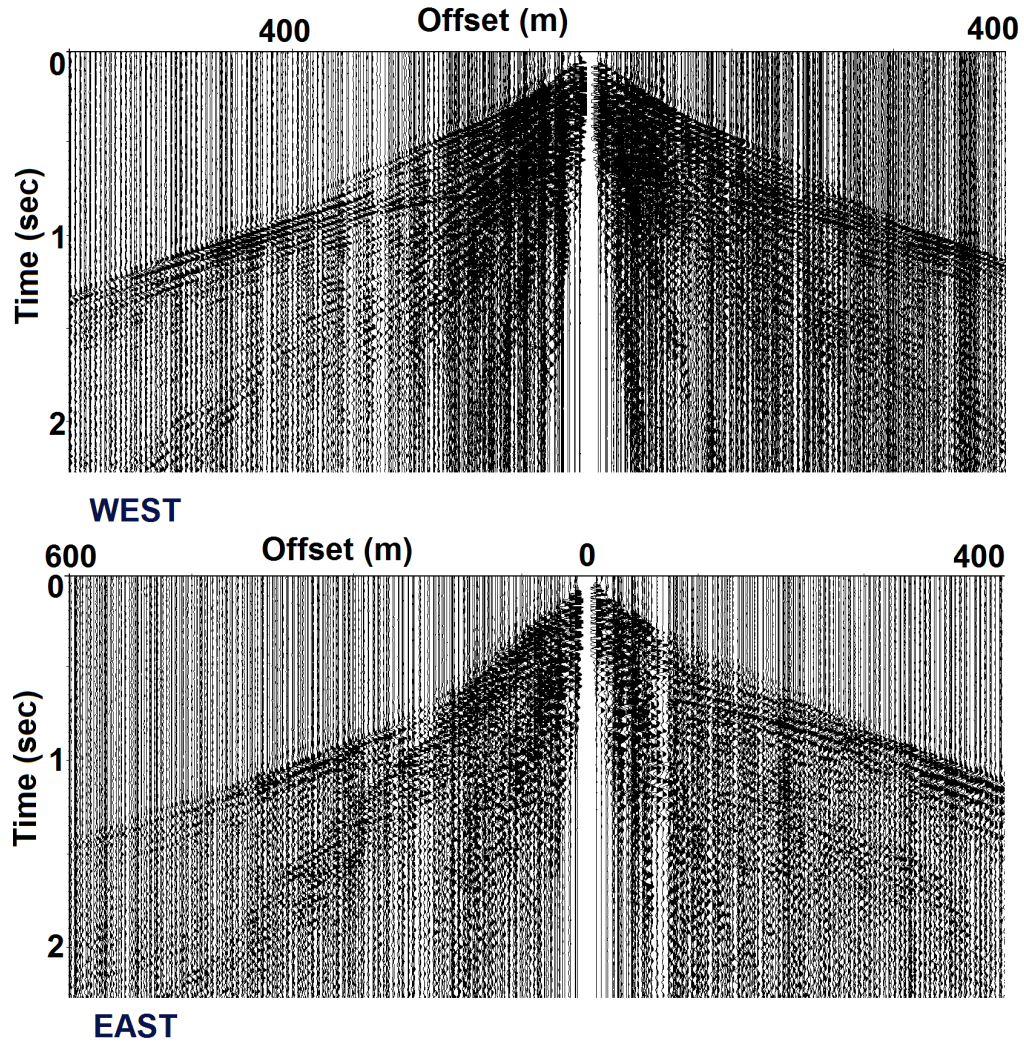

Figure 5.14: Comparison of CMP gathers from the east and west part of the survey, probably due to different geometry of the layers, such as sharply dipping reflector in the east evident from assymetrical first arrival

5.6.1 3D subset

The green rectangle in Figure 5.15 is a subset of the survey used for preliminary 3D parameter analysis. The reason for using a subset initially was to speed up testing appropriate processing parameters to be applied to the entire dataset. These parameters correspond to processes such as band-pass frequency filters, gain conrol, noise suppression techniques, wavelet deconvolution, migration, residual static removal and diversity stacking. Some of these techniques proved to be more useful (e.g. like diversity stacking) than others (e.g. wavelet deconvolution, migration and residual static removal) and were applied to the entire dataset (see 5.6.2).

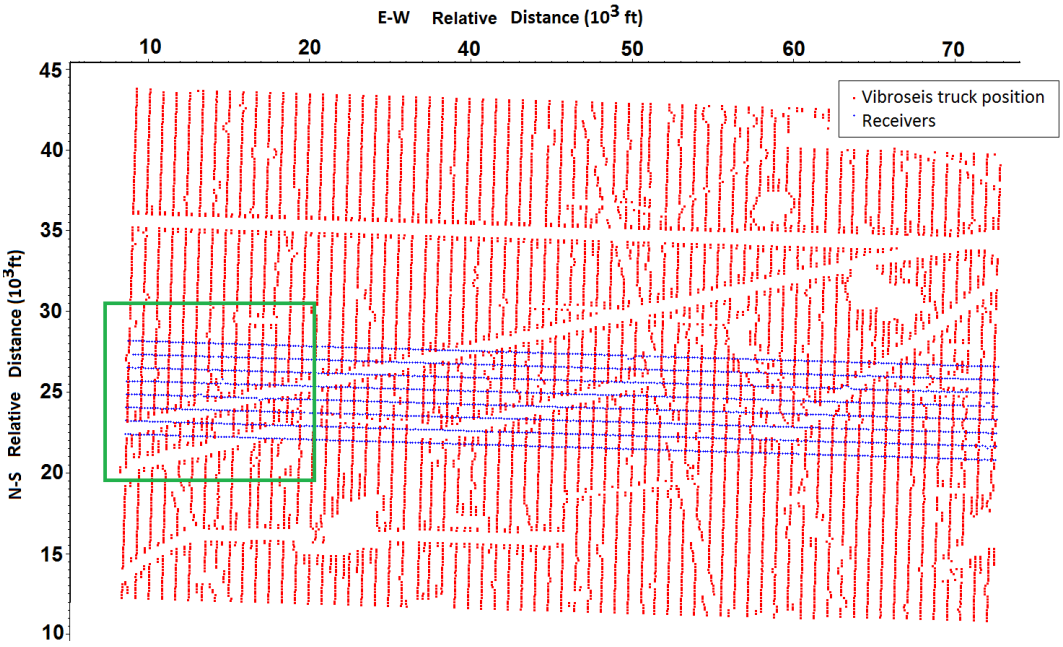

Figure 5.15: Shot-receiver geometry for the 3D section, green rectangle shows the extent of the 3D subset

Exceptionally noisy traces (e.g. Figure 5.16) were identified using their particularly high signal-to-noise ratio and rejected before further processing. Such

editing helped eliminate numerous high amplitude hyperbolic seismic arrivals attributed to noise on the surface.

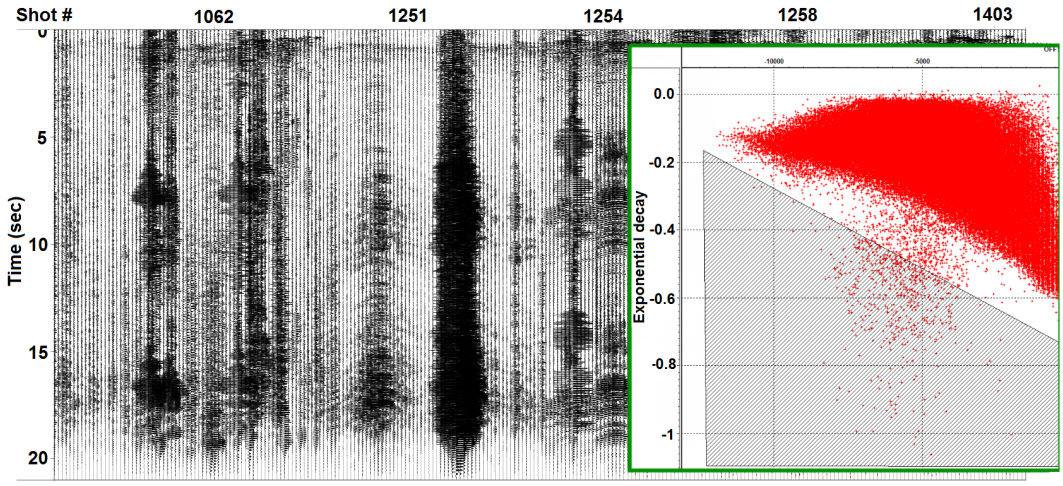

Figure 5.16: Example of noisy traces edited before stacking

As with the 2D processing, stations recording sources at far offsets (more than 15,000 ft or approximately 4.6km) were zeroed in the processing.

Figure 5.17 and Figure 5.18 show depth slices of amplitude (color coded) through shallow and deep portions of the datacube section, colored by amplitude. The shallow slice is associated with the Delaware Mt. Group - Leonard series interface (Figure 5.4). The depth slice shown in Figure 5.18 is at 22,000 ft, and presumably represents either the basement or a near basement sedimentary layer. Deeper coherent events may represent more discontinuous inter-basement reflections, although it is possible that at least some correspond to multiple reflections from the sedimentary layers.

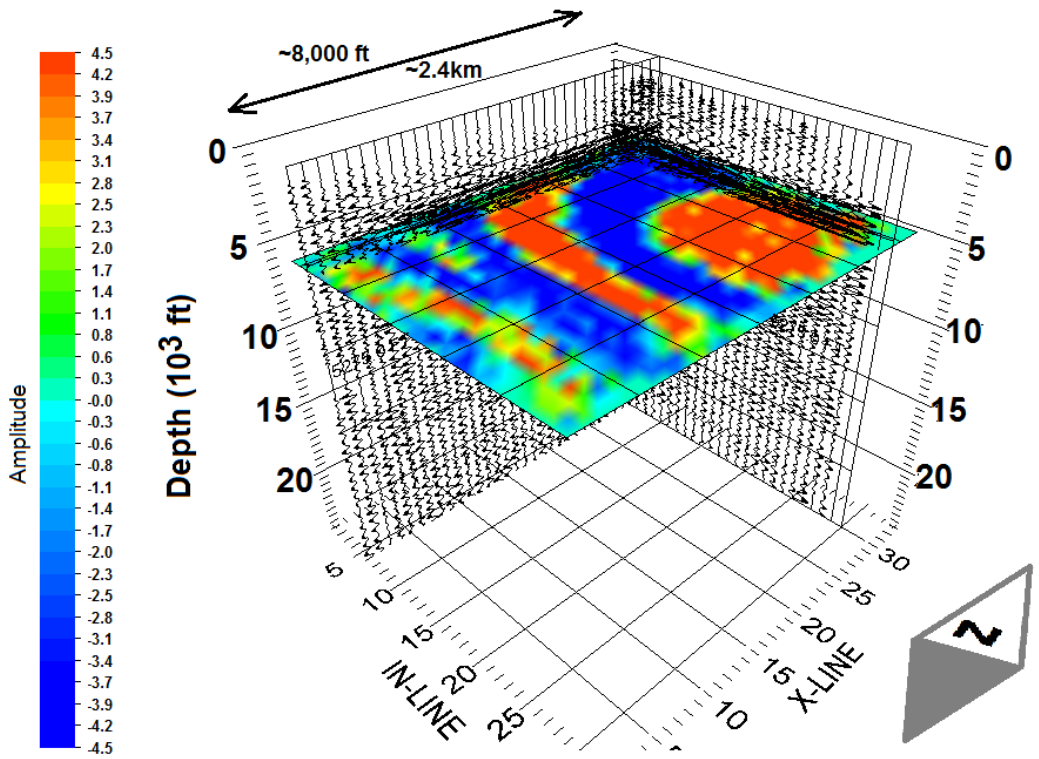

Figure 5.17: 3D stack using picked 3D velocity model, showing structure in layering within the sedimentary basin rocks

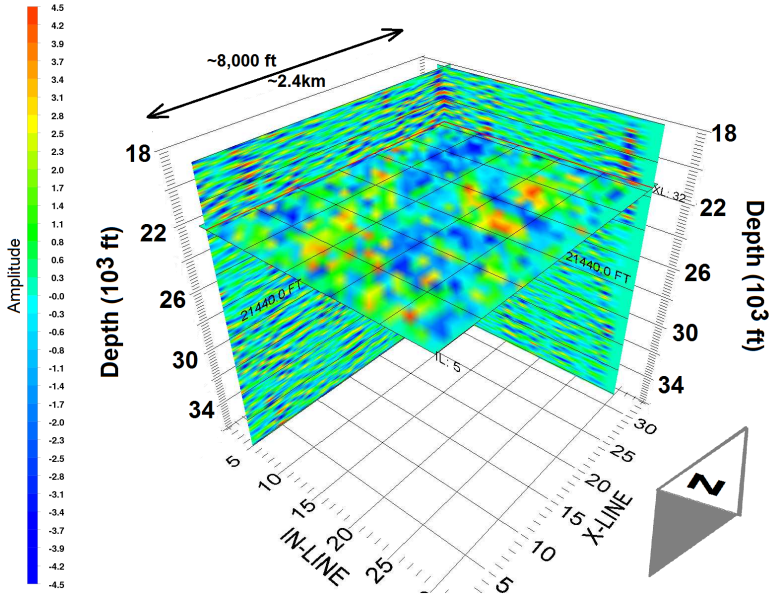

(a) 3D subset stack with a depth slice

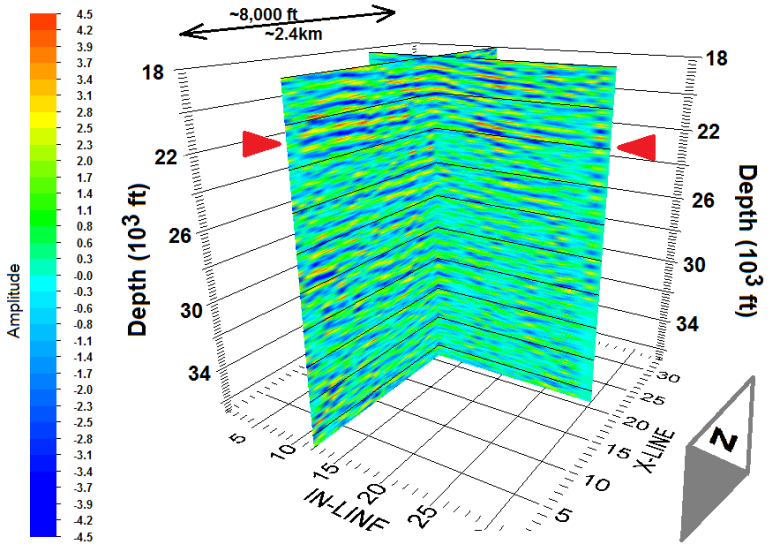

(b) 3D subset stack without a depth slice

Figure 5.18: 3D stack with depth slice near the top of the presumed basement. We identified the top of basement with a prominent reflector at approximately 22,000ft with (top) and without (bottom) the depth slice

5.6.2 Basement in 3D

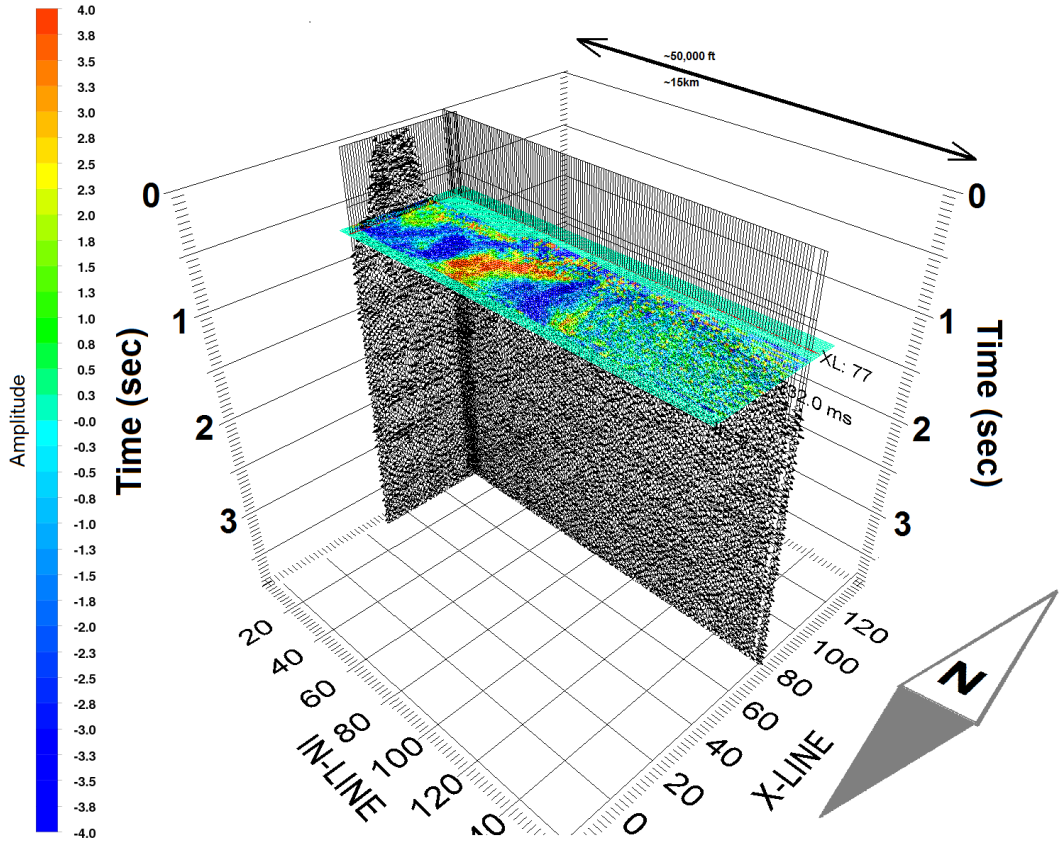

Figure 5.19: Shallow time slice at 732msec showing amplitude variations (color bar)

3D reflection imagery of the continental basement is extremely rare (e.g. Welford and Clowes, 2004), which is not surprising given the costs involved. The unique value of any deep reflections extracted from these modern surveys is the promise of substantial new 3D imagery of the basement and sub-basement structures. Figures 5.20 and 5.21 contain 3D representations of this pilot dataset. Figure 5.20 is focused on reflections near the top of basement (presumably at or just below). Whether these are from basement lithology proper, from a sedimentary marker just above the basement or from a structure just below, is less impor-

tant that the fact that the image contains valuable information about basement structure. Such information is not only a key to unraveling basement tectonics and its role in basin evolution, it could help, for example, identify basement structures to be avoided in waste water disposal (Keranen et al., 2013, 2014).

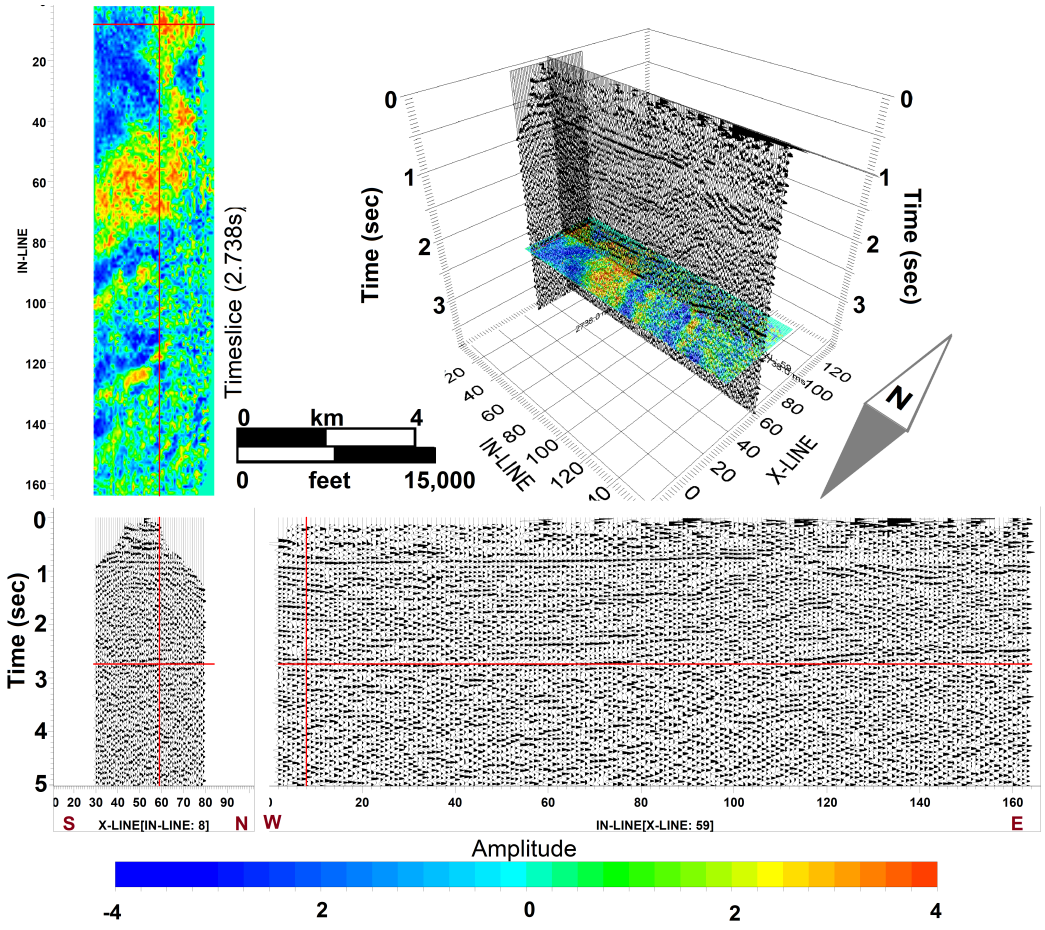

Figure 5.20: 3D processed volume with a time slice across the interpreted basement reflection. Top left is the time-slice colored by the recorded amplitude at 2.738 seconds; top right is the full 3D stacked volume; bottom right is NS trending 2D section, and bottom left is EW trending 2D seismic section.

Figure 5.21 shows the 3D morphology of a reflector we interpret lies just within the crystalline basement or the basement reflection itself (at depth of 6.1-7.2 km based on our velocity model). The colder colors represent smaller arrival

time and thus shallower depth. The thinning of the basin from west to east by approximately 1km along 15km profile is clear. This reflector is continuous throughout the entire 3D volume, although its amplitude and morphology is variable.

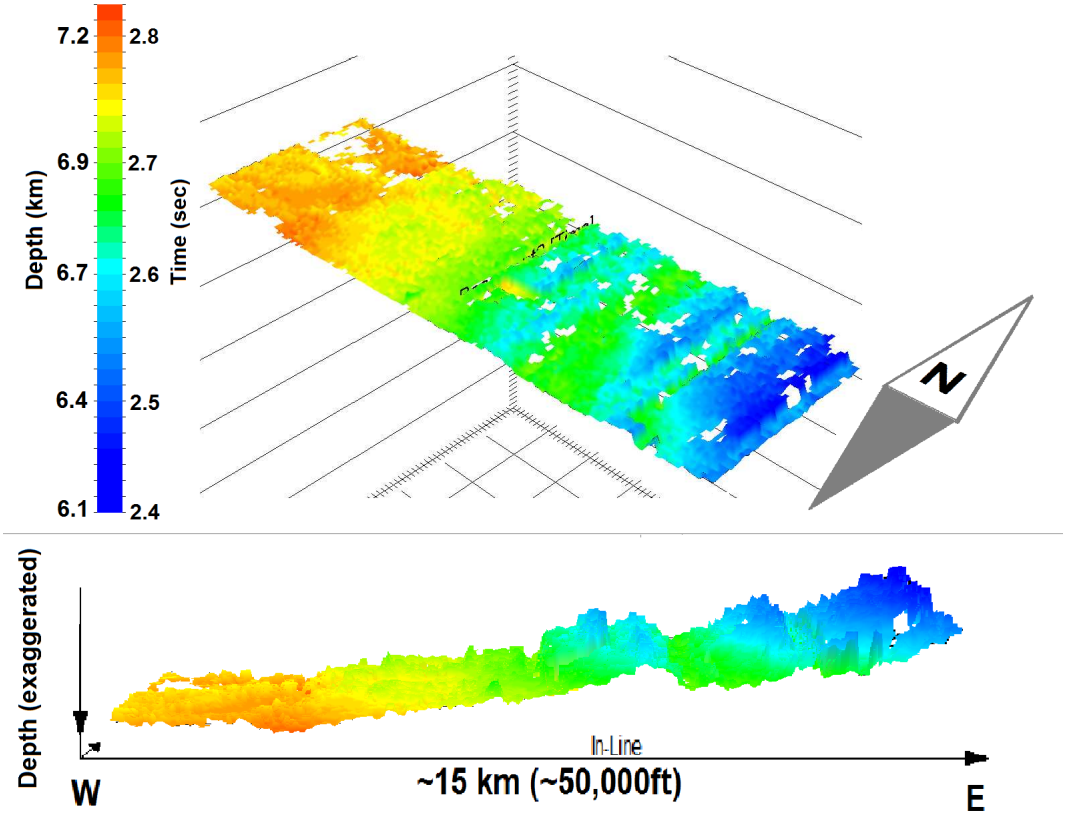

Figure 5.21: Basement (or near basement) reflector colored by arrival time

5.7 Conclusions

Our results demonstrate that 3D industry seismic datasets provide a unique opportunity for more accurate and extensive mapping of the deep geological structures of the continental basement. Although attenuation of a thick sedimentary

cover in this example has apparently limited penetration to the uppermost crystalline basement, there is no reason to doubt that in many, if not most, cases this approach will produce useful information about the basement in general, and could even reach all the way to the Moho discontinuity under more favorable circumstances.

As the depth of interest for oil exploration is primarily within a sedimentary basin, investigations of deep structure using the normally discarded portions of these new seismic datasets represent no threat to the proprietary value of these data. To the contrary, these studies offer valued added to the conventional treatment by revealing aspects of basement tectonics that may have influenced basin evolution and/or revealing basement structures so as to minimize the risk of induced seismicity associated with waste water injection.

Last, but certainly not least, the analyses of these surplus recordings is an excellent training tool to populate the pipeline of future talent for the exploration industry.

5.8 Acknowledgement

We would like to acknowledge the generosity of Fairfield Nodal for providing these data and guidance on the details of the survey, with special thanks to Rob Windels and Joe Dryer. We thank TM Schlumberger (Gedco) for providing the Vista Processing software used in this analysis.

CHAPTER 6

BENEFITS OF FREQUENT SEISMIC MONITORING AND COMPUTER SIMULATIONS IN THERMAL EOR PROJECTS

6.1 Abstract

This paper discusses the results of seismic modeling using a history matched dynamic reservoir model for a heavy oil field undergoing thermal EOR in Canada. Through the use of 4D RMS (Root Mean Squared) amplitudes and time-shifts maps in an integrated interpretation, we argue that there are important benefits in performing frequent seismic repeats commensurate with the time scale of the impact of steam injection on reservoir dynamics. These benefits may enable timely adjustments to production operations and more robust characterizations of reservoir behavior.

6.2 Introduction

Reservoir monitoring is an important element of oil field management and production operations. It provides essential information about changes in the subsurface and gives an opportunity to respond to these changes. When implementing 4D seismic one is faced with a variety of known issues including: (1) intrusive and expensive seismic acquisition, (2) potentially low Signal-to-Noise Ratio (SNR), and (3) ambiguous interpretation of changes in seismic attributes.

Cabolova, A., Lopez, J. L., and Wills, P. (2014, October 29). Benefits of Frequent Seismic Monitoring and Computer Simulations in Thermal EOR Projects. Society of Exploration Geophysicists, Extended Abstracts Publication.

These issues are particularly problematic onshore and even more so for the Enhanced Oil Recovery (EOR) operations.

Our work shows the potential of frequent seismic survey repeats for unambiguous interpretation and demonstrates how gas saturation and pressure changes influence seismic response at different times in field history. We argue that generation of synthetic seismic in conjunction with these surveys, especially for oil fields with complex dynamic histories (steam, water, oil, temperature, pressure are all changing), is essential for understanding subsurface changes when interpreting actual seismic datasets.

Here we focus on a thermal EOR development in Alberta, Canada, where multiple production pads are undergoing steam injection in various guises using vertical and horizontal wells. The pad is subdivided into three parts: Pad A, Pad B and Pad C - inflills. Pad A is original 5 horizontal wells trending NW-SE, Pad B are 2 horizontal wells drilled above Pad A and trending NE-SW at the toe, and finally, Pad C infills are three J shaped wells trending similaly to Pad A (Figure 6.1).

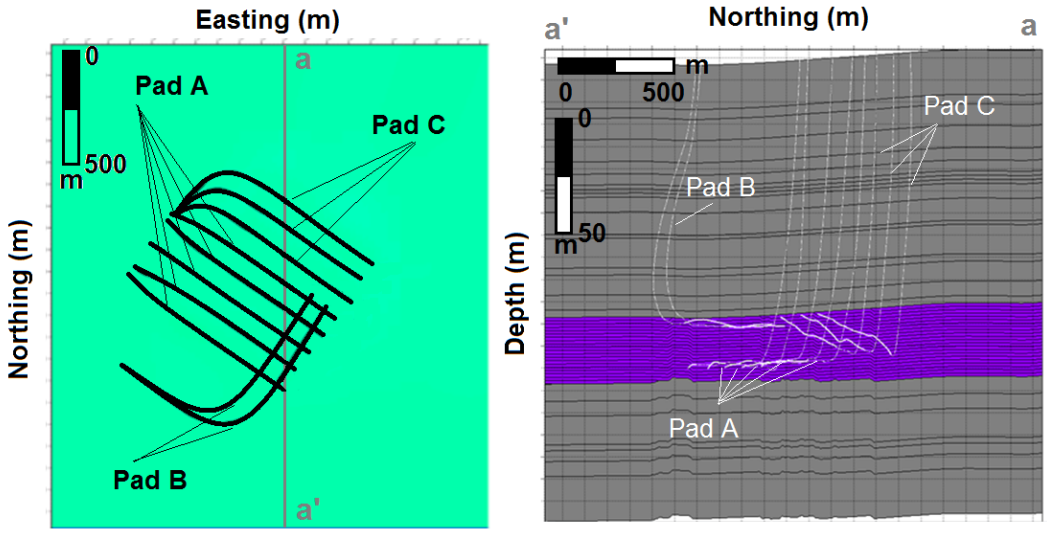

Figure 6.1: Geometry of the pads A, B and C in the map view (left) and a profile (right)

The well pads in this study have been in operation since 1997 utilizing an evolving set of injection schemes to increase ultimate recovery over time: first Steam Assisted Gravity Drainage (SAGD), then Cyclic Steam Stimulation and finally, Top Down Steam Drive with two additional wells (Pad B) (Figure 6.2). All of these techniques are considered to be a part of Enhanced Oil Recovery (EOR) and introduce a level of complexity when interpreting seismic acquired during this process.

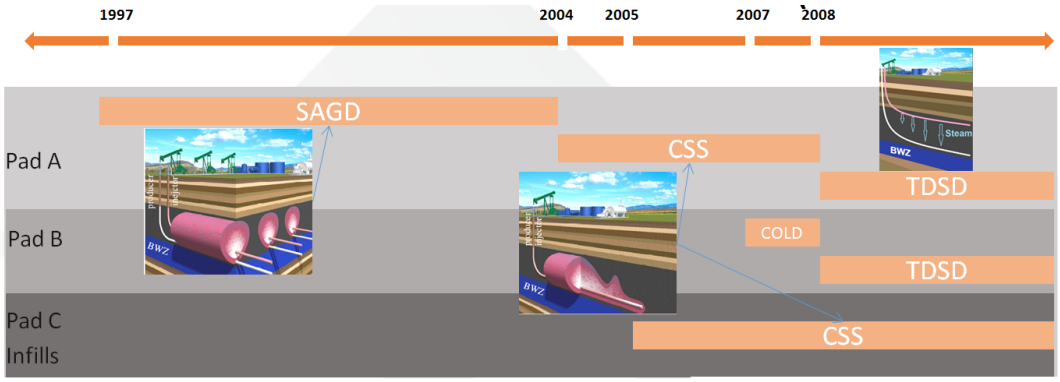

Figure 6.2: Complex Pad History, which involves Steam Assisted Gravity Drainage, Cyclic Steam Stimulation and Top-Down Steam Drive

First static and then dynamic models were created using a proprietary software to simulate the changes in the reservoir for the entire pads' history. These models were used in this study to create synthetic seismic datasets for each vintage of the dynamic model. The synthetics was then analyzed using standard techniques (i.e. amplitude and time shift extraction) to predict seismic sensitivity to the rapid changes in the reservoir properties.

6.3 Steam Injections

Steam injection is one of the techniques used by industry to recover heavy, high viscosity oil from the ground (Cornelius et al., 1961). There are different techniques however to the way steam gets injected into formation and the ones used in the field here are Steam Assisted Gravity Drainage (SAGD), Cyclic Steam Stimulation (CSS) and Top-Down Steam Drive (TDSD) (Figure 6.2). The Pad was under SAGD (Steam Assisted Gravity Drainage) from 1997 to 2004, under CSS (Cyclic Steam Stimulation) from 2004 to 2008 and currently under TDSD

(Top-Down Steam Drive, Pad B wells were drilled).

SAGD is a two horizontal wells steam injection procedure, where one well in an injector and the other one is a producer. The producer in such configuration can operate continuously during the injections. The injector well is drilled above the producer and steam is injected to heat up and change the viscosity of the oil, which then flows into the producer.

CSS is a single vertical or horizontal well operation. The well serves as both injector and producer and is operated in two separate phases: injection and production, which constitute one cycle. The idea is the steam changes the properties of the oil around the well, which allows it to flow during the production phase.

Steam Drainage is, similarly to SAGD, a two well operation. The distance between injector and producer is generally greater in this case, which allows steam not only to change the properties of the oil but also push it towards the producer. TPSD means the both of the wells are horizontal and injector is on the top.

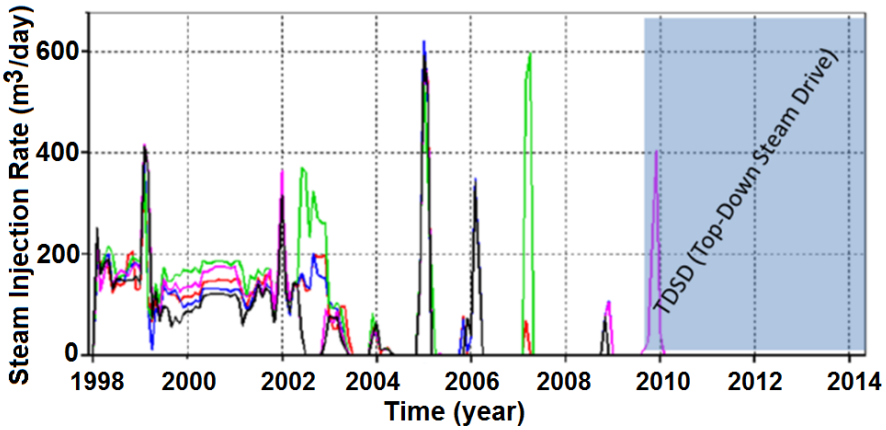

Figure 6.3: Steam injection history (colors represent different wells on the pad).

Figure 6.3 show a complex steam injection curve. During TDSD some of the old injection wells in Pad A were changed to producers, and new injectors were drilled (Pad B) close to the top of the reservoir (Figure 6.2).

In fields with such complicated operation history, it is not possible to time the acquisition of 4D seismic to obtain an ideal "baseline" dataset, and therefore, we argue that frequent seismic repeats become necessary. Seismic synthetic for each of these repeats helps the interpretations of real data, as well as any necessary adjustment of the input model (Cotton et al., 2012).

6.4 Synthetic seismic workflow

We use Shell's proprietary software package for synthetic seismic generation and integrated analysis. It takes a user defined rock and fluid-mix models to compute bulk velocities and densities for each grid cell in the reservoir model, and from that Acoustic Impedance (AI). The program then uses a wavelet to

produce synthetic seismic by convolving it with AI matrix. The workflow, with inputs in shaded boxes and calculated properties in white boxes, is shown in Figure 6.4 using Mukherjee et al. (2012) and Rocco et al. (2010) examples.

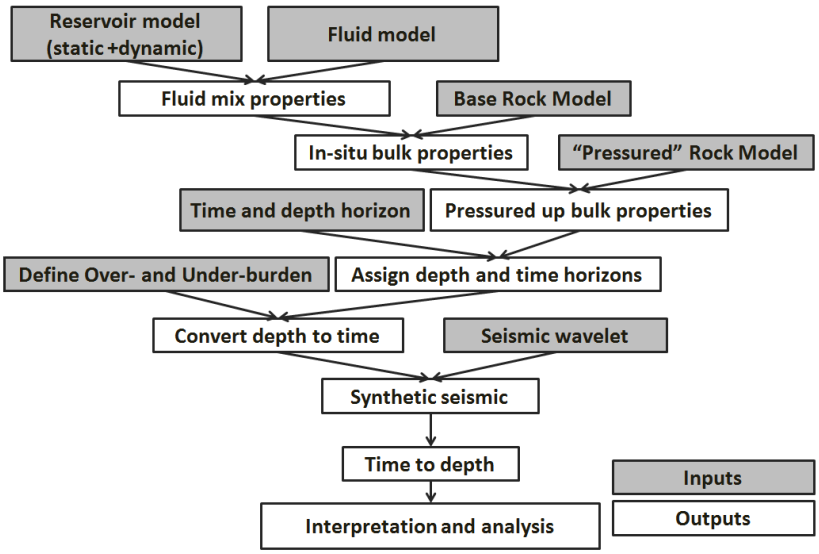

Figure 6.4: Synthetic seismic generation workflow using Mukherjee et al. (2012) and Rocco et al. (2010) examples

The rock model used for this area (Appendix F) assumes that shear μ and dry K moduli during steam injection depend only on their initial values and on pressure following the Hertz-Mindlin model (μ_0 is initial shear modulus before injection, P_{ov} is overburden pressure, P_0 is initial pore fluid pressure of the reservoir, P is current pore fluid pressure):

$$\mu = \mu_0 \left(\frac{P_{ov} - P}{P_{ov} - P_0} \right)^{1/3} \tag{6.1}$$

In reality, the relation between the overpressured and initial moduli for the rock model may be more complicated: (a) the exponent in equation (1) in the original Hertz-Mindlin equation can be different for different geological set-

tings; (b) the moduli can depend on other reservoir variables, like temperature, to a smaller degree.

Another component of the synthetic AI model is the reservoir fluid properties. These properties include fluid-mix density, K-modulus, etc. and were calculated using the FLAG8 relations by Han and Batzle (2000) for isothermal fluid compressibility.

Finally, the rock and fluid models transform the input reservoir dynamic properties into AI for each model grid using Equations 6.2-6.6. Here K_{dry} is K modulus of dry rock, subscript 0 denotes time zero before injection and/or production, bulk K modulus depends on K_{dry}, K_{fluid} (K_{fluid} modulus embeds K modulus of all fluids in the reservoir: gas, which is steam and some methane, water and oil), K_{grain} (i.e. K modulus of individual grains) and porosity ϕ. The bulk density of the rock depends on porosity, density of the grains and density of the fluids according to Equation 6.4. Once bulk density, shear modulus and bulk K modulus are determined for all grids, we can calculate p-wave velocity (v_p, Equation 6.5) and Acoustic Impedance (AI, Equation 6.6).

$$K_{dry} = \frac{K_{dry,0}}{\mu_0}\mu \tag{6.2}$$

$$K_{bulk} = K_{dry} + \frac{\left(1 - \frac{K_{dry}}{K_{grain}}\right)^2}{\frac{\phi}{K_{fluid}} + \frac{1-\phi}{K_{grain}} - \frac{K_{dry}}{K_{grain}^2}} \tag{6.3}$$

$$\rho_{bulk} = (1 - \phi) \cdot \rho_{grain} + \phi \cdot \rho_{fluid} \tag{6.4}$$

$$v_p = \sqrt{\frac{K_{bulk} + \frac{4}{3}\mu}{\rho_{bulk}}} \tag{6.5}$$

$$AI = \rho_{bulk} * v_p \tag{6.6}$$

Equation 6.6 shows that acoustic impedance depends on velocity and density of the subsurface material, both of which have a natural variability within the reservoir due to variations in rock properties such as porosity, permeability, K-modulus, etc. Therefore, interpretation of a single-time seismic image (one vintage) even for large seismic responses to dynamic changes, may be ambiguous due to this inherent variability. We argue that 4D seismic is the preferred methodology for more robust reservoir monitoring, as it allows differentiating between static variability of AI and dynamic effects.

The calculations above are embedded in the workflow in Figure 6.4: all the zero-time rock properties, such as initial shear (μ_0) and $K_{dry,0}$ modulus are calculated in Base Rock Model; equations 6.3 (Gassmann, 1951), 6.4 - 6.6 are applied in the "Pressurized" Rock model step, and K_{fluid} is calculated in the "Fluid model", defined by the FLAG8 relations by Han and Batzle (2000).

6.5 Quality Control

Quality Control (QC) is a very important step before synthetic generation. There are two main reasons for performing QC. The first is to confirm that the patterns of maximum change in the properties are centered or somewhat centered

around the wells but not necessarily symmetrical around them. This is to validate the location of the wells relative to the dynamic modeling grid and to confirm that there is no artificial shift between the model and the measurements due to different coordinate systems. The second is to observe the area affected by changes in different properties around the well, such as pressure, temperature, etc. This observation will help with interpretations.

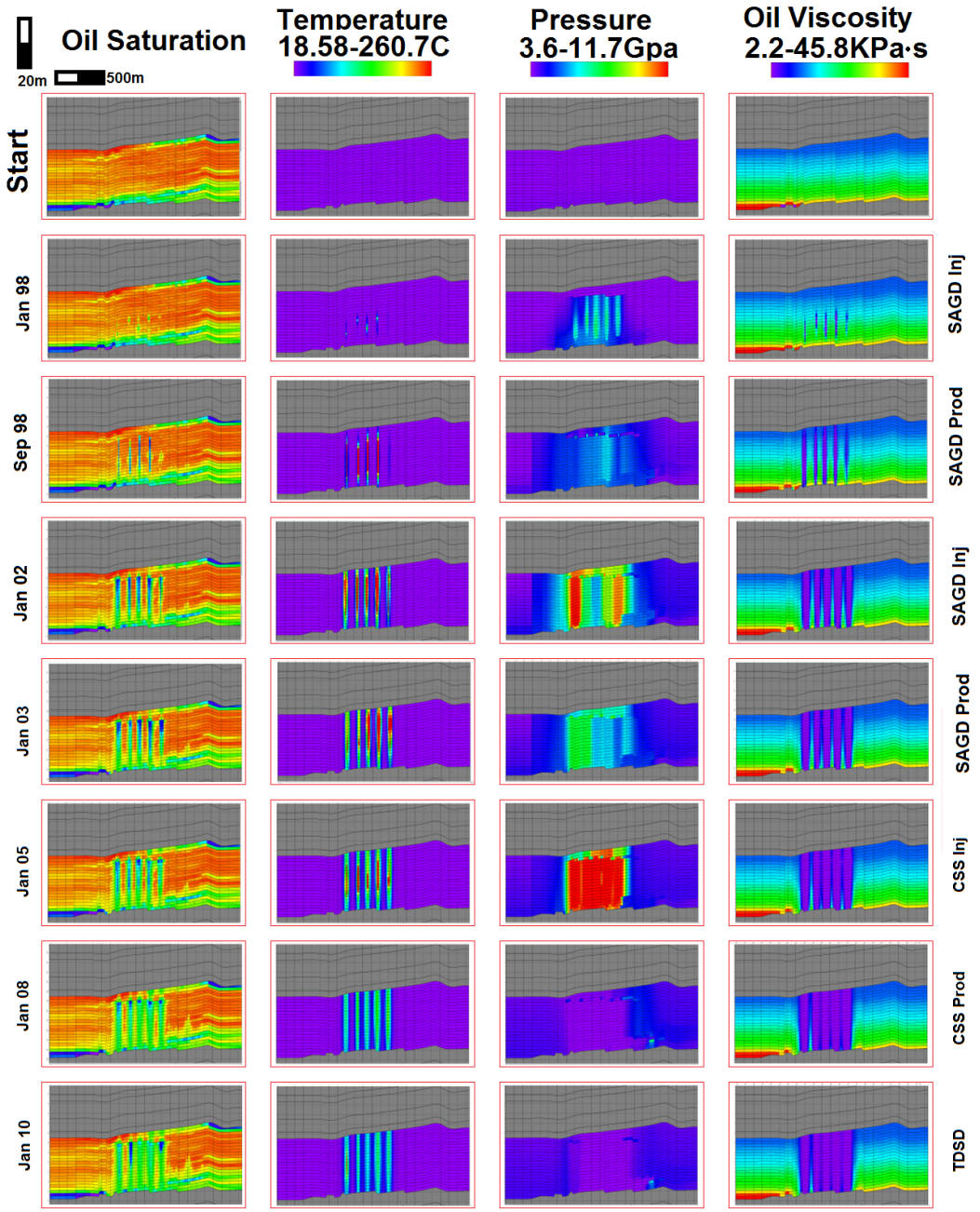

Figure 6.5: QC Oil Saturation, Temperature, Pressure and Oil Viscosity

An example of QC analysis is shown in Figure 6.5. Here, we examine a profile aa' (Figure 6.1) and check the correspondence of four properties (oil saturation, temperature, pressure and oil viscosity) with the injection-production

schedule. All time vintages for each property are scaled the same with the ranges shown right below the property name, and saturation ranges from 0 to 1. We concluded that the wells are positioned properly within the model and the model behaves as expected, e.g. temperature increases during injection, oil saturation decreases during production, etc. Also note that the pressure footprint is broader (i.e. the area affected by a change in pressure extends further from the well) than temperature footprint both during injections and productions. Even thought the temperature changes a lot during injections, it does not seem to decrease dramatically farther away from the wells during the production.

As a part of QC analysis we cross-plotted some static and dynamic properties prior the synthetic seismic generation to determine the their dependence on one another as well as their influence on the calculated properties, such as acoustic impedance. An example of such analysis is shown in Figure 6.6, where we can see that Pressure and Temperature are not independent, thus when steam is injected both of them increase. Therefore, at locations where we see higher pressures, higher temperatures are expected and they both influence acoustic impedances (and seismic response) at the same time. On the other hand, the relation between Temperature and Pressure is not linear, therefore regions exist where either temperature or pressure has a dominant effect on seismic.

Figure 6.7 shows the fluid Viscosity dependence on the Temperature of the reservoir during an injection. The steam increases the temperature of the fluids, which consequently changes the viscosity in agreement with Beggs et al. (1975). However, depending on the different composition of the fluids in the pores of the reservoir rock, the Temperature effects on the Viscosity manifest differently.

This is shown in Figure 6.7, where for a single fluid the relationship between temperature and double log of viscosity is expected to be linear (Figure 6.7(a)) and the points outside of the main cloud are associated with fluid substitution and differences in initial conditions (Figure 6.7(b)).

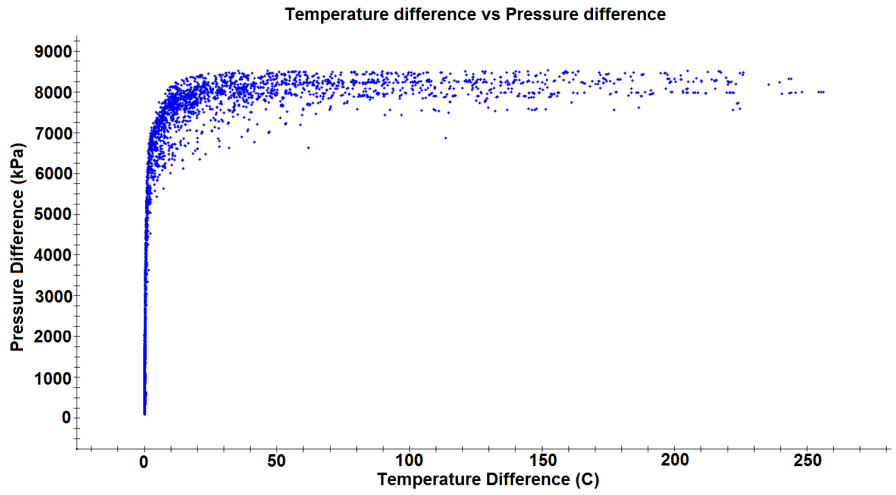

Figure 6.6: Temperature (C) plotted against Pressure (KPa), Jan 2005

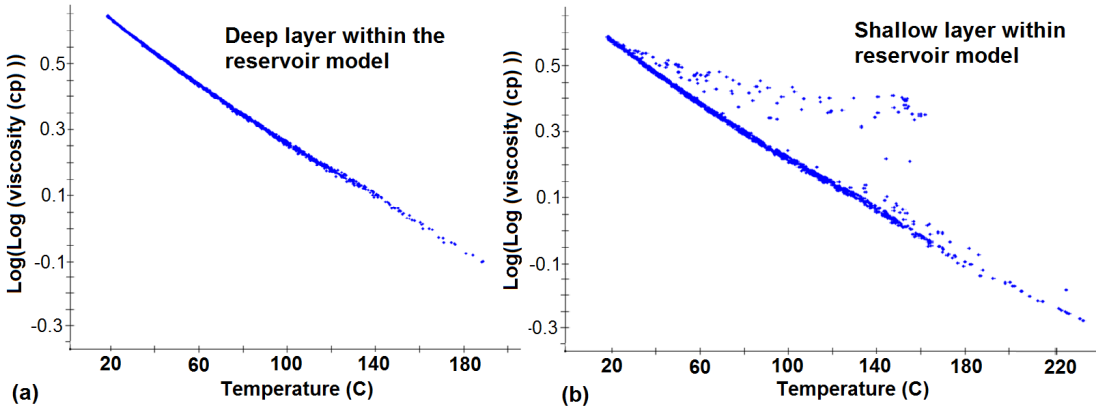

Figure 6.7: Viscosity dependence on Temperature (C) for two layers within reservoir: deeper layer (left) and shallower layer (right). Y-axis is double log of viscosity, deviation from linear relationship corresponds to difference in initial properties

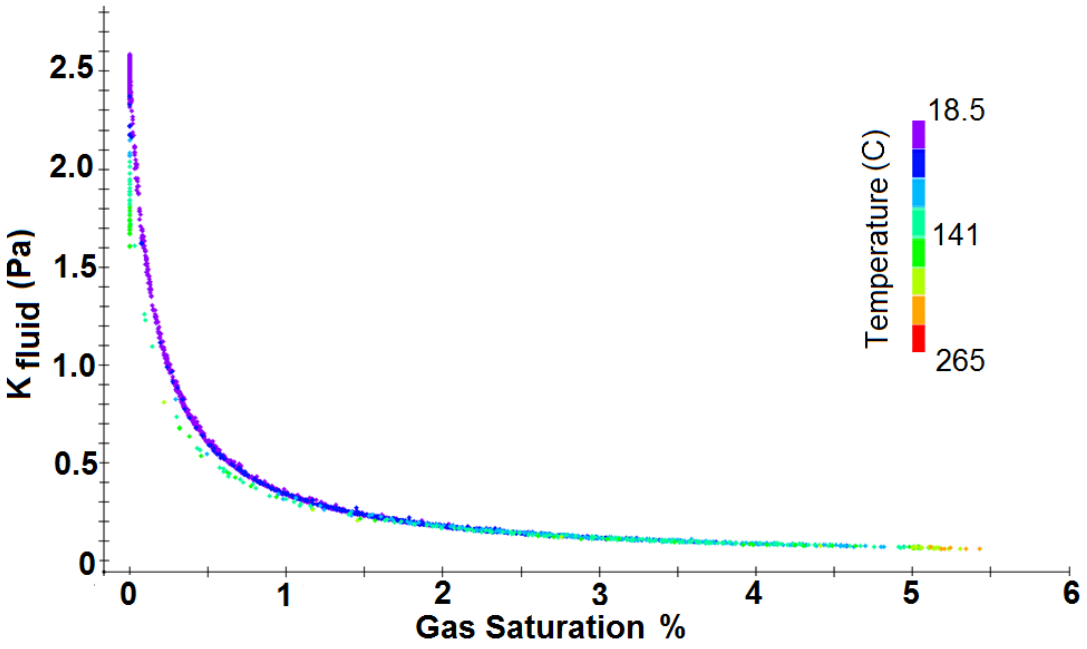

Figure 6.8: Gas Saturation against K fluid modulus (Note the biggest decrease in K corresponds to small increase in gas saturation)

Figure 6.8 is the effect of the gas saturation on fluid K modulus. It is very important to note that gas saturation affects K_{fluid} significantly during the initial injection, where saturation increases from 0 to 0.5% and then the effect tapers down and subsequent injection does not change the modulus much. Also, our model does not differentiate between hydrocarbon gas coming out of the solution during a decrease in pressure and the steam during an injection. However, the same effect on seismic is expected for hydrocarbon gas as for the steam, where small initial changes of hydrocarbon saturation have significant effects on the modulus and thus on the synthetic seismic amplitudes.

In complicated systems like enhanced oil recovery operation sites, multiple variables change over time (e.g. oil viscosity and saturation, gas and steam saturations, water content, temperature and pressure). It is important to understand

that these variables affect seismic amplitudes simultaneously. Having frequent seismic repeats help follow these changes and synthetic provides a way of better constraining interpretations and allows modifications of the static models for a better match with real seismic.

6.6 Synthetic seismic vintages

The last two steps before synthetic generation is defining overburden and underburden velocity models and choosing a seismic wavelet. The overburden and underburden velocity models are computed using "velocity blocking". Velocity blocking is a common technique to compute a coarsely layered velocity and density grids from finely sampled in-well velocity measurement (Cox et al., 2009). The wavelet for the synthetics was extracted from a well-tie using seismic reflection data acquired in the field. Its phase is close to zero with a dominant frequency around 20Hz (Figure 6.9).

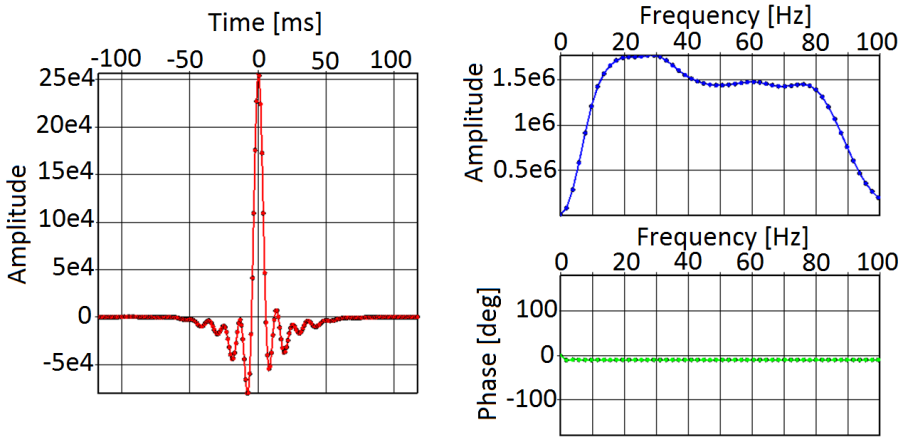

Figure 6.9: Well-tie wavelet used for synthetic seismic generation (left), frequency (top right) and phase (bottom right) spectrum of this wavelet

Figure 6.10 is an example of produced 2D synthetic seismic profile for two time steps: before and during operations for aa' profile. Seismic is "hanged" on the top horizon (denoted by T), which means that the depth of the reservoir is set to be the same for both time steps even if there is a reservoir compaction. Some of the effects of productions and/or injections are evident by visually comparing these 2D profiles, however it is easier to analyze 3D seismic volumes using extraction of seismic attributes, like Minimum Amplitude, Root Mean Square of Amplitudes etc and plotting them in a map view.

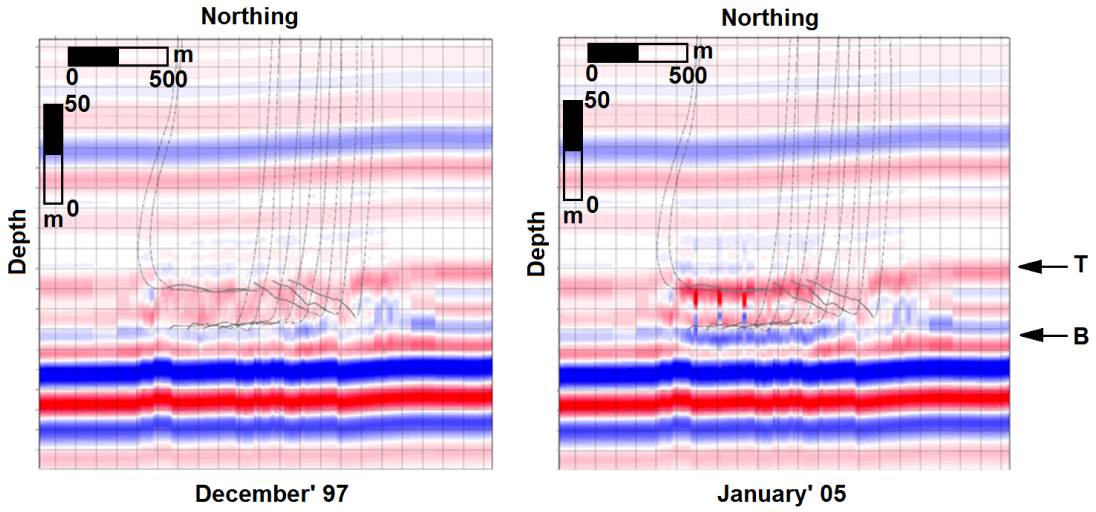

Figure 6.10: Example of produced seismic for profile a'a (Figure 6.1 for before the production in December 97 (left) and during the operation in January 05 (right). T corresponds to the Top of the reservoir and B corresponds to the Base of the reservoir

Seismic amplitudes however can be indicative not only of dynamic processes, like changes is steam and oil saturations, but also of static properties, like varying porosities, densities, initial oil saturation, even thickness (Widess, 1973) within the reservoir. An example of how static properties affect seismic amplitudes in conjunction with dynamic properties, is demonstrated in Figure 6.11, where acoustic impedance is plotted against porosity (i.e. dynamic prop-

erty vs. static property). Colors represent different saturation, with blue highlighting grids with no gas (steam or hydrocarbons). The general linear trend of blue dots is due to porosity only, which is broken slightly by increase in pressure and temperature. The linear trend of the blue datapoints is irrelevant during the assessment of dynamic properties, and therefore is generally subtracted. Note that most of the black dots (change below 11%) are around the high porosities contributing to the biggest changes in acoustic impedance. It is interpreted as more gas is able to penetrate the rock at higher porosities. Thus, even after the subtraction of the trend, static properties will often determine the behaviour of the reservoir.

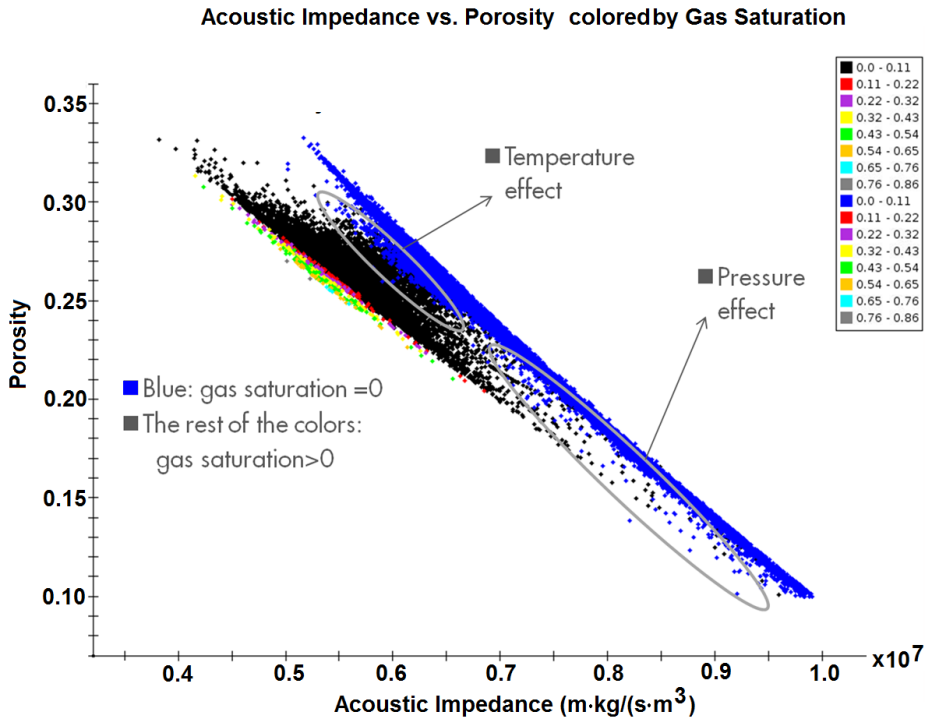

Figure 6.11: January 2008, Acoustic impedance vs. porosity with colors representing gas saturations

As we are interested in dynamic changes within the reservoir, any trends

that are associated with the static variations should be subtracted. The easiest way of doing it is to acquire a base survey prior to steam injections and oil extraction. Figure 6.12 demonstrates the base case by means of amplitude map, where minimum amplitude was extracted from generated seismic at the reservoir (between T and B in Figure 6.10). The variations in amplitudes are due to initial conditions of both static and dynamic properties. In reality, however, extensive seismic surveys are often carried out after the operations have begun and thus such base case is not available. Therefore, a later synthetic vintage was chosen as a base (referred to as ”Base” and is ”Jan07” vintage) to simulate an actual field study for our model’s interpretations . The ”Base0” refers to the synthetic amplitudes before the operations begun (December 1997), which is used for the QC and preparation for interpretation analysis.

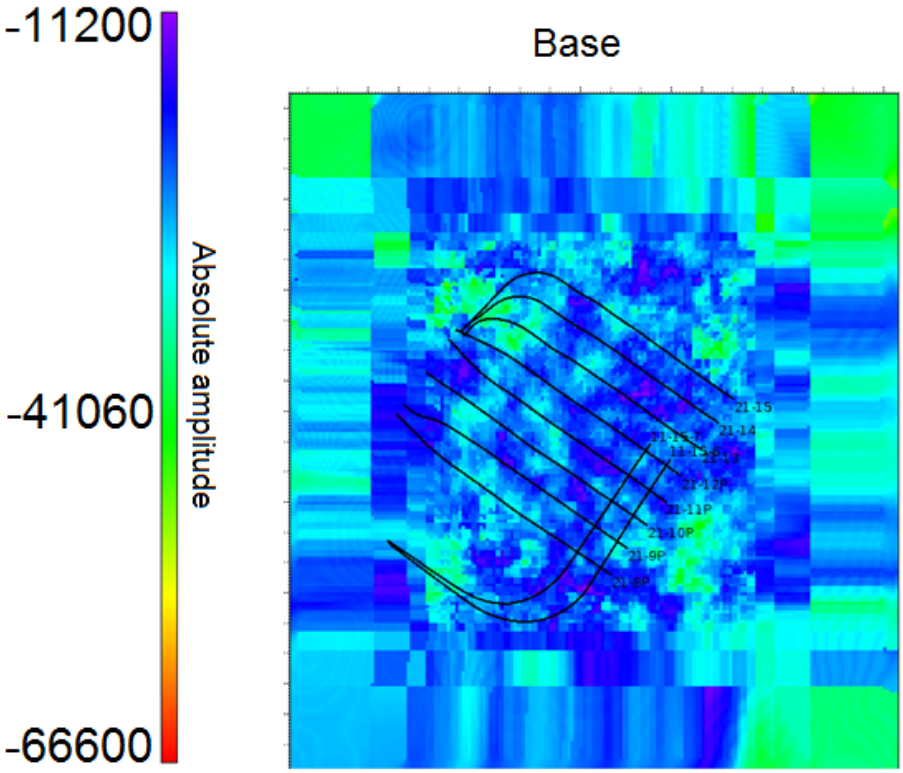

Figure 6.12: Minimum Amplitude measurement for the base case synthetics

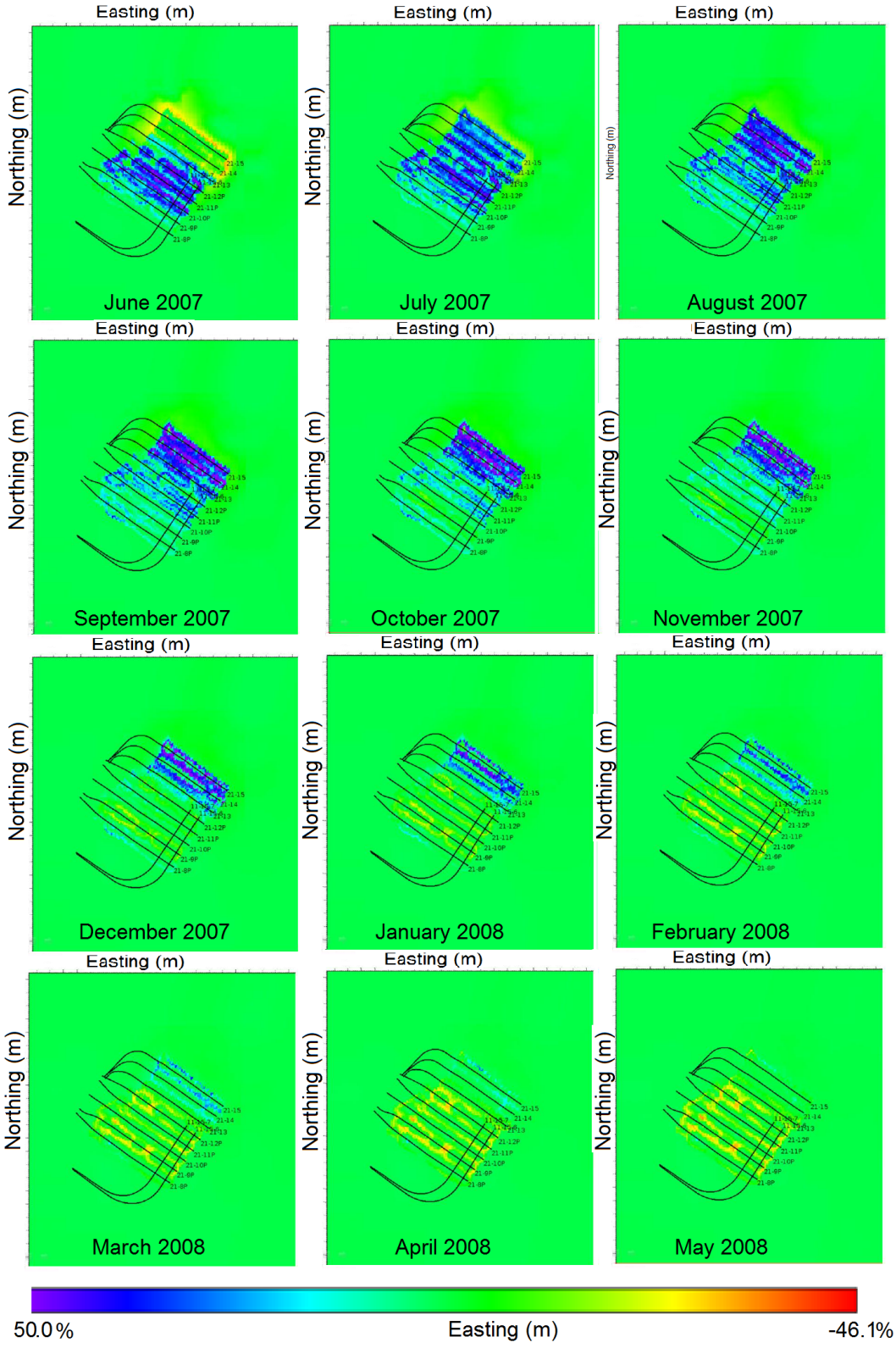

Figure 6.13: Monthly synthetic seismic RMS differences between monitor and base survey (January 2007) to simulate one year of time-lapse seismic responses in the middle of multi-year field operations.

Figure 6.13 shows 12 monthly synthetic seismic RMS (root mean square of all amplitudes within the reservoir) differences with the Base survey for one year in 2007-2008. Note that regions far from the wells (green) have 0% change between the base and the subsequent vintage, which is what is expected in the far-field. We see noticeable monthly amplitude variations close to the wells suggesting that frequent seismic repeats would provide timely information for subsurface monitoring. Annual or biannual repeats would miss much of the reservoir dynamic changes in this case. Also note that the change in amplitudes can reach 50% from the Base survey and therefore can be picked up within the noise for real data easily even for significantly shorter than monthly intervals.

Maron et al. (2005) showed that by differencing RMS amplitudes we can cancel the imprint of variability in static parameters on seismic amplitudes, therefore increasing the sensitivity to small time lapse signals. When surveys are repeated only very sparsely, this conventional 4D analysis becomes difficult and one is often left with interpreting individual time vintages. The interest here however is to quantatively interpret the changes in seismic with the exact knowledge of the reservoir properties in the model, therefore the differencing methodology was chosen (Eq. 6.7).

$$dATTRIBUTE(\%) = 2 \cdot 100\% \frac{ATTRIBUTE_{base} - ATTRIBUTE_{monitor}}{ATTRIBUTE_{base} + ATTRIBUTE_{monitor}} \tag{6.7}$$

6.7 Preparation for simulated interpretation

This section discusses complexities of seismic amplitude interpretations in more details for systems like enhanced oil recovery sites.

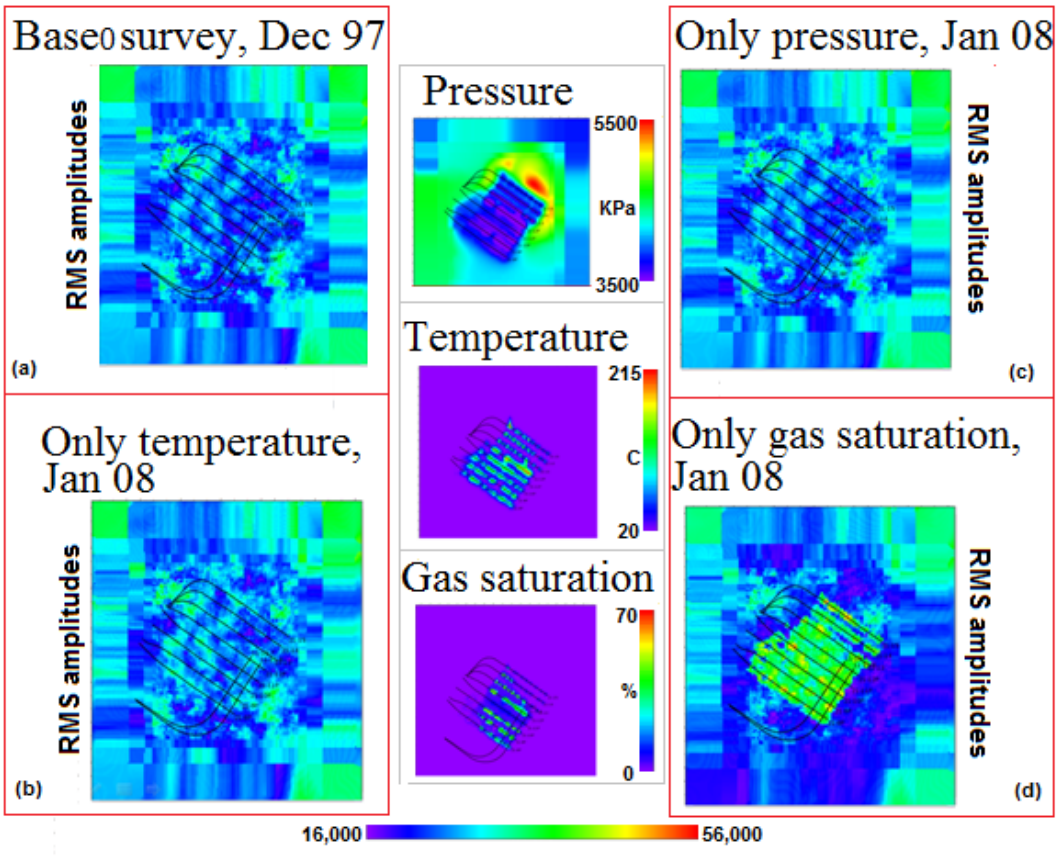

Figure 6.14: RMS Amplitude maps of the December 97 survey (top left) and January 08 (a) only temperature is changing (bottom left), (b) only pressure is changing (top right), and (c) only fluid saturations are changing (bottom right)

Figure 6.14 is a preparation for real seismic interpretation: we generated three different synthetics for a production stage vintage (Jan08) but let only one variable change over time, keeping the rest constant. Here, we are interested in overall effect of one property changing on seismic and not simmulated in-

terpretation, therefore Base0 (prior operations) was chosen to compare with the attribute maps Figure 6.14(a). The first one (Figure 6.14(b)) is generated using reservoir model where only temperature is changing with time and fluid saturations and pressure are kept constant as in Base0 model (December 1997) . The second synthetics (Figure 6.14(c)) is for reservoir model where only pressure is changing and the third one (Figure 6.14(d)) is where only fluid saturations (i.e. gas, oil and water) are changing.

Only in Figure 6.14 the amplitude change is apparent even without differencing with the Base0 survey. Thus, during the production stage most important contributor to the amplitude increase is the change fluid saturations (namely, hydrocarbon gas coming out of solution at decreasing pressures). The effect of gas (steam and methane) on seismic amplitudes is well known; the novelty here is that we cannot differentiate between methane coming in/out of solution with the bitumen and condensing steam vs. live steam.

For the same Jan08 vintage, pressure and temperature effects on seismic are very small and impossible to resolve without subtracting the Base0 from the Jan08. However, Figure 6.15 is an amplitude map computed to illustrate the advantage of having a base survey. This map is s result of subtracting Figure 6.14(a) from 6.14(b), where only the temperature changes affect seismic amplitudes. The pattern in temperature change correlates well with the pattern of the amplitude change, which was not evident in Figure 6.14(b).

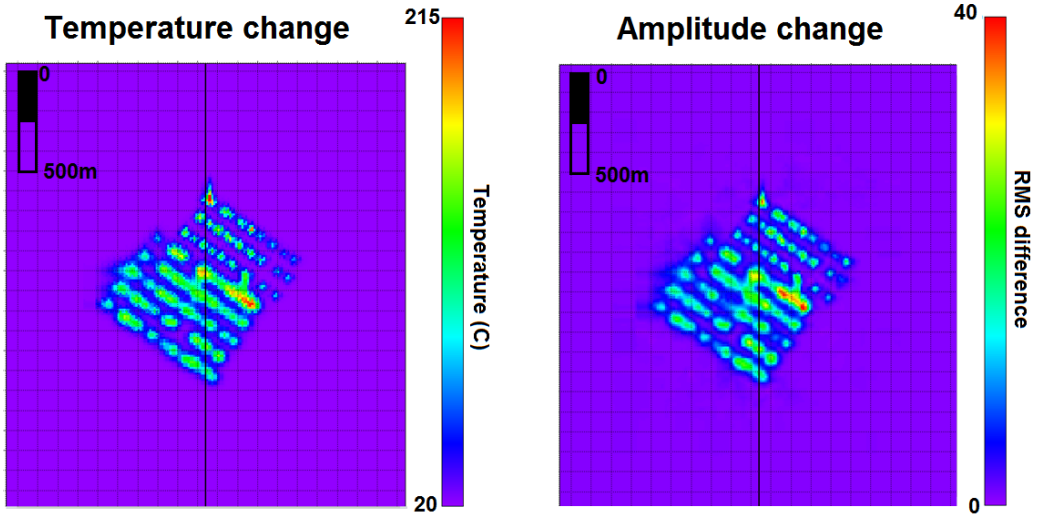

Figure 6.15: Amplitude difference between Base0 and Jan 08, where only temperature is changing (Figure 6.14(b))

To illustrate how seismic is responding to different variable at different times, same one variable (in this case pressure) model was run on the injection stage vintage (Jan05, Figure 6.16). There is an obvious difference in amplitude between the Base0 survey, which was not visible for production stage vintage Figure 6.14(d). Thus amplitude increase can be indicative of two different processes at separate phases in pad's operation history.

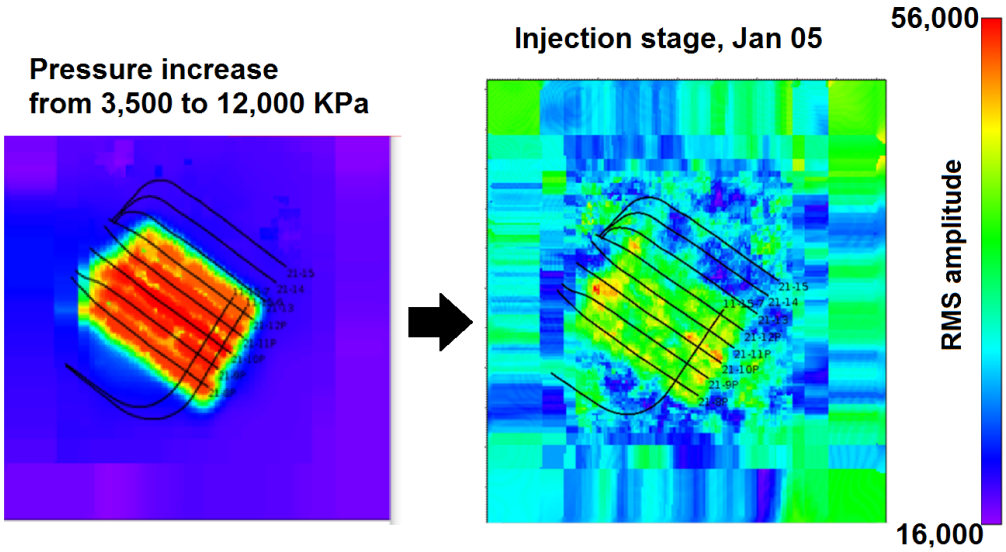

Figure 6.16: Amplitude map for Jan 05 vintage (injection stage), where only pressure is allowed to change

Amplitude measurement is not the only attribute generally used in interpretations. Hornman et al. (2012) has shown that time-shifts can be indicative of pressure changes. As reservoir pressure builds up during steam injection, when it becomes comparable to the overburden pressure and gas saturations are minimal, pressure has the biggest effect on time-shifts, especially away from the wells (Figure 6.17). Note that we are able to correlate pressure changes to time-shifts at every point in the reservoir at this stage, therefore, if we can calibrate this relationship at one or more pressure observation wells, we can extrapolate and generate an areal pressure distribution map based on the observed 4D time-shift maps as in Hornman et al. (2012). However, our model implies that pressure has poor correlation with time-shifts during production stage, when pressure decreases.

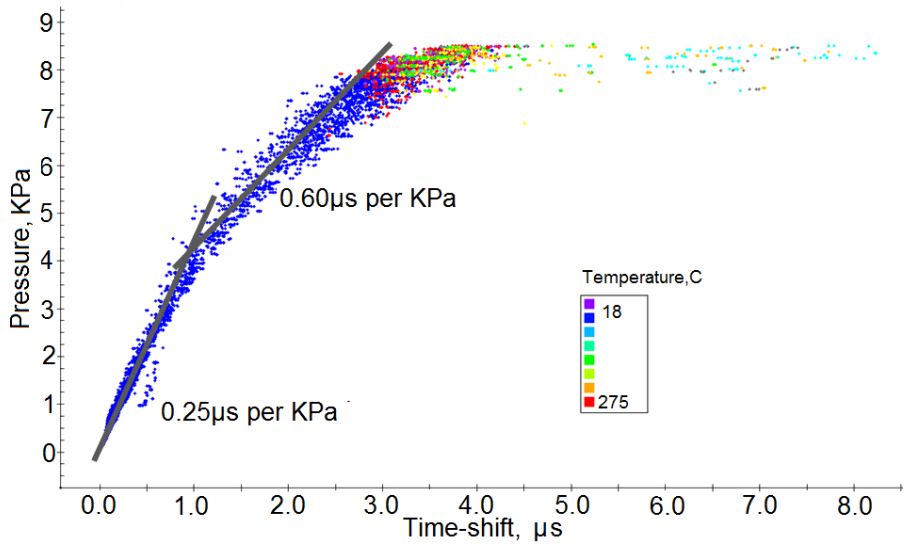

Figure 6.17: Time shift vs. Pressure change across the entire reservoir. Colors are different temperatures (Jan 2005, injection) (as in Hornman et al. (2012)).

Interpretation of 4D seismic amplitude and time-shifts requires knowledge of the production history. However, it can be difficult to interpret specific changes in amplitudes with changes in properties without frequent seismic repeats due to variable influence of certain properties on seismic response. These changes can be hard to follow, especially during the switch between injection and production and vice versa.

6.8 Simulated interpretation examples

Having established the effect that the dynamic properties have on the seismic amplitudes, the interpretation of all seismic vintages was carried out. This simulates real seismic interpretations and allows us to assess the limitations of seismic amplitude analysis.

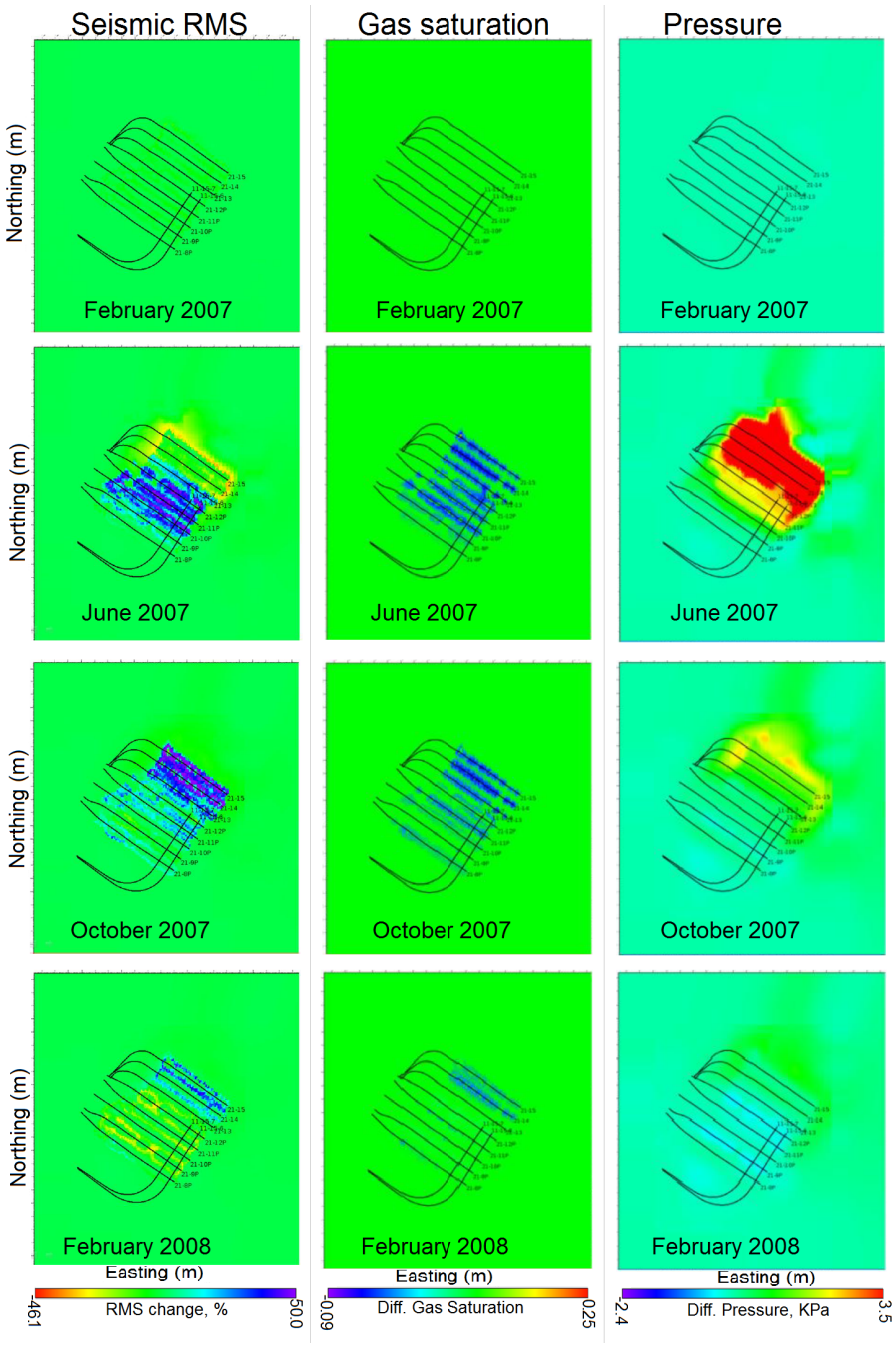

Figure 6.18: Example of RMS difference between a base in the middle of the production history (January 2008) and 3 vintages with underlying change in pressure and gas saturation. Bar scale for RMS is +50% to -46% (blue - red), Pressure from +3500 KPa to -2500 KPa

Figure 6.18 is an example of RMS differences with a synthetic Base survey (Jan07) and 3 monitor vintages, showing how these differences correlate depending on the impact of production/injection on pressure and gas saturation. The changes in amplitudes are large and can be very rapid especially during injection. For June 2007 amplitude distribution for bottom 5 wells correlates with gas saturations decrease; for top three wells negative amplitudes increase due to pressure increase at these wells. For later vintages the pore pressure remains well below the overburden pressure, therefore seismic response is driven mostly by gas saturation in the reservoir.

After this amplitude analysis described above was applied to 24 monthly vintages and 14 annual vintages, we inferred that during the injection stages the amplitudes can change very rapidly such that even more frequent than monthly surveys would be useful. On the other hand, during long production, when pressure and gas saturation are changing slowly, frequent surveys are not required. In reality, however, in large developments with many contiguous production patterns, injection and production are taking place in nearby patterns simultaneously, and the timescales of these reservoir processes are difficult to predict or disentangle, making frequent monitoring very desirable.

6.9 Conclusions

Gas saturations in the reservoir have the biggest effect on seismic amplitudes, especially for steam at the beginning of injection and methane during production. Moreover, the dependence is logarithmic, which means that saturation increase from 0 to 0.5% has a significant effect on the modulus. Pressures can

have large effects on 4D time-shifts but only during injection, when they can approach overburden pressure.

Large changes in amplitudes between monthly repeats suggest that amplitude response may be detectable at even more frequent intervals. Short intervals between seismic surveys are beneficial as: (1) frequent information about the subsurface, when comparing history matched dynamic modeling and 4D seismic, would allow timely adjustments to pad operations, (2) steam operations introduce extra variables into the system, not only temperature, pressure and oil saturation are changing but also gas and water saturations, which affect seismic response differently at different times depending on the phase of production, therefore following closely these changes in amplitudes and time-shifts will allow us to interpret them more robustly.

We also argue that generating synthetic seismic in conjunction with real seismic surveys will help interpretation: if synthetic seismic is vastly different from one vintage to another from real seismic images, adjustments can be made in static and dynamic parameters, thus making history matching and future production prediction more accurate.

6.10 Acknowledgments

Many colleagues at Shell for their input and guidance: Marcus Patterson, Hossein (Ali) Dortaj, Rob Bialas, Kurang Mehta, Gunnar Holmes, Izu Ariwodo, Barbara Cox, Bob Whale, Barbara Wingate. We thank Shell for permission to publish this paper.

APPENDIX A

ABBREVIATIONS AND DEFINITIONS

AGC: Automatic gain control (balances out the amplitudes along the whole trace)

CMP: Common Mid-Point

Common Receiver Stack: Summation of traces recorded by the same receiver

CSS: Cyclic Steam Stimulation

EOR: Enhanced Oil Recovery

f-k: Frequency (f) - wavenumber (k)

Head Wave: Critically refracted wave

LAB: Lithosphere-Asthenosphere Boundary

Move-out: Change of the arrival time with offset

NMO: Normal Move-Out

QC: Quality Control

RMS: Root Mean Square (Amplitude)

SAGD: Steam Assisted Gravity Drainage

SNR: Signal to Noise ratio

Stack: Summation of a record according to sorting (e.g. common-receiver, common-reflection point etc.)

Stationary point: the location of the source of energy, which comes in phase stationary for the receivers

TDSD: Top Down Steam Drive

VS: Virtual Shot

ZOP: Zero Offset Profile (or Profiling)

APPENDIX B

SYNTHETIC SEISMIC GENERATION FOR CHAPTER 2

B.1 Source record generation

```
clear
dx=10; %distance between grids
 %%%%%%%%%%%%%%%%%% Setting up velocity model %%%%%%%%%%%%%%%%%%
    xmax=10000;zmax=2000;%grid size, max line length, max depth
    x=0:dx:xmax;z=0:dx:zmax; % x and z coordinate vector
    vhigh=3750;vlow=2500;vrange=vhigh-vlow; % high and low velocities
    vel=vlow*ones(length(z),length(x));%initialize velocity matrix
    z1=400;z2=zmax;v1=2000; %vlow+vrange/2;%first layer
    xpoly=[-dx xmax+dx xmax+dx -dx];zpoly=[z1 z1 z2 z2];
    vel=afd_vmodel(dx,vel,v1,xpoly,zpoly);%install first layer
 %%%%%%%%%%%%%%%%%%%%%%%%%%%%%%%%%%%%%%%%%%%%%%%%%%%%%%%%%%%%%%%%
    %do a shot record model
    dt=.004; %temporal sample rate
    lap=2;%laplacian flag
    dtstep=sqrt(3/8)*dx/max(vel(:));
    dtstep=floor(dtstep/.0001)*.0001; %modelling step size

    tmax=4*zmax/vlow; %maximum time
    xrec=x;
    zrec=zeros(size(x));
    snap1=zeros(size(vel));
    snap2=snap1;
    snap2_size=size(snap2);

 %%%%%%%%%%%%%%%%%%%% Ploting Velocity Model %%%%%%%%%%%%%%%%%%%%%%%
 plotimage(vel-.5*(vhigh+vlow),z,x,4,'cool');%plot the velocity model
 hold on;
 text(800,40,'2500 m/s','fontname','arial','fontsize',14,'color','w');
 text(800,700,'3750 m/s','fontname','arial','fontsize',14);

 xlabel('Distance (m)','fontname','arial','fontsize',16);
 ylabel('Depth (m)','fontname','arial','fontsize',16);
 set(gca,'fontname','arial','fontsize',14);
 title('velocity model');
 hold on;
```

```
36
37 %%%%%%%%%%%%%%%%%%%%%%%%%%%%%%%%%%%%%%%%%%%%%%%%%%%%%%%%%%%%%%%%%%%%%%%
38     shot_x=randi(length(x)-round(length(x)*0.8),1,50)+round(length(x)*0.4);
39     %shot_z=randi(round(z1*length(z)/zmax),1,50);
40     shot_z=randi(round(snap2_size(1)/4)-1,1,50)+round(snap2_size(1)*1/12);
41    text(shot_x*xmax/length(x),shot_z*zmax/snap2_size(1),...
42        '\bullet','fontname','arial','fontsize',14);
43    hold off
44    axis equal
45   %%
46   t=0:dt:tmax;
47    for k=1:length(shot_z)
48     snap2(shot_z(k),shot_x(k))=1; %shot at depth
49     %create the synthetics:
50    [seisfilt_depth,seis_depth,t]=afd_shotrec(dx,dtstep,-dt,tmax,vel,...
51        snap1,snap2, xrec,zrec,[10 15 40 50],0,lap);
52    filename=[ 'ShallowL2LOW_Shot_x_' num2str(shot_x(k)) '__Shot_z_' ...
53        num2str(shot_z(k))  'grid10.sgy' ];
54      altwritesegy(filename, seis_depth, dt); %save unfiltered seismic
55      WriteSegyTraceHeaderValue(filename, k, 'key', 'FieldRecord');
```

APPENDIX C

MATLAB CODES FOR BRADFORD EXPERIMENT

C.1 Cross-correlation function

```
function [xcorr_sim, xcorr_stacked] = xcorr_matrix_all(datain,tr_number)
% function crosscorrelates tr_number trace with all the others and stack
% negative and positive lags
%by Anastasija Cabolova
%trace_auto=datain(:,tr_number);

[r,c]=size(datain);
xcorr_sim=zeros(2*r-1,c);
parfor (trace=1:c,2)
   xcorr_sim(:,trace)=xcorr(datain(:,tr_number), datain(:,trace));
end

samples=length(xcorr_sim);
negative_lag=zeros((samples+1)/2,c);
negative_lag(2:end,:)=xcorr_sim((samples-1)/2:-1:1,:);
positive_lag=xcorr_sim((samples+1)/2:end,:);

xcorr_stacked=negative_lag+positive_lag;
end
```

C.2 Frequency correlation

```
function xcorr_fft_simm=xcorr_freq_simm2(data_fft,receiver)

%function receives fourier transformed data and computes xcorr in frequency
%space, the output is also in frequency space and therefore has to be
%converted to time domain
[s,r]=size(data_fft);

ifft_xcorr=zeros(s,r); %correlated data will come here
data_a=conj(data_fft(:,receiver));%conjugate of the virtual shot station
```

```
  for i=1:r
      ifft_xcorr(:,i)=data_a.*data_fft(:,i);%multiply in Fourier space
   if isempty(find(isnan(ifft_xcorr(:,i))))==0
                       ifft_xcorr(:,i)=zeros(size(ifft_xcorr(:,i)));
   end
  end

 xcorr_fft_simm=ifft_xcorr;

end
```

C.3 Frequency correlation and clipping

```
function fft_clipped_matrix=fft_clip_matrix(datain,clp)

%function first finds Fourier transform of an array then clips frequency of
%the power spectra (abs(data_fft)), by
%calculating an average of power, than assigning that maximum power should
%not be more than clp*mean(power), and if it is larger, that point of
%data_fft will be devided by it's power and multiplied by clp*mean(power)
%A.Cabolova

[s,r]=size(datain);
fft_clipped_matrix=zeros(2*s-1,r);
for i=1:r
    data=datain(:,i);
    data=detrend(data); %debias
    av=mean(abs(data));
if av~=0
    data=data/av; %normalize data before calculating its spectra
end
data_fft=fft(data, 2*s-1);%Fourier transform
power=abs(data_fft); %power spectra
av_power=mean(power);

fft_clipped=data_fft;
if clp~=0 %do not clip if clp==0
locations=find(power>clp*av_power);
  if isempty(locations)==0
```

```
    fft_clipped(locations)=clp*av_power*data_fft(locations)./power(locations);
  end
end
  fft_clipped_matrix(:,i)=fft_clipped;
end

end
```

C.4 f-k filter setup

```
clear all
%FK filter setup for evenly spaced array
%Hfilter is a matrix filled manually
%A.Cabolova

Nx = 15; % Number of samples collected along first dimension
Nt = 30000; % Number of samples collected along second dimension
dx = 260;  % Distance increment (i.e., Spacing between each column)
dt = 2e-3; % Time increment (i.e., Spacing between each row)
x = 0 : dx : (Nx-1)*dx; % distance
t = 0 : dt : (Nt-1)*dt; % time
freq=1/dt;
[wavelet,tw]=ricker(dt,2,max(t));
[wavelet2,tw2]=ricker(dt,2,max(t));
data_spacetime=zeros(Nt,Nx);
slow1=30;
slow2=60;
load('Hfilter.mat');
%%
for i=1:Nx
  data_spacetime(1+(i-1)*slow1,i)=1;
  data_spacetime(:,i)=conv(squeeze(data_spacetime(:,i)),wavelet,'same');
end

data_spacetime2=zeros(Nt,Nx);
for i=1:Nx
 data_spacetime2(1+(i-1)*slow2,i)=1;
 data_spacetime2(:,i)=conv(squeeze(data_spacetime2(:,i)),wavelet2,'same');
end
```

```
data_spacetime=data_spacetime+data_spacetime2;

%%
Nyq_k = 1/(2*dx); % Nyquist of data in first dimension
Nyq_f = 1/(2*dt); % Nyquist of data in second dimension
dk = 1/(Nx*dx);   % Wavenumber increment
df = 1/(Nt*dt);   % Frequency increment
k = -Nyq_k : dk : Nyq_k-dk; % wavenumber
f = -Nyq_f : df : Nyq_f-df; % frequency


fft2result = fftshift(fft2(data_spacetime));%*dx*dt;

figure
subplot(2,1,1);
imagesc(k,f,abs(fft2result));
 colorbar; v=caxis;
title('FFT2');

subplot(2,1,2);
imagesc(k,f,abs(fft2result).*abs(Hfilter));
colorbar; caxis(v);
title('FFT2filtered');
```

C.5 Array synthesis (mixing)

```
function data_mixed=mixing3(data_prep)
mix=3;
[s,w]=size(data_prep);
data_mixed=zeros(s,w);

first=(mix-1)/2;
data_mixed(:,1)=mean(data_prep(:,1:2),2);
data_mixed(:,w)=mean(data_prep(:,w-1:w),2);
for skip=1:w-mix+1
    data_mixed(:,skip+first)=mean(data_prep(:,skip:skip+mix-1),2);
end
end
```

C.6 Example of Cross-correlation m-file

```
clear
%%%%%%%%
% code for crosscorrelations of Bradford Receivers
% Anastasija Cabolova
%%%%%%%%
SIGN=0;%0=>no sign_bit, 1 with sign_bit
av_before_stack=0; %if =1, then normalize before stacking autocorrelations
filt_apply=0; %apply filter if filt_apply=1
%receivers=dir('30*');
channels=1;%how many of channels in a single sgy to crosscorrelate
sampint=2e-3;
Fs=1/sampint;
decim=1; % the factor to decimate the traces if necessary
sampint_d=decim*sampint; %sampling after decimation
data_time=60;%length of each datafiles
data_lenght=data_time*Fs; %how many samples in each datafile per channel
if filt_apply==1
filter_band=fdesign.bandpass('Fst1,Fp1,Fp2,Fst2,Ast1,Ap,Ast2',...
    4,6,48,60,60,1,60,Fs);%setting up the frequency filter
filter_des = design(filter_band,'butter');%type of frequency filter
% fvtool(filder_des); %to look at the filter shape
end
%% making an array of all receivers at 880ft
line=[dir('Line 20*3'); dir('Line 20*7'); dir('Line 20*1');...
    dir('Line 20*5');dir('Line 20*9') ];
receivers=struct;
for i=1:length(line)
   recev=dir([ line(i).name '/3*']);
   s=length(receivers);
   for ii=1:length(recev)
       if s==1
           a=1; else a=0;
       end
   receivers(s+ii-a,:).name=[line(i).name '/' recev(ii).name];
   end
end
clear i
%%
number_receivers=length(receivers);
dataout_sim=zeros(2*data_lenght/decim-1,channels*(length(receivers))-15);
for rec=1:length(receivers)
```

```
tic
    current_receiver=receivers(rec).name;
    files=dir([current_receiver '/*sgy']);% all sgy files in the folder
    r1=0;%reading header until it is not zero

    for fl=1:length(files) % all files
        rec_time=files(fl).name(16:end);
        if strcmp(rec_time(1:6),'091205')==1 %bad data, skip
            continue;
        elseif strcmp(rec_time(1:13),'091207_171000')==1 %bad data, skip
            display('skipping the shot');
            continue;
        end
        %read the first sgy file to set up the matrix and filter:
        dat=ReadSegyFastAna([current_receiver '/' files(fl).name]);
        data=dat(:,2);%only second channel
        if length(data)~=data_lenght
            disp('skipped receiver');
            continue
        end
        %normalize and debias. !!!!for only second channel:
        datain_p=data_preparation(data,SIGN);
        if filt_apply==1
        %filtered data, desimated if needed at the end:
        datain_filter=filter_matrix(datain_p,filter_des,decim);
        else
            sampint_d=decim*sampint;
            datain_filter=datain_p;
        end
 chan=1;
       %%% simmetrical crosscorrelation => 2 lags
       dataout_a=xcorr(datain_filter(:,chan),datain_filter(:,chan));
       if av_before_stack==1
          dataout_a=dataout_a/mean(abs(dataout_a));
       end
       if isempty(find(isnan(dataout_a)))==0
          dataout_a=zeros(size(dataout_a));
       end
    dataout_sim(:,chan)=dataout_sim(:,chan)+dataout_a/mean(abs(dataout_a));

        cross_rec=rec+1;
        gps=2; %ith receiver my matrix starts with 2 (1st is auto)
        for cr=cross_rec:length(receivers)

```

```
86              rec_i=dir([receivers(cr).name '/*' rec_time]);
87              if isempty(rec_i)==1
88                  gps=gps+1;
89                  continue
90              end
91              da=ReadSegyFastAna([receivers(cr).name '\' rec_i.name]);
92              d=da(:,2);
93               if length(d)~=data_lenght
94                   gps=gps+1;
95                  continue
96               end
97              d_p=data_preparation(d,SIGN);%normalize and debias.
98
99              if filt_apply==1
100             d_filter=filter_matrix(d_p,filter_des,decim);%filtered data
101             else
102                 d_filter=d_p;
103             end
104
105               for chan=1:channels
106       %%% simmetrical crosscorrelation => 2 lags
107                 dataout=xcorr(d_filter(:,chan),datain_filter(:,chan));
108                 if av_before_stack==1
109                    dataout=dataout/mean(abs(dataout));
110                 end
111                 if isempty(find(isnan(dataout)))==0
112                     dataout=zeros(size(dataout));
113                 end
114                 dataout_sim(:,(cr-cross_rec)*channels+chan+channels)=...
115 dataout_sim(:,(cr-cross_rec)*channels+chan+channels)+dataout/mean(abs(dataout));
116                 clear dataout
117
118               end
119           gps=gps+1;
120         end
121     end
122
123     i=1;
124
125         for r=rec:length(receivers)
126         output_file_name_cross=[receivers(rec).name(11:15) '_' ...
127             receivers(rec+i-1).name(11:15) 'all_final_scaled'];
128         for cha=1:channels
129         output_file_name_sim= ...
```

```
            ['Cross_880_chan2_xcorrTimeDomain_noFilter_noShot2/Chan_2_'...
            output_file_name_cross '.sgy'];

        altwritesegy(output_file_name_sim, ...
            dataout_sim(1,(i-1)*channels+cha), sampint);

        WriteSegyTraceHeaderValue(output_file_name_sim, ...
           str2double(output_file_name_cross(1:5)), 'key', 'ShotPoint');
        WriteSegyTraceHeaderValue(output_file_name_sim, ...
           str2double(output_file_name_cross(7:11)), 'key', 'TraceNumber');
        WriteSegyTraceHeaderValue(output_file_name_sim, ...
           str2double(output_file_name_cross(1:5)), 'key', 'FieldRecord');

        end
        i=i+1;
        end
%% do not x-correlate two channels that have already been correlated+.
% decrease # of receivers after each VS
    dataout_sim(:,end-channels+1:end)=[];


    dataout_sim=zeros(size(dataout_sim));


    display('Finished:');
    display(current_receiver);
    time=toc;
    display(time);
end
```

C.7 Synthetic Seismic for 3D array and an offset shot

```
%%%%% 3D Simple interferometry test
%%% distribution of ambient sources in 3D array
%%% direct waves ONLY
% by Anastasija Cabolova, Cornell 2014
clear
close all

```

```
v=6;%velocity of the medium (km/s)
dt=0.002;%temporal sampling (s)
t=10;%total time of the record (s)
space=1;%spacing of the stations in x and y direction
freq=1;%dominant frequency of ricker wavelet, Hz
stat_line=15;% number of stations in one line
vir1=5;% station number to be a virtual source in x-direction
vir2=1;% station number to be a virtual source in y-direction
if stat_line > 25
    stat_line=25;
end
stat_num=stat_line^2;%total number of stations
shot=[-10 0]; %location of the seismic source
[wavelet,tw]=ricker(dt,freq,t);%creating ricker wavelet
%% geometry of the stations

temp=linspace(0,space*stat_line-1,stat_line);
X=zeros(stat_line,stat_line);
Y=X;
Distance=X;
Time=X;
loc_sample=X;
%setting up the geometry of the stations
for i=1:stat_line
    X(i,:)=temp;
    Y(:,i)=temp';
end
clear i temp

%% plot geometry
figure
plot(shot(1), shot(2), 'r*');
hold on
for i=1:stat_line
    for j=1:stat_line
    plot(X(i,j),Y(i,j), 'b.');
    end
end
plot(vir1-1,vir2-1,'mo');
hold off
axis('equal')
hold off
xlabel('X-Direction, km');
ylabel('Y-Direction, km');
```

```
%% calculating distance and time for each shot-station (km, sec)
for i=1:stat_line
    for j=1:stat_line
    Distance(i,j)=sqrt((shot(1)-X(i,j))^2 + (shot(2)-Y(i,j))^2);
    Time(i,j)=Distance(i,j)/v;
    loc_sample(i,j)=round(Time(i,j)/dt);
    end
end
clear i j

%% creating traces
traces=zeros([size(Time) t/dt]);
for i=1:stat_line
    for j=1:stat_line
    traces(i,j,loc_sample(i,j))=1;
    traces(i,j,:)=conv(squeeze(traces(i,j,:)),wavelet,'same');
    end
end
clear i j

%% crosscorrelate
traces_xcor=zeros(stat_line,stat_line, 2*t/dt -1);
for i=1:stat_line
    for j=1:stat_line
    traces_xcor(i,j,:)=xcorr(squeeze(traces(i,j,:)),squeeze(traces(vir1,vir2,:)));
     filename=[ 'VirtShot_X' num2str(vir1) '_Y' num2str(vir2)
'Source' num2str(shot(1)) '_' num2str(shot(2)) 'Stat' num2str(i) '_' num2str(j) '.sgy' ];
     %altwritesegy(filename, seisfilt_depth, dt);
     altwritesegy(filename, squeeze(traces_xcor(i,j,:)), dt);
     WriteSegyTraceHeaderValue(filename, i, 'key', 'cdpX');
     WriteSegyTraceHeaderValue(filename, j, 'key', 'cdpY');
     WriteSegyTraceHeaderValue(filename, vir1, 'key', 'SourceX');
     WriteSegyTraceHeaderValue(filename, vir2, 'key', 'SourceY');
    end
end
```

*ricker.m is Ricker wavelet generation function from Crewes seismic modeling toolbox (Margrave, 2003).

*altwritesegy and WriteSegyTraceHeaderValue are modified functions from

SAC2SEGY toolbox ((Hansen, 2010)).

APPENDIX D

SUPLEMENTARY FIGURES

The observed difference between the quality of arrivals retrieved by cross-correlations in Bradford and MASE are mainly related to ambient noise sources, the duration of the experiments and different response functions of the stations (geophones vs. broadband).

Figure D.1 is an example of one month cross-correlation of MASE data, Mexico. It was shown by Vargas (Thesis) that seismic ambient noise recording for this dataset is very well suited for interferometry, because oceanic wave action serves as a constant source of seismic noise in addition to the region being seismically active. In addition, broadband stations were used to record seismicity for MASE survey and therefore low frequencies are more prevalent in this data when compared with Bradford dataset. Vargas used Vista Seismic Processing software (Schlumberger, 2010) to retrieve reflection response from MASE array using "vibroseis cross-correlation" technique and observed surface waves and even hints of the body waves for longer stacking fold. For that reason, one month of recording used in Vargas thesis was used to test the Matlab Cross-correlation code before running it on the Bradford dataset. The result of this test is shown in Figure D.1. As expected, we see prominent surface waves in the direction away from the Pacific ocean (from A to B).

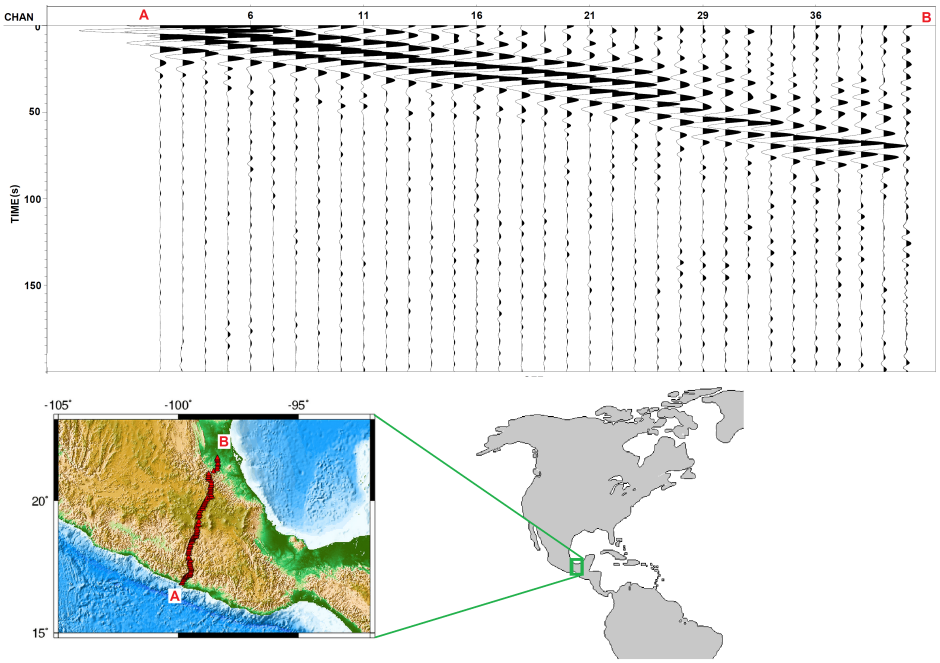

Figure D.1: Cross-correlation example with prominent surface wave using clipping in time domain and no frequency filter on MASE (Mexico) data (array location map inset modified from Clayton (2006))

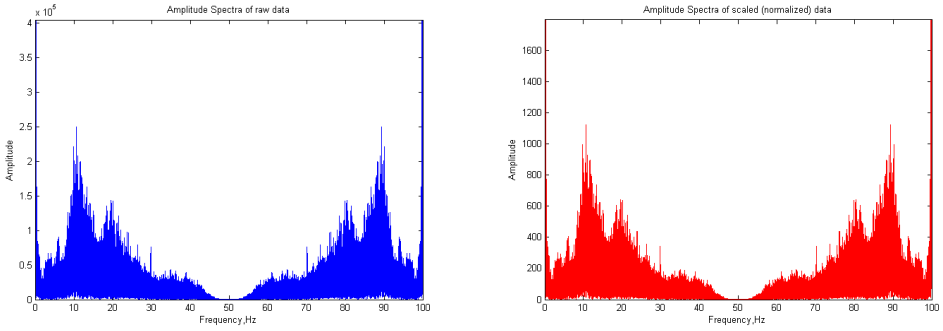

Figure D.2: Power Spectra of sample MASE data. Blue is power spectra of raw data, red power spectra of normalized data (note the change in y-axis)

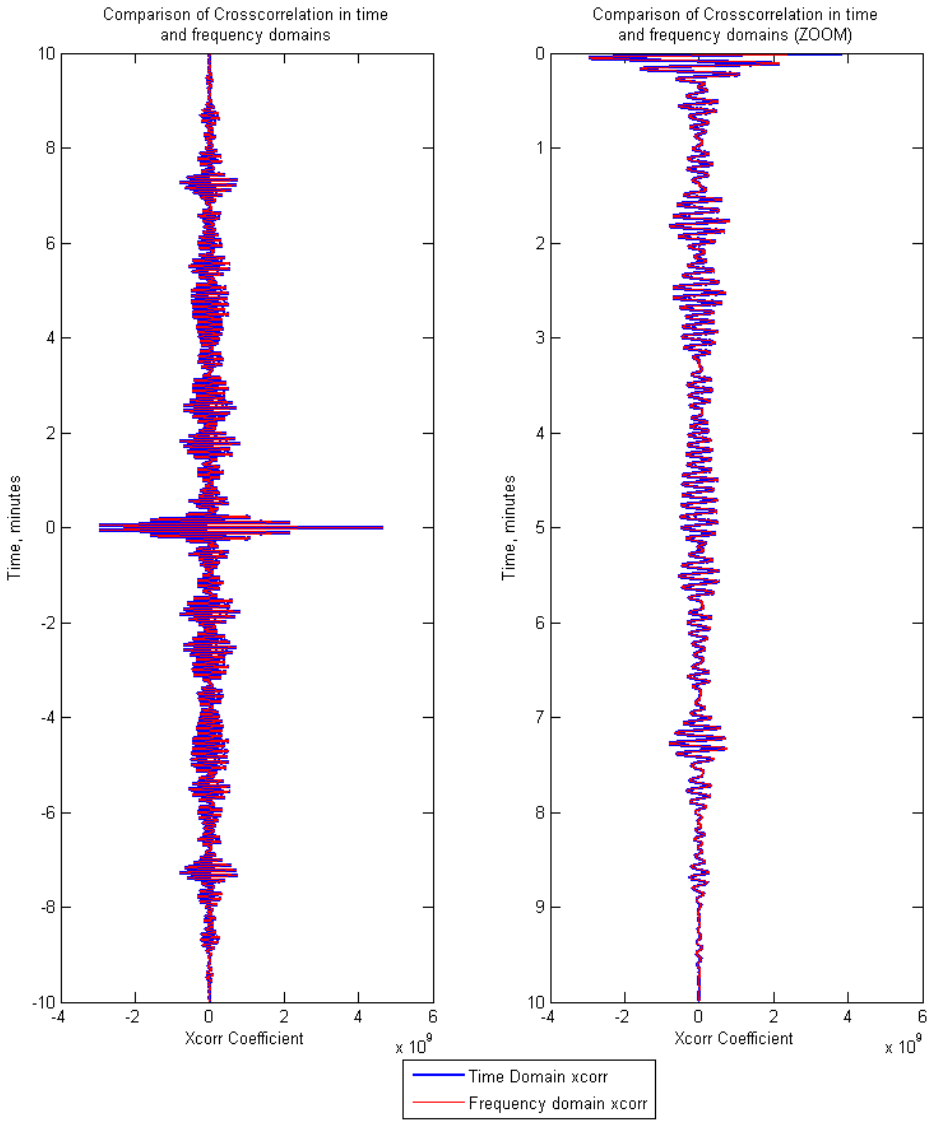

Figure D.3: Comparison of cross-correlation in time (blue) and frequency (red) domain. Full data on the left and zoom into positive lag on the right. (De-trend after correlation)

APPENDIX E

AMPLITUDE PICKS FOR BRADFORD VIRTUAL SHOT

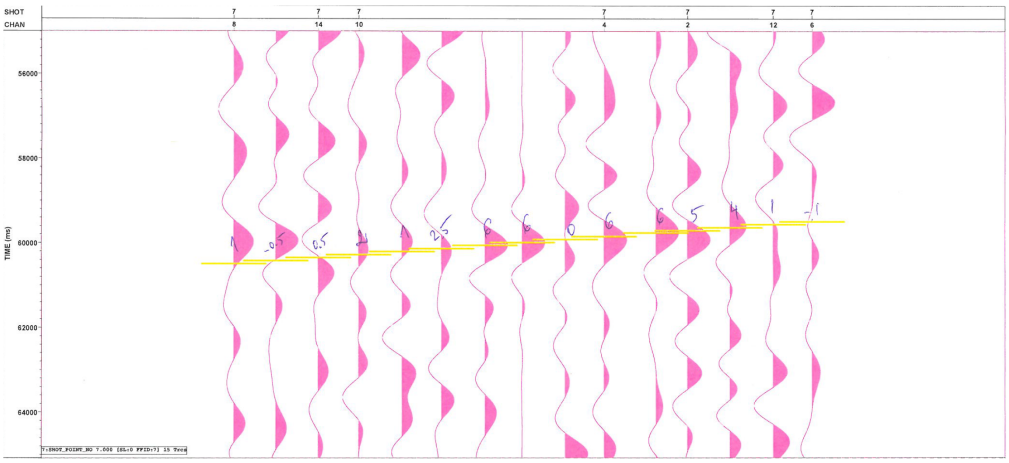

Figure E.1: Amplitude picks, Low frequency, day 1

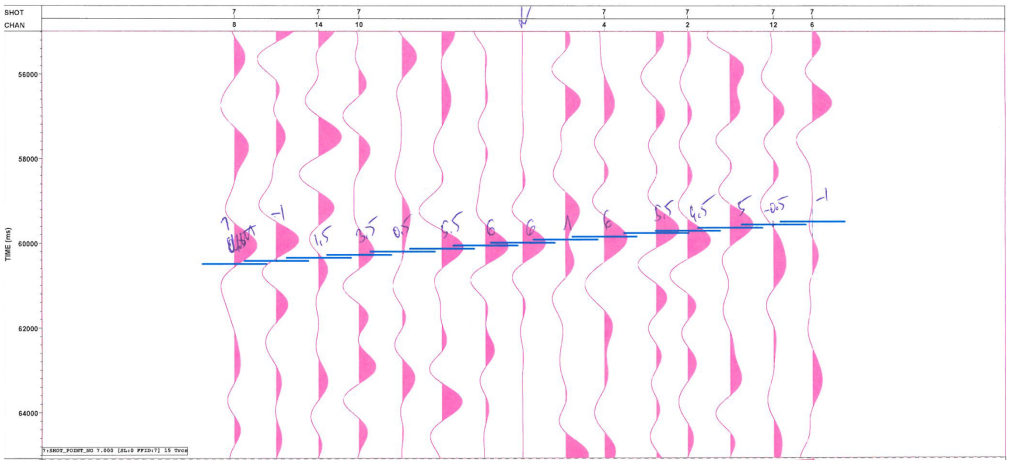

Figure E.2: Amplitude picks, Low frequency, day 2

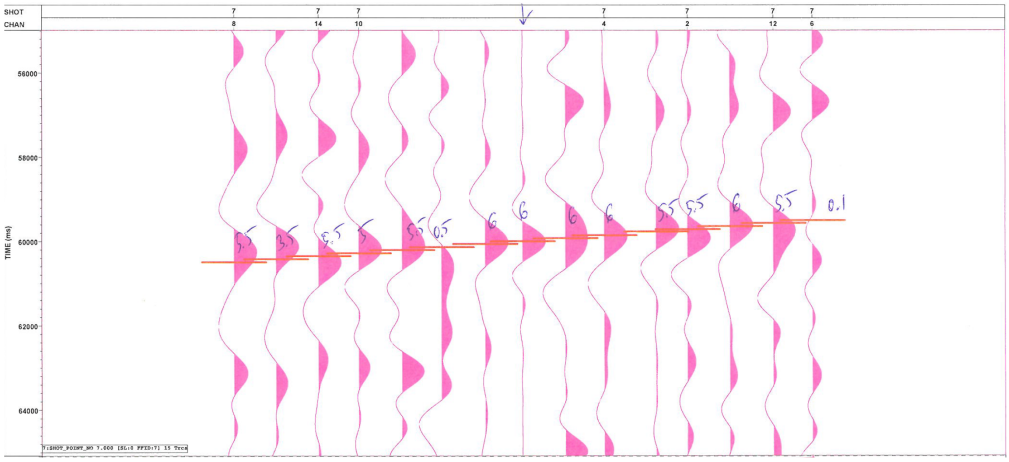

Figure E.3: Amplitude picks, Low frequency, day 3

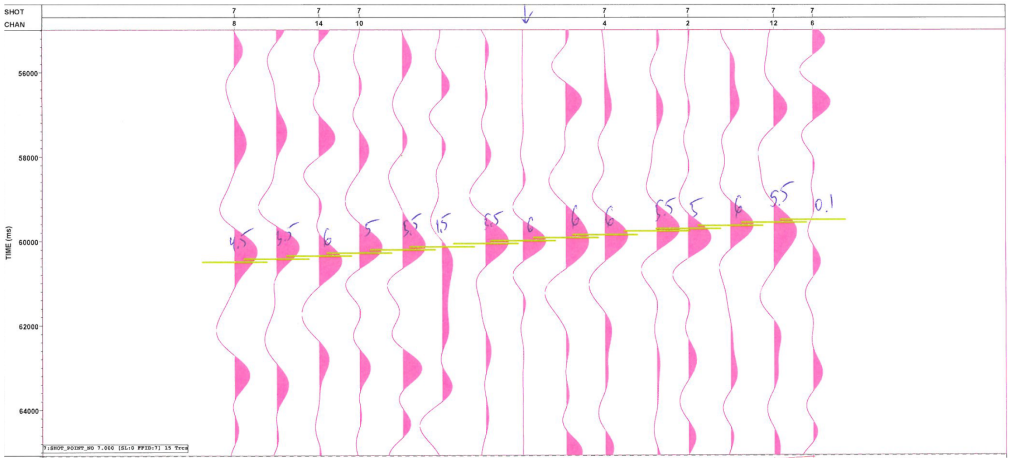

Figure E.4: Amplitude picks, Low frequency, day 4

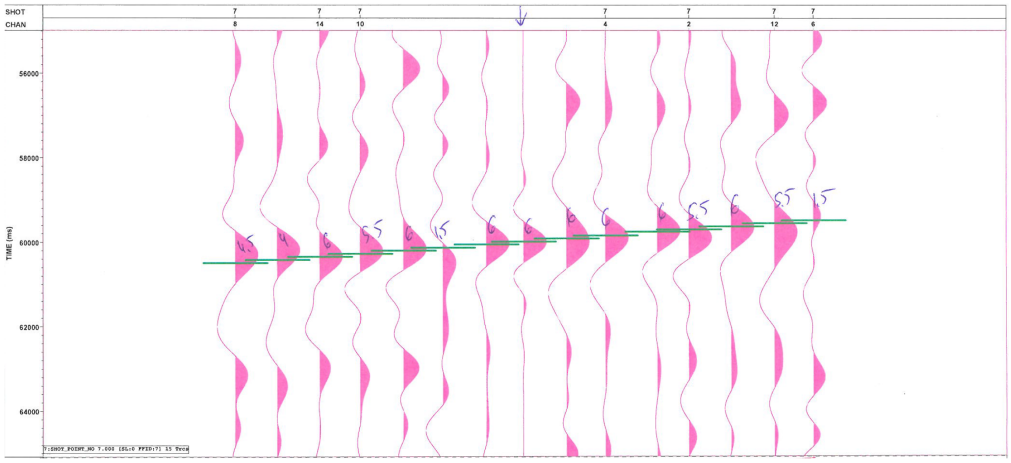

Figure E.5: Amplitude picks, Low frequency, day 5

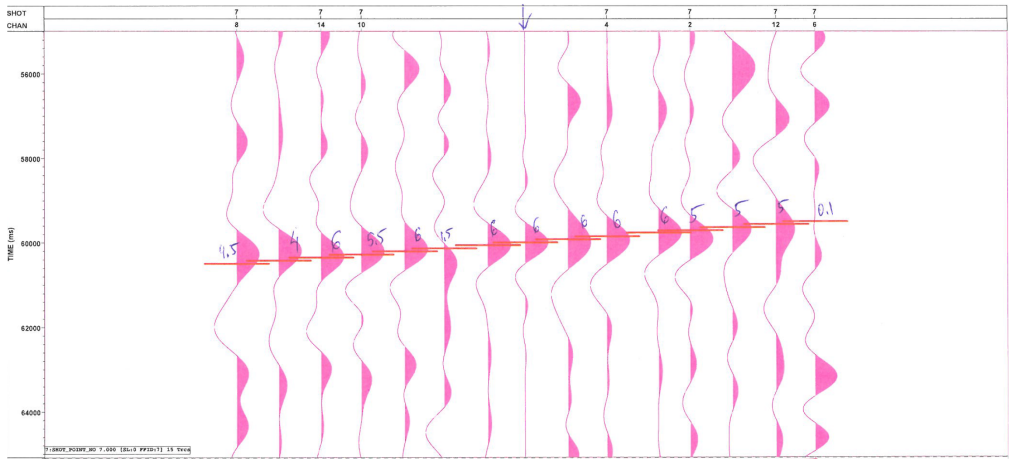

Figure E.6: Amplitude picks, Low frequency, day 6

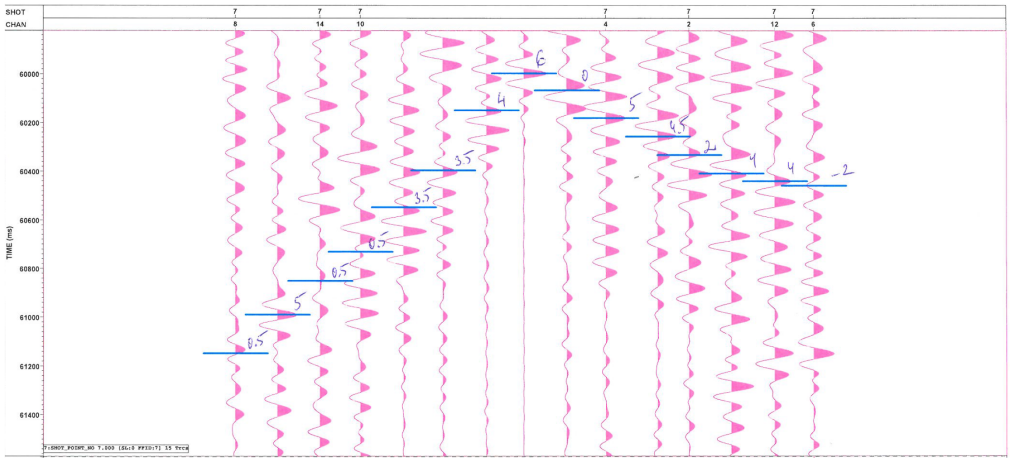

Figure E.7: Amplitude picks, High frequency, day 1

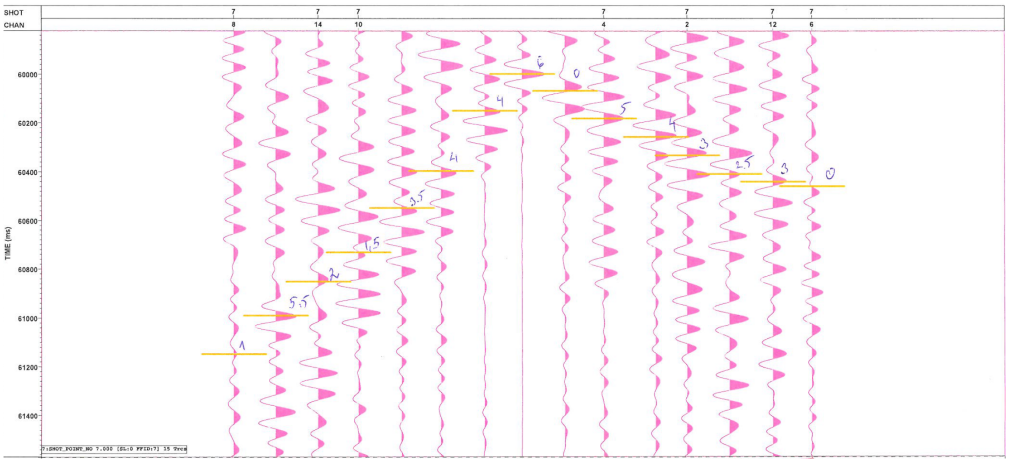

Figure E.8: Amplitude picks, High frequency, day 2

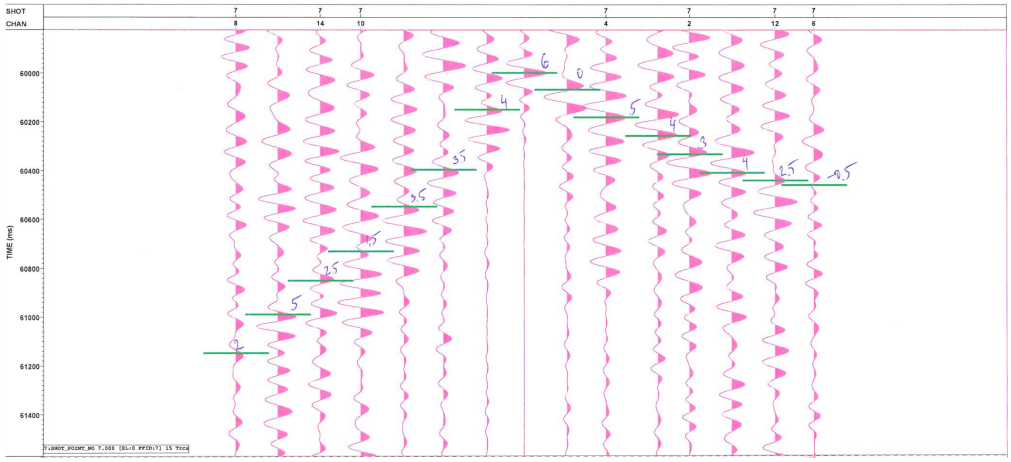

Figure E.9: Amplitude picks, High frequency, day 3

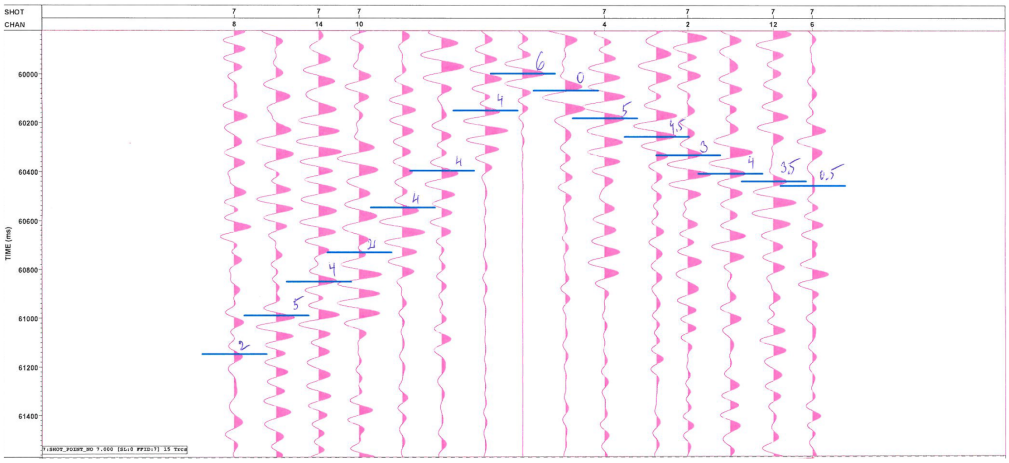

Figure E.10: Amplitude picks, High frequency, day 4

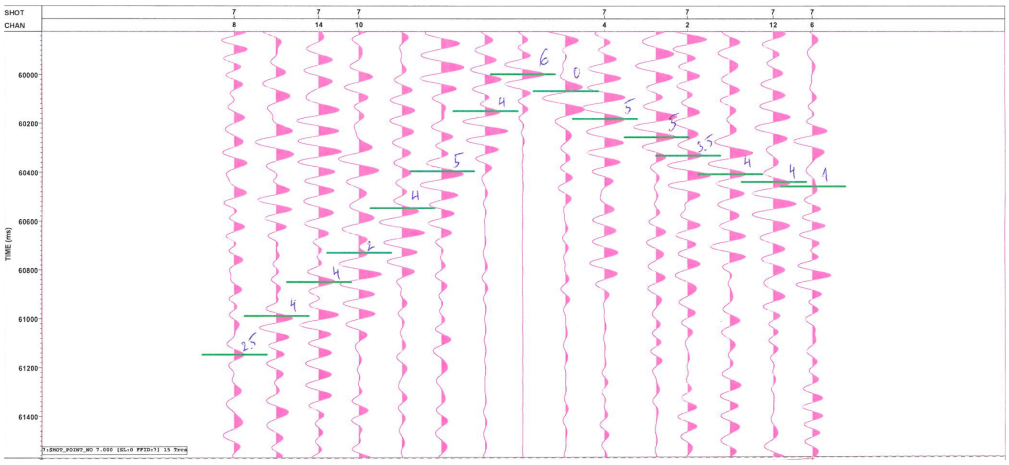

Figure E.11: Amplitude picks, High frequency, day 5

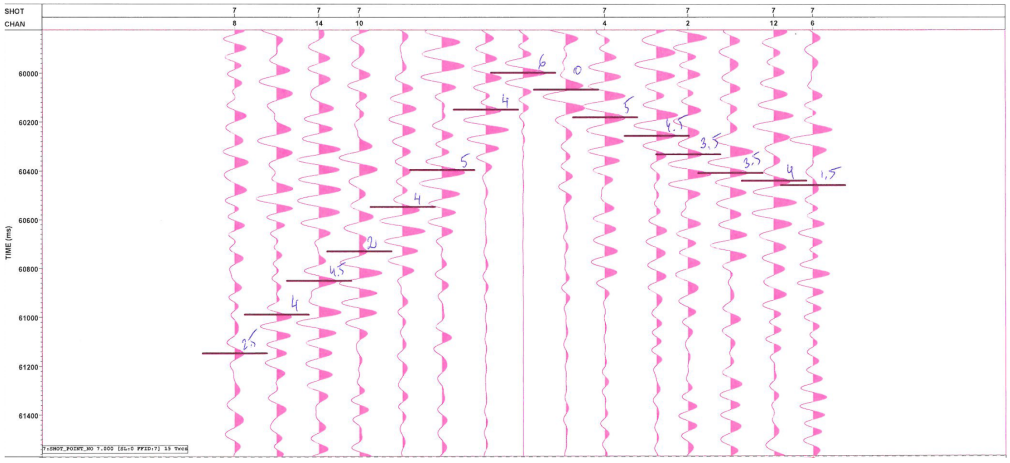

Figure E.12: Amplitude picks, High frequency, day 6

APPENDIX F

ROCK MODEL (CHAPTER 6)

Label	Property
ϕ	Porosity
P	Pressure
T	Temperature
S	Saturation
ρ	Density (FLAG8-fluid, Rock model - bulk)
K	K modulus (FLAG8-fluid, Rock model - bulk)
$v_{p,grain}$	P-wave velocity, 6050m/s
$v_{s,grain}$	S-wave velocity, 4090m/s

Table F.1: Properties for the rock model

In-situ bulk properties at time 0:

$$\rho_{bulk} = (1 - \phi)\,\rho_{grain} + \phi\rho_{fluid} \tag{F.1}$$

Equations F.2 and F.4 from (Cox et al., 2009):

$$v_{p,bulk,0} = 4 \cdot \rho_{bulk,0} - 5950 \tag{F.2}$$

$$K_{bulk,0} = \rho_{bulk,0} \cdot v_{p,bulk,0}^2 - \frac{4}{3}\mu_0 \tag{F.3}$$

$$v_{s,bulk,0} = 0.85\,(\rho_{bulk,0} - 2930) + 1514 \tag{F.4}$$

$$\mu_0 = \rho_{bulk,0} \cdot v_{s,bulk,0} \tag{F.5}$$

$$K_{dry,0} = \frac{K_{dry}\left(\frac{\phi K_{grain}}{K_{fluid,0}} + 1 - \phi\right)^2 - K_{grain}}{\frac{\phi K_{grain}}{K_{fluid,0}} + \frac{K_{bulk,0}}{K_{grain}} - 1 - \phi} \tag{F.6}$$

For vintages at later times, assuming that the shear/dry moduli depend on pressure only, we can use Hertz-Mindlin equation, where P_{ov} is overburden pressure:

$$\mu = \mu_0 \left(\frac{P_{ov} - P}{P_{ov} - P_0}\right)^{1/3} \tag{F.7}$$

$$K_{dry} = \frac{K_{dry,0}}{\mu_0}\mu = K_{dry,0}\left(\frac{P_{ov} - P}{P_{ov} - P_0}\right)^{1/3} \tag{F.8}$$

Once fluid properties are calculated using FLAG8 (Han and Batzle, 2000), we can calculate the remaining reservoir properties, namely K_{bulk}, ρ_{bulk}, v_p and AI.

BIBLIOGRAPHY

Aki, K. (1967), Scaling law of seismic spectrum, *Journal of Geophysical Research*, 72, 1217–1231.

Allenby, R., and C. Schnetzler (1983), United States crustal thickness, *Tectonophysics*, 93, 13—31.

ANCORP, W. G. (1999), Seismic reflection image revealing offset of Andean subduction-zone earthquake locations into oceanic mantle, *Nature*, 397(6717), 341–344.

Arai, R., T. Iwasaki, H. Sato, S. Abe, and N. Hirata (2009), Collision and subduction structure of the Izu-Bonin arc, Japan, revealed by refraction/wide-angle reflection analysis, *Tectonophysics*, 475(3), 438–453.

Asten, M., and J. Henstridge (1984), Arrays estimators and the use of microseisms for reconnaissance of sedimentary basins, *Geophysics*, 49-11, 1828–1837.

Backus, G. E., and J. Gilbert (1967), Numerical applications of a formalism for geophysical inverse problems, *Geophysical Journal International*, 13(1-3), 247–276.

Bakulin, A., and R. Calvert (2004), Virtual source: New method for imaging and 4d below complex overburden, *74th Annual International Meeting, SEG, Expanded Abstracts*, iD:2477-2480.

Bangs, N. L., M. J. Hornbach, and C. Berndt (2011), The mechanics of intermittent methane venting at South Hydrate Ridge inferred from 4d seismic surveying, *Earth and Planetary Science Letters*, 310(1), 105–112.

Beggs, H. D., J. Robinson, et al. (1975), Estimating the viscosity of crude oil systems, *Journal of Petroleum technology*, 27(09), 1–140.

Bensen, G., M. H. Ritzwoller, M. Barmin, A. Levshin, F.-C. Lin, M. Moschetti, N. Shapiro, and Y. Yang (2007), Processing seismic ambient noise data to obtain reliable broad-band surface wave dispersion measurements, *Geophysical Journal International*, 169(3), 1239–1260.

Bickford, M., W. V. Schmus, and I. Zietz (1986), Proterozoic history of the midcontinent region of North America, *Geology*, 14, 492 — 496, doi:10.1130/0091-7613(1986)14.

Bonnefoy-Claudet, S., F. Cotton, and P.-I. Bard (2006), The nature of noise wavefield and its applications for site effects studies: A literature review, *Earth-Science Reviews*, 79, 205–227.

Brewer, J., R. Good, J. Oliver, L. Brown, and S. Kaufman (1983), Cocorp profiling across the southern oklahoma aulacogen: Overthrusting of the wichita mountains and compression within the anadarko basin, *Geology*, 11(2), 109–114.

Brown, L., K. Irie, and B. Voight (2009), Extraction and analysis of seismic body waves from ambient noise for crustal imaging on montserrat, with implications for temporal monitoring, in AGU Fall Meeting Abstracts, vol. 1, p. 2106.

Burdick, L. J., and C. A. Langston (1977), Modeling crustal structure through the use of converted phases in teleseismic body-wave forms, *Bulletin of the Seismological Society of America*, 67(3), 677–691.

Capon, J., R. Greenfield, and R. Kolker (1967), Multidimensional max-likelihood processing of a large aperture seismic array, *Proceedings of the IEEE*, 55(2), 192–211.

Cartwright, L. (1930), Transverse section of Permian Basin, west Texas and

southeast New Mexico, *Bulletin of the American Association of Petroleum Geologists*, 14.

Claerbout, J. (1964), Detection of P-wave from weak sources at great distance, *Geophysics*, 29, 197–211.

Claerbout, J. F. (1968), Synthesis of a layered medium from its acoustic response, *Geophysics*, 33, 264—269.

Clayton, R. (2006), Mase progress report.

Cornelius, A., B. Willman, V. Valleroy, and G. R. L. Powers (1961), Laboratory studies of oil recovery by steam injection, in Paper presented at 35th Annual Fall Meeting-of SPE. Oct, vol. 2, p. 5.

Cotton, J., E. Forgues, J. Hornman, et al. (2012), Land seismic reservoir monitoring: Where is the steam going?, in 2012 SEG Annual Meeting, Society of Exploration Geophysicists.

Coussy, O. (1987), *Acoustics of porous media*, Editions Technip.

Cox, B., P. Wills, and R. Bos (2009), A wokflow for seismi moninoring of pressure and temperature changes in thermal eor eservoirs.

Dietrich, R., and G. Colton (1967), Basement map of N. A. between latitudes 24 and 60n by the American Asscociation of Petrolium Geologists and the U.S. Geological Survey, Washington : U.S. Geological Survey.

Dixon, T. H., and J. C. Moore (2007), *The seismogenic zone of subduction thrust faults*, Columbia University Press.

Dobrin, M. B. (1951), Dispersion in seismic surface waves, *Geophysics*, 16(1), 63–80.

Dougherty, S. L., R. W. Clayton, and D. V. Helmberger (2012), Seismic structure in central mexico: Implications for fragmentation of the subducted cocos plate, *Journal of Geophysical Research: Solid Earth (1978–2012)*, 117(B9).

Draganov, D., K. Wapenaar, and J. Thorbecke (2006), Seismic interferometry: Reconstructing the earth's reflection response, *Geophysics*, 71(4), 161—870, doi: 10.1190/1.2209947.

Draganov, D., K. Wapenaar, W. Mulder, and J. S. andArie Verdel (2007), Retrieval of reflections from seismic background-noise measurements, *Geophysical Research Letters*, 34, doi:10.1029/2006GL028735.

Draganov, D., X. Campman, J. Thorbecke, A. Verdel, and K. Wapenaar (2009), Reflection images from ambient seismic noise, *Geophysics*, 74(5), A63–A67.

Draganov, D., X. Campman, J. Thorbecke, A. Verdel, and K. Wapenaar (2013), Seismic exploration-scale velocities and structure from ambient seismic noise (above 1 hz), *Journal of Geophysical Research: Solid Earth*, 118(8), 4345–4360.

Ferris, A., G. A. Abers, D. H. Christensen, and E. Veenstra (2003), High resolution image of the subducted Pacific plate beneath central Alaska, 50–150 km depth, *Earth and Planetary Science Letters*, 214(3), 575–588.

Flawn, P., A. Young, and J. Foster (1967), Basement map of N. A. between latitudes 24 and 60N by the American Association of Petroleum Geologists and the U.S. Geological Survey, Washington : U.S. Geological Survey.

Forghani, F., and R. Snieder (2010), Underestimation of body waves and feasibility of surface-wave reconstruction by seismic interferometry, *The Leading Edge*, 29(7), 790–794.

Friedrich, A., F. Krüger, and K. Klinge (1998), Ocean-generated microseismic noise located with the gräfenberg array, *Journal of Seismology*, 2(1), 47–64.

Galley, J. (1955), Oil and geology in the Permian Basin of Texas and New Mexico.

Gans, C. R., S. L. Beck, G. Zandt, H. Gilbert, P. Alvarado, M. Anderson, and L. Linkimer (2011), Continental and oceanic crustal structure of the pampean flat slab region, western argentina, using receiver function analysis: new high-resolution results, *Geophysical Journal International*, 186(1), 45–58.

Gassmann, F. (1951), Elastic waves through a packing of spheres, *Geophysics*, 16(4), 673–685.

Gerstoft, P., P. Shearer, N. Harmon, and J. Zhang (2008), Global p, pp, and pkp wave microseisms observed from distant storms, *Geophysical Research Letters*, 35-23, 1828–1837, doi:10.1029/2008GL036111.

Giulio, G. D., C. Cornou, M. Ohrnberger, M. Wathelet, and A. Rovelli (2006), Deriving wavefield characteristics and shear-velocity profiles from two-dimensional small-aperture arrays analysis of ambient vibrations in a small-size alluvial basin, colfiorito, italy, *Bulletin of the Seismological Society of America*, 96(5), 1915–1933.

Gulick, S. P., N. L. Bangs, G. F. Moore, J. Ashi, K. M. Martin, D. S. Sawyer, H. J. Tobin, S. Kuramoto, and A. Taira (2010), Rapid forearc basin uplift and megasplay fault development from 3D seismic images of Nankai margin off Kii peninsula, Japan, *Earth and Planetary Science Letters*, 300(1), 55–62.

Gutenberg, B. (1945), Amplitudes of surface waves and magnitudes of shallow earthquakes, *Bulletin of the Seismological Society of America*, 35(1), 3–12.

Gutenberg, B. (1958), Microseisms, *Geophysics*, 5, 53–92.

Halliday, D., and A. Curtis (2008), Seismic interferometry, surface waves and source distribution, *Geophysical Journal International*, 175, 1067—1087, doi: 10.1111/j.1365-246X.2008.03918.x.

Han, D., and M. Batzle (2000), Velocity, density and modulus of hydrocarbon fluids - empirical modeling, *2000 SEG conference paper*, iD: SEG-2000-1867.

Hansen, T. (2010), Segymat, www.gek0n.ru/external.

Harmon, N., P. Gerstoft, C. A. Rychert, G. A. Abers, M. S. de la Cruz, and K. Fischer (2008), Phase velocities from seismic noise using beamforming and cross correlation in Costa Rica and Nicaragua, *Geophysical Research Leters*, 35, doi: 10.1029/2008GL035387.

Harmon, N., C. Rychert, and P. Gerstoft (2010), Distribution of noise sources for seismic interferometry, *Geophysical Journal International*, 183(3), 1470–1484, doi:10.1111/j.1365-246X.2010.04802.x.

Herrmann, R. B. (2013), Computer programs in seismology: An evolving tool for instruction and research, *Seismological Research Letters*, 84(6), 1081–1088.

Hills, J. (1984), Sedimentation, tectonism, and hydrocarbon generation in Delaware basin, west Texas and southeastern New Mexico, *AAPG Bulletin*, 68(3), 250–267.

Hills, J. (1985), Structural evolution of the Permian basin of west Texas and New Mexico, *Structure and tectonics of trans-Pecos Texas: West Texas Geological Society Publication*, pp. 85–81.

Horike, M. (1985), Inversion of phase velocity of long-period microtremors to the s-wave-velocity structure down to the basement in urbanized areas., *Journal of Physics of the Earth*, 33(2), 59–96.

Hornman, J., J. V. Popta, S. C. Didraga, and H. Dijkerman (2012), Continuous monitoring of thermal EOR at Schoonebeek for intelligent reservoir management, *SPE Intelligent Energy*, iD: SPE 150215.

Hyndman, R., and K. Wang (1995), The rupture zone of Cascadia great earthquakes from current deformation and the thermal regime, *JOURNAL OF GEOPHYSICAL RESEARCH-ALL SERIES-*, 100, 22–133.

Ito, Y., and K. Shiomi (2012), Seismic scatterers within subducting slab revealed from ambient noise autocorrelation, *Geophysical Research Letters*, 39(19).

Keller, G. R., J. Hills, and R. Djeddi (1980), A regional geological and geophysical study of the Delaware basin, New Mexico and West Texas, *New Mexico Geological Society Guidebook, 31st Field Conference, Trans-Pecos Region*.

Keranen, K., M. Weingarten, G. Abers, B. Bekins, and S. Ge (2014), Sharp increase in central oklahoma seismicity since 2008 induced by massive wastewater injection, *Science*, 345(6195), 448–451.

Keranen, K. M., H. Savage, G. Abers, and E. Cochran (2013), Potentially induced earthquakes in oklahoma, USA, Links between wastewater injection and the 2011 mw 5.7 earthquake sequence, *Geology*, 41(6), 699–702.

Kim, D., L. D. Brown, and D. Quiros (2015), Body wave imaging with interferometry of aftershock sources, in SEG extended abstract.

Kim, Y., R. W. Clayton, and F. Keppie (2011), Evidence of a collision between the Yucatán block and mexico in the miocene, *Geophysical Journal International*, 187(2), 989–1000.

Landes, M., F. Hubans, N. Shapiro, A. Paul, and M. Campillo (2008), Studying

the origin of deep ocean microseisms using teleseismic body waves, in AGU Fall Meeting Abstracts, vol. 1, p. 1893.

Landès, M., F. Hubans, N. M. Shapiro, A. Paul, and M. Campillo (2010), Origin of deep ocean microseisms by using teleseismic body waves, *Journal of Geophysical Research: Solid Earth (1978–2012)*, 115(B5).

Larose, E., A. Derode, M. Campillo, and M. Fink (2004), Imaging from one-bit correlations of wideband diffuse wave fields, *Journal of Applied Physics*, 95(12), 8393–8399.

Lin, F.-C., M. Moschetti, and M. Ritzwoller (2008), Surface wave tomography of the western united states from ambient seismic noise: Rayleigh and love wave phase velocity maps, *Geophysical Journal International*, 173(1), 281–298.

Lin, F.-C., V. Tsai, B. Schmandt, Z. Duputel, and Z. Zhan (2013a), Extracting seismic core phases with array interferometry, *Geophysical Research Leters*, 40, doi:10.1002/grl.50237.

Lin, F.-C., D. Li, R. Clayton, and D. Hollis (2013b), High-resolution 3D shallow crustal structure in long beach, california: Application of ambient noise tomography on a dense seismic array, *Geophysics*, 78-4, doi:10.1190/geo2012-0453.1.

Margrave, G. F. (2003), Numerical methods of exploration seismology with algorithms in matlab, www.crewes.org/ResearchLinks/FreeSoftware/ NumMeth.pdf, university of Calgary.

Maron, K., S. Bourne, K. Wit, P. McGillivray, and S. Brissenden (2005), Integrated reservoir surveillance of a heavy oil field in peace river, canada, paperNum: C034.

MASE (2007), Meso America Subduction Experiment, doi:10.7909/C3RN35SP.

Mayer, J., and L. D. Brown (1986), Signal penetration in the COCORP Basin and Range - Colorado Plateau survey, *Geophysics*, 51(5), 1050–1055.

McFarland, J. (2009), How do seismic surveys work, Oil and Gas laweyer blog, graves Dougherty Hearon and Moody.

Mikesell, D., K. van Wijk, A. Calvert, and M. Haney (2009), The virtual refraction: Useful spurious energy in seismic interferometry, *Geophysics*, 74(3), A13–A17.

Mohsen, A. (2004), A receiver function study of the crust and upper mantle across the dead sea transform, Ph.D. thesis, Freie Universität Berlin, Germany.

Mukherjee, T., K. Mehta, J. Lopez, and R. Stewart (2012), Closing the loop via scenario modeling in a time-lapse study of an EOR target in oman, *SEG Technical Program Ezpanded Abstract 2012*, pp. 1—5, doi:10.1190/segam2012-0804.1.

Nábělek, J., G. Hetényi, J. Vergne, S. Sapkota, B. Kafle, M. Jiang, H. Su, J. Chen, B.-S. Huang, et al. (2009), Underplating in the Himalaya-Tibet collision zone revealed by the Hi-CLIMB experiment, *Science*, 325(5946), 1371–1374.

Nakata, N., R. Snieder, T. Tsuji, K. Larner, and T. Matsuoka (2011), Shear wave imaging from traffic noise using seismic interferometry by cross-coherence, *Geophysics*, 76(6), SA97–SA106.

Nicholson, T., M. Bostock, and J. Cassidy (2005), New constraints on subduction zone structure in northern cascadia, *Geophysical Journal International*, 161(3), 849–859.

Okaya, D. (1986), Seismic profiling of the lower crust: Dixie Valley, Nevada, *Reflection Seismology: The continental crust, AGU, Geodynamics series*, 14, 269 — 279.

Oliver, J., and S. Kaufman (1977), Complexities of the deep basement from seismic reflection profiling, *The earth's crust by J. Heacock*.

Oliver, J., M. Dobrin, S. K. R. Meyer, and R. Phinney (1976), Continious seismic reflection profiling of deep basement, Hardeman county, Texas, *Geological Society of America Bulletin*, 87(11), doi:10.1130/0016-7606(1976)872.0.CO;2.

Pardo, M., and G. Suarez (1995), Shape of the subducted rivera and cocos plates in southern mexico: Seismic and tectonic implications, *Journal of Geophysical Research: Solid Earth (1978–2012)*, 100(B7), 12,357–12,373.

Pedersen, H. A., and F. Krüger (2007), Influence of the seismic noise characteristics on noise correlations in the baltic shield, *Geophysical Journal International*, 168(1), 197–210.

Pérez-Campos, X., Y. Kim, A. Husker, P. M. Davis, R. W. Clayton, A. Iglesias, J. F. Pacheco, S. K. Singh, V. C. Manea, and M. Gurnis (2008), Horizontal subduction and truncation of the cocos plate beneath central mexico, *Geophysical Research Letters*, 35(18).

Poletto, F., and B. Farina (2010), Synthesis of a seismic virtual reflector, *Geophysical Prospecting*, 58(3), 375–387.

Poli, P., H. Pedersen, and M. Campillo (2012a), Emergence of body waves from cross-correlation of short period seismic noise, *Geophysical Journal International*, 188(2), 549–558.

Poli, P., M. Campillo, H. Pedersen, and L. working group (2012b), Body-wave imaging of earths mantle discontinuities from ambient seismic noise, *Science*, 338(6110), 1063–1065.

Quiros, D., L. Brown, and D. Kim (2014), Seismic interferometry of cultural noise body waves extracted from auto and train traffic, in AGU Fall Meeting Abstracts, vol. 1, p. 4447.

Rhie, J., and B. Romanowicz (2004), Excitation of earth's continuous free oscillations by atmosphere–ocean–seafloor coupling, *Nature*, 431(7008), 552–556.

Rocco, G., R. Adawi, F. Kindy, S. Busaidi, S. Farsi, A. Maamari, P. Jorgensen, D. Kiyashchenko, K. Mehta, J. Lopez, et al. (2010), Steam development areal surveillance programme in petroleum development oman: Speeor conference at oil and gas west asia, Tech. rep., SPE–129137–PP, Society of Petroleum Engineers.

Roux, P., S. K. G, P. Gerstoft, W. Kuperman, and M. Fehler (2005), P-waves from cross-correlation of seismic noise, *Geophysical Research Letters*, 32(19).

Roy, S. (2013), Near-surface characterization via seismic surface-wave inversion, Ph.D. thesis, University of Houston.

Ruigrok, E., and K. Wapenaar (2012), Global-phase seismic interferometry unveils p-wave reflectivity below the himalayas and tibet, *Geophysical Research Leters*, 39, doi:10.1029/2012GL051672.

Ruigrok, E., X. Campman, and K. Wapenaar (2011), Extraction of p-wave reflections from microseisms, *Comptes Rendus Geoscience*, 343(8), 512–525.

Ruppel, S., and R. Jones (2006), Key role of outcrops and cores in carbonate reservoir characterization and modeling, lower Permian Fullerton field, Per-

mian basin, United States, in Giant hydrocarbon reservoirs of the world: From rocks to reservoir characterization and modeling, vol. 88, edited by P. M. Harris and L. J. Weber, pp. 355–394, doi:10.1306/1215882M88698.

Ruppel, S., and W. B. Ward (2012), Outcrop-based characterization of the Leonardian carbonate platform in west Texas: Implications for sequence-stratigraphic styles in the lower Permian, *AAPG Bulletin*, 97(2), 223–250, doi:10.1306/05311212013.

Ryberg, T. (2011), Body wave observations from cross-correlations of ambient seismic noise: A case study from the karoo, rsa, *Geophysical Research Letters*, 38(13).

Satoh, T., H. Kawase, and S. Matsushima (2001), Estimation of s-wave velocity structures in and around the sendai basin, japan, using array records of microtremors, *Bulletin of the seismological society of America*, 91(2), 206–218.

Schlumberger, T. (2010), Vista seismic data processing.

Schurr, B., G. Asch, A. Rietbrock, R. Trumbull, and C. Haberland (2003), Complex patterns of fluid and melt transport in the central Andean subduction zone revealed by attenuation tomography, *Earth and Planetary Science Letters*, 215(1), 105–119.

Schuster, G. (2001), Theory of daylight/ interferometric imaging: Tutorial, *63rd Conference and Technical Exhibition, EAGE, Extended Abstracts*, a32.

Schuster, G., J. Yu, J. Sheng, and J. Rickett (2004), Interferometric / daylight seismic imaging, *Geophysical Journal International*, 157(3), 838—852, doi:10.1111/j.1365-246X.2004.02251.x.

Sellards, E. (1932), The pre-paleozoic and paleozoic systems in texas, *Texas Univ. Bull*, 3232, 15—238.

Shao, G., X. Li, C. Ji, and T. Maeda (2011), Focal mechanism and slip history of the 2011 m w 9.1 off the Pacific coast of Tohoku earthquake, constrained with teleseismic body and surface waves, *Earth, planets and space*, 63(7), 559–564.

Shapiro, N., M. Campillo, L. Stehly, and M. Ritzwoller (2005), High-resolution surface-wave tomography from ambient seismic noise, *Science*, 307(5715), 1615–1618.

Snieder, R., and K. Wapenaar (2010), Imaging with ambient noise, *Physics Today*, 63(9), 44–49.

Snieder, R., K. Wapenaar, and K. Larner (2006), Spurious multiples in seismic interferometry of primaries, *Geophysics*, 71(4), SI111–SI124.

Stein, S., and M. Wysession (2009), *An introduction to seismology, earthquakes, and earth structure*, 120-123 pp., John Wiley & Sons.

Tanimoto, T. (1999), Excitation of normal modes by atmospheric turbulence: source of long-period seismic noise, *Geophysical Journal International*, 136(2), 395–402.

Toksöz, N., and R. Lacoss (1968), Microseisms: Mode structure and sources, *Science*, 159(3817), 872–873.

VEOX (2010), Veracruz-Oaxaca Subduction Experiment in Mexico, doi:number 10.7909/C3MW2F2C.

Wapenaar, K., and J. Fokkema (2006), Greens function representations for seismic interferometry, *Geophysics*, 71(4), SI33–SI46.

Wapenaar, K., D. Draganov, R. Snieder, X. Campman, and A. Verdel (2010), Tutorial on seismic interferometry: Part 1 - Basic principles and applications, *Geophysics*, 75, 195–209, doi:10.1190/1.3457445.

Ward, R., C. Kendall, and P. Harris (1986), Upper Permian (Guadalupian) facies and their association with hydrocarbons, Permian Basin, west Texas and New Mexico, *The AAPG Geologists Bulletin*, 70(3), 239—262.

Wathelet, M., D. Jongmans, M. Ohrnberger, and S. Bonnefoy-Claudet (2008), Array performances for ambient vibrations on a shallow structure and consequences over v s inversion, *Journal of Seismology*, 12(1), 1–19.

Weaver, R., and O. Lobkis (2001), Ultrasonics without a source: Thermal fluctuation correlations at mhz frequencies, *Physical Review Letters*, 87(13), 134,301.

Welford, J. K., and R. Clowes (2004), Deep 3-d seismic reflection imaging of Precambrian sills in southwestern Alberta, Canada, *Tectonophysics*, 388(1), 161–172.

Widess, M. (1973), How thin is a thin bed, *Geophysics*, 38(6), 1176–1180.

Widiyantoro, S., B. Kennett, and R. Van Der Hilst (1999), Seismic tomography with P and S data reveals lateral variations in the rigidity of deep slabs, *Earth and Planetary Science Letters*, 173(1), 91–100.

Willis, R. (1929), Preliminary correlation of the Texas and New Mexico Permian, *AAPG Bulletin*, 13(8), 997–1031.

Yamauchi, M., K. Hirahara, and T. Shibutani (2003), High resolution receiver function imaging of the seismic velocity discontinuities in the crust and the uppermost mantle beneath southwest japan, *Earth, planets and space*, 55(1), 59–64.

Yang, T., S. P. Grand, D. Wilson, M. Guzman-Speziale, J. M. Gomez-Gonzalez, T. Dominguez-Reyes, and J. Ni (2009), Seismic structure beneath the rivera subduction zone from finite-frequency seismic tomography, *Journal of Geophysical Research: Solid Earth (1978–2012)*, 114(B1).

Yao, H., R. van Der Hilst, and V. Maarten (2006), Surface-wave array tomography in se tibet from ambient seismic noise and two station analysis and phase velocity maps, *Geophysical Journal International*, 166(2), 732–744.

Yilmaz, Ö. (1990), *Seismic data processing*, Society of Exploration Geophysicists.

Zhan, Z., S. N, D. Helmberger, and R. Clayton (2010), Retrieval of moho-reflected shear wave arrivals from ambient seismic noise, *Geophysical Journal International*, 182(1), 408–420.